



Catalytic conversion of biomass

Susana Guadix-Montero

**Thesis submitted in accordance with the requirements for
the degree of Doctor of Philosophy**

June 2019

Supervisor:
Dr Meenakshisundaram Sankar

**Cardiff Catalysis Institute,
School of Chemistry
Cardiff University**

STATEMENTS AND DECLARATION

STATEMENT 1

This thesis is being submitted in partial fulfilment of the requirements for the degree of PhD.

Signed  (Susana Guadix-Montero)

Date 6th June 2019

STATEMENT 2

This work has not been submitted in substance for any other degree or award at this or any other university or place of learning, nor is being submitted concurrently for any other degree or award (outside of any formal collaboration agreement between the University and a partner organisation)

Signed  (Susana Guadix-Montero)

Date 6th June 2019

STATEMENT 3

I hereby give consent for my thesis, if accepted, to be available in the University's Open Access repository (or, where approved, to be available in the University's library and for inter-library loan), and for the title and summary to be made available to outside organisations, subject to the expiry of a University-approved bar on access if applicable.

Signed  (Susana Guadix-Montero)

Date 6th June 2019

DECLARATION

This thesis is the result of my own independent work, except where otherwise stated, and the views expressed are my own. Other sources are acknowledged by explicit references. The thesis has not been edited by a third party beyond what is permitted by Cardiff University's Use of Third Party Editor by Research Degree Students Procedure.

Signed  (Susana Guadix-Montero)

Date 6th June 2019

WORD COUNT 47,458

(Excluding summary, acknowledgements, declarations, contents pages, appendices, tables, diagrams and figures, references, bibliography, footnotes and endnotes)

ACKNOWLEDGEMENTS

This thesis is the culmination of an excellent experience that I was fortunate to enjoy thanks to Cardiff University. All this would not have been possible without my supervisor, Dr M. Sankar. I would like to thank him for his academic support but also for giving me so many wonderful opportunities. I feel very grateful for his endless enthusiasm, something that I admire. Besides my supervisor, I would like to thank Prof. Stuart H. Taylor and Dr Nikolaos Dimitratos for their mentoring at the meetings evaluations during the research process. Moreover, thanks go to the research collaborators mentioned in the different sections of the thesis; with special mention to Dr Alberto Roldan and Dr David Willock for their computational contribution. Furthermore, thanks must be given to the technicians and members of the analytical services, with special mention to Simon Wallet and Dr Robert Jenkins for their help in offering me the resources that I needed for my research.

Also, I would like to express my very great appreciation to Prof. Graham Hutchings, who made the Cardiff Catalysis Institute the prestigious research institute that it is today. I will not forget to express the gratitude to the rest of the members of the CCI and Sankar's group. I came to learn so many things from all of you.

I would like to express my gratitude to all the people who have made my time in Cardiff unforgettable. Heartfelt thanks go to my friends for that daily lunch at the Maxnet's room debating about politics among other topics and those Catan evenings. Special mention goes to Sara, Maco, Guilia, Anna, Keiko and Tatti for our amazing dancing nights. Moreover, to my flatmates, Guilia and Laura for the delicious Italian delicatessen meals. Likewise, a big thank you to my friends in Spain for encouraging and help me to switch off every time we did a skype call or we could meet.

Last but not least, I would like to thank my family, who supported me throughout my life. To my parents, who always believe that I could make any dream become true. To my sisters for their wise counsel and sympathetic ear. And to my brother who I still feel close to, even living in different countries. Finally, a special thanks to my partner in the journey of life, who kept me on track during the course of this thesis, despite the distance. They are the most important people in my world. They gave me enough moral support and strength to accomplish my personal goals; hence, I dedicate this thesis to them.

AGRADECIMIENTOS

Esta tesis es la culminación de una excelente experiencia que tuve la suerte de disfrutar en la Universidad de Cardiff. Todo esto no hubiera sido posible sin mi supervisor, el Dr. M. Sankar. Me gustaría darle las gracias por su apoyo académico, pero también por darme tantas oportunidades maravillosas. Me siento muy agradecida por su entusiasmo interminable, algo que admiro. Además de mi supervisor, me gustaría agradecer al profesor Stuart H. Taylor y al Dr. Nikolaos Dimitratos por su tutoría en las evaluaciones durante el proceso de investigación. Y a los colaboradores de investigación mencionados en las diferentes secciones de la tesis por su contribución a este trabajo; con mención especial al Dr. Alberto Roldan y al Dr. David Willock por la contribución computacional. También debo dar las gracias a los técnicos y miembros de los servicios analíticos, especialmente a Simon Wallet y al Dr. Robert Jenkins por su ayuda para ofrecerme los recursos que necesitaba para mi investigación.

Además, me gustaría expresar mi gran aprecio al Prof. Graham Hutchings, quien hizo del Instituto de Catálisis de Cardiff el prestigioso instituto de investigación que es hoy. No me olvidaré de expresar mi agradecimiento al resto de los miembros de la ICC y el grupo de Sankar. Aprendí muchas cosas de todos vosotros.

Me gustaría expresar mi gratitud a todas las personas que han hecho que mi estancia en Cardiff sea inolvidable. Un sincero agradecimiento a mis amigos por esos almuerzos en la sala de Maxnet, debatiendo sobre política entre otros temas y por esas noches de Catan. Mención especial para Sara, Maco, Guilia, Anna, Keiko y Tatti por nuestras increíbles noches de baile. Por otra parte, a mis compañeras de piso, Guilia y Laura por las deliciosas delicatessen italianas. De la misma forma, quería darle las gracias a mis amigas en España por animarme y ayudarme a desconectar cada vez que hicimos una llamada de Skype o nos pudimos ver.

Por último, pero no menos importante, me gustaría agradecer a mi familia que me apoyó durante toda mi vida. Para mis padres que siempre han creído que podía hacer realidad cualquier sueño. A mis hermanas por sus consejos y por ser tan comprensivas. Y mi hermano con quien siempre me siento cerca, incluso viviendo en diferentes países. Además, no puede faltar un agradecimiento muy especial a mi compañero de viaje, Ismael, que me mantuvo en el camino durante uno de los períodos más difíciles de este proceso, a pesar de la distancia. Son las personas más importantes de mi mundo. Me dieron suficiente apoyo moral y fuerza para lograr mis objetivos personales; por eso les dedico esta tesis.

*“I have come to learn that every great dream begins with a dreamer.
Always remember, you have within you the strength, the patience, and the
passion to reach for the stars to change the world.”*

- Harriet Tubman-

ABSTRACT

There is a global need to deal with the growing chemical and energy demands without compromising the environment. The conversion of different biomass-derivate feedstock still needs to improve to accomplish a biorefinery able to compete with the conventional refineries. The work presented in this thesis investigates two different catalytic approaches to selectively cleave the C-O bond over the C-C bond and *vice versa* for bio-derived feedstock molecules. In the industrial biodiesel production, the by-product obtained in large proportion – glycerol – requires to be converted into more valuable products, such as propanediols. Therefore, the design of heterogeneous catalyst for the selective scission of the C-O bond in the presence of the C-C bond of glycerol is one of the objectives of this thesis. Another kind of biomass is lignocellulosic biomass (waste biomass). Depolymerisation of lignin requires the breaking of C-C bond over the C-O bond. In this context, the second objective is to develop a catalytic system that selectively cleaves C-C bond for lignin model compounds, aiming at lignin depolymerisation.

The first part of the thesis reports the synthesis, catalytic activity, and characterisation of monometallic Pd, Ru, Pt and bimetallic PdRu, RuPt nanoparticles supported on TiO₂ for the hydrogenolysis of glycerol at relatively low temperatures (165 °C) using gaseous H₂. All these catalysts were found to be active but showing different products distributions. It was found that the incorporation of a second metal to monometallic Pt and Pd catalysts resulted in a compromise between conversion and selectivity towards C₃ products *via* C-O bond cleavage. Detailed characterisation using XPS, SEM-EDX, STEM, TGA and computational modelling was employed to rationalise the difference in the catalytic properties of monometallic and bimetallic catalysts. The data revealed the important correlation between metal oxidation state, nanostructure and their catalytic properties. Among all the catalysts tested, PdRu over TiO₂ catalysts presented good conversion, selectivity and reusability upon glycerol hydrogenolysis.

For glycerol hydrogenolysis reaction, the role of support was investigated using the best PdRu bimetallic combination. Several metal oxides and zeolites with diverse framework structure types were employed for the study. The textural properties of these catalysts were analysed (BET surface area and pore size distribution) and their elemental and structural properties were further characterised using XPS, MP-AES, SEM, and TEM. Furthermore, the hydrothermal stability of the zeolite-based catalyst was investigated. Finally, the relative acid site density of the samples was determined by NH₃-TPD for all the catalysts. Pyridine DRIFT of the most

significant catalysts was also performed. The effect of the catalyst acidity was found to correlate with the bifunctional catalyst activity, showing an optimum value within a volcano plot.

In the next part of the thesis, the study of lignin model compounds bearing similar linkages and functionalities, present in native lignin, are used to investigate lignin depolymerisation research. This thesis reports the catalytic bond cleavage of different inter-unit linkages present in lignin model compounds. Ruthenium ion catalysed oxidation, known as RICO reaction, is an effective method to disrupt the most recalcitrant inter-unit linkages in lignin, such as β -5 and 5-5', at room temperature and atmospheric pressure. Oxidation of simple model compounds and degradation of a polymeric model as β -O-4 polymer and a hexamer model compound, closer to the lignin structure, was accomplished at rapid reaction times. Several techniques, namely, FT-IR, ^1H , ^{13}C , HSQC, HMBC and ^{31}P NMR, were used to characterise the materials and monitor the reactions. A detailed description of the methodology employed for the estimation of the potential bond cleavage of the inter-unit linkages is detailed in this thesis. From the data reported, RuO_4 could play an important role in the oxidative depolymerisation of technical and native lignin *via* the opening of aromatic rings to form carboxylic acids and aldehydes. Finally, a summary of all the results and potential ideas for future research in the areas of bimetallic catalysts for glycerol hydrogenolysis and RICO for oxidative depolymerisation of lignin are presented.

PREFACE

Publication related to the content of the chapters of this thesis:

Review on Catalytic Cleavage of C-C Inter-unit Linkages in Lignin Model Compounds: Towards Lignin Depolymerisation, **Susana Guadix-Montero**, Meenakshisundaram Sankar, Topics in Catalysis, April 2018, Volume 61, Issue 3–4, pp 183–198

CONTENTS

1	Introduction.....	13
1.1	Biorefinery and biomass valorisation	13
1.2	Triglyceride feedstocks biomass.....	15
1.2.1	Glycerol as a platform molecule	16
1.2.2	Catalytic hydrogenolysis of glycerol to propanediols	18
1.3	Lignocellulosic feedstocks biomass.....	28
1.3.1	Chemical composition and structure of lignin	29
1.3.2	Lignin valorisation	35
1.3.3	Ruthenium ion catalysed oxidations	45
1.4	Aim and outline of the Thesis	53
1.5	References.....	55
2	Experimental	69
2.1	Introduction.....	69
2.2	Glycerol hydrogenolysis	69
2.2.1	Catalyst preparation	69
2.2.2	Catalyst testing.....	70
2.2.3	Analytical techniques.....	74
2.2.4	Catalyst characterisation	77
2.3	Lignin depolymerisation	94
2.3.1	Synthesis of model substrates	94
2.3.2	RICO reaction protocol.....	96
2.3.3	Analytical techniques.....	100
2.4	References.....	111
3	Ruthenium-based bimetallic catalyst for selective glycerol hydrogenolysis.....	116
3.1	Introduction.....	116
3.1.1	Batch reactor	118

3.1.2	Continuous fixed bed reactor	140
3.1.3	Catalyst characterisation by electron microscopy.....	144
3.2	Conclusions.....	148
3.3	References.....	150
4	Role of support in glycerol hydrogenolysis	157
4.1	Introduction.....	157
4.2	Catalytic activity	159
4.3	Catalyst characterisation	164
4.3.1	Analysis of the textural properties of the catalysts.	164
4.3.2	Elemental analysis and oxidation state species of the catalysts.....	167
4.3.3	The surface chemistry and structure of the supported catalyst for glycerol hydrogenolysis	175
4.3.4	Effect of catalysts acidity on hydrogenolysis of glycerol.....	185
4.4	Conclusions.....	188
4.5	References.....	190
5	Catalytic cleavage of C-C inter-unit linkages in lignin model compounds.	197
5.1	Introduction.....	197
5.2	Carbon-carbon bond cleavage in dimeric model compounds using RICO.....	198
5.2.1	Oxidative cleavage of 5-5' inter-unit linkage in biphenyl.	199
5.2.2	Oxidative cleavage of β -1' inter-unit linkage in bibenzyl	210
5.3	Carbon-Carbon bond cleavage in complex lignin model compounds using RICO. Towards lignin depolymerisation	215
5.3.1	Oxidative cleavage of C-C bond in β -O-4' lignin model polymer.	215
5.3.2	Oxidative cleavage of different inter-unit linkages in a hexamer model compound	219
5.4	Conclusions.....	239
5.5	References.....	241
6	General conclusions and prospects	247

6.1	Conclusions.....	247
6.2	Future work.....	250
6.3	References.....	252
7	Appendix.....	253
7.1	EDX	253
7.2	SEM-EDX.....	254
7.3	XRD	255
7.4	NH ₃ -TPD.....	256
7.5	RICO.....	261

CATALYTIC CONVERSION OF BIOMASS

CHAPTER 1. INTRODUCTION

S. Guadix-Montero
CARDIFF UNIVERSITY | CARDIFF CATALYSIS INSTITUTE

Contents

1	Introduction.....	13
1.1	Biorefinery and biomass valorisation	13
1.2	Triglyceride feedstocks biomass.....	15
1.2.1	Glycerol as a platform molecule	16
1.2.2	Catalytic hydrogenolysis of glycerol to propanediols	18
	• Non-noble metal catalyst for the conversion of glycerol to propanediols.....	20
	• Noble metal catalyst for the conversion of glycerol to propanediols	21
	○ Catalytic hydrogenolysis over Pd-based catalysts	22
	○ Catalytic hydrogenolysis over Pt-based catalysts	23
	○ Catalytic hydrogenolysis over Ru-based catalysts	26
1.3	Lignocellulosic feedstocks biomass.....	28
1.3.1	Chemical composition and structure of lignin	29
	• Native and technical lignins	33
1.3.2	Lignin valorisation	35
	• Catalytic C-C bond cleavage in lignin model compounds and technical lignins..	36
	○ Oxidative C-C bond cleavage	37
1.3.3	Ruthenium ion catalysed oxidations	45
	• Ruthenium (VIII) chemistry	46
	○ Oxidation of aromatic compounds	51
1.4	Aim and outline of the Thesis.....	53
1.5	References.....	55

1 Introduction

1.1 Biorefinery and biomass valorisation

The greatest challenge that our society faces nowadays is the growing demand for energy and commodity chemicals because of population growth along with the increasing demand from emerging large economies.¹ This situation is further complicated due to the depletion of fossil fuel-based feedstock to produce them, the greenhouse effect and consequent climate changes.² There is a need to deal with chemical and energy security issues without compromising the environment. One of the alternatives for achieving this is to use green and sustainable alternatives to conventional feedstock for producing commodity chemicals and fuels.³ The concept of biorefinery has been proposed by the International Energy Agency (IEA).⁴ Its widely accepted definition is: *Biorefinery is the sustainable processing of biomass into a spectrum of marketable products (food, feed, materials, chemicals) and energy (fuels, power, heat).*⁵ The development of the biorefinery concept in the 1990s promoted a great interest in the research on sustainable chemical production.⁶ The investment is then heading in the direction of discovering new technologies to deal with the new range of raw materials. Many of these technologies are now at their pre-commercial stage.⁷

There are many ways of classifying biomass. However, one of the most accepted is categorising according to its molecular structure of the feedstock in three main groups, a) triglycerides, b) starch and oligomeric sugars and c) lignocellulose.⁸ We can find different kinds of biorefineries depending on the feedstock, platform, products obtained, or the conversion technology/process employed to produce it. According to the IEA Bioenergy Task 42 individual biorefineries can be combined,⁹ since there are some processes which are suitable for more than one platform. Platforms and conversion processes are linked together in a complex biorefinery system, *Figure 1-1*. This biorefinery network leads to replacing fossil-energy-based marketable products most efficiently, keeping socio-economic demands.¹⁰ Nevertheless, new issues derivative of the resources of biomass needs to be addressed after the fuel vs food debate.¹¹ The disputes from the implementation of the 1st generation of biofuels led to the development of 2nd generation biofuels. Lignocellulosic biomass from waste biomass that does not compete with food crops is used as the feedstock to produce chemicals and fuels.¹²⁻¹⁴ Therefore is necessary not only a competitive economic biorefinery able to replace as much as possible the conventional refinery but also attending the social and ethical challenges in its establishment.¹⁵

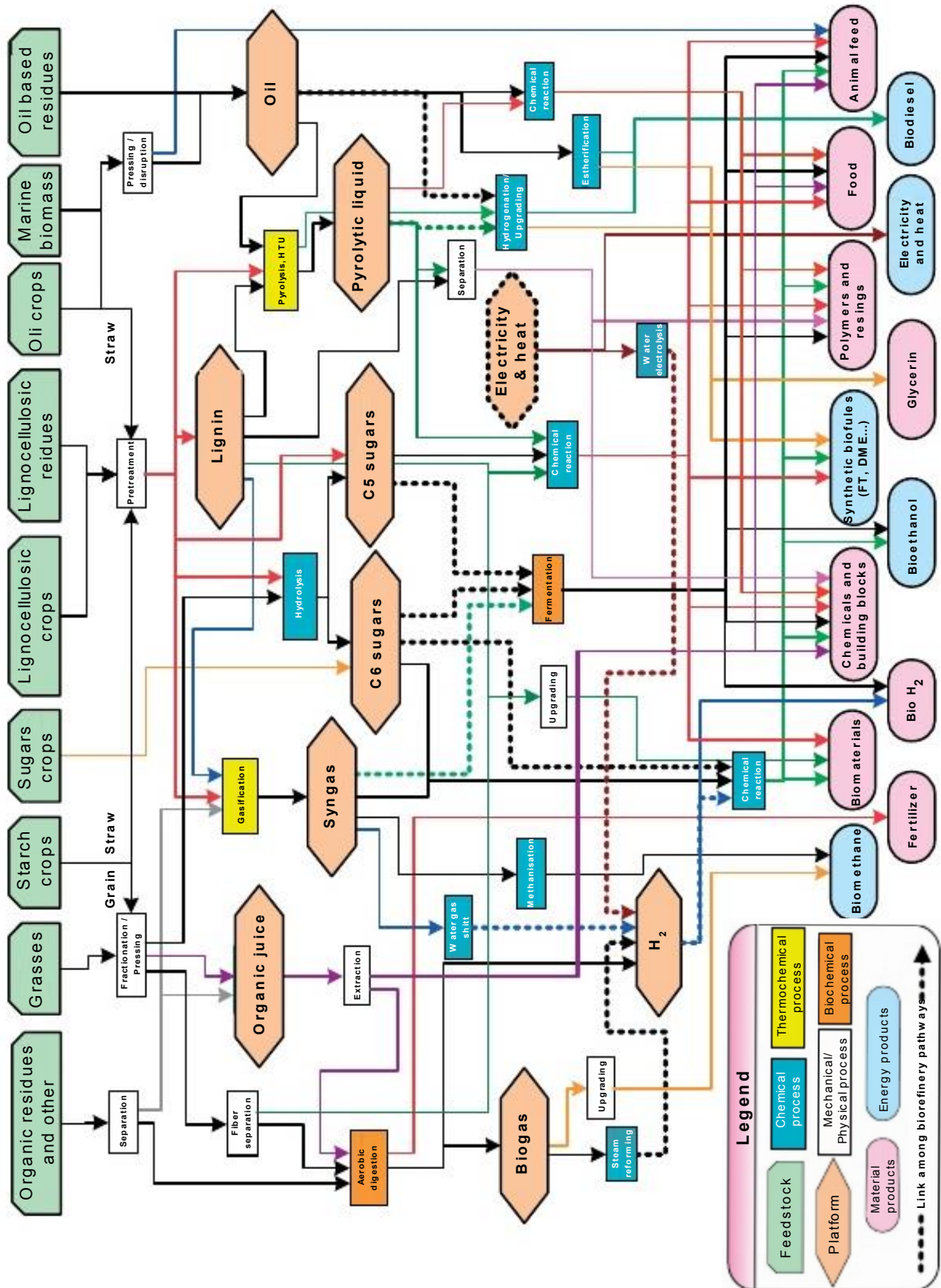


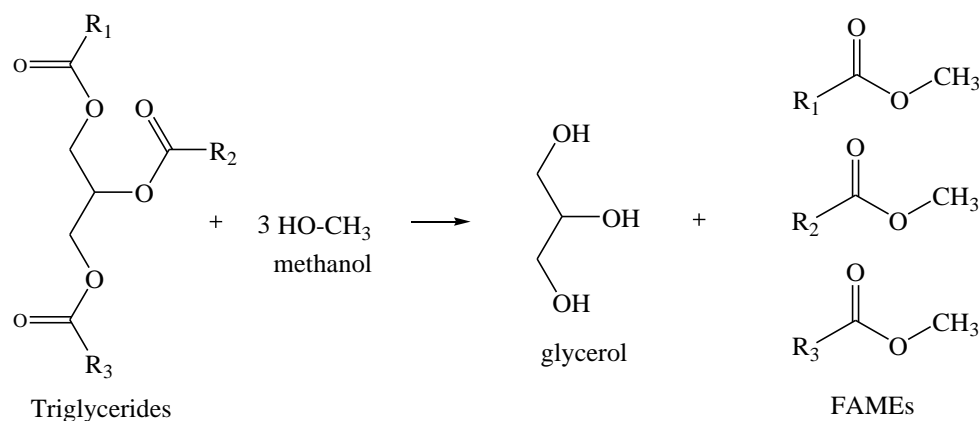
Figure 1-1 Network where the individual biorefinery systems are combined. Copyright © 2009, John Wiley & Sons, Ltd. Reproduced with permission of Ref.⁹

1.2 Triglyceride feedstocks biomass

In our endeavour for clean energy sources, catalytic biomass conversion has a crucial role in replacing fossil fuel for renewable fuels.^{16,17} Biofuels production comprises biohydrogen, biogas, biodiesel and bio-alcohols, which are assuring tendency of alternative energy.^{8,18,19} The current consumption of fossil fuel accounts for more than half of the global greenhouse gases (GHGs) emissions.²⁰ Some sectors still question the future and potential of biofuels, although recent studies proved that it could contribute to mitigating the GHGs since they are carbon neutral.^{20–23} Nowadays, the urgent need to reduce the impact of global warming is on the global agenda with the ongoing transition to a low-carbon and climate resilient society.^{24–27}

Biodiesel is unquestionably the most produced biofuel in Europe; it involves about 37 % of the global production.¹⁹ Biodiesel is a derivative of vegetable oils from the seeds of different plants, i.e. rapeseed, palm, soya bean, sunflower, peanut and olive; and from lipids from animal fats.^{19,28} Both oils and fats are known as triglycerides, which are esters of three fatty acids and one glycerol derivation.²⁹ This kind of biofuel is industrially produced *via* transesterification of triglyceride-rich biomass feedstock.³⁰ In this process triglycerides are converted to FAMES (Fatty Acid Methyl Esters), using alcohols and an acid/base catalyst (*Scheme 1-1*).^{31,32} This process is providing renewable feedstocks and less hazardous chemical syntheses, answering to the principles of green chemistry.

However, a disadvantage that the biorefining industry brings is that although the energy resource is deemed renewable, many by-products are produced and they need to be treated. This inconvenience can be addressed firstly developing a biorefinery that can minimise the production of undesirable by-products; if there is no potential market or find an efficient process to revalorise them. Glycerol is the main by-product of the transesterification process into biodiesel production. It is produced when triglycerides are treated with methanol and a surfactant to produce the FAMES. Indeed, about 10 % of the weight of biodiesel is converted in glycerol.^{33,34} The crude glycerol produced has a purity of around 50 %.³³ It contains impurities such as methanol, soap, catalysts, organic materials and water. Until recent studies, it was deemed as a waste product.³⁵ The global production and price of glycerol are affected by the massive demand for biodiesel.³⁶ Crude glycerol, also known as glycerine, has a low price due to the massive expansion of biodiesel production.^{37,38}



Scheme 1-1 Generation of glycerol by biodiesel processes. Adapted from Ref.³²

1.2.1 Glycerol as a platform molecule

According to the US Department of Energy (DoE, 2004), glycerol as pure chemical (1,2,3-propanetriol) has been considered as one of Top-12 building block from biomass.²⁸ Due to its availability and low cost, glycerol has excellent potential as emerging renewable bio-derived feedstock to produce high-value products.^{34,39,40} Glycerol as a platform molecule can produce a broad and diverse range of commodity products depending on the process employed (i.e. oxidation, dehydration, esterification and carboxylation), see *Figure 1-2*.^{32,36,41–43} From all the possible products, the formation of acrolein is the most widely studied.^{44–46} As a chemical intermediate, acrolein, has large industrial applications, i.e. acrylic acid, DL-Methionine and superabsorbent polymer production.³⁶ In the last decades, attention has been the focus on glycerol conversion. The combination of both dehydration and hydrogenation, hence given the term, hydrogenolysis.^{47,48} Glycerol contains a high ratio of O/C, which makes it suitable for hydrogenolysis.⁴¹ The cleavage of the C-C and C-O bond occurs in the presence of hydrogen.⁴⁶

C2-diol ethylene glycol (EG) is a significant product obtained from glycerol hydrogenolysis.⁴⁹ EG, also known as mono-ethylene glycol (MEG) is a useful by-product, commonly used as automobile antifreeze, but also as the raw material of polyester for fibres, films and bottles.⁵⁰ For instance, it is one of the two compounds needed to produce bio-based Polyethylene terephthalate (PET). Bio-PET leads the bio-based polymer production, which is impelled by The Coca-Cola Company.⁵¹ It is currently produced by hydration of ethylene oxide (EO) in very high yields.^{50,52} However, hydrogenolysis of glycerol to C3 diols, such as propanediols has an enormous profitable status.^{53,54} Propylene glycol in the form of 1,2-propanediol (1,2-PDO) has gained the most consideration as a non-toxic commodity. It is used for a very diverse range of applications, from the pharmaceutical industry to the food additives, cosmetics and as

a precursor to polymerisation reactions.^{32,55} On the other hand, in 1881 Freund first found 1,3-propanediol (1,3-PDO) as a fermentation product, which was considered a useless product.⁵⁶ Lately, 1,3-PDO is becoming of highest interest as a building block for the production of bio-based polymers, such as polyesters and polyurethanes. More specifically, it is required for the production of a biodegradable polymer, polytrimethylene terephthalate (PTT) polyester, which has excellent potential for use in textile manufacturing.^{32,56} However, currently, they are produced employing fossil fuel-based sources.⁴¹

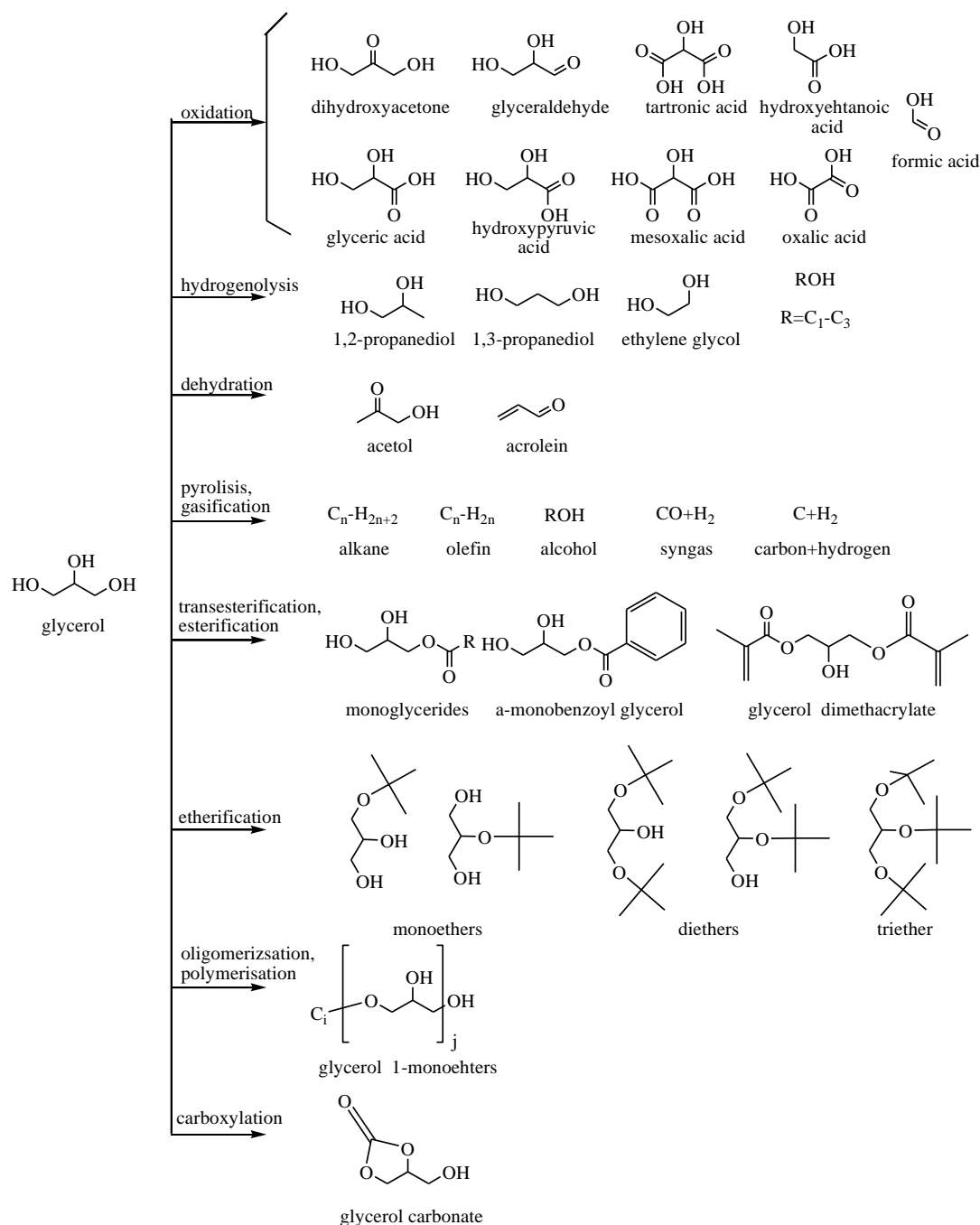


Figure 1-2 Glycerol conversion methods to produce value-added products. Adapted from Ref.⁴²

1.2.2 *Catalytic hydrogenolysis of glycerol to propanediols*

Selective production of C3-diols from glycerol has attracted the interest of both research and industry community. In contrast, C1 and C2 diols can be obtained from other inexpensive biomass-derived platform molecules such as carbon monoxide and ethanol.^{55,57,58}

In the late 1980s, Celanese Corporation patented the first process for the production of propanediols in the presence of Rh(CO)₂ acetylacetonate, soluble tungsten and Group VIII metal-containing catalyst composition.⁵⁹ Later, Shell Oil Company patented another homogeneous catalytic system using Pd complexes, obtaining *ca.* 30 % 1,3-PDO yield.⁶⁰ Nevertheless, the separation and recovery of the homogeneous catalyst lead to the development of a heterogeneous catalyst for this reaction.⁶⁰

Hydrogenolysis of glycerol on heterogeneous catalysts can be carried out in liquid or vapour phase reactions.⁶¹ Studies of liquid-phase catalytic conversion of biomass-derived oxygenated hydrocarbons to fuels and chemicals were reviewed by Dumesic *et al.*⁴⁶ Based on the numerous reports of liquid-phase hydrogenolysis of glycerol; it can be concluded that metal surfaces can catalyse C-O hydrogenolysis.^{32,46,62–64} A large variety of metals, both noble metals (Ru, Rh, Pd, Ir, Pt, Re, Ag, Au) and non-noble metals (Co, Ni, Cu, Zn, Al, Fe, Mg, Si) catalysts have been tested for this reaction.^{65–67} Supported nanoparticles or nanoclusters as a catalyst using pure or monometallic catalyst do not always get a satisfactory performance. In those cases, careful catalysts design can improve the catalytic properties such as activity, selectivity and/or stability system. For instance, using a bifunctional catalyst, base or acid, ligands, a good support selection, or even the addition of other metals are some of the strategies used to enhancing catalytic properties. A good example is the work carried out by Tomishige's group, a pioneer in the development of Re-based modified catalyst.^{53,68,69}

The use of bimetallic catalysts was first introduced by Sinfelt *et al.*^{70,71} After that, several research groups have developed many bimetallic catalysts for a variety of organic transformations.^{72–75} It has been proved that the addition of a second metal to a primary metal to form bimetallic nanoparticles can influence the catalytic properties of supported pure/monometallic catalysts.^{76,77} However, the catalytic properties can be different from nanoparticles of 'bulk' alloys, depending on the type of metals patterns.⁷⁸ Mixing two metals (A and B) to form a bimetallic nanoalloy catalyst could produce different mixing patterns: a) Core-shell structure (A_{core}B_{shell}), b) Sub-cluster segregated nanoalloys (A-B bonds), c) homogeneous alloys (ordered and random A & B), and d) Multi-shell alloys (layered or onion-

like alternating -A-B-A- shells).⁷⁶ Therefore, it is of great interest the design of bimetallic catalyst to solve the challenges for the successful biomass conversion, which also applies to glycerol hydrogenolysis.

Regarding the support, many researchers have focused their attention on the use of carbon as support.^{47,79–84} But also metal oxides such as CoO,^{48,85,86} SiO₂,^{65,87–89} Al₂O₃,^{62,90} TiO₂,⁹¹ ZrO₂^{92,93} were used for this reaction. On the other hand, zeolites are solid catalysts exhibiting both Brønsted and Lewis acidity. These materials have been used for promoting the dehydration of glycerol.^{94–96} Their use for hydrogenolysis has been used more extensively in the vapour phase reaction.^{97,98} The use of mixing oxides would also be described in this chapter. A summary of the literature discussed in the next subsection is presented in *Table 1-1*.

Table 1-1 Glycerol hydrogenolysis over heterogeneous catalyst

<i>Metal</i>	<i>Support</i>	<i>wt, %</i>	<i>t, h</i>	<i>T, °C</i>	<i>P, bar</i>	<i>Conversion, %</i>	<i>1,2-PDO Sel., %</i>	<i>1,3-PDO Sel., %</i>	<i>Ref.</i>
Cu	Al ₂ O ₃					100	93	-	61
Ni₂P	SiO ₂			220	30	95.1	85.9	-	89
Ni	SiO ₂			220	30	73.2	49.9	-	89
NiCu	Al ₂ O ₃	35	24	220	45*	90	82	-	62
NiCu	-		10	220	45*			-	90
NiCu	γAl ₂ O ₃	20	12	210	45	71.6	92.8	-	67
Co	MgO	15		200	20	44.8	42.2	-	105
Cu-ReOx	SiO ₂	25.5	10	200	80	63.2	92.6	-	106
ZrNi	H-beta	5	10	200	41	77	26	14	107
Rh	Al ₂ O ₃	5	168	180	80	27	46	12	64
Rh	SiO ₂	4	10	120	80	8	30	30	65
Ir-ReOx	SiO ₂	4	4	120	80	9.7	32	21	108
Ir-ReOx	SiO ₂					81	47	-	109
Ag	OMS-2	30	8	200	50	25	70	-	111
PdCo				180	40	70	87	-	48
PdFe	Fe ₃ O ₄	5		180	40	42	90	-	48
PdRe	SBA-15	15	18	200	80	45	60	-	115
PtRe	CNT	10	8	200	80	55	50	15	121
PtRe	SiO ₂	1	8	120	40	8.3	40	24	122
Pt	WO _x /Al ₂ O ₃	9	4	200	90	62	8	60	123
Pt	WO _x	2	12	160	55	60	3.1	36.3	128
Pt	WO _x	0.1	12	140	10	37.4	2.3	35.1	129
Pt	WO _x /Al ₂ O ₃	2	12	140	10	23.2	7.2	48.2	129

AuPt	WO _x / Al ₂ O ₄	0.1	12	140	10	81.4	1.5	51.6	130
Pt	H- MOR	2	3	225	10	95	12	48	98
Ru	TiO ₂	3		230	1	60	42	-	131
Ru	MgO	3		230	1	24	22	-	131
Ru	CeO ₂	3		230	1	29	14	-	131
Ru	MCM- 4	3				62	38	20	132
Ru	TiO ₂ - bentonite	5	7	150	20	69.8	80.6	-	133
Ru	C + Amberlyst	5	10	180	80	48.8	70.2	1.3	134
RuIr	ReO _x / SiO ₂	4.4	4	200	80	44.6	16	38.5	135
RuRe	SiO ₂ - c350	6.8	8	160	80	51.7	44.8	4.2	138
RuCu	TMGL (ionic liquid)	3	18	230	80	100	85	-	139
RuCu	ZrO ₂	3.19	24	180	80	100	78.5	-	140
RuCo	ZrO ₂	10.8	10	180	50	56.2	70.3	-	93
RuAu	AC	1	8	150	7	15	64	-	141
AuRu	AC	1	8	150	7	33	73	-	141
AuRu	C	5.85	5	200	40	25	30	-	81
PtRu	C	6.6	5	200	40	42	25	-	81

* Pressure under N₂ atmosphere using hydrogen donor molecules

- **Non-noble metal catalyst for the conversion of glycerol to propanediols**

Inexpensive non-noble metals such as Cu, Ni and Co catalysts are widely used for high selectivity towards 1,2-PDO.^{57,99} Suppers and co-workers explored the performance of a copper-chromite catalyst for the dehydration of glycerol producing high acetol selectivity (90 %).^{100,101} The same group yielded for propanediols in the presence of hydrogen, using mild conditions and low pressure (200 °C and 200 psi).¹⁰² In their catalyst, chromium acts as a stabiliser to preventing sintering. Sato *et al.* studied the vapour phase reaction, achieving 93 % of selectivity using Cu/Al₂O₃.⁶¹ They also concluded that 1,2-PDO is favoured at high hydrogen partial pressure. However, the activity and stability of the Cu catalyst needed to be improved.^{67,103}

In general, nickel and ruthenium catalysts gave more degradation products than copper catalysts, obtained from the glycerol C-C bond cleavage. Huang *et al.* found that Ni catalyst could be improved using the Ni₂P phase, due to the synergism between acid sites (P-OH) and the metal sites (Ni).⁸⁹ Gandarias *et al.* developed a Ni-Cu bimetallic catalyst tested for glycerol

conversion under hydrogen generated *in-situ*.^{62,90} This interesting approach avoids the use of hydrogen gas under relatively high pressure. It is thought that the decomposition of formic acid produces the donate hydrogen. This process is forming CO₂ as a by-product, and thus the subsequent hydrogenation reaction on the metal catalyst surface can occur to afford the desired product. They achieved excellent yields, but the metal loadings used was about 35 wt. %. Then, Pudi *et al.* employed the same bimetallic combination. The latter authors found an increase in the glycerol conversion from 20 % in the monometallic Cu to 45-59 % with the Cu-Ni/ γ -Al₂O₃.⁶⁷ However the metal loading used was quite large (up to 20 wt. %). Besides, note that the addition of a second metal not always results favourably. For instance, Tomishige and co-workers experienced that the incorporation of Pt into a Ni/SiO₂ catalyst improved the C-C scission increasing the yield of EG and CH₄.¹⁰⁴

Guo *et al.* reported a bifunctional 15 wt. % Co/MgO catalyst that was also tested for the production of 1,2-PDO (selectivity between 50-70 %).¹⁰⁵ Again, the conversion decreased substantially from 45 % to 14 % by reusing the catalyst, indicating insufficient catalyst stability. Efforts to amend this critical aspect had been made. Recently, Huang *et al.* found that incorporation of rare-earth additives (such as Y and La) to a 25.5 wt. % Cu-ReO_x/SiO₂ catalysts would improve the active Cu catalyst stability.¹⁰⁶ Here, the rare-earth additives can work inhibiting partially the sintering and leaching of Cu.

Metals transition such as Ni, Cu, Zn, and Zr supported on zeolites (H-beta) showed that it could be a good support choice as a bifunctional catalyst. These have Brønsted and Lewis acidity convenient for the conversion of glycerol to 1,3-PDO.¹⁰⁷ The best metal was the bimetallic Zr-Ni/H-beta that gives a 77 % of glycerol conversion and 14 % 1,3-PDO selectivity.

- ***Noble metal catalyst for the conversion of glycerol to propanediols***

In general, it has been reported that supported noble-metal catalysts are more active than non-noble transition metal oxide catalysts but less selective.⁶⁴ Chaminand *et al.* reported Rh catalyst supported on different materials (ZnO, C, Al₂O₃), using different solvents for this reaction (H₂O, sulfolane, dioxane).⁶⁴ The authors concluded that the solvent had a strong effect, being water the most suitable for the selectivity towards 1,2-PDO. Regarding the support, C and Al₂O₃ showed the highest conversion 21 and 27 % respectively, being C the one that exhibits the higher selectivity (*ca.* 70 %). The authors also proved that by adding an additive (H₂WO₄), the conversion improved from 2.5 and 10 %. In the case of Rh, the addition of a second metal (Fe or Cu) reduced the activity (< 10 % of conversion). The second metal was considered to

act as if the catalyst is poisoned. Tomishige and co-workers also studied Rh catalysts, achieving better activity and selectivity with Rh/SiO₂ than Ru/C. However, the values towards 1,2-PDO were lower than 30 %, at conversion < 8 %, using high pressure of H₂ (80 bar) and 120 °C.⁶⁵ They also reported the effect of Amberlyst on the Rh/SiO₂, which enhance the conversion about an extra 10 %. The same research group developed a novel rhenium-oxide-modified supported rhodium nanoparticle on silica (Rh-ReO_x/SiO₂), which shows small ReO_x clusters on the Rh metal surface.¹⁰⁸ However, Nakagawa *et al.* reported that the use of the bimetallic Ir-ReO_x/SiO₂ catalyst increase the selectivity towards 1,3-PDO.^{69,109} These authors proposed a possible mechanism for the glycerol hydrogenolysis through Ir-ReO_x/SiO₂ catalyst. In the first- place glycerol is adsorbed on the ReO_x while the hydrogen is activated on the Ir metal. Then, H₂ attacks the 2-position of the 2,3-dihydroxypropoxide to form 3-hydroxypropoxide. In the last step, 3-hydroxypropoxide releases 1,3-propanediol *via* hydrolysis.

On the other hand, Ag-based catalysts are also selective to 1,2-PDO more similar than Cu catalyst, unlike most supported noble metal catalyst.³² Ag supported on γ -Al₂O₃ was tested for this reaction giving good activity (*ca.* 46 mol% conversion and 96 mol% 1,2-PDO).¹¹⁰ However, Ag sintering produced deactivation of the catalyst. Another active and, in this case, very stable catalysts was developed by Yadav *et al.* (30 wt. % Ag-OMS-2).¹¹¹ In this catalyst Ag is incorporated in an octahedral molecular sieve producing about 25-30 % of conversion and 1,2-PDO selectivity between 70-80 %. Bimetallic Ag-Ni catalyst enhanced the hydrogenation ability of Ni catalysts.¹¹² Bimetallic involving Pd, Pt or Ru metals will be detailed in the following sections.

- *Catalytic hydrogenolysis over Pd-based catalysts*

Pd monometallic catalyst has been used for this reaction showing very poor conversion.⁶⁴ Musolino *et al.* reported an active Pd catalyst synthesis based on the coprecipitation technique.^{48,85,86} Bimetallic Pd-M catalyst was then developed (M = Co, Fe, Zn, Ni) and tested using 2-propanol as a solvent. The best catalyst performance was achieved with the PdCo and PdFe (70 % and 42 % conversion in 24 h, at 180 °C and 40 bar of H₂).⁴⁸ However, Pd/NiO showed the highest selectivity value (85 %) towards 1,2-PDO. The results gave better performance than the Pd catalyst prepared by the wet impregnation method.

In 2012, Sankar *et al.* developed a Pd-based bimetallic catalyst synthesis using a strategy based on the addition of excess chloride ions during the conventional wet-impregnation method.^{76,113} The excess of chloride ions was effective for dissolving the water-insoluble palladium

precursor salts (PdCl_2). This advantage allowed them to control both, particle size and composition; producing small average particle size (2-6 nm), an optimised random alloy composition. This stabiliser-free modified impregnation (M_{Im}) method was first used to prepared Au-Pd bimetallic catalyst.^{75,113,114} After that, Li *et al.* applied this technique for preparing Pd-Re bimetallic catalyst for hydrogenolysis of glycerol.¹¹⁵ They found that adding Re to Pd improved the activity of Pd catalyst due to an increase in the catalyst acidity from ReO_x (see *Figure 1-3*).¹¹⁶ They studied a PdRe/SBA-15 catalyst, obtaining a 45 % conversion and 60 % selectivity towards 1,2-PDO at 200 °C and 80 bar H_2 for 18 h with 5 wt. % Pd – 10 wt. % Re/SBA-15 catalyst. The latter authors also reported that basic oxides (MgO , La_2O_3 and CeO_2) could limit further reduction of the products and maintain the selectivity to 1,2-PDO instead of 1-propanol, observed with acid oxides (Al_2O_3).

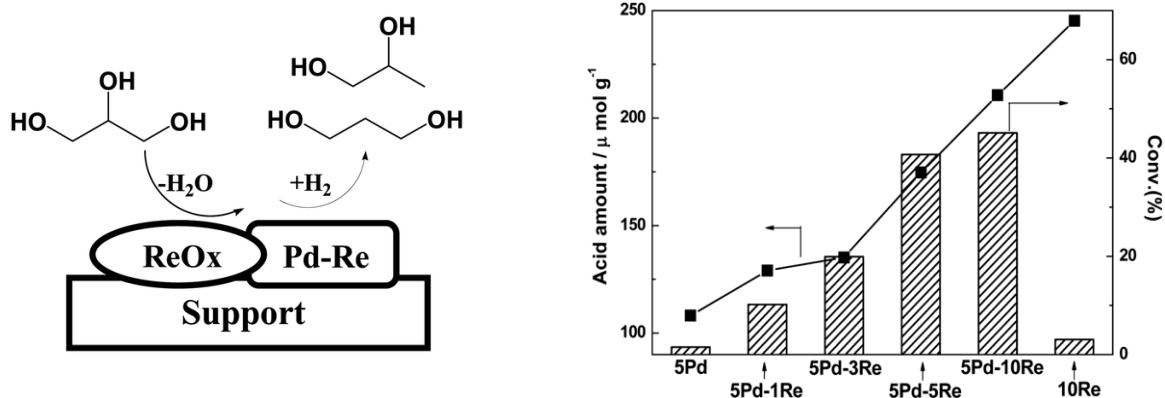


Figure 1-3 Proposed working mechanism of the Pd-Re/SBA-15 catalyst and the relationship of glycerol conversion, acid amount and Re content of the 5Pd- x Re/SBA-15 catalysts. Copyright © The Royal Society of Chemistry 2014. Reproduced with permission from Ref. ¹¹⁶

- *Catalytic hydrogenolysis over Pt-based catalysts*

Checa *et al.* confirmed that for glycerol conversion order follows the sequence $\text{Pt} > \text{Rh} \gg \text{Pd} \gg \text{Au}$.¹¹⁷ They also tested Pt nanoparticles supported on different metal oxides (TiO_2 , SnO_2 , ZrO_2 , Al_2O_3 , CeO_2 , La_2O_3 and ZnO) by wet impregnation.^{117,118} Among all studied catalysts, Pt/ZnO, presented the best behaviour in terms of yield to 1,2-PDO. Incorporation of Pt to the ZnO support (which is the least acidic one) induced an increase in acidity by a factor of 10 in the final catalyst.

In aqueous phase reforming (APR), Pt seems to be also the best choice.¹¹⁹ A report by Shabaker *et al.*¹²⁰ provided good APR results of glycerol and other bio-based derivatives, producing hydrogen in high yields and decreasing the volume of methane formed in the system.

Deng *et al.* studied the effect of the particle size of the bimetallic Pt-Re catalyst supported on carbon nanotubes (CNTs), using a range of metal loading between 1 to 30 wt. %.¹²¹ The results showed that a volcano plot with a maximum reaction rate was obtained with the particle size of 1.9 nm Pt-Re/CNTs catalyst. This result was *ca.* 7.5 times higher than that of bigger nanoparticles of 4.9 nm. Smaller particles were found to be Re-rich particles, which increased the surface acidity of the catalyst. However, coke formation was detected on the particles smaller than 1.5 nm, that would contribute to a decrease in the catalyst acidity. In this study, it was also reported that 5 wt. % Pt-Re (1:1 ratio) was the best option.¹²¹ After this, Falcone *et al.* continue the study on this bimetallic supported on carbon and SiO₂.¹²² They found that Pt was reduced entirely to Pt metal, while Re showed a distribution of rhenium oxides even after the catalyst reduction in H₂ at 200 °C. Therefore, ReO_x would favour the dehydration and Pt the hydrogenation.

In the last decade, the development of Pt–W-based catalysts such as tungsten oxide supported platinum Pt/WO_x, have been intensively investigated. This catalytic system can produce 1,3-PDO with high yields (*ca.* 60 %). The role of tungsten oxide was studied in detail by Garcia-Fernández *et al.*¹²³ To produce this C3 diol as the desired product the authors reported a novel approach that depends on the tungsten surface density that controls the kind of tungsten oxide species deposited on the catalyst surface of a Pt-WO_x/Al₂O₃ catalyst.¹²⁴ *Figure 1-4* shows the mechanism proposed, where Pt metal homolytically dissociates H₂ to two H species, while the WO_x is adsorbing the glycerol molecule, analogous to ReO_x in previous examples. The hydride formed can then interact with the carbocationic diol species to produce 1,3-PDO. The highest yield was achieved when the largest Brønsted to Lewis ratio was obtained.^{123,124}

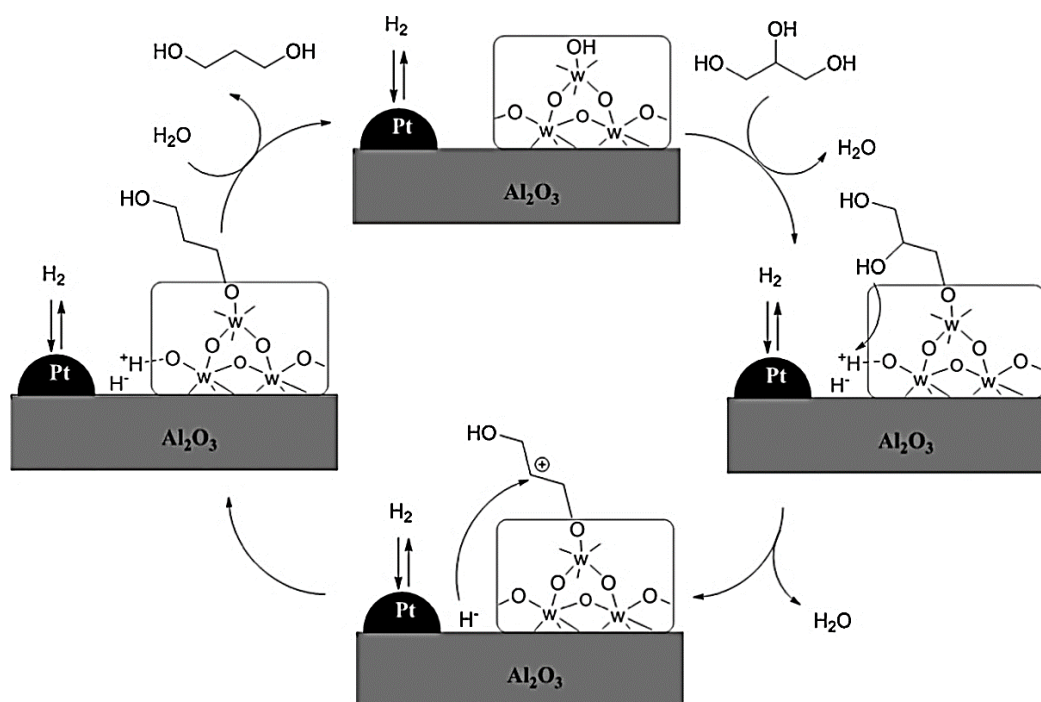


Figure 1-4 Proposed mechanism for glycerol hydrogenolysis to 1,3-PDO with Pt-WO_x/Al₂O₃. Copyright © Elsevier Inc. 2015. Reproduced with permission from Ref. ¹²⁴

The use of supported single-atom catalysts has been exploited recently for many applications, such as oxidation of CO and alcohols, selective hydrogenation, dehydrogenation and reforming reactions.^{125–127} These catalysts have a strong dependence on the type of support they interact with, and thus, a range of activities are conveyed. Wang *et al.* reported the hydrogenolysis of glycerol over a Pt/WO_x catalyst, where the dispersion of Pt on a single-atom scale was confirmed. These studies achieve a high conversion (*ca.* 60 %) and good yield to 1,3-PDO (21 %) at a low pressure of H₂ (1 MPa).¹²⁸

Wang *et al.* also studied the effect of adding a promoter to the tungsten oxide supported platinum Pt/WO_x and Pt/WO_x-Al₂O₃ catalysts.¹²⁹ The use of a promoter is to improve the stability of the catalyst by altering the electronic structure of the noble metal, in this case, platinum. Also, it also increases stability through blocking active sites on the catalyst that would promote the dehydration reaction. Thus, catalytic activity is improved with the selectivity to the desired products 1,3-PDO rather than 1-propanol. Various promoters were introduced to the tungsten oxide supported platinum catalyst. For example, lanthanum proved to be the most effective on both Pt/WO_x-Al₂O₃ and Pt/WO_x; affording a higher yield. According to their most recent report, a highly dispersed Au-promoted Pt/WO_x achieved an 81.4 % glycerol conversion and 51.6 % selectivity towards 1,3-PDO.¹³⁰ In this case, Au provided more activated W species for the formation of frustrated Lewis-pair (FLP) analogues.

Platinum is also known for its high dispersion on zeolite supports. Pt/H-mordenite catalyst was employed for glycerol conversion in a fixed bed reactor a vapour phase reaction under atmospheric pressure.⁹⁸ The catalyst was reduced *in-situ* after the previous calcination at 550 °C for 4 h in air. Different metal loading was tested from 0.5 to 3 wt. %. They found 2 wt. % Pt/H-Mordenite the optimal loading, obtaining around 48 % 1,3-PDO selectivity at 95 % glycerol conversion. However, the catalyst deactivates due to Pt seems to agglomerate during the reaction blocking the pore of the zeolite structure.

- *Catalytic hydrogenolysis over Ru-based catalysts*

Among the reported catalysts, Ru-based catalysts are found to be extremely active even under relatively low temperature for the hydrogenolysis of glycerol.^{83,82} The superior catalytic activity of Ru catalysts is found with good Ru dispersion and smaller average particle size. Under neutral conditions, Ru favours the formation of ethylene glycol.⁸² Vanama *et al.* probed that in vapour phase reaction, Ru/TiO₂ showed 3 times more activity and better 1,2-PDO selectivity than using MgO or CeO₂ as support.¹³¹ Later, the same group developed a Ru-based catalyst with MCM-4 as support.¹³² This support is a mesoporous material with very high surface area (> 1000 m²/g), uniform pore size and relatively hydrophobic nature. They obtained a 62 % of glycerol conversion and 38 and 20 % selectivity toward 1,2-PDO and 1,3-PDO respectively. The catalyst had a 3 wt. % of metal loading as optimum. 5 wt. % Ru monometallic using a combination of bentonite and TiO₂ as support was also tested, resulting in high conversion (69.8 %) and 1,2-PDO selectivity (80.6 %).¹³³

Tomishige and his co-workers also reported Ru catalysts supported on carbon compared with the Rh/SiO₂.¹³⁴ The authors found that the monometallic Ru/SiO₂ showed low activity for this reaction. Nevertheless, Ru-added IrReOx/SiO₂ catalyst showed high activity for the hydrogenolysis of glycerol to 1-propanol (71 % yield).¹³⁵ Ru can dissociate H₂ for the hydrogenolysis. Recently, Li *et al.* developed a different Re promoted Ru in porous SiO₂ encapsulated prepared by coating silica onto the surface of chemically reduced Ru-polyvinylpyrrolidone colloids.¹³⁶

Ruthenium has been used as an active metal site in different bimetallic catalysis for glycerol hydrogenolysis. For example, Ma *et al.* have made some progress on the research of glycerol hydrogenolysis with RuRe bimetallic catalyst.^{112,137} They found that RuRe/SiO₂-c350 showed much higher activity (51.7 %) and less selectivity to degradation product (EG) than Ru/SiO₂-c350 (16.8 %).¹³⁸

Another metal that shows good synergistic properties with Ru as a bimetallic partner is Cu. Huizhen Liu *et al.* employed copper and ionic liquid TMGL, where the cations would stabilise the catalyst.¹³⁹ The authors reported that a 100 % conversion of glycerol and 85 % yield of 1,2-PDO could be achieved at 230 °C and 8 MPa.¹³⁹ After that, the same group reported a 100 % conversion of glycerol with molar ratio 1:10 RuCu alloy over zirconia 100 % of glycerol conversion and 78.5 % yield of 1,2-PD at 180 °C and.¹⁴⁰ On the contrary, bimetallic 5 wt. % Ru-5.8 wt.% Co over ZrO₂ functions more like monometallic Ru in terms of catalytic activity. They stated that the Co oxide is an important component for that behaviour to enhances the selectivity to 1,2-PDO.⁹³

RuAu bimetallic catalyst has been tested for hydrogenolysis of both biomass-derived glycerol and levulinic acid by Villa *et al.*¹⁴¹ When Ru was deposited on Au, a Ru_{core}-Au_{shell} structure was formed. The corresponding Energy-Dispersive X-ray (EDX) spectra of those two components show that AuRu is not alloyed. On the contrary, when Au was deposited on Ru a different Au-Ru bimetallic catalyst was formed, with a partial surface Ru enrichment, resulting in the most active catalyst. Maris *et al.* also employed AuRu supported over activated carbon prepared by a surface redox method.⁸¹ The results showed more than fourfold with the monometallic Ru in terms of catalyst activity. The authors also studied bimetallic PtRu/C, but it functioned more like monometallic Ru. In both cases, the presence of a base was favourable for the improvement of propanediol over ethylene glycol.

Further development of catalysts is necessary to ensure the successful development of an industrial process for hydrogenolysis of glycerol. It is essential to design a highly stable, active and selective catalyst to perform the reaction under mild conditions. It requires a dual active site for both dehydration and hydrogenation. Therefore, the development of catalysts having both functionalities may be a good alternative. Evidence exists to think that RuPd nanoally catalyst for hydrogenolysis of glycerol combined with an appropriated acidic support would be a potential alternative.⁷⁹ In the case of the hydrogenation of levulinic acid to γ -valerolactone, bimetallic RuPd nano-alloy catalysts prepared by M_{Im} method was used by Luo *et al.*¹⁴² The results were exceptionally active, selective and stable. To the best of knowledge, this bimetallic catalyst has not been reported for this reaction. Developing heterogeneous catalyts for the improvement of the production of propanediols from glycerol would make the production of biodiesel more competitive economically. Moreover, it would help to reduce the actual fossil fuel dependence, and to mitigate the GHGs emissions. In this regards, the incorporation of

conversion of lignocellulosic feedstock is crucial to improve the current performance of the biorefinery.

1.3 Lignocellulosic feedstocks biomass

Concerning bio-based chemicals, lignocellulosic biomass is one of the most promising sustainable platforms. It consists of three main components: a) cellulose, which is a semi-crystalline homopolysaccharide comprised of unbranched D-glucose units which are linked through β -glycosidic bonds (β -1,4 glycosidic bonds); b) hemicellulose, which is an amorphous polysaccharide with different short sugars lateral chains; and c) lignin, which is a naturally amorphous and tridimensional polymer.¹⁴³ The later is found in all vascular plants, filling the space between the hemicellulose and cellulose (*Figure 1-5*).¹⁴³ Therefore, it gives plants their structural shape and strength through cross-linkages with the carbohydrate polymers.

Valorisation of both cellulose and hemicellulose polysaccharides have been extensively studied and successfully converted in the industrial production of bio-based polymeric materials^{44,144} and biofuels such as bioethanol, biohydrogen and biogas.^{145,146} It is important to highlight that after cellulose, lignin is the most abundant carbon source on earth.¹⁴⁷ Lignin contains highly functionalised aromatic units that make them a potentially sustainable feedstock to produce aromatics products. However, the residual lignin is usually burnt as a low-grade fuel for power generation or steam production in most of the processes nowadays. In the best scenario, it is used as low-value products such as animal feed, phenolic and epoxy resins, carbon fibres, wood panel, automotive brakes, emulsifying agents, among others.^{143,148} An integrated conversion of all the components of lignocellulosic biomass in a biorefinery would make the process economically viable and sustainable; this is the first target to accomplish.

Lignin is of particular interest because it is formed of highly functionalised aromatic moieties. In fact, known platform commodity chemicals can be sustainably produced from lignin such as BTX (benzene, toluene and xylene), phenols, and aliphatic fractions (C1-3). Lignin is the only abundant volume renewable source of aromatics for this purpose.^{143,149} Economically, fully deoxygenated BTX products from lignin may not be desirable because in specific processes BTX is again oxidised. Consequently, strategies to valorise lignin that can preserve the aromatic rings and functionalities already present in this feedstock have to be developed. Converting lignin into small aromatic molecules can be used in existing (without changing the current processes and technologies) or new routes to produce base chemicals.¹⁵⁰

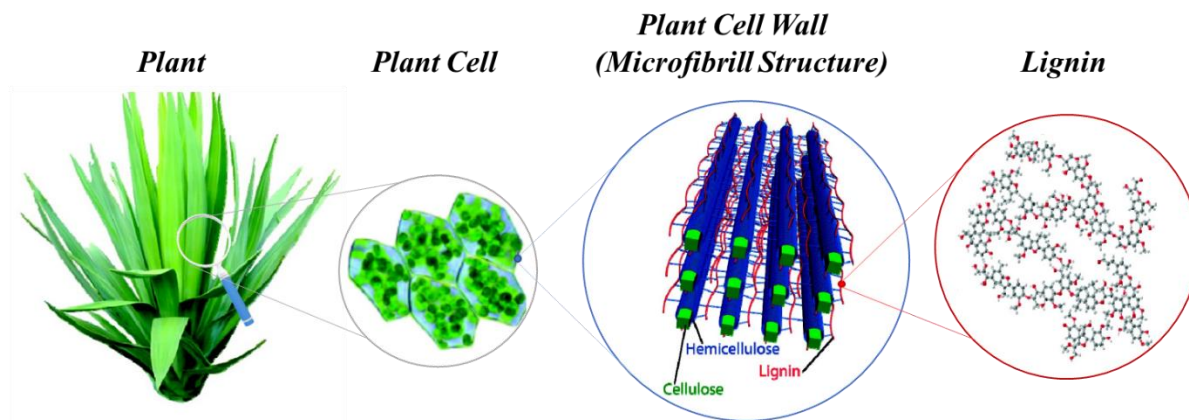
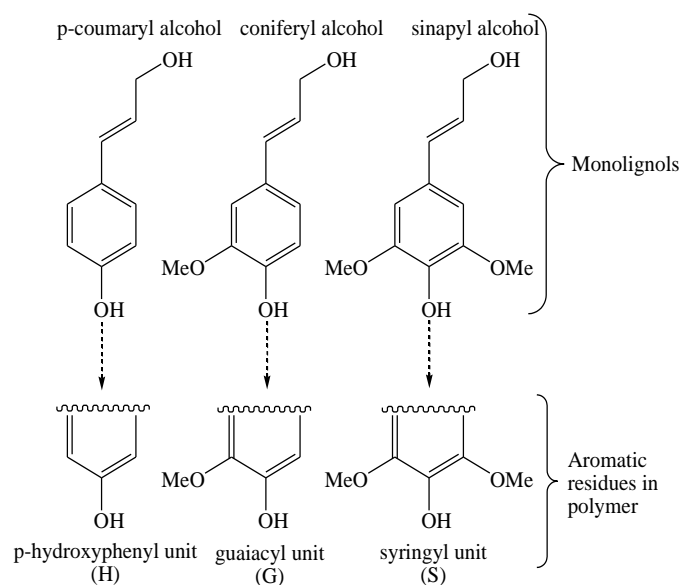


Figure 1-5 Representation of the location of lignin in a plant. Copyright © American Chemical Society, 2010. Reproduced with permission, Adapted from Ref.¹⁴³

1.3.1 Chemical composition and structure of lignin

The lignin structure is the result of the polymerisation of three types of phenylpropane units, known as monolignols.¹⁵¹ Monolignols are considered the primary building blocks of lignin. They consist of several aromatic sub-units: p-hydroxyphenyl type (H), guaiacyl type (G) and syringyl type (S). The difference between them is the number of methoxy groups attached to the aromatic ring. For instance, p-coumaryl does not contain methoxy groups, while coniferyl and synapyl alcohol comprise one and two methoxy groups, respectively (*Scheme 1-2*).^{152,153} The proportion of these three monolignols depend on the type of biomass.¹⁵² In general, hardwood lignin contains nearly equal amounts of G and S units and some traces of H units. In contrast, softwood lignin contains G units predominantly with deficient H units. On the other hand, the grass lignins contain a higher proportion of H units in comparison to hardwood and softwood lignins.^{143,146,151} The H: G: S ratio of a specific lignin sample can be estimated using wet chemical methods and spectroscopic techniques. Several methods such as acidolysis, nitrobenzene oxidation (NBO), permanganate oxidation, cupric oxide and thioacidolysis have been used for this purpose.^{154,155} Regarding spectroscopic techniques, Fourier Transform Infra-Red (FTIR)¹⁵⁶ and 2-dimensional Nuclear Magnetic Resonance (2D-NMR) are the most used.^{157,158} For instance, Kline *et al.* employed a methodology based FTIR on normalised spectroscopy for the quantitative analyses of lignin samples.¹⁵⁶ This method assigned the peaks at 1327, and 1267 cm^{-1} to G units, those at 1223 and 1123 cm^{-1} to S units and the 1167 cm^{-1} peak to H units.¹⁵⁶ Besides, Heteronuclear Single Quantum Coherence (HSQC) 2D-NMR spectroscopy can be used for the semi-quantitatively estimated S/G molar ratios.^{157,158}

The diversity found in plants due to different lignin structures is not only caused by the ratio of monolignols. It is also due to the way that these monolignols are covalently linked with each other, called inter-unit linkages. These inter-unit linkages can be classified into two groups, C-O and C-C inter-unit linkages.^{143,151,159} It is crucial to have a good understanding of the relative strengths of these inter-unit linkages in order to design methodologies to break them. *Figure 1-6* shows the typical C-O and C-C inter-unit linkages present in softwood lignin.



Scheme 1-2 Monolignol structures and their corresponding residues in lignin polymers. Adapted from Ref.¹⁵¹

Density functional theory (DFT) calculations are useful to predict the bond dissociation energies (BDE). Huang *et al.* used DFT on 63 representative lignin model compounds with different types of inter-unit linkages.¹⁶⁰ *Table 1-2* presents the BDE data along with the common names and structures of different lignin model compounds having different inter-unit linkages. This *Table* further shows the abundance of each linkage for different lignocellulosic biomass (softwood, hardwood and grass). As can be seen, C₅-C_{5'} is the strongest bond of all inter-unit linkages having a BDE around 115-118 kcal/mol. In general, C-C inter-unit linkages are stronger than C-O linkages making them more challenging to break.¹⁵²

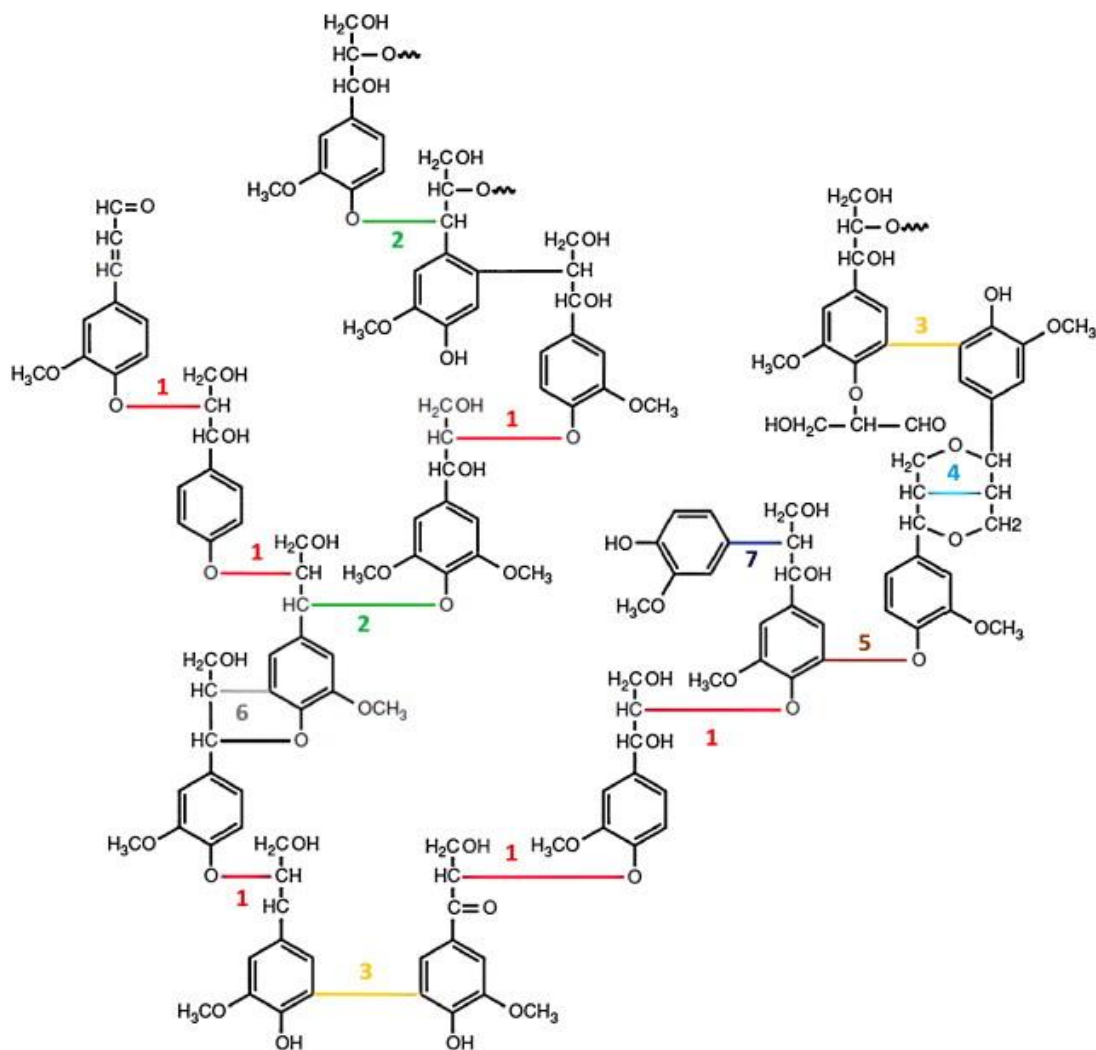
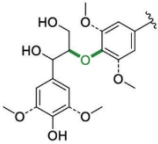
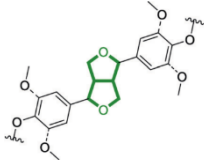
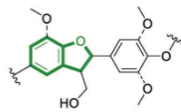
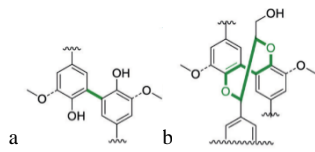
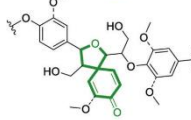
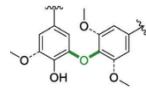


Figure 1-6 Typical inter-unit linkages present in softwood lignin: (1) β -O-4', (2) α -O-4', (3) 5-5', (4) β - β' , (5) 4-O-5', (6) β -5', (7) β -1'. Copyright © Elsevier, 2012. Reproduced with permission from Ref.¹⁶¹

Table 1-2 List of lignin model compounds representing various inter-unit linkages, their structure and abundance plus bond dissociation energies. Adapted from Ref. ¹⁵²

Name	β -aryl ether	Resinol	Phenylcoumaran	Biphenyl + Dibenzodioxocin	Spirodienone	Diaryl ether
Structure						
Inter-unit linkage	β -O-4	(β - β)+(γ -O- α)	(β -5)+(α -O-4)	5-5 ^a (5-5)+(α -O-4)+ β -O-4) ^b	β -1+(α -O- α)	4-O-5
Softwood (%)	45-50	2-6	9-12	5-7 ^b	1-9	2
Hardwood (%)	60-62	3-16	3-11	<1 ^b	1-7	2
Grasses (%)	74-84	1-7	5-11	n.d.	n.d.	n.d.
BDE (kcal/mol)	C β -O-C $4'$ 54-72 C α -C β 75-80	C α -O 68 C α -C β 67 C γ -O 79 C β -C β 81	C α -O-C $4'$ 50-56 C α -C β 54-63	C 5 -C $5'$ 115-118	C β -C $1'$ 65-69 (for open structure)	C 4 -O-C 5 78-83

a: Biphenyl, b: Dibenzodioxocin.

- *Native and technical lignins*

The raw plant biomass contains what is known as natural or native lignins. As previously mentioned, the native structure of lignin varies from plant to plant. Indeed, within the same plant, it could differ from one part to the other of the plant. It is important to highlight that it has not yet been possible to isolate the real native lignin from plant tissues.¹⁶² The structure always modifies during the lignin isolation process. Nevertheless, the structures of complex native lignins, in the cell wall, have been studied in great detail using advanced NMR techniques.¹⁶³ Another way to study the structure of native lignins is by chemical degradation techniques such as thioacidolysis or milled wood lignin (MWL).^{164,165}

Extracting native lignins from lignocellulosic biomass are future targets to achieve. Efforts are currently being made to separate native lignins from biomass with minimal structural changes.^{152,166} It has also been reported that native lignins are relatively more straightforward to depolymerise compared to technical lignins because of the presence of a higher proportion of C-O inter-unit linkages, (*ca.* two-thirds or more of the total linkages are ether bonds).¹⁴⁶

Currently available lignins often called as technical lignins are the by-products of conventional pulping routes. Lignins obtained from pulping routes such as kraft, soda, organosolv, hydrolysis and sulphite processes are called kraft lignin, soda lignin, organosolv lignin, hydrolysis lignin and lignosulphonates respectively.^{167,168} All these lignins have different structures and impurities, depending on the pulping and pre-treatment or fractionation processes employed.¹⁶⁹ As mentioned before, native lignin contains a higher proportion of C-O inter-unit linkages. However, during the lignin fractionation processes, condensation reactions between compounds cleaved from the native lignin and remaining oligomers chains occur, forming new C-C bonds (*Figure 1-7*).^{170,171,172} This C-C bond formation evidence the need for developing strategies more effective in the cleavage of these strong bonds.

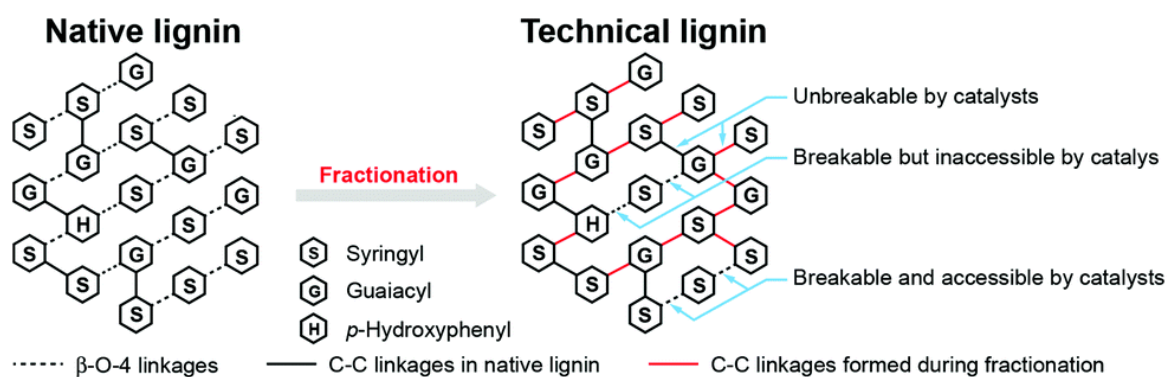


Figure 1-7 Schematic representation of the formation of the C-C bond during the delignification process. Copyright © The Royal Society of Chemistry, 2017. Reproduced with permission from Ref.¹⁷¹

Nevertheless, many researches are currently investigating how to minimise condensation reactions. One option is by the stabilisation of native lignin *via* the addition of biological or chemicals capping agents, solvents, catalytic trapping pathways, and careful tuning of reaction parameters.^{173,152} For example, formaldehyde has been reported to be a good stabiliser.¹⁷⁴ This compound reacts with alpha and gamma- hydroxyl groups on the lignin side-chain to form a stable 1,3-dioxane ring structure. In this way, formaldehyde prevents further condensation and hence the formation of new C–C linkages.

Other major challenges in the catalytic processing of these technical lignins are the presence of these impurities, especially sulphur. For this reason, the extraction of technical lignin (delignification process) from biomass are classified into two types: (a) sulphur based processes and (b) non-sulphur based processes (*Figure 1-8*).¹⁶⁹ The disadvantages of sulphur containing lignin is that they are typically not suitable for catalysts containing noble metals because of sulphur poisons the catalysts. Therefore, non-sulphur lignins (organosolv & soda lignin) are preferred for catalytic valorisation. However, sulphur content can be beneficial for some specific catalytic processes where sulphided hydrodeoxygenation catalysts are used.¹⁷⁵ Because of the absence of sulphur, soda lignin and organosolv lignins have been used as feedstock for catalytic valorisation reactions increasingly compared to kraft lignin.¹⁵³ In addition, other physicochemical properties of technical lignins have to be taken into consideration during feedstock selection for valorisation reactions, (e.g. molecular weight, polydispersity, moisture, ash content, homogeneity, the presence of certain functional groups).^{169,176}

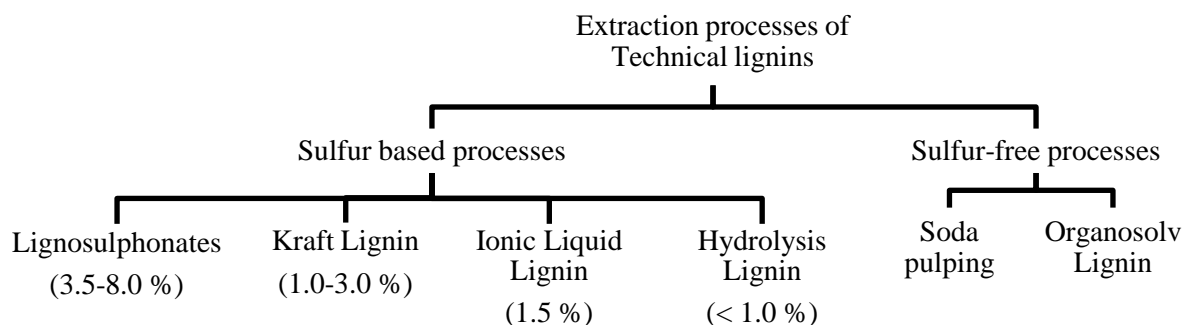


Figure 1-8 Classification of delignification processes and the resultant technical lignin. The sulphur content in % is given within brackets for lignins from sulphur-based processes. Adapted from Ref.¹⁶⁹

1.3.2 Lignin valorisation

Depolymerisation of lignin to smaller molecular weight compounds is a very promising reaction. It can potentially generate value-added products, especially aromatics and functionalised aromatics. These aromatics can be used for the sustainable production of fuels, base chemicals and some high-value fine chemicals.¹⁷⁷ Six major strategies have been reported for the depolymerisation of lignin, namely pyrolysis, hydrolysis, oxidation, hydrogenolysis, photocatalytic and enzyme catalysis (biocatalysis).¹⁷⁸ Some of these routes like pyrolysis are thermal and non-catalytic while others are catalytic.

Depolymerisation involves the breaking of C-O and C-C inter-unit linkages present in lignin. Using whole lignin involves complexities such as the presence of impurities and heterogeneous structures, and dealing with compounds which contain too many functionalities.^{169,179} Lignin model compounds are commonly used to design strategies for the selective cleavage of inter-unit linkages. These model compounds contain specific kind of inter-unit linkages that are present in lignin. *Figure 1-9* present a few examples of the model compounds, representing different inter-unit linkages in lignin that are typically used in literature; 1-phenyl-2-phenoxyethanol (1), pinoresinol (2), bibenzyl (3), benzofuran (4), diphenyl ether (5) and biphenyl (6) representing β -O-4', β - β' , β -1', β -5', 4-O-5' and 5-5' linkages respectively. These less complex model compounds are beneficial to study the kinetics and mechanism of these cleavage reactions. They are useful for designing catalysts able to depolymerise lignin. Nevertheless, it is essential to highlight that translating the catalytic results from these model compounds to real lignin is not straightforward as the presence of substituents, and other functionalities severely complicate the process. However, these model compounds are a good starting point for catalyst development.

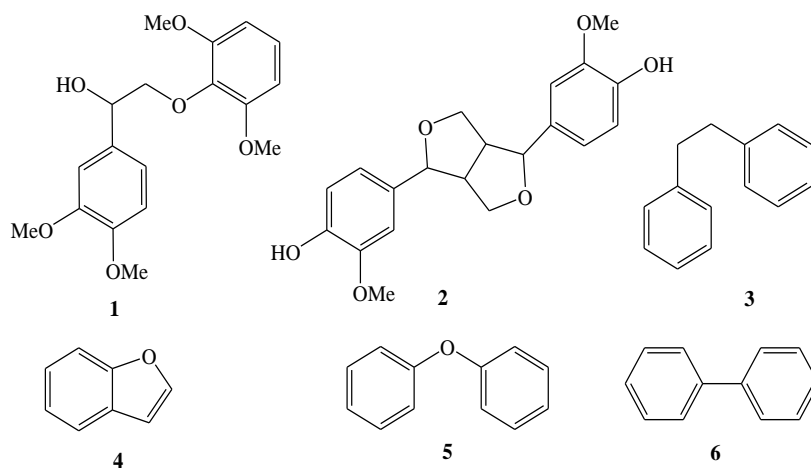


Figure 1-9 Structures of some lignin model compounds that contain typical linkages present in lignin: **1** (β -O-4'), **2** (β - β'), **3** (β -1'), **4** (β -5'), **5** (4-O-5') and **6** (5-5').¹⁸⁰

- **Catalytic C-C bond cleavage in lignin model compounds and technical lignins.**

Catalytic conversion of the components of lignocellulosic biomass to chemicals and fuel components has been the subject of research efforts during the past decade. Indeed, the annual increase in the number of publications on this subject is about 20 %.¹⁸¹ Among these reports, catalytic depolymerisation of lignin has received more considerable attention recently.

Several catalytic routes including oxidative, reductive, redox neutral, photocatalytic and enzyme catalytic routes have been reported for the cleavage of C-O linkages, typically β -O-4' inter-unit linkage in lignin model compounds (Compound **1**, Figure 1-9).¹⁸² However, in most cases, during these catalytic depolymerisation reactions, C-C linkages are not broken.¹⁸³ Previous reviews have been published on lignin valorisation; focus on the cleavage of C-O inter-unit linkages.^{152,184,185} However, reports on the cleavage of C-C inter-unit linkages are scarce because of the recalcitrant nature of these bonds. For the valorisation of technical lignins, as they contain more C-C linkages than C-O linkages, the breaking of C-C interunit linkages is crucial. For catalytic systems focussed on the cleavage of C-C inter-unit linkages in lignin model compounds as well as whole lignin techniques, readers are encouraged to read our recently published review on this subject.¹⁸⁰ This thesis is covering exclusively the oxidative C-C bond cleavage. Typically, the oxidative depolymerisation reaction results in aromatic acids, aldehydes and occasionally aliphatic acids *via* the opening of the aromatic ring.¹⁵⁰ The challenge in designing these strategies is to get the desired product(s) in high selectivity by selectively breaking specific inter-unit linkages to avoid complex separation processes.

- *Oxidative C-C bond cleavage*

Catalytic oxidation is one of the most widely used methods for the breaking of the inter-unit linkages in lignin. This also applies to C-C linkages because of the abundance of hydroxyl groups in lignin.¹⁸⁶ Behling *et al.* have reported an overview of the recent advances in the oxidative depolymerisation of lignin, including some oxidative C-C cleavages.¹⁸⁷ Paper and pulping industries use some of the most advanced oxidative routes for the depolymerisation, and eventual removal of traces of lignin present in cellulosic materials.^{178,187,188}

Most of the reported C-C bond cleavages correspond to the breaking of the C_α-C_β bond and some examples of C_{Ph}-C_α bonds within the β-O-4 model compound **7** (Figure 1-10). It is also found the breaking of the β-1' bond of the lignin model **8** (Figure 1-10). However, examples on the breaking of β-β'¹⁸⁹, β-5'¹⁸⁶ and 5-5'¹⁸⁷ linkages are scarce in the literature. In general, these lignin model compounds with different functional groups (OH or OCH₃ or OC₂H₅) at different positions on the aromatic rings, are used as substrates (substrates **7** & **8** in Figure 1-10). Notice that these are derivatives of model compounds **1** and **3**, respectively (Figure 1-9).

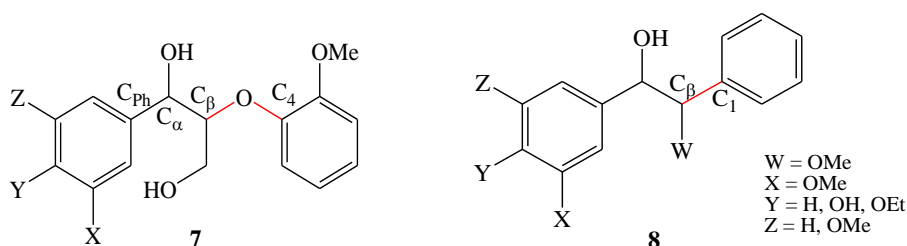


Figure 1-10 Commonly used lignin model compounds containing β-O-4' linkage (methoxylated phenolic/non-phenolic dimer (β-aryl ether, **7**) and β-1' linkage (bibenzyl dimer, **8**).

The oxidative depolymerisation of lignin typically result in monomeric oxygenates like carbonyl compounds and carboxylic acids. Hanson *et al.* reported a correlation between the oxidative breaking of specific linkage and the resultant product for the model compound **7** (see Figure 1-11).¹⁹⁰ For example, C_α-C_β cleavage results in aromatic aldehydes (or corresponding carboxylic acid), while the C_α-H cleavage yields corresponding ketones. The breaking of C_β-O bond yields ketones and finally the C_{Ph}-C_α cleavage results in acrolein and quinone derivatives.¹⁹¹ This correlation is used to rationally design catalytic systems for the targeted cleavage of specific bonds to get the specific compound in high yield.

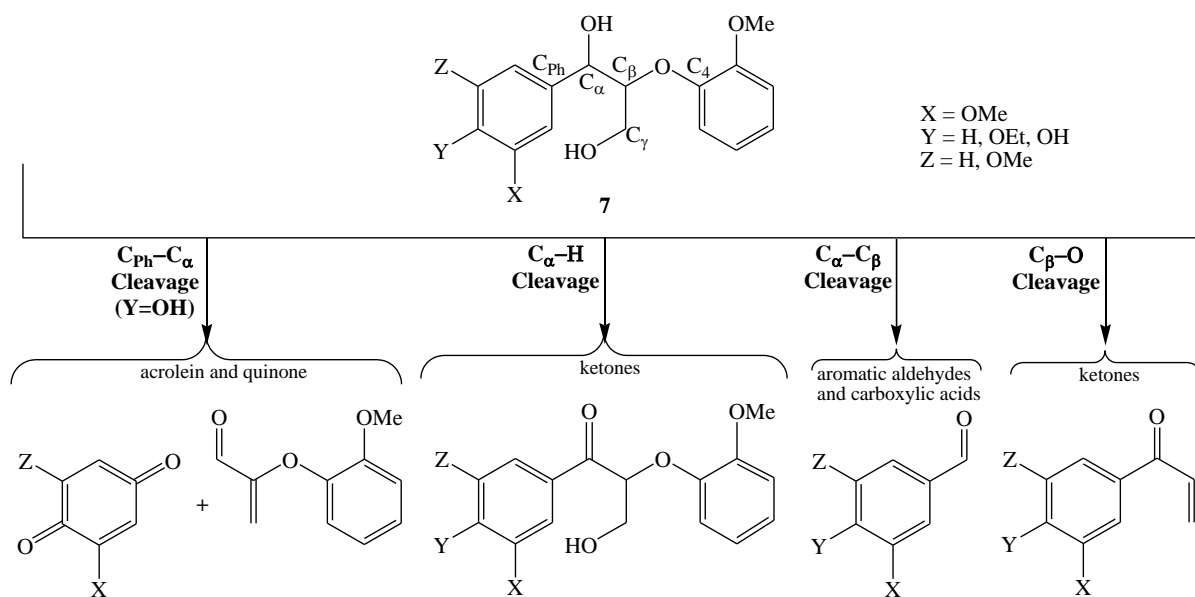


Figure 1-11 Potential bond breakage pathways and possible products during the catalytic oxidation of lignin model compound **7**. Adapted from Ref. ¹⁹¹

Crestini *et al.* reported a catalytic, chlorine-free, oxidative cleavage of inter-unit linkages in an array of monomeric and dimeric, phenolic and non-phenolic lignin model compounds using a homogeneous methyltrioxorhenium (VII) (MeReO_3) (MTO) catalyst and H_2O_2 as the oxidant.¹⁹² To study the C-C bond cleavage, they used different substituted lignin model compounds having $\beta\text{-O-4}'$ units **9** and diphenylmethane units **10** as substrates (Figure 1-12). The model compound **9** is a highly functionalised version of the simple model compound **1** (Figure 1-9). During the catalytic reaction using phenolic model compound **9**, (substrate-1 in Figure 1-12) > 98 % of the substrate was converted to products. The products mixture includes carboxylic acid on the C_{α} position (4-hydroxy-3-methoxybenzoic acid), carbonyl group on the C_{β} position (hydroxyl-ketone), 2,6-dimethoxyphenol and muconolactone. Among these products, 4-hydroxy-3-methoxy benzoic acid was formed by the cleavage of the $\text{C}_{\alpha}-\text{C}_{\beta}$ bond. However, the yield of this product was only 16 %. Similarly, when substrates 2 and 3 (Figure 1-12) were oxidised, evidence for the cleavage of the $\text{C}_{\alpha}-\text{C}_{\beta}$ bond was also observed.¹⁹² The $\text{C}_{\alpha}-\text{C}_1$ linkage present in **10** is not found in native lignins. However, it is formed because of the condensation reactions during the delignification processes, hence it is prevalent in technical lignins (see Figure 1-7).¹⁹³ In an effort to break this $\text{C}_{\alpha}-\text{C}_1$ linkage, two versions of model compound **10** were oxidised using MTO and H_2O_2 . For substrate 4 (phenolic model compound in Figure 1-12) a higher proportion of $\text{C}_{\alpha}-\text{C}_1$ cleavage was observed resulting in aromatic carboxylic acids. For the substrate 5 (non-phenolic model compound in Figure 1-12) only trace

amount of C_α-C₁ cleavage was observed. They have concluded that C_α-C₁ cleavage is easier in phenolic model compounds, compared to non-phenolic compounds.

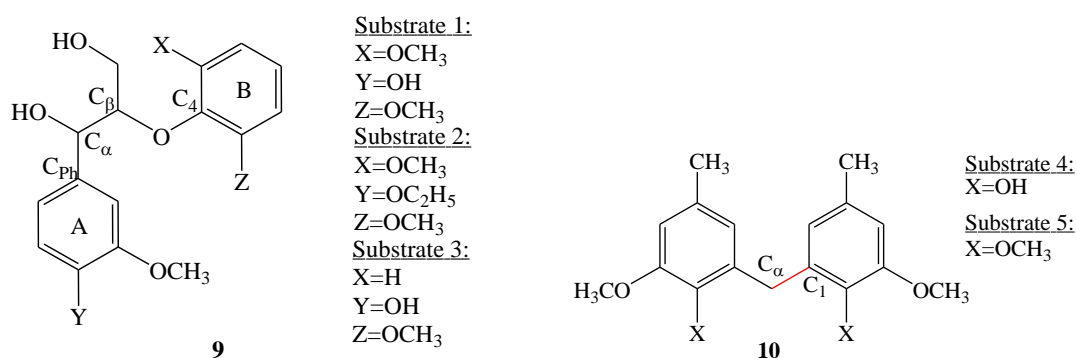


Figure 1-12 Phenolic and non-phenolic lignin model compounds with β -O-4 units (9) and diphenylmethane units (10) models for substrates 1-5. Adapted from Ref. ¹⁹²

Encouraged by these results, Crestini *et al.* depolymerised technical lignins such as hydrolytic sugarcane lignin (SCL), red spruce kraft lignin (RSL) and hardwood organosolvent lignin (OSL).¹⁹² This catalytic oxidation using MTO and H₂O₂ resulted in a decrease in the content of aliphatic OH groups (43 %, 14 % and 67 % reduction in SCL, OSL and RSL, respectively). This also produced more soluble lignin fragments and higher yields monomeric carboxylic acids. Because of this, additional C-C cleavage for this catalytic system, it is useful for the depolymerisation of complex technical lignins.

Hanson *et al.* reported the cleavage of C_{Ph}-C_α, C_α-C_β and C_β-C₁ inter-unit linkages during the aerobic oxidation of different lignin model compounds **7** and **8** (Figure 1-10) by using different vanadium metal complexes.^{194,190} During the aerobic oxidation of derivatives of model compound **8** with β -1' linkage using (HQ)₂V^V(O)(OⁱPr) (HQ = 8-oxyquinolate) catalyst, they observed substantial C_{Ph}-C_α and C_β-C₁ cleavage¹⁹⁴. Again, phenolic model compounds resulted in substantially higher C-C cleavage compared to non-phenolic model compounds. Also, it was observed that the solvents altered product distribution. Employing DMSO solvent, benzaldehyde and methanol were the major products, while in pyridine solvent, the main products obtained were benzoic acid and methyl benzoate (Figure 1-13).¹⁹⁴

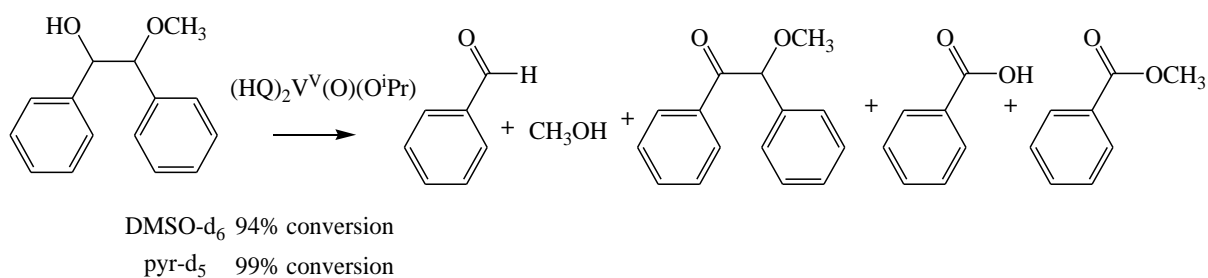


Figure 1-13 Effect of solvent on products distribution during the oxidative cleavage of **8** using $(\text{HO})_2\text{V}^{\text{V}}(\text{O})(\text{O}^i\text{Pr})$ catalyst. Adapted from Ref. ¹⁹⁴

More recently, Ma *et al.* reported the selective oxidative C–C cleavage in model **1** using $\text{VO}(\text{acac})_2$ catalyst with molecular oxygen as the oxidant. They further show the effect of solvents on the selectivity with acetic acid being the most desired solvent for C–C cleavage.¹⁹⁵ Amadio *et al.* reported the oxidative cleavage of model compound **7** (Figure 1-10), phenolic X, Z= OCH₃, Y=OH) using the vanadium complexes (**V1**, **V2** and **V3**) showed in Figure 1-14, where they have found the effect of solvent on the selectivity of C_{Ph}–C_α cleavage over C_α–C_β. The yield of the products as a result of the breaking of C_{Ph}–C_α bond follows the order ethylacetate > 2-methyl THF > pyridine > THF using **V3**. When a non-phenolic version of the model compound **7** (X=H, Z= MeO, Y=EtO) was used, C–C cleavage was not observed at all.¹⁹¹

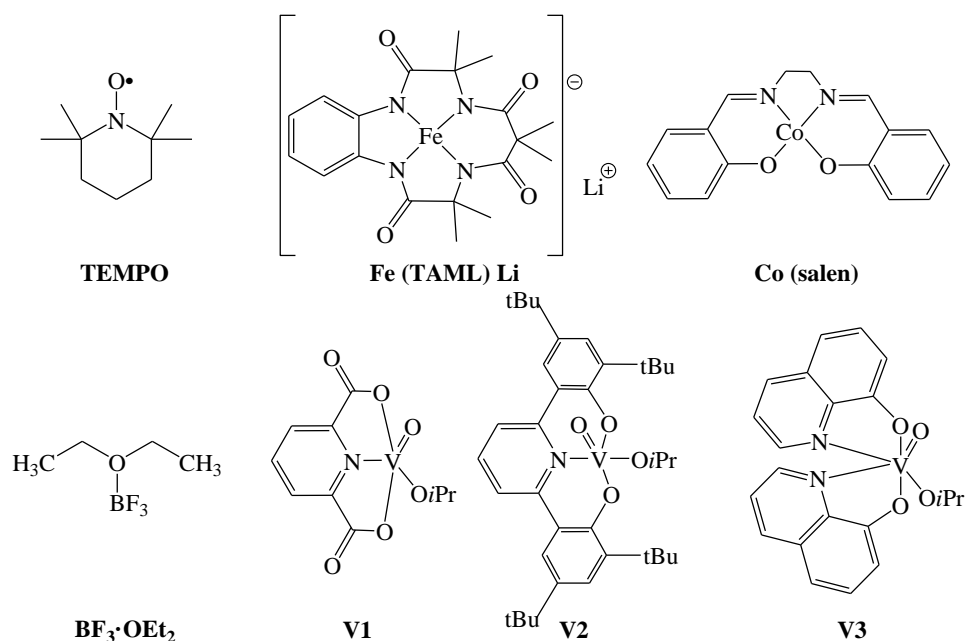


Figure 1-14 Structures of some of the catalyst used for the oxidative C–C bond cleavage as described in the text.

TEMPO (2,2,6,6-tetramethyl-1-piperidin-1-yl-oxyl in Figure 1-14) is used as it is or in combination with metal catalysts for the breaking of inter-unit linkages in lignin. Sedai *et al.* reported an effective combined catalytic system containing CuCl and TEMPO for the oxidation of 1,2-diphenyl-2-methoxyethanol (model **8**, W = OCH₃, Figure 1-10), having β -1' linkage, using O₂ as the oxidant.¹⁹⁶ After 48 hours of reaction at 100 °C, they achieved more than 80 % of β -1' cleavage. However, under similar condition, when (dipicolinate)V^V(O)(OⁱPr) **V1** (Figure 1-14) was used as a catalyst, the oxidation of secondary alcohol to ketone was followed by β -1 cleavage in a two-step process. However, when the intermediate ketone was oxidised by **V1**, > 90 % of cleavage was observed. The CuCl+TEMPO catalytic system is more effective and better than the vanadium catalyst in breaking the β -1 bond in one step. The same group reported Cu(OTf)/2,6-lutidine/TEMPO catalyst system for the aerobic oxidation of model compound **8** having β -1' linkage.¹⁹⁷ In comparison to vanadium complexes, generally, this Cu catalyst is superior in breaking C-C linkages for non-phenolic models.^{197,198} For phenolic β -1' model compounds, catalytic amounts of TEMPO were not effective in breaking any C-C linkages, however when stoichiometric amounts of TEMPO were used a substantial amount of C_{Ph}-C _{α} cleavage was observed.¹⁹⁷ When non-phenolic β -1' model compounds were tested, even with catalytic amounts of TEMPO substantial amount of C _{α} -C _{β} bond is broken. From these results, we can conclude that for efficient cleavage of C-C bonds, CuOTf + TEMPO (stoichiometric) system is more suitable for phenolic model compounds, whereas catalytic amount CuOTf+TEMPO is preferred for non-phenolic model compounds. When a 1:1 mixture of non-phenolic β -1' and β -O-4' model compounds (**7** & **8**) was used for the oxidation reaction using this catalytic system. A substantial amount of C-C cleavage was observed, and β -1 model compound got converted more readily compared to the β -O-4' model compound.¹⁹⁷ Rahimi *et al.* used a catalytic amount of 4-acetamido TEMPO, without any metal, for the oxidation of β -O-4 model compound **9** using O₂ (Figure 1-15). In this reaction, C _{α} -C _{β} cleavage has been observed. This oxidation methodology has been extended to the depolymerisation of real lignin (Aspen lignin). Through a detailed analysis of the product mixture, they propose C-C inter-unit cleavage.¹⁹⁹

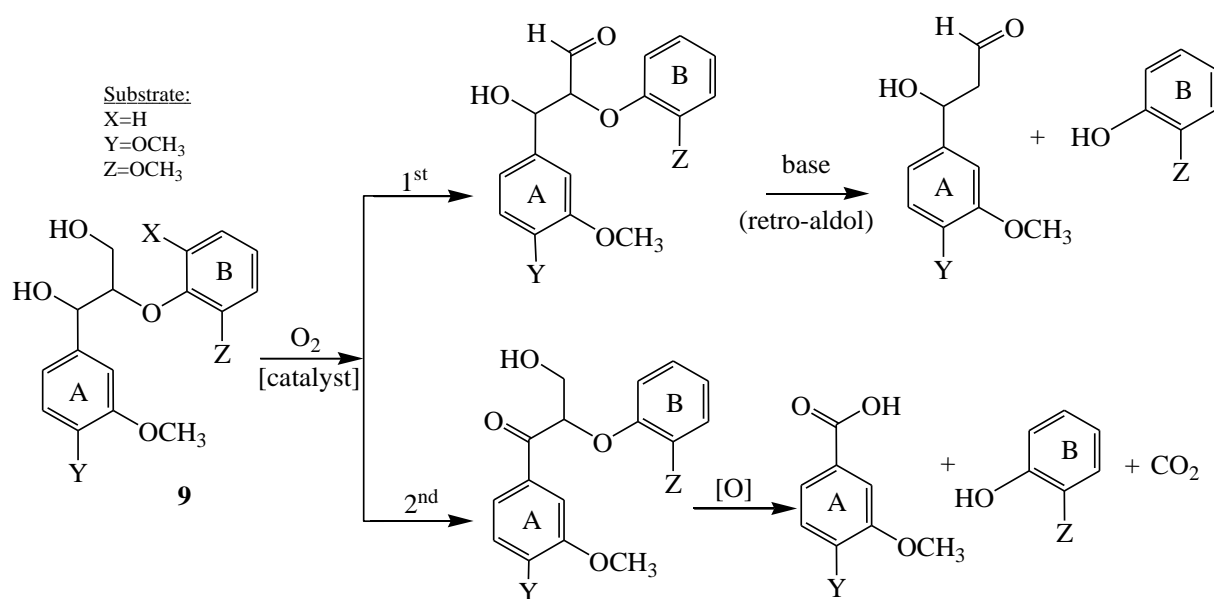


Figure 1-15 Schematic representation of the chemoselective oxidation of β -O-4 model compound (**9**) using TEMPO and O₂. Adapted from Ref. ¹⁹⁹

Díaz-Urrutia *et al.* compared the catalytic activities of a few vanadium complexes for the oxidative depolymerisation of organosolv lignin and studied the mechanism of the oxidative catalytic cleavage with model compounds. Among all the tested catalysts, only bis(8-oxyquinoline) oxovanadium (**V3**) (Figure 1-14) resulted in C-C cleavage under basic condition. However, under their condition, CuOTf + TEMPO and TEMPO did not result in C-C cleavage.^{200,201} Another interesting method for the cleavage of C _{α} -C _{β} linkage was reported by Patil *et al.*^{202,203} Using simple model compounds, in the first step they oxidised the OH group in C _{α} in β -O-4' model compound to form ketone using TEMPO/O₂ system. In the second step, they converted the ketone to an ester using Baeyer-Villiger oxidation (*i.e.* introduced O in between C _{α} and C _{β}), which is then hydrolysed *in situ* to form a carboxylic acid, aldehyde and phenol (Figure 1-16). Though this indirect method of breaking C _{α} -C _{β} is interesting, however, it will be less applicable for the depolymerisation of pure lignin due to these oxidative methods are not fully compatible with unprotected phenolic hydroxyls.²⁰²

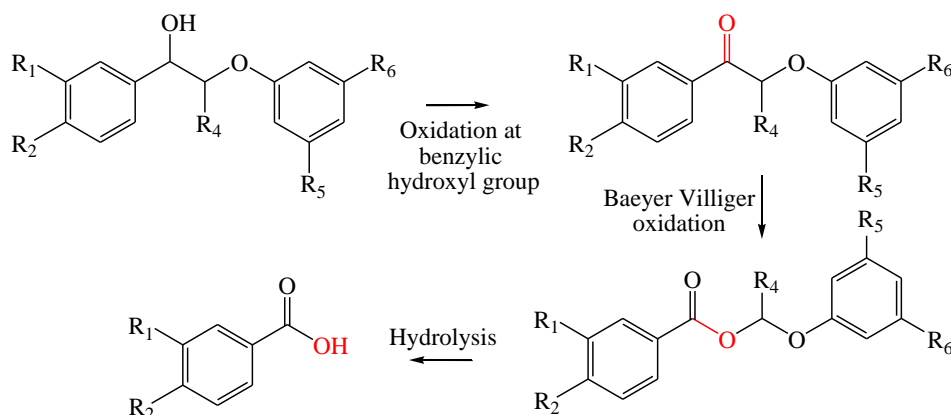


Figure 1-16 Schematic representation of the two-step method for the breaking of C_α-C_β bond via Baeyer-Villiger (BV) oxidation. Adapted from Ref.²⁰³

Wang *et al.* proposed another two-step strategy for the cleavage of C_α-C_β bond in a β-O-4' lignin model compound **1** (Figure 1-9). In the first step, the secondary OH group is oxidised to a ketone using VOSO₄/TEMPO catalyst and O₂ as the oxidant. In the second step, the ketone is converted to monomeric phenols and carboxylic acids through the cleavage of C_α-C_β bond using Cu/1,10-phenanthroline catalyst and O₂ as the oxidant.²⁰⁴ The bond energy of the C_α-C_β bond decreases from the alcohol to the ketone by 102 kJ mol⁻¹, making the ketone an easier substrate for C-C cleavage.²⁰⁴ More recently, the same group developed Cu(OAc)₂/BF₃·OEt₂ catalyst for the cleavage of C_α-C_β bond in β-O-4' model compound **1** to produce esters and phenols.²⁰⁵ Napoly *et al.* reported Fe (TAML) Li (Fe tetraamido macrocyclic complex, see Figure 1-14) catalyst for the oxidative cleavage of C_α-C_β bond in β-O-4 model compound **1** using (diacetoxyiodo) benzene (DAIB) as the oxidant at 25 °C (Figure 1-15).²⁰⁶ They further report that by increasing the water content in the reaction mixture from 5 % to 20 % the extent of C_α-C_β bond cleavage increased from 45 to 95 %. Though the exact role of water in increasing the selectivity of C_α-C_β bond cleavage is not clearly understood. They have extended this methodology for the cleavage of β-1' linkage as well in a lignin model compound similar to **8**.²⁰⁶

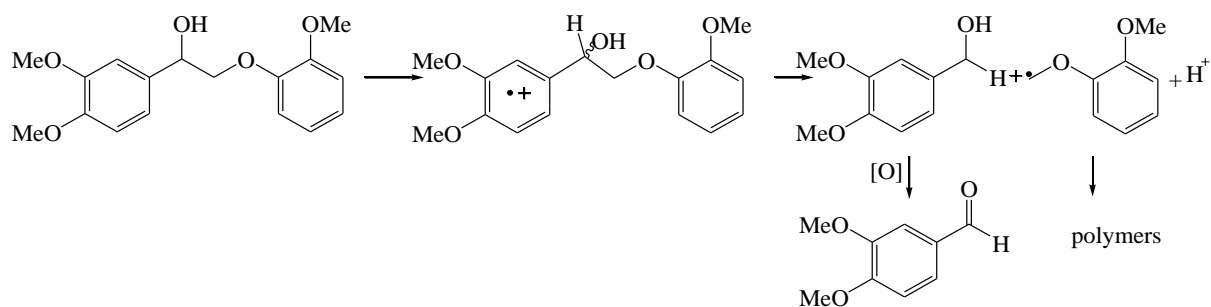


Figure 1-17 C_{α} - C_{β} bond cleavage in β -O-4 model compound **1** using Fe (TAML) Li as catalyst and DAIB as the oxidant at 25 °C. Adapted from Ref. ²⁰⁶

Luo *et al.* developed a transition-metal free protocol for the selective oxidative C-C cleavage in lignin model compounds with sodium persulfate as the oxidant.²⁰⁷ They tested this system for the oxidative cleavage of different inter-unit linkages in many model compounds. Luo *et al.* were able to break β -1' linkage in model compound **3** into benzaldehydes in good yields (ca. 60 %) using sodium persulfate. However, they could not translate this methodology for the oxidative depolymerisation of real lignins because of their poor solubility. Cobal salen [Co(salen)] complexes (see Figure 1-14) have also been used as homogeneous catalysts for the oxidative cleavage of phenolic and non-phenolic phenylcoumaranes (lignin model compound **4**). The results regarding the cleavage of β -5' inter-unit linkages to form benzoquinone derivatives, alkylphenyl ketones, benzoic acid derivatives and densely functionalized phenoxyacrylaldehydes. Some quantities of benzofuran (with β -5' intact) have also been found.²⁰⁸ Biannic, *et al.* used Co-Salen complexes for the selective cleavage of the C_{Ph} - C_{α} bond cleavage in β -O-4' model compound instead of the typically weaker β -aryl ether linkage (C-O linkage) (Figure 1-18). This oxidative cleavage reaction was performed at a milder reaction condition compared to other reported examples. This is one of the few examples where the C-C bond is broken selectively compared to the C-O bond.²⁰⁹

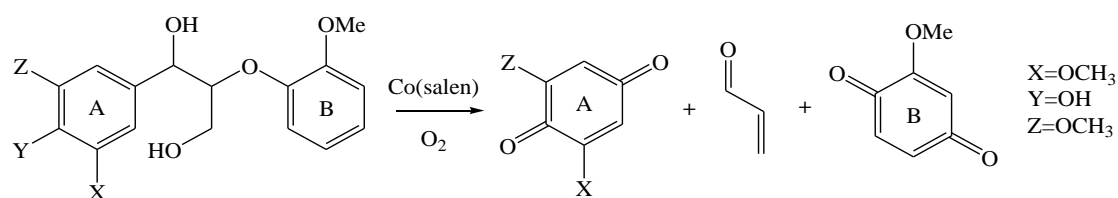


Figure 1-18 Cobalt salen catalysed the selective oxidative cleavage of C_{Ph} - C_{α} linkage in the β -O-4 model compound to form benzoquinones. Adapted from Ref. ²⁰⁹

Moreover, Mottweiler *et al.* reported the catalytic oxidative depolymerisation of organosolv beech and kraft lignins using transition-metal-containing hydrotalcites or combinations of vanadium and copper species using $V(\text{acac})_3$ and $\text{Cu}(\text{NO}_3)_2 \cdot 3\text{H}_2\text{O}$ as catalysts using O_2 .²¹⁰ Significant reduction in the molecular weight was observed due to the effective cleavage of β -O-4' and other inter-linkages. NMR could not fully confirm the structure of the modified (depolymerised) lignin post reaction. However, based on the resinol structure, they have confirmed that the cleavage of β - β' inter-unit linkage. This is again one of the very few examples where the β - β' inter-unit linkage is broken.

Therefore, an integrated approach towards the complete depolymerisation of lignin (with C-C bond cleavage included) to smaller aromatic compounds should be designed to realise the dream of a green and sustainable society. Ruthenium ion catalysed oxidation reactions appear as potential.

1.3.3 *Ruthenium ion catalysed oxidations*

The first use of ruthenium tetroxide (RuO_4) as organic oxidation is thought to stretch back to 1953, as shows the chronological diagram in *Figure 1-19*. Djerassi and Engle began using RuO_4 for the oxidation of a variety of organic substrate, developing what is now known as Ruthenium ion catalysed oxidations (RICO) chemistry.²¹¹ Until then, the analogous osmium tetroxide (OsO_4) was employed as oxidant despite its toxicity, even at low exposure levels. RuO_4 is extremely reactive, and therefore, it was challenging to use selectively. During the first decades, several studies were carried out using RuO_4 in stoichiometric quantities, which provide the advantage that it is neither explosive nor poisonous. Nowadays, ruthenium oxidations are performed catalytically, becoming economically feasible.²¹² RICO has been reported to be useful for the petroleum and coal industries.²¹³⁻²¹⁷

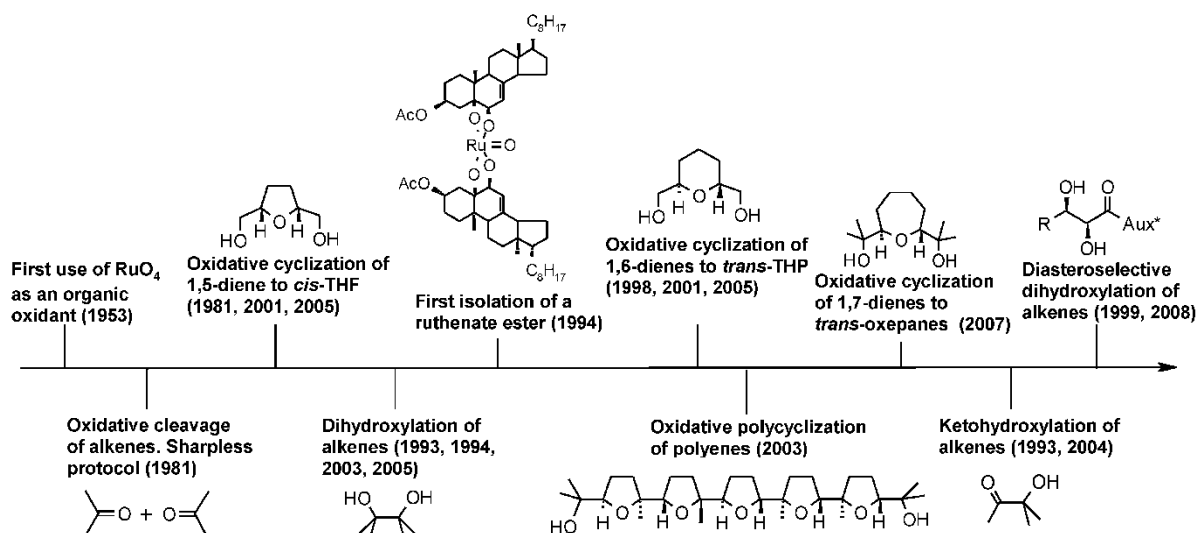
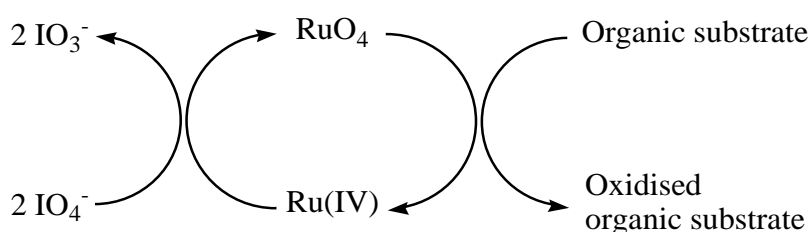


Figure 1-19 Chronological development of the oxidative transformations of alkenes, dienes and polyenes catalysed by RuO₄. Significant dates are shown in parentheses. Copyright © Vincenzo Piccialli, 2014. Licensed under a Creative Commons Attribution 3.0, Ref.²¹⁸

- **Ruthenium (VIII) chemistry**

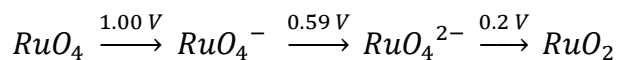
RuO₄ is generated *in-situ* during the reaction using typically as the metal precursor ruthenium(III) chloride (RuCl₃·xH₂O) or ruthenium dioxide hydrate (RuO₂·xH₂O) in the presence of a co-oxidant such as sodium periodate (NaIO₄).²¹⁹ The catalytic cycle showed in Scheme 1-3 indicated that a reduce organic substrate can be oxidised in an efficient re-oxidation process, while Ru (VIII) is reduced to Ru (IV). Then, in the presence of a strong oxidant, RuO₂ can be regenerated back to the original RuO₄. Many oxidants have been reported apart of NaIO₄, such as NaOCl, HIO₄, NaBrO₃, Oxone®, O₃, Ce(SO₄)₂, K₂S₂O₈ for this kind of reactions.^{220–223}



Scheme 1-3 Representation of catalytic cycle for the RICO reaction. Adapted from Ref.²²⁰

RuO₄ is far more oxidising than its isoelectronic homologue OsO₄ in the oxidation of C-C double bonds.²²⁴ Scheme 1-4 shows the oxidation potentials of oxoruthenates. Note that the oxidation potential from RuO₄⁻ to RuO₄²⁻ is almost fourfold higher with the potential from

RuO_4^{2-} to RuO_2 , which makes high oxidation state better oxidant. This property makes ruthenium catalyst of greater interest due to its potential ability to act as a multipurpose oxidising agent.²²⁵



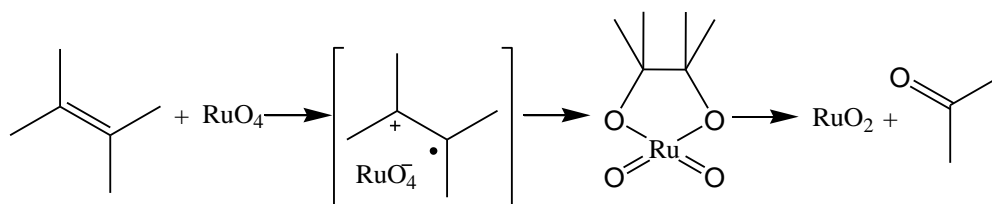
Scheme 1-4 Oxidation potentials of oxoruthenates. Adapted from Ref.²²³

Mills *et al.* further studied the nature of these oxoruthenate species formed during the reaction. It was found that the RuO_4 was stable up to pH 9. Above this value, $\text{pH} > 9$ RuO_4 is reduced to $[\text{RuO}_4]^-$, which is more stable and less reactive.²²⁶ On the contrary, RuO_2^{2-} results less stable and more reactive. Henceforth, reaction conditions using this catalyst are often performed under slightly acidic medium, to get more reactive conditions. Despite this fact, reactions can also be carried out with mild basic conditions.²²³

On the other hand, the stability of the catalyst was thought to cause problems, e.g. Ru complexes formation during reaction or inactivation of ruthenium catalysts.²²⁷ Almost 30 years later, this potential issue was tackled by Sharpless, who observed an increase in reactivity with the use of acetonitrile as a cosolvent.²¹⁹ The lack of stability was believed to be caused by the carboxylate products coordinating to the Ru catalyst. Nevertheless, the introduction of nitrile groups prevents the formation of ruthenium-carboxylate. Using this protocol, known as Sharpless protocol, the catalyst lifetime increases and reactivate the catalytic cycle described above.^{222,223}

After these findings, RuO_4 chemistry is efficient for the oxidation of various substrates such as alcohol, olefins, aromatic rings and even aliphatic C-H bonds.^{227,228} It is an excellent catalyst to break C-C double bonds. Specifically, different studies show the success of ruthenium tetroxide as a selective catalyst in the dehydroxylation of olefins,²²⁷ oxidative cleavages of olefins to aldehydes,²²⁹ alkyl-substituted polyaromatics²³⁰ and alkynes to carboxylic acids.²³¹ RICO reactions for oxidation of saturated hydrocarbons are highly regioselective to the most electron rich C-H bond with retention of configuration.²²³

In 1976, Lee *et al.* were the first to report kinetics studies for the catalysed mechanism with ruthenium tetroxide for the C=C scission. They studied the oxidation of methyl cinnamate by ruthenium tetroxide. The mechanism proposed assumes that RuO_4 binds to the carbon-carbon double bond to produce a cyclic ruthenium-monoester intermediate (*Scheme 1-5*).^{232,233}



Scheme 1-5 Proposed mechanism for the oxidative cleavage of carbon-carbon double bonds by ruthenium tetroxide. Adapted from Ref.²³²

Theoretical studies by DFT confirmed this reaction mechanism almost two decades later. Norrby et al. were the first to report DFT calculations on several Ru(VI) and Ru(VIII) complexes to investigate the mechanism of the dihydroxylation of olefins catalysed by both OsO₄ and RuO₄.²³⁴ After that, Frenking and co-workers published the systematic quantum chemical investigation of the oxidation of ethylene with RuO₄. Their theoretical study suggests that the ruthenium (VI) monoester is formed and a [3+2]-cycloaddition is an intermediate.²²⁴ For both metals tetraoxides, RuO₄ and OsO₄, cyclic ruthenates and osmates are primary intermediates.²²⁴ Indeed, they found that the concerted [3+2] cycloaddition has much lower activation barriers than the [2+2] addition (Figure 1-20). Nevertheless, the main difference is that olefins oxidised by RuO₄ produce the cleavage of the carbon-carbon bond, whereas oxidation by OsO₄ yields cis-Diols instead. The reason is that in the case of RuO₄, the ruthenium compound has a very low activation barrier of $\Delta H_q = 2.5$ kcal/mol compared with the activation barrier of the Os compound ($\Delta H_q = 18.9$ kcal/mol).²²⁴ These results are compatible with the experimental observation that shows the oxidation reaction of olefins at mild conditions proceeds under rupture of the C-C bond.

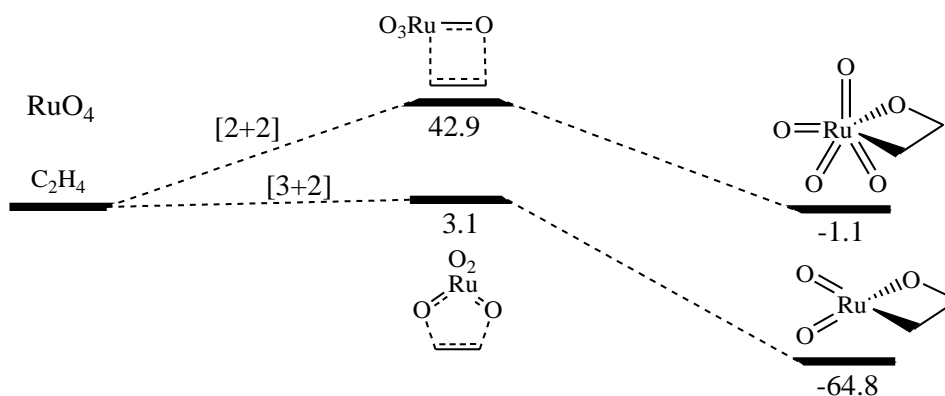
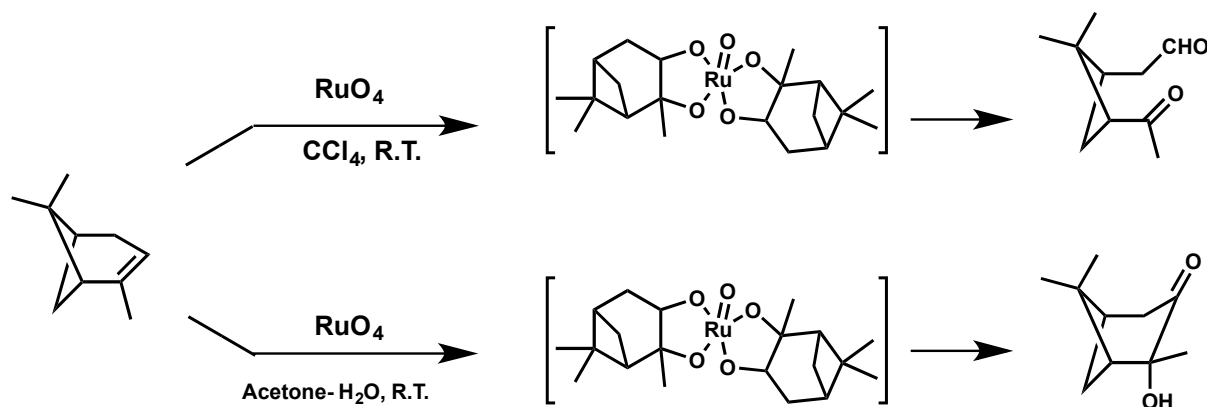


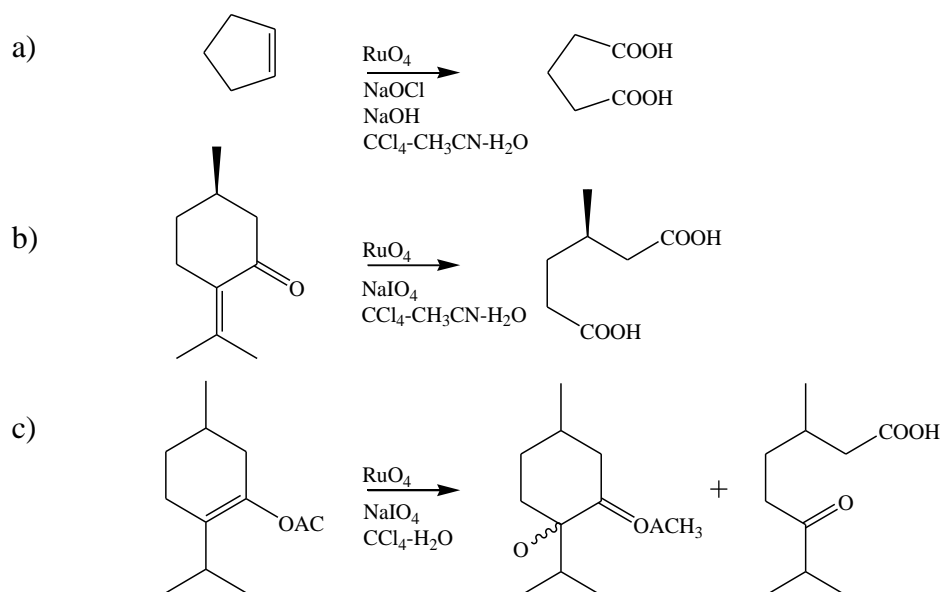
Figure 1-20 Energy diagram of [2+2] vs [3+2] cycloaddition between RuO₄ and olefins. Adapted from Ref.²²³

Detailed studies on the interaction between the ruthenium catalyst and carbon-carbon double bond present in olefins were carried out later on by Piccialli and Sica.^{218,235} They also showed the scission of carbon-carbon double bond using a RuO_4 oxidation reaction. This reaction gives a ketoaldehyde or a α -ketol product, using either in CCl_4 or acetone-water respectively as solvent at room temperature (*Scheme 1-6*). These authors suggested that in this case, the reaction proceeds through ruthenium (VI) diester intermediate. They also concluded that reaction between RuO_4 and olefins could be compared to that of the isoelectronic OsO_4 (less reactive) with olefins. Although these authors claim that this mechanism is also valid for the oxidation of aromatic compounds, these experiments did not provide any strong evidence confirming this.



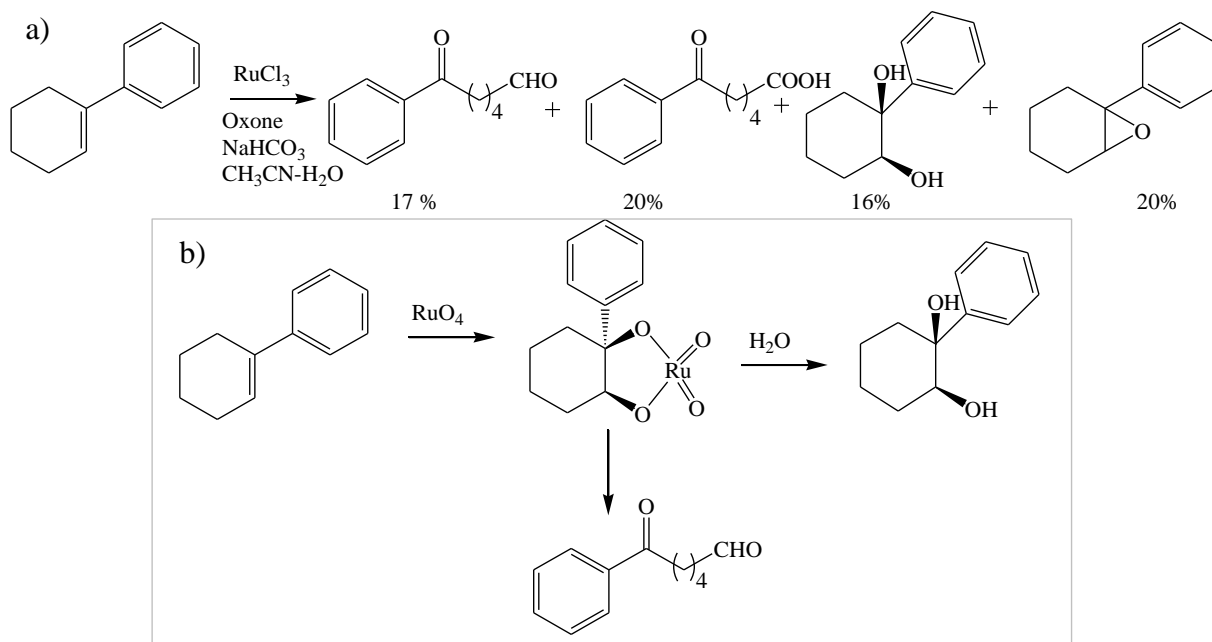
Scheme 1-6 Reaction Scheme showing the scission of a carbon-carbon double bond, giving ketoaldehyde or α -ketol products. Copyright © 1995, Elsevier Science, Ltd. Reproduced with permission of Ref.²³⁵

In this oxidation as the reaction produces precipitation of large quantities of iodate using periodate as re-oxidant. For this reason, some researchers decided to employ sodium hypochlorite instead in the presence of alkali (e.g. oxidation of cyclopentene to glutaric acid, *Scheme 1-7-a*).²²² In the case of aromatic olefins, the compound is cleaved by reacting with RuO_4 . *Scheme 1-7-b* shows how the pulegone compound is cleaved again by the well-known periodate reaction with the loss of one or more carbon atoms. Finally, any remaining aldehyde groups are oxidised to acids, which gave a 92 % yield of 3-methyladipic acid. The compound now must contain vicinal oxygen atoms in unspecified oxidation states. In the same way that for enolic olefins where the cleaved products are obtained in excellent yields (*Scheme 1-7-c*). Using RuO_4 , the product mixture obtained was α -hydroxy ketone (53 % yield) and keto acid (44 % yield).



Scheme 1-7 Oxidative cleavage to afford the corresponding carbonyl compound. Mechanisms for the oxidation of a) cyclopentene,²²² b) pulegone,²³⁶ and c) enol acetate with RuO_4 .²³³ Adapted from Ref.²²⁷

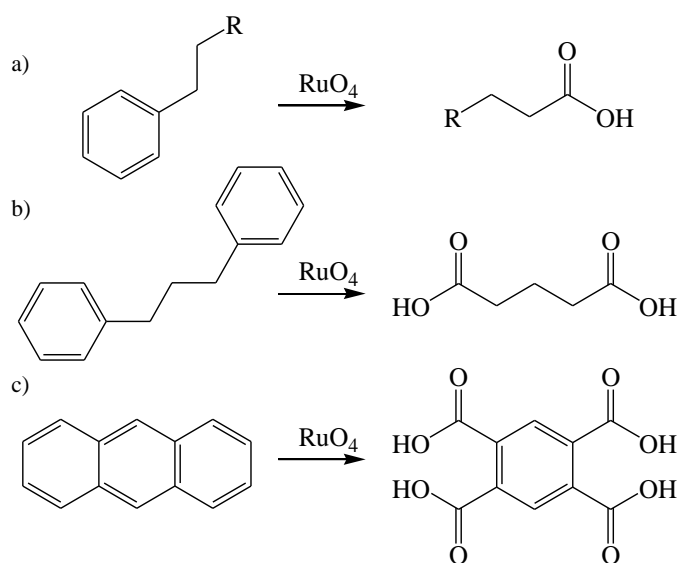
Another example of oxidative C-C bond cleavage is 1-phenylcyclohexene. Yang *et al.* obtained a complex mixture of oxidation products from this reaction (*Scheme 1-8-a*).²²⁹ The author also suggested that a cyclic ruthenium (VI) diester was probably the intermediate, which yielded keto aldehyde (*Scheme 1-8-b*).



Scheme 1-8 Mechanisms suggested for the oxidation of 1-phenylcyclohexene with RuO_4 and product distribution. Adapted from Ref.²²⁹

- *Oxidation of aromatic compounds*

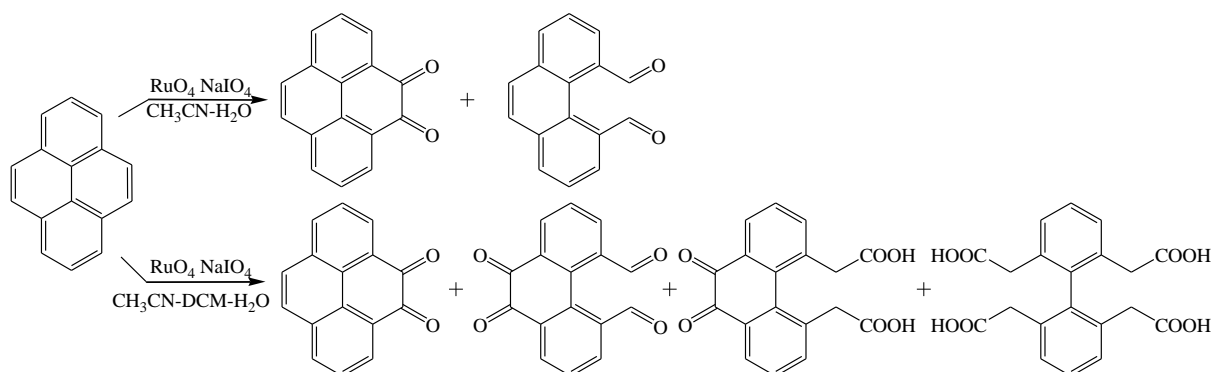
Amongst the many oxidation applications of using the ruthenium tetroxide catalyst includes the oxidative fragmentation of aromatic compounds to carboxylic acids.²³⁷ Zi-Shuo Yao *et al.* applied ruthenium ion oxidation reactions to aromatics compounds and found that ring opening of the aromatic rings had occurred.^{238,239} This process produces carboxylic acids, with aromatics oxidised to CO₂ and H₂O leaving the aliphatic chain intact (*Scheme 1-9*).²²¹ The use of ruthenium tetroxide for degrading aromatic steroids has also been explored.



Scheme 1-9 Mechanisms for the oxidation of a) alkylbenzene, b) 1,3-diphenylpropane and c) anthracene with RuO₄. Adapted from Ref.²²¹

Recently, Nowicka *et al.* studied the use of RuO₄ for the oxidation of a range of alkylated polyaromatics.²³⁰ The authors proved that RICO chemistry could be used selectively to reduce the aromaticity of alkylated polynuclear aromatics preserving aliphatic chain substituents. They studied two solvent systems, a monophasic solvent system (miscible acetonitrile and water) and a biphasic solvent system (with the incorporation of an organic phase, dichloromethane in the reaction). The product distribution obtained from the monophasic system was the same as the biphasic one. Later, the same group reported the oxidation of polynuclear aromatic hydrocarbons (PAHs) such as naphthalene, phenanthrene and pyrene using RICO.²⁴⁰ Kinetic studies of molecules with differing numbers of fused aromatic rings (2–5) in the molecular core showed that larger molecules reacted faster than smaller ones. At the same time, they found significant differences in the product distribution depending on the solvent system employed for larger molecules (*Scheme 1-10*). The result suggested that there

is a higher pyrene solubility using the DCM, and the oxidation proceeded further than using the monophasic solvent system. Moreover, DFT calculations showed regioselectivity in these reactions.²⁴¹



Scheme 1-10 Products of pyrene oxidation in the monophasic (top) and the biphasic (bottom) solvent systems. Adapted from Ref. ²⁴⁰

These results suggest that RICO proceeds by following the steps:²⁴⁰ 1) The aromatic hydrocarbons are oxidised to CO₂ and H₂O in high yield. 2) Attached aliphatic chains are only likely to be oxidised at benzylic positions. 3) The aliphatic chain is not further oxidised.

1.4 Aim and outline of the Thesis

Biorefineries emerged as a consequence of the need for producing chemicals and fuels from sustainable feedstocks. Effective biomass conversion requires new technology development where catalysis will play a very important role. The aims for this thesis are to investigate and optimise catalytic systems of both homogeneous and heterogeneous catalyst for different kind of biomass, triglycerides and lignocellulosic feedstock biomass to contribute to the improvement of efficiency of the current biorefinery.

In the first instance, with the increasing demand for this biofuel, of course, there will be an increase in by-products that will need to have commercial value themselves or be converted into value-added products. Waste glycerol is considered a platform molecule since many useful products that can be made from glycerol. The formation of 1,2- and 1,3-propanediol is an exciting challenge. The conversion of glycerol is becoming a vastly studied area due to the ever-growing production of biodiesel. High conversions have been reported in the literature using noble and non-noble metals as catalysts for the hydrogenolysis of glycerol, with Ruthenium proving to be the most active metal. However, the design of stable catalyst for effective glycerol hydrogenolysis to form C3 products needs more research.

The objectives of **Chapter 3** are to study the effect of combining two metals and to investigate their synergistic effect for the hydrogenolysis of glycerol into C3 diols. The catalytic properties of Ru, Pd and Pt monometallic will be compared against the PdRu and PtRu bimetallic catalyst supported on TiO₂. Characterisation of the oxidation properties of the metal nanoparticles for the understanding of their influence in the activity will also be discussed in this chapter.

In **Chapter 4**, the best combination of metal found will be studied as long with the best support to favour the dehydration of glycerol instead of the degradation *via* C-C bond cleavage to gas phase products. Extense characterisation of the most relevant catalyst will be carried out to understand the nature of the metal-support interaction in supported bimetallic catalysts. Based on the state-of-the-art, bifunctional catalysts need to be investigated. This Chapter discuss the results obtained regarding the influence of the acid properties of the support and to relate these effects to the catalytic properties. For this purpose, several types of zeolites with a range SiO₂: Al₂O₃ ratio would be used as support, along with different metal oxides.

On the other hand, one of the promising strategies to produce chemicals and fuels from sustainable feedstocks is to depolymerise lignin to smaller aromatic compounds. Lignin

contains two inter-unit linkages, namely C-O and C-C linkages. For the complete depolymerisation of lignin, it is essential to break these two linkages effectively. Many catalytic and non-catalytic strategies have been reported for the breaking of C-O linkages. However, reports on the successful breaking of C-C inter-unit linkages are scarce. This is because the C-C inter-unit linkages are inherently stronger than the C-O linkages, hence more robust to break. However, all technical lignin (derived from paper and pulping industries) have a higher proportion of C-C linkages than C-O linkages. Since technical lignin is available in vast quantities, it is essential to design strategies to break the C-C linkages to achieve complete depolymerisation of technical lignin to smaller aromatic compounds.

Chapter 5 focus on the development of a catalytic system able to cleave C-C bond in lignin model compounds, towards lignin depolymerisation. To achieve this goal, ruthenium ion catalysed oxidation reactions (RICO) is going to be applied on simple model compounds (only one inter-unit linkage). Using the previous as a basis, it will be studied a more sophisticated fully functionalised model compound with a combination of different inter-unit linkages.

Finally, **Chapter 6** will review the concluding remarks for the entire thesis results and objectives. It will also expose the possible future actions that can be addressed base on the findings of this work.

1.5 References

1. Popp, J.; Lakner, Z.; Harangi-Rákos, M.; Fári, M., *Renew. Sustain. Energy Rev.* **2014**, *32*, 559–578.
2. Miller, R. G.; Sorrell, S. R., *Philos. Trans. A. Math. Phys. Eng. Sci.* **2014**, *372* (2006), 20130179.
3. Glenn, J. K.; Morgan, M. A.; Mayfield, M. B.; Kuwahara, M.; Gold, M. H., *Biochem. Biophys. Res. Commun.* **1983**, *114* (3), 1077–1083.
4. Clark, J. H.; Budarin, V.; Deswarte, F. E. I.; Hardy, J. J. E.; Kerton, F. M.; Hunt, A. J.; Luque, R.; Macquarrie, D. J.; Milkowski, K.; Rodriguez, A.; et al., *Green Chem.* **2006**, *8* (10), 853–860.
5. McKendry, P., *Bioresour. Technol.* **2002**, *83* (1), 37–46.
6. Ptasincki, K. J. *Efficiency of Biomass Energy : An Exergy Approach to Biofuels, Power, and Biorefineries*; John Wiley & Sons, 2019.
7. Kamm, B.; Gruber, P. R.; Kamm, M. *Biorefineries - Industrial Processes and Products*. In *Ullmann's Encyclopedia of Industrial Chemistry*; Wiley-VCH Verlag GmbH & Co. KGaA: Weinheim, Germany, 2007.
8. Zharmukhamedov, S. K.; Nejat Veziroglu, T.; Rodionova, M. V.; Allakhverdiev, S. I.; Voloshin, R. A., *Int. J. Hydrogen Energy* **2016**, *41* (39), 17257–17273.
9. Axelsson, L.; Franzén, M.; Ostwald, M.; Berndes, G.; Lakshmi, G.; Ravindranath, N. H., *Biofuels, Bioprod. Biorefining* **2012**, *6* (3), 246–256.
10. Cherubini, F., *Energy Convers. Manag.* **2010**, *51* (7), 1412–1421.
11. Speirs, J.; McGlade, C.; Slade, R., *Energy Policy* **2015**, *87*, 654–664.
12. Tuck, C. O.; Perez, E.; Horvath, I. T.; Sheldon, R. a.; Poliakov, M., *Science*. **2012**, *337* (6095), 695–699.
13. Thompson, P., *Agriculture* **2012**, *2* (4), 339–358.
14. Saini, J. K.; Saini, R.; Tewari, L., *3 Biotech* **2015**, *5* (4), 337–353.
15. Boboc, M.; Achiricesei, R.-I.; Bouriaud, L.; Nichiforel, R. *Social and Ethical Challenges of Using Biomass -a Renewable Energy Source*; 2016; Vol. IV.
16. Huber, G. W.; Iborra, S.; Corma, A., *Chem. Rev.* **2006**, *106* (9), 4044–4098.
17. Huber, G. W.; Corma, A., *Angew. Chemie - Int. Ed.* **2007**, *46* (38), 7184–7201.
18. Su, Y.; Zhang, P.; Su, Y., *Renew. Sustain. Energy Rev.* **2015**, *50*, 991–1003.
19. Xu, J.; Li, M., *Energy Convers. Manag.* **2017**, *141*, 48–62.
20. Reay, D.; Sabine, C.; Smith, P.; Hymus, G., *Nature* **2007**, *446* (7137), 727–728.
21. Barry, S. *Biofuels and Sustainability*; Takeuchi, K., Shiroyama, H., Saito, O., Matsuura, M., Eds.; Science for Sustainable Societies; Springer Japan: Tokyo, 2018; Vol. 1185.
22. Holzman, D. C., *Environ. Health Perspect.* **2008**, *116* (6), A246-52.
23. Fargione, J.; Hill, J.; Tilman, D.; Polasky, S.; Hawthorne, P., *Science*. **2008**, *319* (5867), 1235–1238.
24. Otto, D.; Breitmeier, H. *The Politics of Climate Change: A Political Science Perspective*. In *T869 LECH-e Module1 Textbook 2012*; 2013.
25. United Nations Climate Change Secretariat, M. P. *Yearbook of Global Climate Action 2018*; 2018.
26. Ireland, G. of. *Project 2040: Investing in the Transition to a Low-Carbon and Climate-Resilient Society: 2018 - 2027*; 2018.
27. *Low-Carbon Research and Innovation. Building a Low-Carbon, Climate-Resilient Future*; 2017.

28. Srivastava, A.; Prasad, R., *Renew. Sustain. Energy Rev.* **1999**, *4* (2000), 111–133.
29. Gallezot, P., *Catal. Today* **2007**, *121* (1–2), 76–91.
30. Behl, R. K.; Chhibar, R. N.; Jain, S.; Bahl, V. P.; Bassam, N. El. “Renewable” Energy Sources and Their Limitations. In *Topics in Safety, Risk, Reliability and Quality*; 2010; Vol. 16, pp 65–75.
31. Vyas, A. P.; Verma, J. L.; Subrahmanyam, N., *Fuel* **2010**, *89* (1), 1–9.
32. Wang, Y.; Zhou, J.; Guo, X., *RSC Adv.* **2015**, *5* (91), 74611–74628.
33. Quispe, C. A. G.; Coronado, C. J. R.; Carvalho Jr., J. A., *Renew. Sustain. Energy Rev.* **2013**, *27* (C), 475–493.
34. Chatwani, B. N.; Mewada, R. K., *Procedia Eng.* **2013**, *51*, 443–450.
35. Yang F, Hanna M a, S. R., *Biotechnol Biofuels* **2012**, *5* (13), 1–10.
36. Talebian-Kiakalaieh, A.; Amin, N. A. S.; Hezaveh, H., *Renew. Sustain. Energy Rev.* **2014**, *40*, 28–59.
37. Luo, X.; Hu, S.; Zhang, X.; Li, Y., *Technol.* **2013**, *139*, 323–329.
38. Hunsom, M.; Saila, P., *Renew. Energy* **2015**, *74*, 227–236.
39. Kim, Y. C.; Moon, D. J., *Catal. Surv. from Asia* **2019**, *23* (1), 10–22.
40. Tendam, J.; Hanefeld, U., *ChemSusChem* **2011**, *4* (8), 1017–1034.
41. Sun, D.; Yamada, Y.; Sato, S.; Ueda, W., *Appl. Catal. B Environ.* **2016**, *193*, 75–92.
42. Zhou, C.-H. (Clayton); Beltramini, J. N.; Fan, Y.-X.; Lu, G. Q. (Max)., *Chem. Soc. Rev.* **2008**, *37* (3), 527–549.
43. Climent, M. J.; Corma, A.; De Frutos, P.; Iborra, S.; Noy, M.; Velty, A.; Concepción, P., *J. Catal.* **2010**, *269* (1), 140–149.
44. Isikgor, F. H.; Becer, C. R.; Becer, R.; Becer, C. R., *Polym. Chem.* **2015**, *6* (25), 4497–4559.
45. Ed de, J.; Adrian, H.; Patrick, W.; Maria, W. *Bio-Based Chemicals Value Added Products from Biorefineries*; 2011.
46. Chheda, J. N.; Huber, G. W.; Dumesic, J. A., *Angew. Chemie - Int. Ed.* **2007**, *46* (38), 7164–7183.
47. Miyazawa, T.; Kusunoki, Y.; Kunimori, K.; Tomishige, K., *J. Catal.* **2006**, *240* (2), 213–221.
48. Musolino, M. G.; Scarpino, L. A.; Mauriello, F.; Pietropaolo, R., *ChemSusChem* **2011**, *4* (8), 1143–1150.
49. Zhang, Y.; Liu, D.; Chen, Z., *Biotechnol. Biofuels* **2017**, *10* (1), 1–20.
50. Rebsdatt, S.; Mayer, D. Ethylene Oxide. In *Ullmann’s Encyclopedia of Industrial Chemistry*; Wiley-VCH Verlag GmbH & Co. KGaA: Weinheim, Germany, 2001; pp 4–6.
51. Carus, M. *Bio-Based Building Blocks and Polymers in the World-Capacities, Production and Applications: Status Quo and Trends toward 2020*; 2015.
52. Kawabe, K., *Catal. Surv. from Asia* **2010**, *14* (3–4), 111–115.
53. Nakagawa, Y.; Tomishige, K., *Catal. Sci. Technol.* **2011**, *1* (1), 179–190.
54. Gilkey, M. J.; Xu, B., *ACS Catal.* **2016**, *6* (3), 1420–1436.
55. Martin, A.; Armbruster, U.; Gandarias, I.; Arias, P. L., *Eur. J. Lipid Sci. Technol.* **2013**, *115* (1), 9–27.
56. Lee, C. S.; Aroua, M. K.; Daud, W. M. A. W. A. W.; Cognet, P.; Pérès-Lucchese, Y.; Fabre, P.-L. L.; Reynes, O.; Latapie, L., *Renew. Sustain. Energy Rev.* **2015**, *42*, 235–244.

57. Nakagawa, Y.; Tamura, M.; Tomishige, K., *Res. Chem. Intermed.* **2018**, *44* (7), 3879–3903.
58. Nanda, M. R.; Yuan, Z.; Qin, W.; Xu, C., *Catal. Rev.* **2016**, *58* (3), 309–336.
59. Che, T. M.; Westfield, N. J. Production of Propanediols. Patent No. 4,642,394, 1987.
60. Drent E, J. Hydrogenolysis of Glycerol. Patent No. 6080898, 1999.
61. Sato, S.; Akiyama, M.; Inui, K.; Yokota, M., *Chem. Lett.* **2009**, *38* (6), 560–561.
62. Gandarias, I.; Requies, J.; Arias, P. L.; Armbruster, U.; Martin, A., *J. Catal.* **2012**, *290*, 79–89.
63. Roy, D.; Subramaniam, B.; Chaudhari, R. V., *Catal. Today* **2010**, *156* (1–2), 31–37.
64. Chaminand, J.; Djakovitch, L. auren.; Gallezot, P.; Marion, P.; Pinel, C.; Rosier, C., *Green Chem.* **2004**, *6* (8), 359–361.
65. Furikado, I.; Miyazawa, T.; Koso, S.; Shimao, A.; Kunimori, K.; Tomishige, K., *Green Chem.* **2007**, *9* (6), 582.
66. Priya Samudrala, S. Glycerol Transformation to Value-Added 1,3-Propanediol Production: A Paradigm for a Sustainable Biorefinery Process. In *Glycerine Production and Transformation - An Innovative Platform for Sustainable Biorefinery and Energy*; IntechOpen, 2019.
67. Pudi, S. M.; Biswas, P.; Kumar, S.; Sarkar, B., *Chem. Soc.* **2015**, *26* (8), 1551–1564.
68. Koso, S.; Nakagawa, Y.; Tomishige, K., *J. Catal.* **2011**, *280* (2), 221–229.
69. Nakagawa, Y.; Shinmi, Y.; Koso, S.; Tomishige, K., *J. Catal.* **2010**, *272* (2), 191–194.
70. Sinfelt, J. H., *Acc. Chem. Res.* **1977**, *10* (1), 15–20.
71. Sinfelt, J. H. *Bimetallic Catalysts: Discoveries, Concepts, and Applications*; Exxon Monographs Series; Wiley, 1983.
72. Shibasaki, M.; Yamamoto, Y. *Multimetallic Catalysts in Organic Synthesis*; Wiley, 2006.
73. Yu, W. Y.; Mullen, G. M.; Flaherty, D. W.; Mullins, C. B., *J. Am. Chem. Soc.* **2014**, *136* (31), 11070–11078.
74. Croy, J. R.; Mostafa, S.; Hickman, L.; Heinrich, H.; Cuenya, B. R., *Appl. Catal. A Gen.* **2008**, *350* (2), 207–216.
75. Guadix-Montero, S.; Alshammari, H.; Dalebout, R.; Nowicka, E.; Morgan, D. J.; Shaw, G.; He, Q.; Sankar, M., *Appl. Catal. A Gen.* **2017**, *546*, 58–66.
76. Sankar, M.; Dimitratos, N.; Miedziak, P. J.; Wells, P. P.; Kiely, C. J.; Hutchings, G. J., *Chem. Soc. Rev.* **2012**, *41* (24), 8099.
77. Gao, F.; Goodman, D. W., *Chem. Soc. Rev.* **2012**, *41* (24), 8009–8020.
78. Alayoglu, S.; Nilekar, A. U.; Mavrikakis, M.; Eichhorn, B., *Nat. Mater.* **2008**, *7* (4), 333–338.
79. Gallegos-Suarez, E.; Guerrero-Ruiz, A.; Rodriguez-Ramos, I.; Arcoya, A., *Chem. Eng. J.* **2015**, *262*, 326–333.
80. Amorim, C.; Keane, M. A., *J. Colloid Interface Sci.* **2008**, *322* (1), 196–208.
81. Maris, E. P.; Ketchie, W. C.; Murayama, M.; Davis, R. J., *J. Catal.* **2007**, *251* (2), 281–294.
82. Maris, E. P.; Davis, R. J., *J. Catal.* **2007**, *249* (2), 328–337.
83. Kusunoki, Y.; Miyazawa, T.; Kunimori, K.; Tomishige, K., *Catal. Commun.* **2005**, *6* (10), 645–649.
84. Li, B.; Wang, J.; Yuan, Y.; Ariga, H.; Takakusagi, S.; Asakura, K., *ACS Catal.* **2011**, *1*, 1521.

85. Musolino, M. G.; Busacca, C.; Mauriello, F.; Pietropaolo, R., *Appl. Catal. A Gen.* **2010**, *379* (1–2), 77–86.
86. Musolino, M. G.; Scarpino, L. A.; Mauriello, F.; Pietropaolo, R., *Green Chem.* **2009**, *11* (10), 1511.
87. Shima, A.; Koso, S.; Ueda, N.; Shinmi, Y.; Furikado, I.; Tomishige, K., *Chem. Lett.* **2009**, *38* (6), 540–541.
88. Vasiliadou, E. S.; Lemonidou, A. A., *Org. Process Res. Dev.* **2011**, *15* (4), 925–931.
89. Huang, J.; Chen, J., *Chinese J. Catal.* **2012**, *33* (4–6), 790–796.
90. Gandarias, I.; Arias, P. L.; Fernández, S. G.; Requies, J.; El Doukkali, M.; Güemez, M. B., *Catal. Today* **2012**, *195* (1), 22–31.
91. Feng, J.; Wang, J.; Zhou, Y.; Fu, H.; Chen, H.; Li, X., *Chem. Lett.* **2007**, *36* (10), 1274–1275.
92. He, B.; Li, C.; Xiao, Z.; Wang, B.; Liang, C., *React. Kinet. Mech. Catal.* **2017**, *122* (1), 101–115.
93. Feng, J.; Zhang, Y.; Xiong, W.; Ding, H.; He, B., *Catalysts* **2016**, *6* (4), 51.
94. Zou, B.; Ren, S.; Ye, X. P., *ChemSusChem* **2016**, *9* (23), 3268–3271.
95. Kim, Y. T.; Jung, K. D.; Park, E. D., *Appl. Catal. A Gen.* **2011**, *393* (1–2), 275–287.
96. Corma, A.; Huber, G. W.; Sauvanaud, L.; O'Connor, P., *J. Catal.* **2008**, *257* (1), 163–171.
97. Kandasamy, S.; Samudrala, S. P.; Bhattacharya, S. Vapour Phase Hydrogenolysis of Glycerol over NaY-Zeolite Supported Ru Catalysts for Targeted Selectivity towards 1,2-Propanediol. In *2018 2nd International Conference on Green Energy and Applications (ICGEA)*; IEEE, 2018; pp 14–18.
98. Priya, S. S.; Bhanuchander, P.; Kumar, V. P.; Dumbre, D. K.; Periasamy, S. R.; Bhargava, S. K.; Lakshmi Kantam, M.; Chary, K. V. R., *ACS Sustain. Chem. Eng.* **2016**, *4* (3), 1212–1222.
99. Jarauta-Córdoba, C.; Ruíz, J.; Oliva, M.; García, L.; Arauzo, J., *Jorn. Jóvenes Investig. del I3A* **2018**, *6*, 5–6.
100. Chiu, C.; Dasari, M. A.; Suppes, G. J., *Am. Inst. Chem. Eng.* **2006**, *52* (10), 3543–3548.
101. Chiu, C.; Tekeci, A.; Sutterlin, W. R.; Ronco, J. M.; Suppes, G. J., *AIChE J.* **2008**, *54* (9), 2456–2463.
102. Dasari, M. A.; Kiatsimkul, P.-P.; Sutterlin, W. R.; Suppes, G. J., *Appl. Catal. A Gen.* **2005**, *281* (1–2), 225–231.
103. Durán-Martín, D.; Granados, M. L.; Fierro, J. L. G. G.; Pinel, C.; Mariscal, R., *Top. Catal.* **2017**, *60* (15–16), 1062–1071.
104. Ueda, N.; Nakagawa, Y.; Tomishige, K., *Chem. Lett.* **2010**, *39* (5), 506–507.
105. Guo, X.; Li, Y.; Shi, R.; Liu, Q.; Zhan, E.; Shen, W., *Appl. Catal. A Gen.* **2009**, *371* (1–2), 108–113.
106. Huang, Z.; Liu, H.; Cui, F.; Zuo, J.; Chen, J.; Xia, C., *Catal. Today* **2014**, *234*, 223–232.
107. Kant, A.; He, Y.; Jawad, A.; Li, X.; Rezaei, F.; Smith, J. D.; Rownaghi, A. A., *Chem. Eng. J.* **2017**, *317*, 1–8.
108. Koso, S.; Watanabe, H.; Okumura, K.; Nakagawa, Y.; Tomishige, K., *Appl. Catal. B Environ.* **2012**, *111–112*, 27–37.
109. Amada, Y.; Koso, S.; Nakagawa, Y.; Tomishige, K., *MRS Proc.* **2011**, *1326*, mrss11-1326-f05-06.
110. Zhou, J.; Zhang, J.; Guo, X.; Mao, J.; Zhang, S., *Green Chem.* **2012**, *14* (1), 156–163.

111. Yadav, G. D.; Chandan, P. A.; Tekale, D. P., *Ind. Eng. Chem. Res.* **2012**, *51* (4), 1549–1562.
112. Ma, L.; He, D.; Li, Z., *Catal. Commun.* **2008**, *9* (15), 2489–2495.
113. Sankar, M.; He, Q.; Morad, M.; Pritchard, J.; Freakley, S. J.; Edwards, J. K.; Taylor, S. H.; Morgan, D. J.; Carley, A. F.; Knight, D. W.; et al., *ACS Nano* **2012**, *6* (8), 6600–6613.
114. Hutchings, G. J.; Kiely, C. J., *Acc. Chem. Res.* **2013**, *46* (8), 1759–1772.
115. Li, Y.; Liu, H.; Ma, L.; He, D., *Appl. Catal. A Gen.* **2016**, *522*, 13–20.
116. Li, Y.; Liu, H.; Ma, L.; He, D., *RSC Adv.* **2014**, *4* (11), 5503.
117. Checa, M.; Auneau, F.; Hidalgo-Carrillo, J.; Marinas, A.; Marinas, J. M.; Pinel, C.; Urbano, F. J., *Catal. Today* **2012**, *196* (1), 91–100.
118. Checa, M.; Marinas, A.; Marinas, J. M.; Urbano, F. J., *Appl. Catal. A Gen.* **2015**, *507*, 34–43.
119. Huber, G. W.; Shabaker, J. W.; Evans, S. T.; Dumesic, J. A., *Appl. Catal. B Environ.* **2006**, *62* (3–4), 226–235.
120. Shabaker, J. W.; Huber, G. W.; Davda, R. R.; Cortright, R. D.; Dumesic, J. A., *Catal. Lett. Vol.* **2003**, *88*, 1–8.
121. Deng, C.; Duan, X.; Zhou, J.; Chen, D.; Zhou, X.; Yuan, W., *Catal. Today* **2014**, *234*, 208–214.
122. Falcone, D. D.; Hack, J. H.; Klyushin, A. Y.; Knop-gericke, A.; Schlögl, R.; Davis, R. J.; Schlo, R.; Davis, R. J.; Schlögl, R.; Davis, R. J., *ACS Catal.* **2015**, *5* (10), 5679–5695.
123. Garcia-Fernandez, S.; Gandarias, I.; Requies, J. J.; Soulimani, F.; Arias, P. L.; Weckhuysen, B. M.; García-Fernández, S.; Gandarias, I.; Requies, J. J.; Soulimani, F.; et al., *Appl. Catal. B Environ.* **2017**, *204*, 260–272.
124. García-Fernández, S.; Gandarias, I.; Requies, J.; Güemez, M. B.; Bennici, S.; Auroux, A.; Arias, P. L., *J. Catal.* **2015**, *323*, 65–75.
125. Liu, L.; Corma, A., *Chem. Rev.* **2018**, *118* (10), 4981–5079.
126. Zhang, L.; Ren, Y.; Liu, W.; Wang, A.; Zhang, T., *Natl. Sci. Rev.* **2018**, *5* (5), 653–672.
127. Wang, A.; Li, J.; Zhang, T., *Nat. Rev. Chem.* **2018**, *2* (6), 65–81.
128. Wang, J.; Zhao, X.; Lei, N.; Li, L.; Zhang, L.; Xu, S.; Miao, S.; Pan, X.; Wang, A.; Zhang, T., *ChemSusChem* **2016**, *9* (8), 784–790.
129. Ma, L.; Jia, I.; Guo, X.; Xiang, L., *Chinese J. Catal.* **2014**, *35* (2), 108–119.
130. Zhao, X.; Wang, J.; Yang, M.; Lei, N.; Li, L.; Hou, B.; Miao, S.; Pan, X.; Wang, A.; Zhang, T., *ChemSusChem* **2017**, *10* (5), 819–824.
131. Kumar, V. P.; Harikrishna, Y.; Nagaraju, N.; Chary, K. V. R., *Indian J. Chem. - Sect. A Inorganic, Phys. Theor. Anal. Chem.* **2014**, *53* (4–5), 516–523.
132. Vanama, P. K.; Kumar, A.; Gijupalli, S. R.; Komandur, V. R. C., *Catal. Today* **2015**, *250*, 226–238.
133. Hamzah, N.; Nordin, N. M.; Nadzri, A. H. A.; Nik, Y. A.; Kassim, M. B.; Yarmo, M. A., *Appl. Catal. A Gen.* **2012**, *419–420*, 133–141.
134. Miyazawa, T.; Koso, S.; Kunimori, K.; Tomishige, K., *Appl. Catal. A Gen.* **2007**, *329* (3), 30–35.
135. Tamura, M.; Amada, Y.; Liu, S.; Yuan, Z.; Nakagawa, Y.; Tomishige, K., *J. Mol. Catal. A Chem.* **2014**, *388–389*, 177–187.
136. Li, K.-T.; Yen, R.-H. *Nanomaterials* **2018**, *8* (3), 153.
137. Ma, L.; He, D., *Top. Catal.* **2009**, *52* (6–7), 834–844.

138. Ma, L.; He, D., *Catal. Today* **2010**, *149* (1–2), 148–156.
139. Jiang, T.; Zhou, Y.; Liang, S.; Liu, H.; Han, B., *Green Chem.* **2009**, *11* (7), 1000–1006.
140. Liu, H.; Liang, S.; Jiang, T.; Han, B.; Zhou, Y., *Clean - Soil, Air, Water* **2012**, *40* (3), 318–324.
141. Villa, A.; Chan-Thaw, C. E.; Campisi, S.; Bianchi, C. L.; Wang, D.; Kotula, P. G.; Kübel, C.; Prati, L., *Phys. Chem. Chem. Phys.* **2015**, *17* (42), 28171–28176.
142. Luo, W.; Sankar, M.; Beale, A. M.; He, Q.; Kiely, C. J.; Bruijninx, P. C. A.; Weckhuysen, B. M., *Nat. Commun.* **2015**, *6* (1), 6540.
143. Zakzeski, J.; Bruijninx, P. C. a; Jongerius, A. L.; Weckhuysen, B. M., *Chem. Rev.* **2010**, *110* (6), 3552–3599.
144. Cherubini, F.; Strømman, A. H., *Biofuels, Bioprod. Bioref.* **2011**, *5* (7491), 548–561.
145. Kaparaju, P.; Serrano, M.; Thomsen, A. B.; Kongjan, P.; Angelidaki, I., *Bioresour. Technol.* **2009**, *100* (9), 2562–2568.
146. Li, C.; Zhao, X.; Wang, A.; Huber, G. W.; Zhang, T., *Chem. Rev.* **2015**, *115* (21), 11559–11624.
147. Kubicek, C. P., *Fungi Lignocellul. Biomass* **2012**, *2*, 1–28.
148. Cotana, F.; Cavalaglio, G.; Nicolini, A.; Gelosia, M.; Coccia, V.; Petrozzi, A.; Brinchi, L., *Energy Procedia* **2014**, *45* (0), 52–60.
149. Fabrizio Cavani, Stefania Albonetti, Francesco Basile, A. G. Chemicals and Fuels from Biomass Based Building Bloks; Wiley, Ed.; 2016; p 758.
150. Ragauskas, A. J.; Beckham, G. T.; Biddy, M. J.; Chandra, R.; Chen, F.; Davis, M. F.; Davison, B. H.; Dixon, R. A.; Gilna, P.; Keller, M.; et al., *Science* **2014**, *344* (6185), 1246843.
151. Calvo-Flores, F. G.; Dobado, J. A.; Isac-García, J.; Martín-Martínez, F. J. *Lignin and Lignans as Renewable Raw Materials*; Wiley Series in Renewable Resource; John Wiley & Sons, Ltd: Chichester, UK, 2015.
152. Rinaldi, R.; Jastrzebski, R.; Clough, M. T.; Ralph, J.; Kennema, M.; Bruijninx, P. C. A.; Weckhuysen, B. M., *Angew. Chemie - Int. Ed.* **2016**, *55* (29), 8164–8215.
153. Laurichesse, S.; Avérous, L., *Prog. Polym. Sci.* **2014**, *39* (7), 1266–1290.
154. Nicholson, D. J.; Guilford, C. R.; Abiola, A. B.; Bose, S. K.; Francis, R. C. *Estimation of the S/G Ratio of the Lignin in Three Widely Used North American Hardwoods, 2015 PEERS Conference*; New York, USA, 2015; Vol. 7.
155. Birch, S.; Fagerstedt, K. V.; Saranpä, P., *Plants* **2015**, *4*, 183–195.
156. Kline, L. M.; Hayes, D. G.; Womac, A. R.; Labbé, N., *BioResources* **2010**, *5* (3), 1366–1383.
157. Lancefield, C. S.; Ojo, O. S.; Tran, F.; Westwood, N. J., *Angew. Chem. Int. Ed. Engl.* **2015**, *54* (1), 258–262.
158. Kang, S.; Xiao, L.; Meng, L.; Zhang, X.; Sun, R., *Int. J. Mol. Sci.* **2012**, *13*, 15209–15226.
159. Rencoret, J.; Marques, G.; Gutiérrez, A.; Ibarra, D.; Li, J.; Gellerstedt, G.; Martínez, a T.; Río, J. C.; Recursos, I. De; Sevilla, A. De; et al. *Structural Characterization of Lignin in Different Eucalypt Species*; 2008; Vol. 62.
160. Jin-bao, H.; Shu-bin, W. U.; Hao, C.; Ming, L. E. I.; Jia-jin, L.; Hong, T., *J. Fuel Chem. Technol.* **2015**, *43* (4), 429–436.
161. Windeisen, E.; Wegener, G. Lignin as Building Unit for Polymers. In *Polymer Science: A Comprehensive Reference*; Matyjaszewski, K., Möller, M., Eds.; Elsevier:

- Amsterdam, 2012; pp 255–265.
162. Sakakibara, A., *Wood Sci. Technol.* **1980**, *14* (2), 89–100.
 163. J. Ralph, L. L. L. *Lignin and Lignans: Advances in Chemistry*; C. Heitner, D. R. Dimmel, J. A. S., Ed.; CRC Press, 2010.
 164. Guerra, A.; Filpponen, I.; Lucia, L. A.; Saquing, C.; Baumberger, S.; Argyropoulos, D. S., *J. Agric. Food Chem.* **2006**, *54* (16), 5939–5947.
 165. Fasching, M.; Schröder, P.; Wollboldt, R. P.; Weber, H. K.; Sixta, H., *Holzforschung* **2008**, *62* (1), 15–23.
 166. Renders, T.; Van den Bosch, S.; Koelewijn, S.-F.; Schutyser, W.; Sels, B. F., *Energy Environ. Sci.* **2017**, *10* (7), 1551–1557.
 167. Mansouri, N. E. El; Salvadó, J., *Ind. Crops Prod.* **2006**, *24* (1), 8–16.
 168. Ramírez-wong, B.; Bello-Pérez, L. A.; Montañó-, B.; Espinoza-Acosta, J. L.; Torres-Chávez, P. I.; Carvajal-Millán, E.; Ramírez-wong, B.; Bello-Pérez, L. A.; Montañó-Leyva, B.; Montañó-, B., *BioResources* **2014**, *9* (2), 3660–3687.
 169. Vishtal, A.; Kraslawski, A., *BioResources* **2011**, *6* (3), 3547–3568.
 170. Brandt, A.; Chen, L.; Dongen, B. E. Van; Welton, T.; Hallett, J. P., *Green Chem.* **2015**, *17*, 5019–5034.
 171. Shuai, L.; Saha, B., *Green Chem.* **2017**, *19* (16), 3752–3758.
 172. Chakar, F. S.; Ragauskas, A. J., *Ind. Crops Prod.* **2004**, *20* (2), 131–141.
 173. Tech, V., *Curr. Opin. Green Sustain. Chem.* **2016**, *2* (November), 59–63.
 174. Forage, U. S. D.; Wavre, D.; Wout Boerjan, J. R.; Baucher, M., *Annu. Rev. Plant Biol.* **2003**, *54*, 519–546.
 175. Constant, S.; Wienk, H. L. J. J.; Frissen, A. E.; Peinder, P. De; Boelens, R.; Van Es, D. S.; Grisel, R. J. H. H.; Weckhuysen, B. M.; Huijgen, W. J. J. J.; Gosselink, R. J. A. A.; et al., *Green Chem.* **2016**, *18* (9), 2651–2665.
 176. Matsushita, Y., *J. Wood Sci.* **2015**, *61* (3), 230–250.
 177. Wang, H.; Tucker, M.; Ji, Y., *J. Appl. Chem.* **2013**, *2013*, 1–9.
 178. Zhu, C.; Ding, W.; Shen, T.; Tang, C.; Sun, C.; Xu, S.; Chen, Y.; Wu, J.; Ying, H., *ChemSusChem* **2015**, *8* (10), 1768–1778.
 179. Parthasarathi, R.; Romero, R. A.; Redondo, A.; Gnanakaran, S., *J. Phys. Chem. Lett.* **2011**, *2* (20), 2660–2666.
 180. Guadix-Montero, S.; Sankar, M., *Top. Catal.* **2018**, *61* (3–4), 183–198.
 181. Besson, M.; Gallezot, P.; Pinel, C., *Chem. Rev.* **2014**, *114* (3), 1827–1870.
 182. Bozell, J. J.; O’Lenick, C. J.; Warwick, S., *J. Agric. Food Chem.* **2011**, *59* (17), 9232–9242.
 183. Chui, M.; Metzker, G.; Bernt, C. M.; Tran, A. T.; Burtoloso, A. C. B. B.; Ford, P. C., *ACS Sustain. Chem. Eng.* **2017**, *5* (4), 3158–3169.
 184. Dai, J.; Patti, A. F.; Saito, K., *Tetrahedron Lett.* **2016**, *57* (45), 4945–4951.
 185. Yang, L.; Seshan, K.; Li, Y., *Chem. Soc. Rev.* **2016**, *43*, 7485–7500.
 186. Pandey, M. P.; Kim, C. S., *Chem. Eng. Technol.* **2011**, *34* (1), 29–41.
 187. Behling, R.; Valange, S.; Chatel, G., *Green Chem.* **2016**, *18* (7), 1839–1854.
 188. Ma, R.; Xu, Y.; Zhang, X., *ChemSusChem* **2015**, *8* (1), 24–51.
 189. Yamaguchi, A.; Mimura, N.; Shirai, M.; Sato, O., *Sci. Rep.* **2017**, *7* (November 2016), 46172.
 190. Hanson, S. K.; Wu, R.; Silks, L. A. P., *Angew. Chemie* **2012**, *124* (14), 3466–3469.

191. Amadio, E.; Di, R.; Zonta, C.; Licini, G., *Coord. Chem. Rev.* **2015**, 301–302, 147–162.
192. Crestini, C.; Pro, P.; Neri, V.; Saladino, R., *Bioorganic Med. Chem.* **2005**, 13 (7), 2569–2578.
193. Ahvazi, B. C.; Pageau, G.; Argyropoulos, D. S., *Can. J. Chem.* **1998**, 76, 506–512.
194. Hanson, S. K.; Baker, R. T.; Gordon, J. C.; Scott, B. L.; Thorn, D. L., *Inorg. Chem.* **2010**, 49 (13), 5611–5618.
195. Ma, Y.; Du, Z.; Liu, J.; Xia, F.; Xu, J., *Green Chem.* **2015**, 17, 4968–4973.
196. Sedai, B.; Baker, R. T., *Adv. Synth. Catal.* **2014**, 356 (17), 3563–3574.
197. Sedai, B.; Díaz-Urrutia, C.; Baker, R. T.; Wu, R.; Silks, L. A., *ACS Catal.* **2013**, 3 (12), 3111–3122.
198. Sedai, B.; Díaz-Urrutia, C.; Baker, R. T.; Wu, R.; Silks, L. A. P.; Hanson, S. K., *ACS Catal.* **2011**, 1 (7), 794–804.
199. Rahimi, A.; Azarpira, A.; Kim, H.; Ralph, J.; Stahl, S. S., *J. Am. Chem. Soc.* **2013**, 135 (17), 6415–6418.
200. Díaz-Urrutia, C.; Chen, W.-C.; Crites, C.-O.; Daccache, J.; Korobkov, I.; Baker, R. T., *RSC Adv.* **2015**, 5 (86), 70502–70511.
201. Díaz-Urrutia, C.; Sedai, B.; Leckett, K. C.; Baker, R. T.; Hanson, S. K., *ACS Sustain. Chem. Eng.* **2016**, 4 (11), 6244–6251.
202. Patil, N. D.; Yao, S. G.; Meier, M. S.; Mobley, K., *Org. Biomol. Chem.* **2015**, 13, 3243–3254.
203. Patil, N. D. A Study of Lignin Depolymerization By Selective Cleavage of the α -C β Linkages in Lignin Model Compounds via Baeyer-Villiger Oxidation, University of Kentucky, 2014.
204. Wang, M.; Lu, J.; Zhang, X.; Li, L.; Li, H.; Luo, N.; Wang, F., *ACS Catal.* **2016**, 6, 6086–6090.
205. Wang, M.; Li, L.; Lu, J.; Li, H.; Zhang, X.; Liu, H.; Luo, N.; Wang, F., *Green Chem.* **2017**, 19, 702–706.
206. Napoly, F.; Jean-gérard, L.; Goux-henry, C.; Draye, M.; Andrioletti, B., *European J. Org. Chem.* **2014**, 2014, 781–787.
207. Luo, F.; Zhou, T.; Li, X.; Luo, Y.; Shi, Z., *Org. Chem. Front.* **2015**, 2, 1066–1070.
208. Lange, H.; Decina, S.; Crestini, C., *Eur. Polym. J.* **2013**, 49 (6), 1151–1173.
209. Biannic, B.; Bozell, J. J., *Org. Lett.* **2013**, 15 (11), 2730–2733.
210. Mottweiler, J.; Puche, M.; Räuber, C.; Schmidt, T.; Concepción, P.; Corma, A.; Bolm, C., *ChemSusChem* **2015**, 8 (12), 2106–2113.
211. Djerassi, C.; Engle, R. R., *J. Am. Chem. Soc.* **1953**, 75 (15), 3838–3840.
212. Gore, B. E. S., *Platin. Met. Rev.* **1983**, 27 (3), 111–125.
213. Lv, J. H.; Wei, X. Y.; Wang, Y. H.; Wang, T. M.; Liu, J.; Zhang, D. D.; Zong, Z. M., *RSC Adv.* **2016**, 6 (66), 61758–61770.
214. Yao, Z.-S.; Wei, X.-Y.; Lv, J.; Liu, F.-J.; Huang, Y. Y.-G.; Xu, J.-J.; Chen, F.-J.; Huang, Y. Y.-G.; Li, Y.; Lu, Y.; et al., *Energy & Fuels* **2010**, 24 (3), 1801–1808.
215. Ma, A.; Zhang, S.; Zhang, D., *Org. Geochem.* **2008**, 39 (11), 1502–1511.
216. Huang, Y.; Zong, Z.; Yao, Z.; Zheng, Y.-X.; Mou, J.; Liu, G.-F.; Cao, J.-P.; Ding, M.-J.; Cai, K.; Wang, F.; et al., *Energy & Fuels* **2008**, 1799–1806.
217. Snowdon, L. R.; Volkman, J. K.; Zhang, Z.; Tao, G.; Liu, P., *Org. Geochem.* **2016**, 91, 3–15.
218. Piccialli, V., *Molecules* **2014**, 19 (5), 6534–6582.

219. Carlsen, P. H. J.; Katsuki, T.; Martin, V. S.; Sharpless, K. B., *J. Org. Chem.* **1981**, *46* (19), 3936–3938.
220. Miranda, L.; Vasconcellos, M., *Synthesis*. **2004**, *2004* (11), 1767–1770.
221. Yao, Z. S.; Wei, X. Y.; Lv, J.; Liu, F. J.; Huang, Y. G.; Xu, J. J.; Chen, F. J.; Huang, Y.; Li, Y.; Lu, Y.; et al., *Energy and Fuels* **2010**, *24* (3), 1801–1808.
222. Orita, H.; Hayakawa, T.; Takehira, K., *Bull. Chem. Soc. Jpn.* **1986**, *59* (8), 2637–2638.
223. Plietker, B., *Synthesis*. **2005**, *2005* (15), 2453–2472.
224. Frunzke, J.; Loschen, C.; Frenking, G., *J. Am. Chem. Soc.* **2004**, *126* (11), 3642–3652.
225. Seddon, K. R.; Seddon, E. A. *The Chemistry of Ruthenium*, Elsevier S.; Clark, R. J. H., Ed.; 2013.
226. Mills, A.; Holland, C., *J. Chem. Res.* **1997**, No. 10, 368.
227. Murahashi, S. I. *Ruthenium in Organic Synthesis*; Murahashi, S.-I., Ed.; Wiley-VCH Verlag GmbH & Co. KGaA: Weinheim, Germany, 2004.
228. Plietker, B., *J. Org. Chem.* **2003**, *68* (18), 7123–7125.
229. Yang, D.; Zhang, C., *J. Org. Chem.* **2001**, *66* (14), 4814–4818.
230. Nowicka, E.; Sankar, M.; Jenkins, R. L.; Knight, D. W.; Willock, D. J.; Hutchings, G. J.; Francisco, M.; Taylor, S. H., *Chem. - A Eur. J.* **2015**, *21* (11), 4285–4293.
231. Yang, D.; Chen, F.; Dong, Z.-M.; Zhang, D.-W., *J. Org. Chem.* **2004**, *69* (6), 2221–2223.
232. Lee, D. G.; Spitzer, U. A.; Cleland, J.; Olson, M. E., *Can. J. Chem.* **1976**, *54* (13), 2124–2126.
233. Torii, S.; Inokuchi, T.; Kondo, K., *J. Org. Chem.* **1985**, *50* (24), 4980–4982.
234. Norrby, P. O.; Kolb, H. C.; Sharpless, K. B., *Organometallics* **1994**, *13* (1), 344–347.
235. Albarella, L.; Giordano, F.; Lasalvia, M.; Piccialli, V.; Sica, D., *Tetrahedron Lett.* **1995**, *36* (29), 5267–5270.
236. Webster, F. X.; Rivas-Enterrios, J.; Silverstein, R. M., *J. Org. Chem.* **1987**, *52* (4), 689–691.
237. Kasai, M.; Ziffer, H., *J. Org. Chem.* **1983**, *48* (14), 2346–2349.
238. Rosen, T. C.; Clercq, E. De; Haufe, G., **2004**, 229–237.
239. Ferraboschi, P.; Grisenti, P.; Manzocchi, A.; Santaniello, E., *J. Chem. Soc. Perkin Trans. I* **1990**, *9*, 2469.
240. Nowicka, E.; Clarke, T. J.; Sankar, M.; Jenkins, R. L.; Knight, D. W.; Golunski, S.; Hutchings, G. J.; Willock, D. J.; Francisco, M.; Taylor, S. H., *Chem. - A Eur. J.* **2018**, *24* (3), 655–662.
241. Nowicka, E.; Hickey, N. W.; Sankar, M.; Jenkins, R. L.; Knight, D. W.; Willock, D. J.; Hutchings, G. J.; Francisco, M.; Taylor, S. H., *Chem. - A Eur. J.* **2018**, *24* (47), 12359–12369.

CATALYTIC CONVERSION OF BIOMASS

CHAPTER 2. EXPERIMENTAL

S. Guadix-Montero
CARDIFF UNIVERSITY | CARDIFF CATALYSIS INSTITUTE

Contents

2	Experimental.....	69
2.1	Introduction.....	69
2.2	Glycerol hydrogenolysis.....	69
2.2.1	Catalyst preparation.....	69
2.2.2	Catalyst testing.....	70
	• Batch reactor.....	70
	• Continuous fixed-bed reactor.....	72
2.2.3	Analytical techniques.....	74
	• High-performance liquid chromatography (HPLC).....	74
	• Gas chromatography.....	74
	○ Liquid phase products analysis.....	75
	○ Gas phase products analysis.....	76
2.2.4	Catalyst characterisation.....	77
	• Microwave-assisted aqua regia digestion of catalyst.....	77
	• Microwave plasma-atomic emission spectrometer (MP-AES).....	78
	• Thermogravimetric analysis.....	79
	• Scanning electron microscopy and energy-dispersive X-ray (EDX) spectroscopy.....	79
	• Transmission electron microscopic (TEM) and scanning transmission electron microscopy (STEM).....	80
	• X-Ray photoelectron spectroscopic (XPS).....	81
	• N ₂ adsorption.....	82
	• Ammonia temperature programmed desorption (NH ₃ -TPD).....	87
	• Pyridine absorption via diffuse reflectance infrared fourier transform spectroscopy (DRIFTS).....	91

•	Raman spectroscopy	92
•	X-ray powder diffraction (XRD)	92
2.3	Lignin depolymerisation	94
2.3.1	Synthesis of model substrates	94
•	β -O-4' lignin model polymer.....	94
•	Hexamer lignin model compound	94
2.3.2	RICO reaction protocol.....	96
2.3.3	Analytical techniques.....	100
•	Gas chromatography coupled with mass spectroscopy	100
•	Nuclear magnetic resonance spectroscopy	100
○	^1H NMR.....	101
○	Heteronuclear single quantum correlation spectroscopy (^1H - ^{13}C HSQC) ...	103
○	Heteronuclear multiple bond correlation (^1H - ^{13}C HSQC)	104
○	^{31}P NMR.....	104
•	Advanced polymer chromatography	105
•	Inductively coupled plasma mass spectroscopy	108
•	Fourier transform Infra-Red spectroscopy	109
•	High-performance liquid chromatography	109
•	Thin layer chromatography and column chromatography	110
2.4	References.....	111

2 Experimental

2.1 Introduction

This chapter describes the different techniques and methods employed in the experiments discussed in this thesis. This includes details of how the catalysts were synthesised and characterised, along with the description of the reaction and post-reaction protocols and analytical techniques for quantification purposes. Also, information about the instrumentation and set-up needed to carry them out. The first section focuses on the glycerol hydrogenolysis project, and the second part describes the lignin depolymerisation study.

2.2 Glycerol hydrogenolysis

2.2.1 Catalyst Preparation

Monometallic Pd, Ru, Pt, and bimetallic PdRu, RuPt nanoparticles supported on TiO₂ were prepared *via* a modified impregnation method.^{1,2} In the case of the bimetallic catalysts, the metals were in a 1:1 molar ratio.

Stock solutions of Ru, Pd and Pt, were prepared initially using the metal precursors RuCl₃.xH₂O (> 99.9 %, Sigma Aldrich, certificate analysis 41.9 %), PdCl₂ (99 %, Sigma Aldrich) and H₂PtCl₆ (from Johnson Matthey, assay 30.21 %), respectively. The metal content of these precursor solutions was quantified using Agilent 4200 MP-AES. As a result, the volume of the metal precursor solution could be calculated for the preparation of each catalyst at the desired metal weight percentage (wt. %).

For instance, to prepare 2 g of a monometallic 2 wt. % Ru/TiO₂ the following methodology was used for the catalyst synthesis: the RuCl₃.xH₂O stock solution was prepared initially (6.238 g mL⁻¹) which allowed the 6.412 mL metal solution added to a round-bottom flask equipped with a stirring bar and placed in an oil bath. Water was then added, to a total volume of 16 mL. The solution was heated to 60 °C, while stirring, before the support (1.98 g of TiO₂ (P-25, Degussa)) was added slowly, during 15-20 min. The resultant mixture was then heated for a further 15 minutes at 60 °C before the temperature being raised to 95 °C. The open-flask reaction mixture was then left to heat overnight (16 h) to leave the solid Ru/TiO₂ catalyst as a dark green powder. The resulting material then collected and fine-grained using a mortar. Then, the catalyst was reduced in a furnace using 5 % H₂/Ar for 4 hours at 400 °C with a heating rate of 10 °C min⁻¹ to leave a grey powder. For instance, to prepare a 2 wt. % PdRu/TiO₂ catalyst with equal molar loadings of the two metals was prepared using a modified impregnation

method. An aqueous solution of PdCl₂ was prepared with a metal concentration of 6 mg_{Pd} mL⁻¹ in a 0.58 M HCl solution. An aqueous solution of RuCl₃.xH₂O with a metal concentration of 6.7 mg_{Ru} mL⁻¹ was also prepared separately. Requisite amounts of metal precursor solutions were added to a 50 mL round-bottom flask fitted with a magnetic stirrer bar. The additional volume of deionised water was added to make the total volume of the impregnation mixture to 16 mL. The solution was stirred continuously vigorously, and the temperature of the solution was increased from room temperature to 60 °C. At 60 °C, the TiO₂ support (1.98 g) was added slowly over a period of 15-20 min with constant vigorous stirring. The slurry was stirred at 60 °C for an additional 15 min, followed by an increase in temperature to 95 °C and the slurry was stirred overnight until full water evaporation (typically 16 h). Subsequently, the resultant dry powder was ground thoroughly and reduced under a flow of 5 % vol. H₂/Ar using a temperature ramp of 10 °C min⁻¹ until 400 °C and hold for 4 hours.

Following the protocol described above, 2 wt.% PdRu bimetallic nanoparticles were supported on different metal oxides (SiO₂, Al₂O₃, WO₃ all of them from Sigma Aldrich) and zeolites. Commercial zeolites were purchased from Alfa Aesar and had different SiO₂/Al₂O₃ mole ratios and frameworks such as NH₄-ZSM-5 ([30:1], [50:1], [80:1] and [400-200:1]), NH₄-Mordenite [20:1] and HY [5.1:1]. The commercial zeolites in ammonium-ion form (NH₄⁺-forms) were calcined to remove the ammonia, obtaining the acid H⁺ zeolite forms. To do so, all the zeolites were calcined (except for the HY) before the impregnation, in flowing air before the synthesis at 550 °C for 4 hours using a temperature ramp of 10 °C min⁻¹.

2.2.2 Catalyst Testing

- **Batch Reactor**

The glycerol hydrogenolysis reactions were carried out in a stainless-steel autoclave reactor “4590 Micro Bench Top Reactor” from Parr Instruments Company. The volume of the reactor is 50 mL and maximum operating pressure of 2000 psi (*Figure 2-1*), equipped with a safety rupture disc attached to the head that is designed to rupture and release the pressure before it reaches any dangerous level. The reactor was fitted with a mechanical stirrer (up to 2000 rpm) (5); a gas sampling tube (4) (which, was subsequently removed to collect gas samples); and a stainless-steel Type J thermocouple for measurement of the reactor temperature (6). The desired temperature was maintained with a jacket-like heating mantle (3), with the pressure and stirring rate and temperature settings all observed and maintained on a digital control box “4848 reactor controller” from Parr Instrument (8).

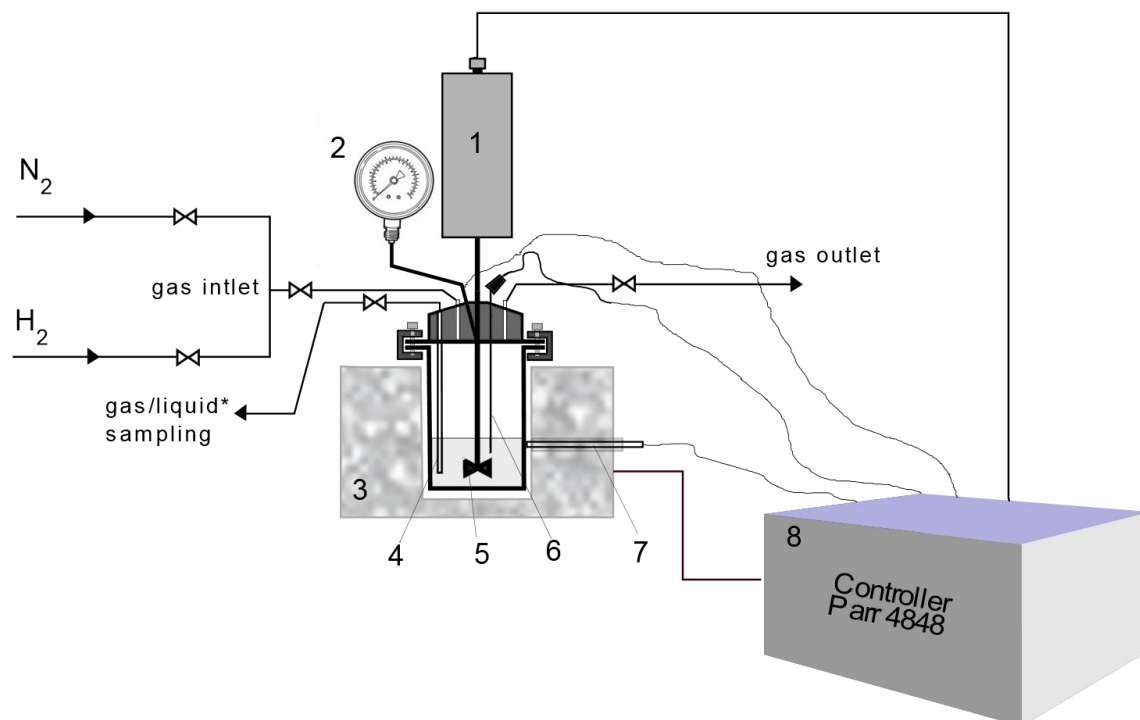


Figure 2-1 Schematic representation of the high-pressure autoclave reactor. 1) Stirrer motor, 2) Pressure gauge, 3) Heating mantle, 4) Sample tube for liquid sampling (*without the tube for gas sampling), 5) Stirrer, 6) Thermocouple, 7) External thermocouple, 8) Temperature and motor control box

A typical reaction with, for example, 2 wt. % Ru/TiO₂ was performed with the following methodology: The 2 wt. % Ru/TiO₂ catalyst (ca. 0.338 g) was added to the autoclave with 24 g of a 5 wt. % aqueous glycerol solution. The reactor was equipped with the mechanical stirrer and sealed. The molar ratio of the metal to the substrate was kept constant at 1:200 in all the reactions. The reactor was purged three times with nitrogen gas (10 bar) followed by further two times purged with hydrogen gas (20 bar), to which the necessary pressure was maintained. The autoclave was then subjected to local stirring at approximately 200 rpm while the reaction temperature reached 160 °C before the reaction mixture was agitated at a remote stirring rate of 800 rpm and heating allowed the temperature rise to the set 165 °C. A definitive start to the hydrogenolysis reaction was from a heating rate profile, to which the temperature plateaued at 160 °C. Therefore this temperature was set as reaction start temperature. Once the reaction was complete, the reactor was cooled in an ice bath to 25 °C before the gas phase products were collected in a gas sampling bag. Then, the reaction mixture was centrifuged to separate the catalyst from the liquid phase. Further filtration of the reaction mixture, using 0.45 μm PTFE syringe filters, ensured even the finest catalytic particles were separated before being

analysed by gas chromatography and high-performance liquid chromatography. The catalysts were recovered and washed for further analysis and characterisation.

- ***Continuous Fixed-bed Reactor***

The previous reactor configuration, batch reactor, has no input or output when the reaction is taking place. In these kinds of reactors, the reaction mixture is assumed perfectly mixed. It depends on time to reduce the initial moles of reactant (N_{A0}) for a volume of reaction, following the design equation (1), where r_A is the reaction rate. On the contrary, a fixed-bed has an input molar flow rate (F_{A0}). It responds to the design equation (2), where W is the weight of the catalyst needed to convert the moles of reactant A .³ For liquid-solid operation in fixed-bed reactors, the concentration gradient is the most valuable parameter. This is due to the lower diffusivities and higher heat conductivity when comparing with gas-solid systems.⁴

$$t = N_{A0} \int_0^x \frac{dX}{-r_A V} \quad (1)$$

$$W = F_{A0} \int_0^x \frac{dX}{-r'_A} \quad (2)$$

The concept of Space-Time (ST) needs to be introduced to compare the catalytic activities of all the catalysts. ST is the required resident time to process a volume on entrance conditions at temperature and pressure constant.⁵ The space-time was worked out for the batch reactor and the fixed-bed reactor using equations (3) and (4) respectively:

$$ST = \frac{\text{mass of catalyst } (g_{cat})}{\text{mass of glycerol } (g_{glycerol})} \times \text{reaction time } (h) \quad (3)$$

$$ST = \frac{\text{mass of catalyst } (g_{cat})}{\text{glycerol mass flow rate } (g_{glycerol}/h)} \quad (4)$$

The test of the catalysts supported on TiO_2 prepared in the CCI was also conducted in a continuous flow reactor during a research stay in the Dalian Institute of Chemical-Physics (DICP), Republic of China. This work was carried out under the supervision of Prof. Aiqin Wang, within Prof. Tao Zhang research group, who is currently the Vice President of the Chinese Academy of Sciences (CAS). Figure 2-2 illustrates the experimental set-up employed. The dimensions of the fixed-bed reactor were 9 mm-ID x 400 mm-High. It was provided with a heating jacket, an MFC (mass flow controller) and it was connected to a gas-liquid separator (Figure 2-2). In a typical reaction, 0.5 g of the catalyst pellets (20-40 mesh) was loading mixed

with 0.5 g of SiO₂ (20-40 mesh, purchased from Tianjin Tianda Chemical Reagent Co. Ltd) and fitted with glass wool in the centre of the column. The column was packed with a total of *ca.* 52 g of SiO₂. After setting the column, the reactor was purged with N₂ at the max flow (500 mL min⁻¹). N₂ pressure was held for 2 h at 208 MPa, to check the leaks. The temperature ramp used was 5 °C min⁻¹. Once the temperature was stable at 165 °C and after sonicating for 1 h at maximum power, a 20 wt. % aqueous glycerol solution was feed into the reactor firstly using the setting flash in the pump (1 mL min⁻¹) to clean (only when was a fresh stock solution). The stock solution of glycerol was placed on a scale to measure the weight consumed by difference before and after the reaction, to make more accurate the flow rate.

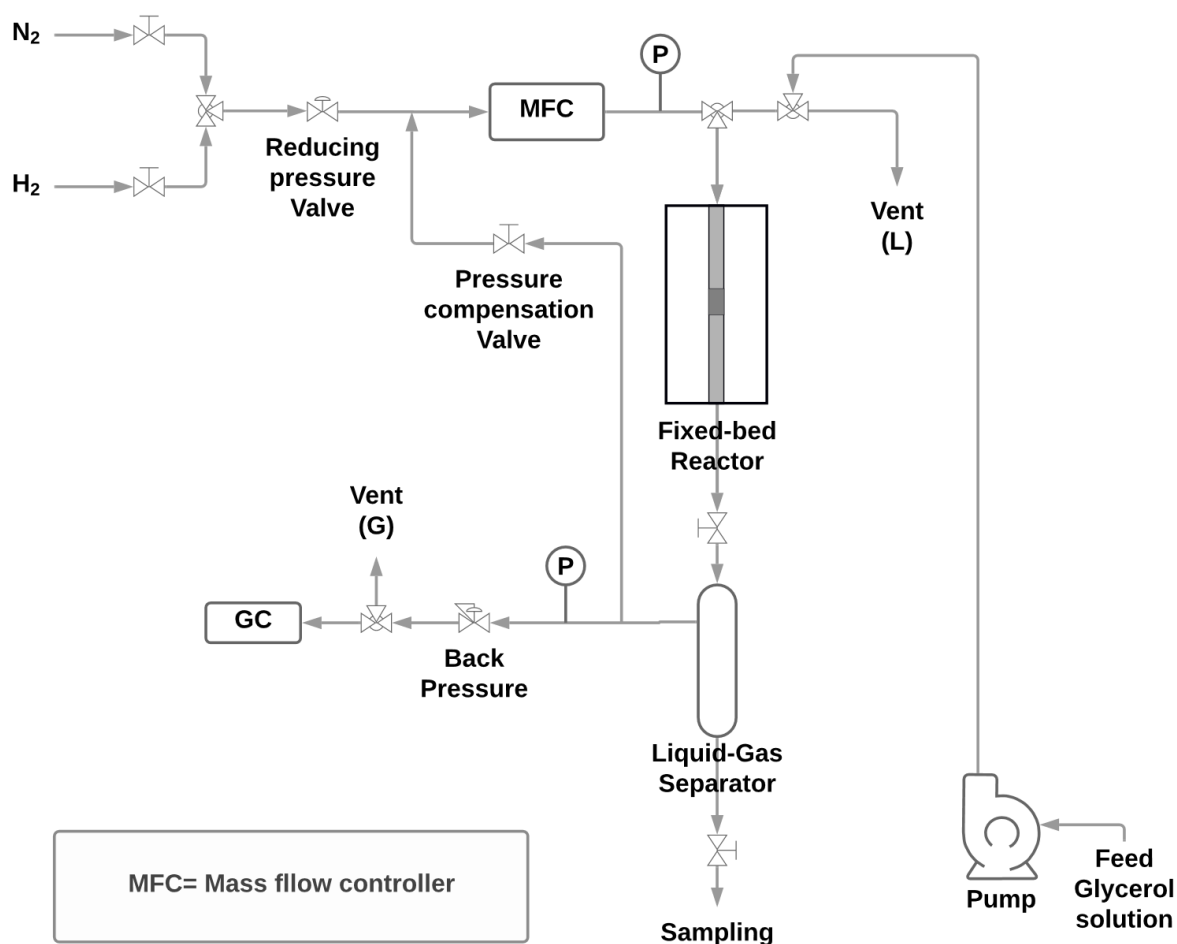


Figure 2-2 Flow diagram of the fixed-bed reactor set up used to test out catalyst in the Dalian Institute of Chemical Physics.

For this study, the reaction conditions in the flow reactor were assessed to be equivalent to 6 h of reaction in the batch reactor. The ST for both kinds of reactors was around 0.31-0.37 g_{catalyst} h g_{glycerol}⁻¹. The space velocity is the reciprocal of the space-time; it can be based on either liquid or gas – hourly space velocities (LHSV, GHSV).⁶ Another way to express the SV is the

weight - hourly space velocity (WHSV). WHSV was used since the weight of catalyst was always kept constant, 0.5 g in all reactions. To maintain the molar ratio between the metal on the catalyst and the reactant, the variation in the flow of glycerol solution per hour changed the WHSV. It was worked out using equation 5.

$$\text{Weight hourly space velocity (WHSV)} = \frac{\text{Hourly mass feed flow rate}}{\text{Catalyst mass}} \quad (5)$$

Therefore, different flow rates were used depending on the catalyst tested in order to keep constant the weight of the catalyst tested (0.5 g) and the substrate vs metal molar ratio and equal to [1:0.005]. This gives a WHSV within a range between 2 to 3.2 h⁻¹, depending on the catalyst used.

Through a back-pressure regulator, the gas phase is conducted to be analysed by GC (Packed column) directly to analyse to reaction products. Meanwhile, an aliquot of the liquid products is sampled manually from the liquid-gas separator. After dilution with the external standard (*n*-butanol), the liquid sample was analysed in a GC (Agilent 7820A). GC samples were prepared using 0.1 g of liquid sampled diluted with 1 mL of deionised water and 0.5 g of *n*-butanol. This GC was fitted with an Agilent DB-WAX GC column and a flame ionisation detector. The reaction was considered finished when it reached a steady state.

2.2.3 Analytical techniques

- **High-Performance Liquid Chromatography (HPLC)**

HPLC technique was used for the separation and analysis of liquid samples. The samples were injected into the column in a mobile phase from the solvent reservoir *via* an HPLC pump. Once in the column, each product was separated at different retention times, and then each product reaches the Refractive Index Detector (RID). In the RID, the effluent passes through a flow-cell, where the light source is shone, and the spectrum is recorded.

This technique was employed to calculate glycerol conversion. However, the peaks for the propanediols (1,2-PDO and 1,3-PDO) were not possible to separate by changing the parameters or the method conditions in this instrument; therefore, gas chromatography was used instead for the quantification of the products of the liquid phase. The HPLC instrumentation was only used as guidance to confirm the conversion of glycerol against the results of the gas chromatography.

- **Gas Chromatography**

Gas chromatography (GC) is a chromatographic technique commonly used in analytical chemistry. It is used for the separating and analysing a sample containing a mixture of products.

During the process, the sample is vaporised and injected into the column. Elution occurs by the flowing of the gaseous mobile phase, which consists of inert gas (e.g. helium or nitrogen gas). This mobile phase gas does not interact with the analyte. The stationary phase is made up of either an adsorbent or a liquid phase on inert material.

- *Liquid phase products analysis*

The liquid phase products were analysed using gas chromatography (Agilent 7820A). This method to separate the reaction mixture is achieved by vaporising the sample from the injection port before the mixture is then transported to the column (Agilent DuraBond-Wax UI) with a carrier gas (helium in this case). Once in the column oven, the sample is separated into its constituents before reaching the Flame Ionisation Detector (FID) where the sample is combusted in hydrogen and air to produce cations that can be analysed. The signal is produced by the electrons flowing from the anode to the cathode and is proportional to the number of carbon-containing compounds combusted in the flame. Varying intensities of the flame can generate different product areas. Thus, an external standard was used to get a constant area ratio of the products.

All the samples were prepared to take 1 mL of the reaction mixture filtrated with a 0.45 μm PTFE syringe filter and 0.1 mL of an external standard solution of n-butanol. The external standard selected was 1-butanol (5 % aqueous solution). Its peak in the chromatogram was normalised depending on the amount of standard added. By taking the area of the standard, the mass used (g), the density (0.81 g L^{-1}) and volume (0.01 mL), the normalised standard area can be calculated as follow,

$$\text{Normalised Standard Area} = \frac{\text{Area standard}}{\text{weight standard (g)}} \cdot \text{density} \left(\frac{\text{g}}{\text{mL}}\right) \cdot \text{volume (mL)} \quad (6)$$

From the normalised area of the 1-butanol standard, the normalised area ratio of products can be calculated. Different concentration of solutions of all possible products was prepared to calibrate the instrument response. The area ratios of the components were plotted against the known concentrations to obtain the response factors. Thus, calculated response factors are used in the quantitative analyses of the components in the reaction mixture. The conversion, selectivity and carbon mass balance were calculated using the following equations 7, 8 and 9. Note that the moles of each compound were multiplied by the number of carbons to determine the C content. Each sample was injected three times to and the average area was used for this calculation.

$$\text{Conversion (\%)} = \frac{(\text{mol}_{\text{glycerol}})_{t=0} - (\text{mol}_{\text{glycerol}})_{t=t}}{(\text{mol}_{\text{glycerol}})_{t=0}} \cdot 100 \quad (7)$$

$$\text{Selectivity}_P (\%) = \frac{\text{mol}_P}{\sum \text{mol of all product}} \cdot 100 \quad (8)$$

$$\text{Total carbon mass balance (\%)} = \frac{\sum \text{mol}_{C1 \text{ products}} + 2 \cdot \sum \text{mol}_{C2 \text{ products}} + 3 \cdot \sum \text{mol}_{C3 \text{ products}} + 3 \cdot (\text{mol}_{\text{glycerol}})_{t=t}}{3 \cdot (\text{mol}_{\text{glycerol}})_{t=0}} \cdot 100 \quad (9)$$

For reusability studies, at the end of the reaction, the recovered catalysts were filtered, washed with acetone several times and dried at 25 °C overnight for further analysis and characterisation. These dried catalysts were dried further in an oven at 120 °C in static air for 1 h and used for the next reaction.

- *Gas phase products analysis*

The gas is collected from the reactor using a Tedlar® bag of 0.6 L of capacity. Prior to use, each Tedlar® bag was purged three times with ultra-pure nitrogen. Using nitrogen purged Tedlar® bag, fill with nitrogen and run a blank before analysing any sample.

The gas phase products were analysed using gas chromatography (Varian 450-GC). This instrument has a similar setup to the liquid-phase product analysis, where a helium carrier gas is used as the mobile phase and separation column used as the stationary phase. This instrument is equipped with a gas sample loop, a gas sampling valve, and an injector. The sample of gas collected from the reactor is fed into the sampling loop, then to the gas sampling valve which directs the sample to the injector. At this point, the sample is loaded into the separation column (Varian Capillary Column CP-Sil 5 CB 50 m 0.32 mm 5 µm #CP7690), in which the flame ionisation detector (FID) is used to generate the chromatogram.

The gas products (CO₂, methane, ethane, and methane) were calibrated by injecting different volume % of the standard products from a pressurised cylinder of known concentration into the gas chromatograph which generates a series of area peaks of varying intensities. This, when plotted, allows the response factor to be calculated which in turn gives the molar fraction of products x_i . By using the very well-known ideal gas equation:

$$P V = n R T \quad (10)$$

where,

P	<i>Total pressure, atm, in the reactor, recorded on the digital control box at the time of gas collection (c.a. 25° C)</i>
V	<i>is the volume, L, of gas in the reactor, calculated by the total volume of the reactor (50 mL) subtracted by the volume of glycerol used (24 mL)</i>
n	<i>is the total number of gaseous moles, mol, in the sample</i>
R	<i>is the ideal gas constant, 0.0821 L atm mol⁻¹K⁻¹</i>
T	<i>is the temperature, K, recorded at the time of gas collection on the control box. (298 K)</i>

moreover, Dalton's law of partial pressure:

$$p_{total} = p_{gas\ 1} + p_{gas\ 2} + p_{gas\ 3} + \dots + p_{gas\ n} \quad (11)$$

The molar fraction of each gas (x_i) in the sample is calculated from the response factor. From this value, the resulting partial pressure and number of moles of gas products can be calculated by the product of the mole fraction and the total number of moles and pressure in the reactor.

$$x_i = \frac{P_i}{P_{total}} = \frac{n_i}{n_{total}} = \frac{V_i}{V_{total}} \quad (12)$$

$$P_{gas\ 1} = x_i \cdot P_{total} \quad (13)$$

2.2.4 Catalyst Characterisation

- **Microwave-assisted aqua regia digestion of catalyst**

The instrument employed was ETHOS EZ Microwave Digestion System from Milestone S.r.l. Fitted with SK-15 is a high-pressure and high-temperature rotor featuring up to 15 TFM vessels with a volume of 100 ml. Milestone uses infrared sensors combined with an in-situ temperature sensor for the temperature control. It is equipped with two 950-Watt magnetrons for a total of 1900 Watt.

25 mg of 2 wt. % metal loading PdRu catalyst was digested in an acid matrix composed of 10 mL of aqua regia (HNO₃+3 HCl) for the digestion of the catalyst. The most likely sample to produce large quantities of gas must be selected as sample No. 1, which is the reference for the worst-case scenario. The method set in the instrument consisted of a temperature ramp of 20 min up to 220 °C, the temperature was held for 40 min with a power of 1200 W, and cooling down for 30 min. The vessels were washed with deionised water for the collection of the sample.

- **Microwave Plasma-Atomic Emission Spectrometer (MP-AES)**

This technique is used for multi-elemental analysis of a sample based on the principles of atomic emission. The instrument used was an ‘Agilent 4200 MP-AES’ which enables superior detection levels over more conventional microwave plasma techniques and can be used for a wide range of samples. The instrument works by microwave energy (2.5 GHz) being coupled to the nitrogen to form a plasma that is subsequently heated to almost 5,000 °C by a conventional quartz torch. Here, the sample is dispersed into the plasma via the spray chamber where it dries, decomposes and then atomises, resulting in electron excitation. The electrons fall from the excited state into lower energy levels; meanwhile, the photons are emitted with wavelengths and energies characteristic to each element. Finally, these wavelengths are detected, and as a result, a ppm concentration can be generated determinate, using a calibration of the specific metal to quantify. Standard solutions of Pd and Ru were prepared for the calibration of the instrument (*Figure 2-3*).

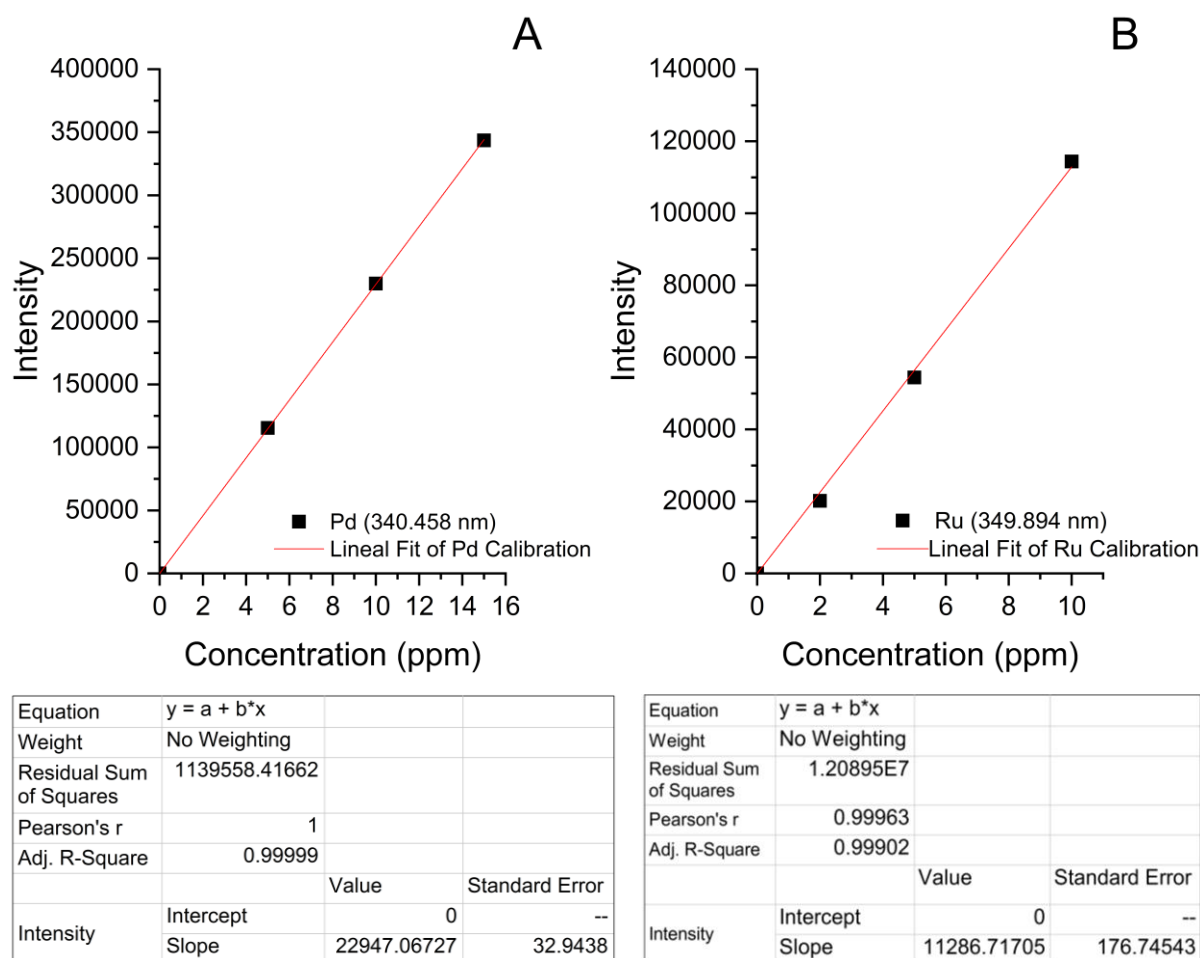


Figure 2-3 Linear fit correlation of Pd (A) and Ru (B) standard calibrations used for MP-AES analysis. obtained using Origin® 9.0. The standard error corresponds to the slope error.

Samples digested previously, overnight, in aqua regia were diluted to a total volume of 100 mL in deionised water before analysing in the MP-AES.

- ***Thermogravimetric Analysis***

Thermogravimetric analysis (TGA) was performed by heating the catalyst at a specific rate under a specific atmosphere (e.g. N₂), where the corresponding mass changes are measured. The rate can either be at a constant temperature or heating rate, giving the respective information on mass loss vs time and mass loss vs temperature. A TGA instrument from Perkin Elmer was used to perform this analysis. This technique consists of a furnace connected to an analytical microbalance which is very sensitive to mass change (as small as 0.1 µg). The recovered catalyst post-reaction, after washed with acetone twice, was decanted onto a watch-glass for drying. Once dry, the sample (*ca.* 40 mg) is loaded onto a crucible which is placed on a hanging balance. The mass change is detected by an optical sensor which uses a current to return the balance beam to its original position. This current relates to the weight on a scale and is amplified to produce a signal, presented as a wt. % loss of the sample. The TGA was used twice for each catalyst: Ru/TiO₂, Ru-Pt/TiO₂, and Ru-Pd/TiO₂ analysing the post reaction (spent) and fresh catalysts (unused).

- ***Scanning Electron Microscopy and Energy-Dispersive X-ray (EDX) Spectroscopy***

Electron microscopy is frequently used as a characterisation technique to study the morphology, topology and composition of a solid sample. Electron microscopy works by firing a primary beam of electrons, known as incident electrons, on to the sample where they are absorbed, resulting in several different kinds of particles or waves being emitted (Auger electrons, secondary electrons, back-scattered electrons, X-rays, photons, etc.)⁷ see *Figure 2-4-A*. The electrons interact with the atomic nucleus and are scattered back to the detector, known as ‘back-scattered electrons’ (BSE, several 10’s of nm to 100 nm). Alternatively, closer to the surface of the specimen, the electrons in the valence or conduction band absorb energy from the incident electrons and get ejected as ‘secondary electrons’ (SE, nm range), and reach the secondary detector. Both BSE and SE are used for imaging, while Energy dispersive X-ray analysis (EDX) provides elemental information of a sample based on the characteristic atomic element wavelength of the X-rays generated. The X-ray emitted is detected by an energy-dispersive X-ray detector. The volume of primary excitation has a probed depth in EDX from 1 to 3 µm generally, region characteristic of X-rays, while the Auger is around 5-75 Å of analysis depth, *Figure 2-4-B*. Therefore, SEM focuses on the surface of the sample and its

composition. The composition and morphology of the Pd, PdRu, Ru, RuPt and Pt supported catalysts were performed on a Hitachi TM3030 table-top microscope.

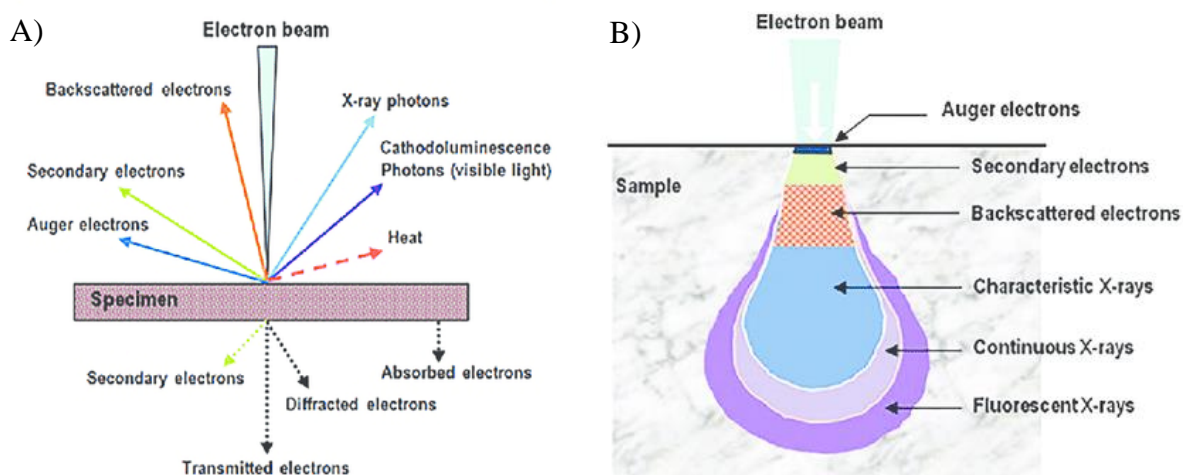


Figure 2-4 A) Scheme of the interaction of the primary electron beam with the sample or specimen and B) Schematic representation of the interaction volume and signal regions. Copyright ©2016, A. Hilal, License IntechOpen, under a Creative Commons Attribution 3.0. Ref.⁷

Each sample was prepared by dusting the sample onto a carbon sticker and placed onto the sample holder. The position of the sample with the electron gun was checked for alignment before being put under vacuum. At this point, the images could be viewed on the built-in image processing software. A series of images were recorded for each catalyst: 600x, 1800x and 6000x magnification.

- **Transmission electron microscopic (TEM) and Scanning transmission electron microscopy (STEM)**

Transmission electron microscopy (TEM) has superior magnification and resolution than SEM. It is based on the detection of diffracted and transmitted electrons.⁸ This electron microscopy technique is used to determinate dispersion and particle size besides morphology of the supported nanoparticles. The electron microscopy can distinguish different operation methods such as Bright or Dark Field (BF/DF), where BF detects the direct beam (transmitted electrons) while DF detects the scattered electrons that are diffracted, which increase the contrast of the image. It can also be used as high-resolution transmission electron microscopy (HRTEM) as well as electron diffraction (ED), which provides information about crystal structure, lattice spacing, orientation, etc.⁹

Scanning transmission electron microscopy (STEM) is a technique that combines both SEM and TEM. Pre-specimen lenses focus the beam into a small probe that is scanned across the sample.¹⁰ To do so, different detectors can be used. Detectors that can detect scattered electrons which gives high-angle annular dark-field (HAADF), Annular Dark-field (ADF) and Bright-field (BF) imaging, where HAADF detects electrons that are scattered (Rutherford scattering cross-section) to higher angles as shows *Figure 2-5*.^{11,9}

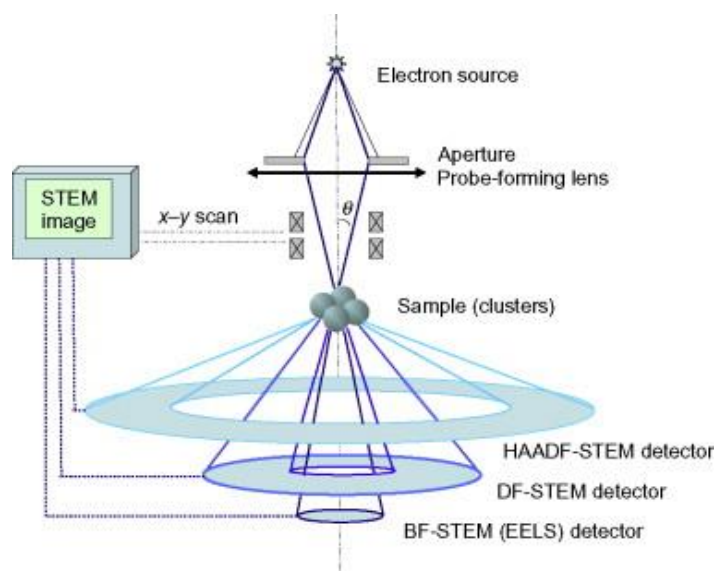


Figure 2-5 Scheme of the image formation in a Scanning transmission electron microscopy (STEM), showing the range of the bright-field (BF) detector, the larger annular dark-field (DF) detector and the high angle annular dark-field (HAADF) detectors. Copyright © Elsevier Science, 2012. Reproduced with permission from Ref.¹¹

The metal particles size distribution of the Pd, PdRu, Ru, RuPt and Pt catalysts supported on TiO₂ and zeolites were performed on a transmission electron microscope. Prior TEM or STEM, the samples were dispersed with ethanol under ultrasonication and deposited on 300 mesh copper grids coated with holey carbon film. The supernatant liquid was dropped on a C grid and dried with a lamp before analysis. TEM and STEM were performed on a JEOL JEM-2100 operating at 200 kV. STEM-EDX mapping was carried out and analysed by Oxford Instrument X-MaxN 80 detector, and the data analysed using the Aztec software.

- ***X-Ray photoelectron spectroscopy (XPS)***

X-ray photoelectron spectrometer (XPS) is a useful qualitative and semi-quantitative spectroscopy technique to determinate chemical composition and oxidation state of metal species on the catalyst surface. When a material is irradiated with X-ray or UV light, based on

the photoelectric effect, an atom absorbs a photon of energy $h\nu$, next to a core or valence electron with binding energy E_b is ejected with kinetic energy E_k of the photoelectron.¹² The emission of electrons resulting from the X-ray irradiation depends on the wavelength of the radiation in accordance with the equation 14.^{12,13}

$$E_k = h\nu - E_b - \varphi \quad (14)$$

where:

- E_k is the kinetic energy of the photoelectron
- h is the Planck's constant
- ν is the frequency of the exciting radiation
- E_b is the binding energy of the photoelectron for the Fermi level of the sample
- φ is the work function of the spectrometer

The probing depth of this technique is in the range of 1.5 to 6 nm, depending on the kinetic energy.¹² The spectra generated is a representation of the photoemission intensity (a.u.) of the electrons emitted versus the binding energy (eV).

Elemental analysis and atom oxidation states of the PdRu/TiO₂, Ru/TiO₂, and RuPt/TiO₂ catalyst surfaces were performed on a Thermo Scientific K-Alpha X-ray photoelectron spectrometer (XPS) using monochromatic Al radiation operating at 72 W power at a spot size of 400 microns. Dual low energy electron and Ar⁺ neutralisation were used, and all data calibrated to the C(1s) line at 284.4 eV when required. All data were analysed using CasaXPS software and using Scofield sensitivity factors corrected with an energy dependence of 0.6 eV, after application of a Shirley background.

- ***N₂ adsorption***

N₂ adsorption at boiling temperature (77 K) is the most common characterisation technique employed to determinate the surface area, pore volume and size distribution analysis of a catalyst.¹⁴ Previous to the analysis, the samples must be cleaned by removing chemicals under vacuum and high temperature in the degasification process. The nitrogen adsorbed volume versus the relative pressure gives us the adsorption isotherm. The shape of this isotherm provided by the pore structure or texture. According to IUPAC, we can distinguish six types of isotherm as shows *Figure 2-6*. Type I isotherm are given by microporous solid material a) with narrow micropores of ~1 nm of width, and b) with wider micropores < 2 nm. Non-porous or

macroporous solids, > 50 nm; give isotherme Type II (in the case the initial increase is sharp, the point B correspond to the complete formation of the monolayer, see *Figure 2-16*) or Type III, in the case that the adsorbed molecules are clustered, there is no Point B. Mesoporous solids (2-50 nm) provide a Type IV isotherm which correspond to a monolayer-multilayer adsorption. This kind of isotherm would be the combination of a Type II isotherm folowed by pore condensation. The pore condensation can be accompanied by hysteresis in Type IV (a), while Type IV (b) shows mesopores of smaller width, and therefore the latest isotherm would be reversible. Type V, as Type III isotherm, are given by material con weak adsorbent-adsorbate interaction. After the formation of clustered molecules, pore filling occurs in Type V isotherm. The last physisorption isotherm, Type VI, is representative of layer-by-layer adsorption given by uniform ultramicroporous or nonporous materials. However, only four types are usually found in catalyst characterisation: Type I, II, IV and VI.^{14,15}

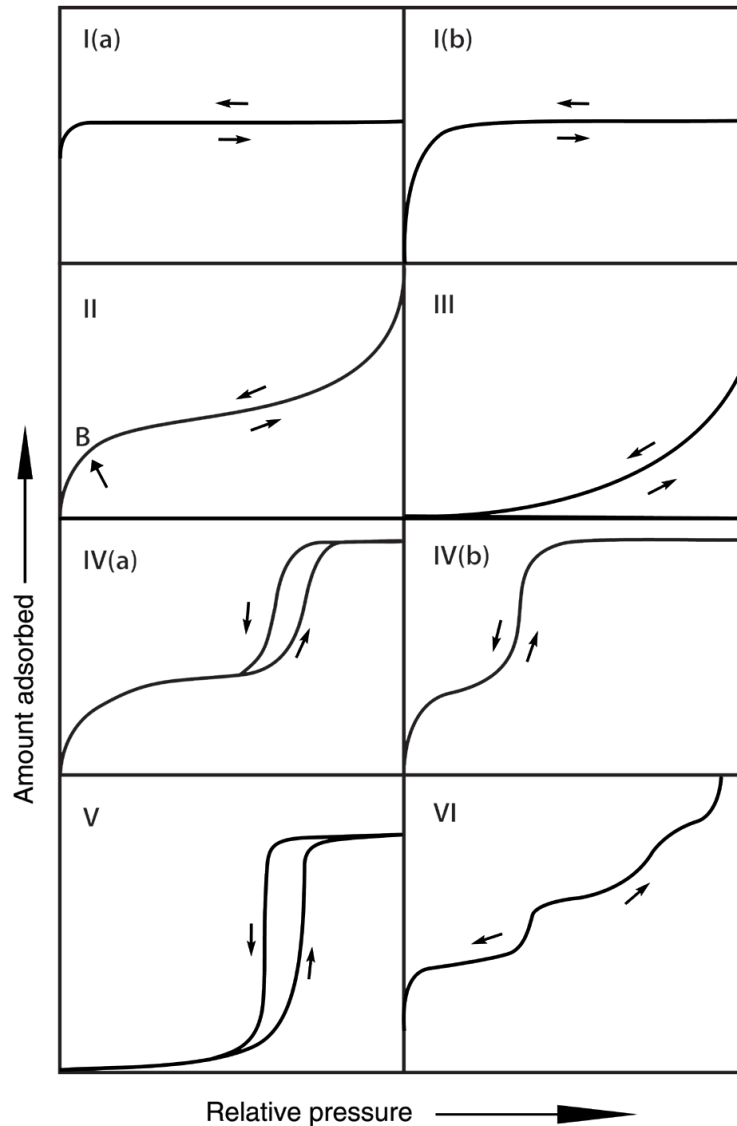


Figure 2-6 IUPAC Classification of physisorption isotherms¹⁵ © Copyright 2015, De Gruyter, IUPAC.

To determine the surface area, there are different models that can be used. Langmuir adsorption model consist on the assumption of the formation of only a monolayer of adsorbate is adsorbed on the surface. However, the use of the Langmuir isotherm, in the case of monolayer only adsorption, can result in the overestimation of the specific surface area. While the Brunauer-Emmett-Teller (BET) surface area model enables the determination of the number of molecules required to form a monolayer. The transformation to a linear version of the BET equation is necessary to determine the monolayer volume:

$$\frac{p}{v_a \left(\frac{p_0}{p} - 1 \right)} = \frac{C-1}{V_m} \cdot \frac{p}{p_0} + \frac{1}{C \cdot V_m} \quad (15)$$

where:

p	<i>partial vapour pressure of adsorbate gas in equilibrium with the surface [at the b.p. of liquid nitrogen, 77.4 K], in pascals</i>
p_o	<i>saturated pressure of adsorbate gas, in pascals</i>
V_a	<i>volume of gas adsorbed at standard temperature and pressure (STP) [273.15 K and atmospheric pressure (1.013×10^5 Pa)], in millilitres</i>
V_m	<i>volume of gas adsorbed at STP to produce an apparent monolayer on the sample surface, in milliliters¹⁶</i>
C	<i>constant related to the enthalpy of adsorption of the adsorbate gas on the powder sample, dimensionless</i>

C constant is the relative error between single and multipoint BET, (typically measured at P/P_0 of 0.3).¹⁷ For low C-value, the error becomes large, for example, $C=1$ has a relative error of $P/P_0=0.7$, while $C=1000$ gives a relative error for the $P/P_0=0.002$.¹⁸

Once the monolayer capacity, V_m , is determined, the surface area can be calculated with the following equation:

$$S = \frac{V_m \cdot N_A \cdot s}{M_v} \quad (16)$$

where:

S	<i>in the total surface area</i>
V_m	<i>is the volume of gas adsorbed at STP to produce an apparent monolayer on the sample surface, in millilitres.¹⁶</i>
N_A	<i>Avogadro's number (6.022×10^{23}).</i>
s	<i>cross-section area of the absorbing species (for nitrogen = 0.162 nm^2).¹⁹</i>
M_v	<i>molar volume (22141 mL).²⁰</i>

To calculate the pore volume, the thickness of the film of adsorptive on pore walls is assumed uniform, what is known as statistical thickness. The statistical thickness, t , is determined through the t-plot method developed by Lippens & DeBoer, which describe the statistical thickness of the absorbed film on a nonporous reference surface.

$$t = \frac{V_a}{V_m} d \quad (17)$$

Where:	t	<i>is the statistical thickness</i>
	V_a	<i>is the volume adsorbed</i>
	V_m	<i>is the volume monolayer</i>
	d	<i>is the effective thickness of the monolayer</i>

The characterisation of the metal oxide, mesoporous material was carried out using a Quadrasorb EVO instrument with 4 stations, see the diagram in *Figure 2-7*. Between 100 mg of sample was weight in a cell of 9 mm large round bottom bulb. The samples were cooled down using liquid N₂ for the analysis, using He with an evacuation time of 3 min and 30 s of delay. Defining adsorption points which lead to a linear plot is required; otherwise, data cannot be evaluated by BET theory. A total of 32 absorption points and 42 desorption points were measured. Once the measurement was finished, multi-points with the standard relative pressure range between 0.05-0.3 P/P₀ to obtain the straight line of the BET and to obtain the surface area. In contrast, to obtain the straight line of the t-plot experiment points between 0.15-0.45 P/P₀ was selected to determinate de micropore volume and the total pore volume.

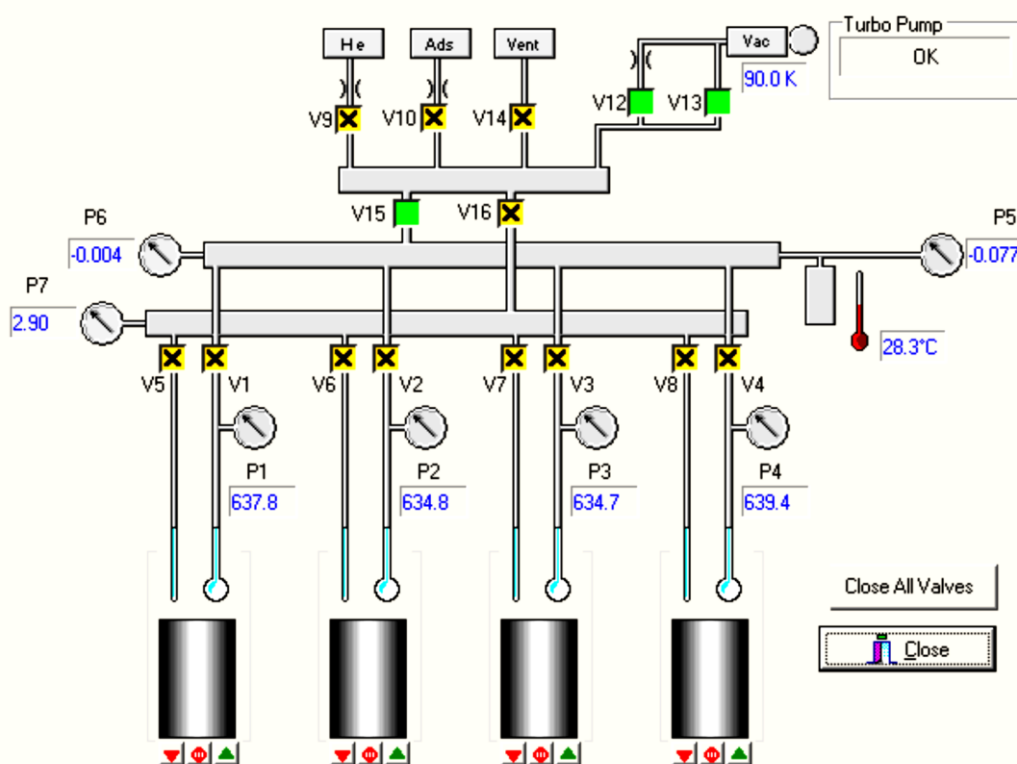


Figure 2-7 Diagram of the Quadrasorb EVO model QDS-30, showing 4 individual sample stations (V1, V2, V3, V4) ports with their correspondent referent (V5, V6, V7, V8) ports. Image obtained from Quadrawin™ software.

All the samples were previously degassed at the highest temperature that will not cause a structural change to the sample, using a FLOVAC degasser. In the case of the zeolites, the catalysts were degassed at 250 °C for 16 h. After degassification the weight of the sample was recorded and introduced in the QuadraWin software for more accurate measurements.

The main disadvantage of this method is the low relative pressure required ($P/P_0=10^{-7}$) and the long measurement times for micropore analysis. In order to amend this issue a more sophisticated instrument 3Flex from Micromeritics (*Figure 2-8*) was used for the characterisation of zeolites, which improved throughput micropore analysis and provides superior mesopore/micropore, physisorption, or chemisorption analyses. The analysis was performed using multipoint measurement using adsorption data in the linear region of the isotherm, in the pressure range of 0.0003-0.05 P/P_0 . Degasification of the samples, in this case, was carried out *in-situ* at 175 °C for 12 h. The weight of the sample after degasification was measured at the end of the N₂ desorption experiment for accurate results.

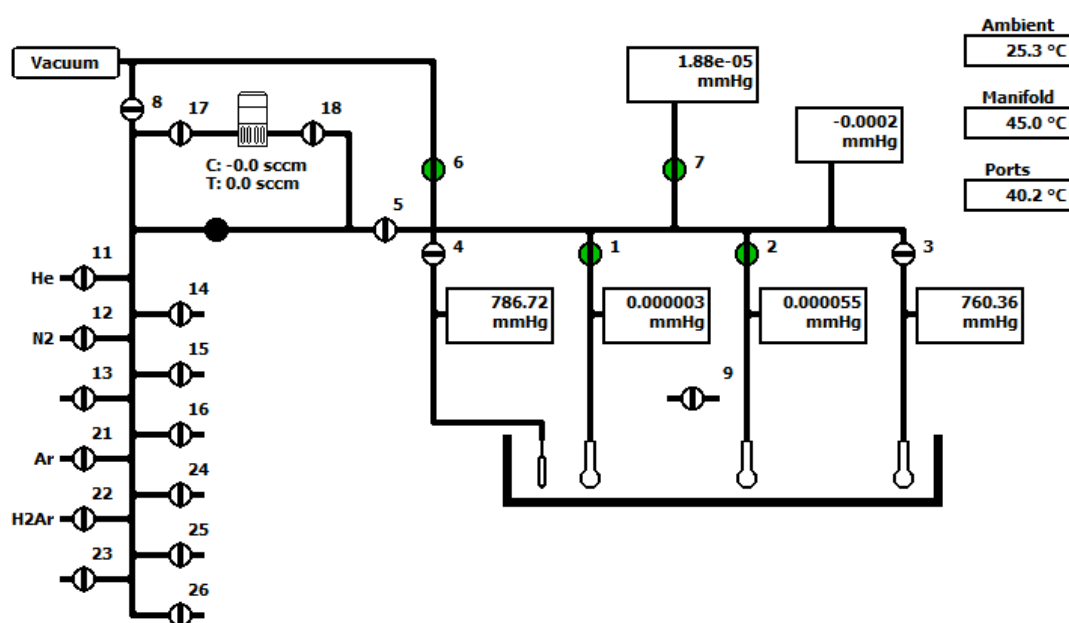


Figure 2-8 Diagram of the 3Flex Physisorption instrument from Micromeritics®, showing three configurable analysis ports (numbers 1, 2 and 3) or sample stations and a common reference port (4). Image obtained from MicroActive™ Data Software.

- **Ammonia temperature programmed desorption (NH₃-TPD)**

Temperature programmed desorption (TPD) is one of the most widely used techniques for the characterisation of acid sites on the metal oxide catalyst surface. It allows to determinate the strength and quantity of the acid sites based on the desorption of a probe molecule (NH₃), after its absorption on the catalyst surface, by heating using a programmed linear temperature ramp.²¹ NH₃-TPD was carried out using a CHEMBET TPR/TPD chemisorption analyser/benchtop from Quantachrome Instruments. The desorption is monitored *via* a thermal conductivity detector (TCD), which senses changes in the thermal conductivity and compares it to the conductivity of carrier gas as the reference, helium in this case.

Calibration of adsorbate was performed via the integration of the peak area of different injection volume of pure ammonia (*Figure 2-9*). The thermal conductivity values for ammonia are shallow, therefore the highest attenuation (1) and TCD sensitivity (180) must be used to ensure a good signal from the desorbed ammonia. The carrier used was Helium, and its flow was set to 145, giving a flow of approximately 50-100 mL min⁻¹.

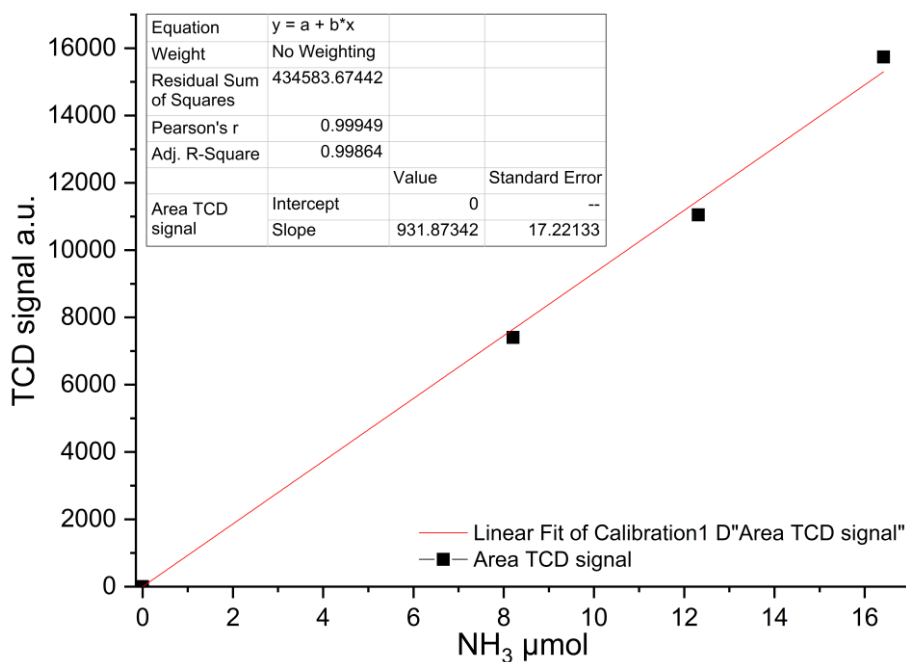


Figure 2-9 Linear fit correlation of ammonia calibration. Peak area vs known volume of ammonia injected was calculated with the area under the curve obtained by integration in Origin®9.1.

For quantification of the acid site density of the samples, approximately 0.05-0.1 g of material was added in a U-shape quartz tube and packed between two quartz wool plugs. First, the sample must be pre-treatment in order to remove the water content. To do so, it was heated up to 130 °C with a temperature ramp of 15 °C min⁻¹ for 1 h. Because the ammonia adsorption must be performed at a stable temperature, it is necessary to allow the temperature to return to RT and stabilise. Then, ammonia could be adsorbed by flowing the sample in ammonia to saturate the surface. However, this is quite difficult with pure ammonia for reasons of micro leaks and equipment damage. Therefore 10 % ammonia in argon was used as the adsorbate. The material was exposed to a constant flow of ammonia for half an hour. It was heated up to 100 °C (15 °C min⁻¹) for 1 h to remove the weakly adsorbed NH₃ (physisorbed) on the material. Finally, the desorption macro was initialised with a ramp to 800 °C, 15 °C min⁻¹, 5 min hold

time to remove the chemisorbed ammonia. Then, the relative acidity was estimated following eq. 18.

$$\text{Acidity (NH}_3 \text{ } \mu\text{mol g}^{-1}) = \left(\frac{\text{Area acid site}}{\text{RF NH}_3 \text{ calibration}} \right) / g_{\text{catalyst}} \quad (18)$$

There are different methods to quantify the areas of acid sites of a catalyst.²² After subtracting baseline, a simple calculation of the areas under the TPD curve is enough to work out the total acidity of the materials. However, this technique is wholly inaccurate to differentiate weak acid sites from strong acid sites since the peaks usually consist of heavily overlapped peaks. Therefore, deconvolution of the curve, which enables us to separate multiplex spectra into single peaks seems to be a good option and then fit peaks using Origin® 9.0. The deconvolution of the data into two peaks underestimates the actual area since the fit would result in a very low correlation. All the curves for the chemisorbed ammonia desorption are separated into 4 distinguish peaks, to make the acidic site strength comparable between different materials. Each peak corresponds to one temperature range. A Gaussian fitting equation was used for the peak fitting. This technique has recently gained importance, and it has been reported to quantify the acidity of zeolites, such as ZSM-5,²³⁻²⁵ HY,²⁶ Beta,²⁷ and Mordenite. In some cases, deconvoluting the curve even in six fixed temperature ranges to get a good fit.²⁸

Figure 2-10 and Table 2-1 shows a fit example of the NH₃-TPD results for the 2 wt. % PdRu/ZSM-5 (30:1) catalyst. The Chi-Square goodness of fit test was employed to measure how the model correlated with the experimental data. This statistical test reaches the best model fit after several iterations, i.e. the one which minimises the square of the difference between the model and data curves. The goodness of the fit is evaluated with the reduced chi-square (χ_v^2), residual sum of squares (RSS) and the correlation coefficient (R^2). χ^2 and χ_v^2 are defined following equations (19 and 20). The sum of squares of residuals (SS) is the sum of squares of estimates the error.

$$\chi^2 = \frac{(\text{Experimental data} - \text{Model data})^2}{\text{Model data}} \quad (19)$$

$$\chi_v^2 = \frac{\chi^2}{\text{Degrees of freedom}} \quad (20)$$

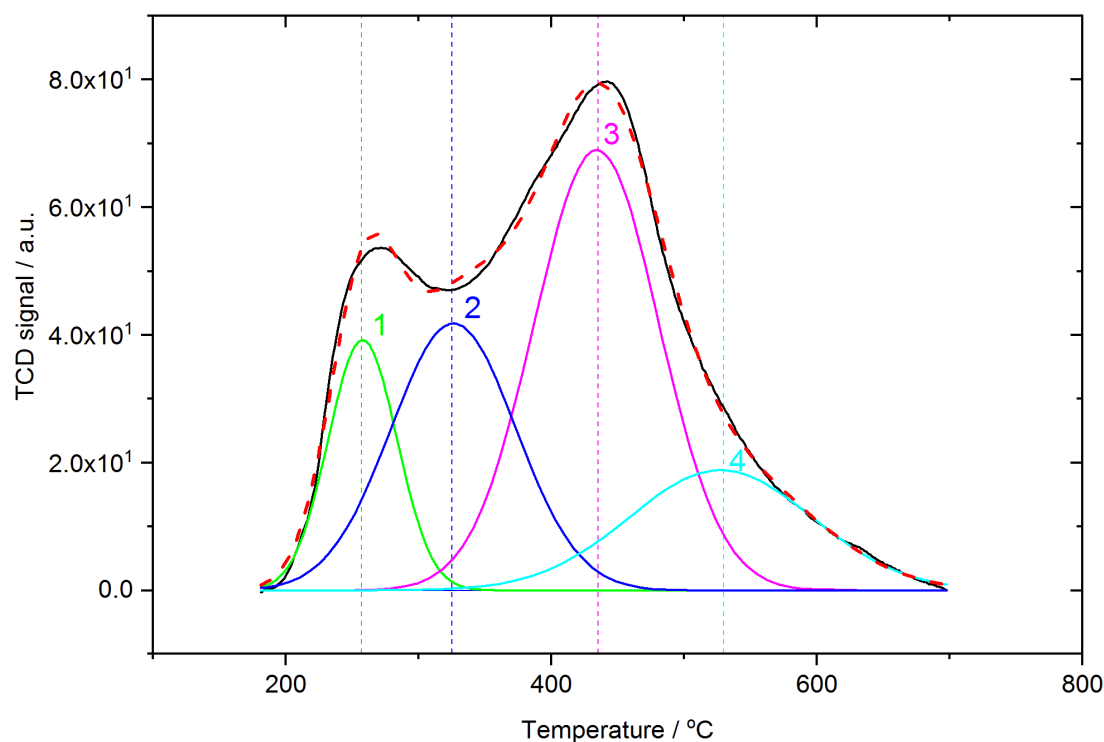


Figure 2-10 NH_3 TPD spectra for a 2 wt.% PdRu/ZSM5 (30:1) catalyst (thick black curve correspond to the experimental data), a fitting result for the deconvolution (red dash line) and component curves obtained by deconvolution (Peaks 1-4). The goodness of fit of the statistical model shows $\chi^2 = 1.57255$, $R^2 = 0.99757$, and $SS = 647.892$ obtained using Origin® 9.0.

Table 2-1 Integration values of the peaks obtained by deconvolution for the 2 wt.% PdRu/ZSM5 (30:1) catalyst

Peak Index	Peak Type	Area Integrated	FWHM	Center Gravity (Temperature, °C)
1	Gaussian	2533.8	60.8	257.8
2	Gaussian	4930.0	110.9	326.1
3	Gaussian	8142.8	111.0	434.0
4	Gaussian	3245.7	163.2	527.6

The deconvolved peaks identified (1-4) by our proposed method have a temperature range with a maximum temperature value around 250 °C associated to weak acid site strength, 330 °C with medium acid site strength, 430 °C with strong acid site strength and 530 °C with very strong acid site strength respectively. See Appendix for the rest of the fit NH_3 -TPD results obtained for the catalysts tested.

- *Pyridine absorption via Diffuse Reflectance Infrared Fourier Transform Spectroscopy (DRIFTS)*

Pyridine IR is a vibrational technique widely used for the characterisation of the acidity of materials such as zeolites. It is possible to reveal the nature of an acid site on the solid acidic catalyst, distinguish between Lewis or Brønsted acidities, employing this technique.²⁹

The instrument employed to obtain the DRIFTS spectra was a Bruker Tenso27 FT-IR spectrometer equipped with a mercury-cadmium-telluride (MCT)-detector for additional sensitive measurements and with a desiccant cartridge. This kind of detector requires to cool down with liquid N₂ until the detector Dewar has been filled to maximum. The IR source is Mid-Infrared (MIR) and with standard KBr beamsplitter, which has a spectral range of 7500-370 cm⁻¹. The software installed was the OPUS data collection and analysis program.

Prior to the analysis, the samples were pre-treated at 110 °C in a conventional oven overnight, then in-situ heating was carried out in a Harrick Praying Mantis high-temperature diffuse reflection chamber (HVC-DRP-4) *in situ* cell at 500 °C for 2 hours under flowing N₂ (40 mL min⁻¹) adjusted using a Brooks mass flow controller (MFC). After pre-treatment, a background spectrum was taken at 30 °C loaded later for each measurement. Pyridine was then absorbed by exposing the sample for 5 min to a flow of 50 mL min⁻¹ of N₂ bubbling into pyridine through a heated line at 110 °C. The excess of pyridine was removed by vacuum for 5 min. The IR spectrum was collected while increasing temperature in a range from 30 to 575 °C. 5 scans were taken after 5 min of reaching the desired temperature, to have a stable measurement, across the range 4000 cm⁻¹ to 1000 cm⁻¹, 2 cm⁻¹ frequency.

According to Lambert-Beer law (eq. 21), the absorbance (peak intensity) in an absorbance spectrum is directly proportional to the component concentration in the sample, the path length of the sample and the absorptivity.³⁰

$$A = \epsilon b C \quad (21)$$

where,

- A* Absorbance at a given wavelength
- ε* Molar absorptivity (proportionality constant *mol⁻¹cm⁻¹*)
- b* pathlength of the sample (cell length for samples on the cell)
- C* analyte concentration in the sample

- **UV Raman spectroscopy**

Raman is a vibrational spectroscopy technique used for the determination of the molecular structure of materials. It is based on the Raman scattering phenomena generated by the interaction of an incident electromagnetic radiation with the sample, determines vibrational and rotational level spacings from the energy shifts of the scattered light.^{31,32} Figure 2-11 Shows a schematic representation of the interaction of light with molecules (a) and a diagram with the typical vibrational and the electronic energy levels of a molecule and the interaction with light during the Rayleigh and Raman (Stokes and anti-Stokes) scattering processes. The molecule should be polarizable and with no centres of symmetry to be Raman active.

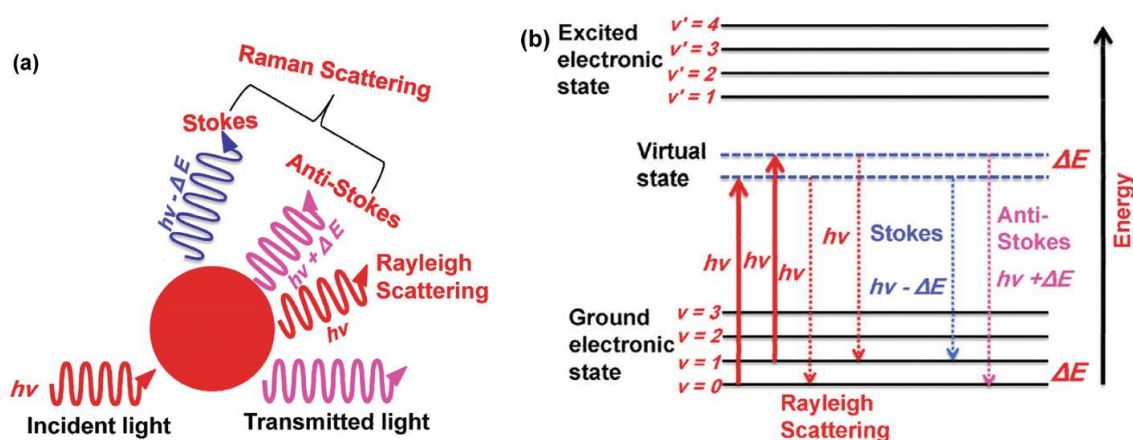


Figure 2-11 a) Schematic representation of various interactions between the molecule and the incident light. b) Molecular energy diagram comparing Rayleigh scattering and Raman scattering (Stokes and anti-Stokes). Copyright © El-Said, 2017. Reproduced with permission from Ref.³³

The instrument employed was a RENISHAW class 4 inVia™ Raman Microscope equipped with a UV laser (266 nm). The acquisition of all the samples was taken at exposition time of 2 seconds with 20 accumulations, 3600 L min⁻¹ and laser power 100 % with cosmic ray removal. All the measurements were carried out after waiting for at least 30 min for the laser to stabilise and focus the sample.

- **X-ray powder diffraction (XRD)**

XRD is a comprehensive characterisation technique to analyse the crystal structure of solid materials. It generates an X-ray diffraction pattern, which is a plot of the intensity of X-ray scattered at different angles by a sample, thanks to the movement of the detector in a circle around the sample (Figure 2-12). The detector measure counts the number of X-rays recorded

at each angle 2θ . To explain the interference pattern of X-ray scattered by crystals is used the Bragg's law (eq. 22). This diffraction pattern is unique for each different phase (specific chemistry and atomic arrangement of a chemical structure).

$$2d_{hkl} \sin\theta = n\lambda \quad (22)$$

where, d_{hkl} is the distance between two lattice planes hkl , (Miller indices)
 n is an integer number, order of reflection
 λ is the wavelength of the incident X-ray
 θ is the incidence angle

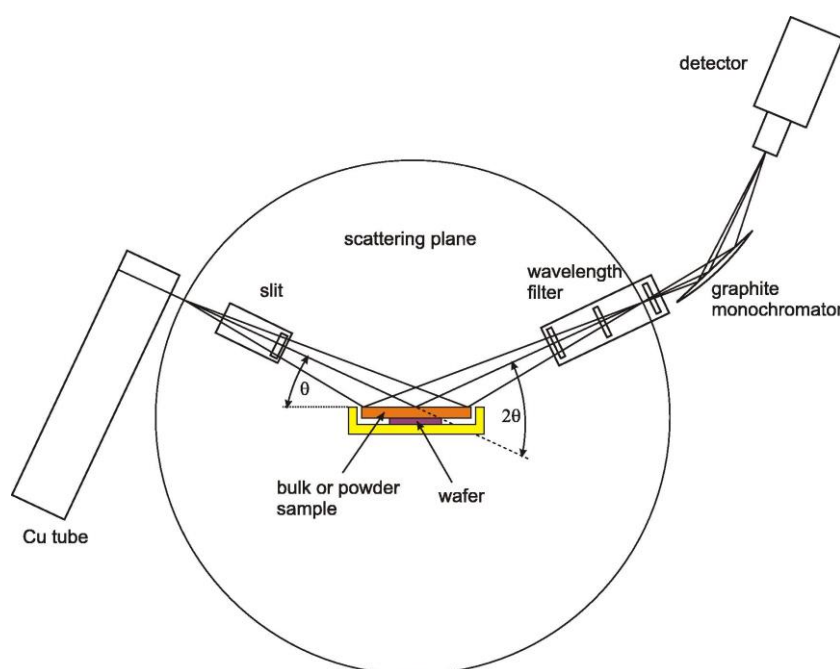


Figure 2-12 Schematic representation of the Bragg–Brentano geometry of the X-ray powder diffractometer. Copyright ©Acta Materialia Inc. Elsevier, 2005. Reproduced with permission from Ref. ³⁴

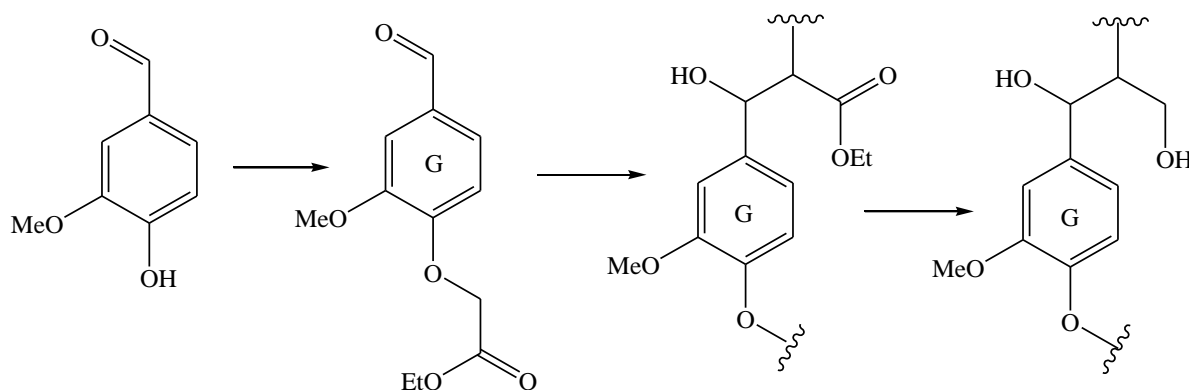
The samples were prepared packing the fine powder into a sample holder. The XRD diffraction of the different materials and catalysts were performed using a PANalytical X'Pert Pro ® diffractometer using a copper anode ($K\alpha$ 1.54184 Å) ray source, operating at 40 kV and 40 mA. The measuring programme was set for collecting the signal in a range of 2θ angle from 5° to 80° with a step of 0.02° . Analysis and treatment of the XRD patterns data were performed using X'Pert High Score software. Firstly, it is necessary to determinate the background. The granularity was fixed to 20, and the bending factor equal to 0 for all the spectrum obtained. The smoothed input of the data was also applied, and the background subtracted. All diffractograms were normalised using an elemental Si standard.

2.3 Lignin depolymerisation

2.3.1 Synthesis of model substrates

- ***β -O-4' lignin model polymer***

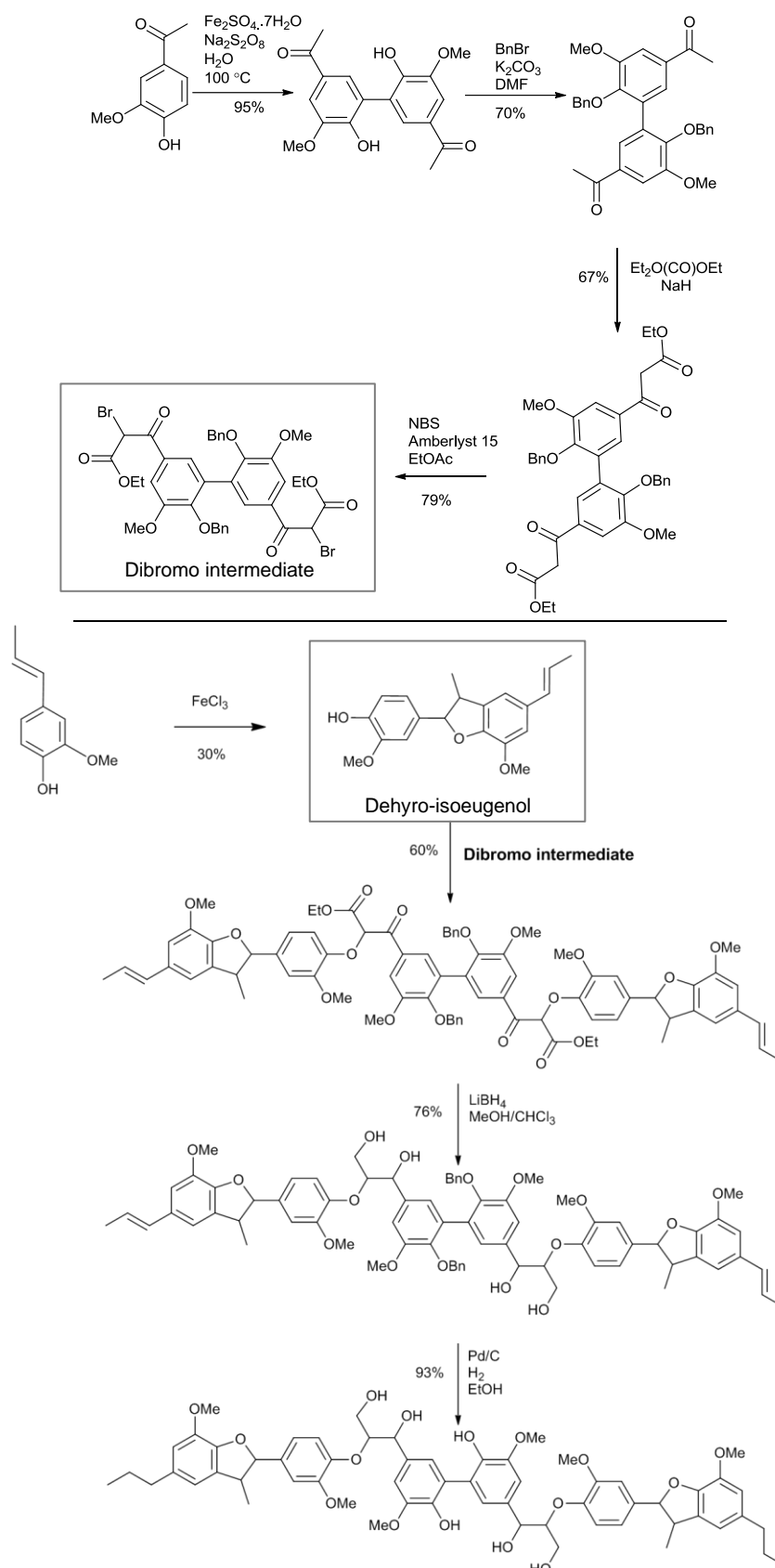
The polymer used was synthesised thanks to our collaborator Dr Christopher S. Lancefield, during a short research stay within the group led by Prof. Nicholas J. Westwood at the School of Chemistry of The University of St. Andrews, UK. It is a β -O-4' model compound with only guaiacyl (G) sub-units, synthesised as described in *Scheme 2-1*.³⁵ Briefly, the synthesis protocol involves vanillin as starting material for the synthesis of Ethyl 2-(4-firmly-2-methoxyphenoxy) using ethyl bromoacetate and K_2CO_3 in acetone. Following the general procedure for polymer reductions, the polymer was dissolved in ethanol using $NaBH_4$ as a reduction agent. Then, the crude polymer precipitates as the solution are acidified with HCl. Finally, the the crude dry polymer is purified and dried *in vacuo*.



Scheme 2-1 Schematic representation of the strategy used to prepare G-only β -O-4' lignin model polymer.

- ***Hexamer lignin model compound***

This hexameric model compound was obtained from another collaborator, Dr Gary N. Sheldrake from the School of Chemistry and Chemical Engineering at Queen's University of Belfast, UK. They synthesised the hexamer from dehydroisoeugenol, and its dibromo intermediate as shows *Scheme 2-2*.³⁶



Scheme 2-2 The Scheme for the synthesis of dibromo intermediate is represented at the top. The bottom Scheme illustrates the synthesis of the hexamer model compound using the dibromo intermediate and dehydro-isoeugenol. Adapted from Ref.³⁶

2.3.2 RICO reaction protocol

The reaction was carried out in a 50 ml bottom flask, under vigorous stirring at 22 °C and atmospheric pressure. Reactions conducted in a monophasic solvent system consisted of two solvents (water and acetonitrile) that are miscible. In the case of the β -O-4' lignin model polymer, the reaction solvent was methanol instead of acetonitrile, due to solubility issues. The substrate: oxidant: catalyst molar ratio was kept at [1:8:0.1]. In a typical reaction, the reactor was charged with the requisite amount of substrate (0.164 mmol) and the solvent acetonitrile (20 mL) and the reaction temperature was set at 22 °C. To this solution, an aqueous solution of NaIO₄ (280 mg, 1.312 mmol dissolved in 10 mL of deionised water) was added after stirred for 1 min (stirring speed: 500 rpm). The metal precursor RuCl₃•xH₂O (0.012 mmol) was added to the above mixture, and this is denoted as the start of the reaction. To make the addition of catalyst precursor easier, an aqueous stock solution of RuCl₃•xH₂O was used (7.178 mg mL⁻¹, analysed by inductively coupled plasma mass spectroscopy, ICP). After a specific reaction time, the reaction mixture was quenched, immediately after sampling, *via* the addition of an aqueous solution of Na₂SO₃, added in excess equivalent than the oxidant added.

A condenser was installed on the reactor, to avoid evaporation of the solvent. Two different kinds of condensers were tested, a conventional water condenser and an air condenser. The concentration of biphenyl dissolved in the solvent mixture of the reaction was checked at the beginning and after 24 h to confirm no evaporation of the solvent, *Table 2-2*. The condenser selected was a Radleys Findenser Air Condense, which does not require any refrigerator or water constantly running, being a more environmentally friendly method (*Figure 2-13*).

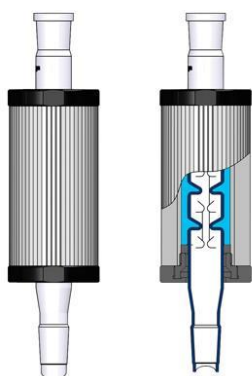


Figure 2-13 Findenser™ Super Air Condenser. Copyright © Radleys, 2018

Table 2-2 Performance of the condenser tested through Biphenyl acetonitrile solution in an HPLC instrument.

	<i>Area at Time 0h</i>	<i>Area at Time 24h</i>
<i>Air Condenser</i>	23738.6	23785.8
<i>Water Condenser</i>	24559.6	24635.9

After the reaction, the solvent was evaporated via freeze dryer or in vacuum depending on the substrate. The solid obtained was dissolved in 0.8 mL of d_6 Acetone and 0.088 mL of deuterated water for NMR analysis in the case of the β -O-4' lignin model polymer and in deuterated chloroform ($CDCl_3$) for the rest of substrates.

For substrates as biphenyl and bibenzyl, a sample of 0.5 mL as a blank was withdrawn from the reactor mixture, before adding any catalysts precursor or oxidant and used it for quantification purposes by HPLC. Besides, for quantitative analyses, it was necessary to reduce the concentration of metal ions in the solution. Amberlyst® (15 % wet) was used to remove the sodium, which is frequently used in the literature for cation exchange processes. The post-reaction sample was stirred with the resin for a few minutes. Then, the filtered sample was analysed by ICP (Table 2-3). The Amberlyst® treatment dilutes the reaction sample because of the wetness. However, the concentration of sodium was substantially reduced; the main issue is that after this treatment, the LC-MS or GC-MS could not detect any reaction product. We believe that this could be because of the adsorption of the products on the Amberlyst® itself.

Table 2-3 ICP analysis before and after the ion-exchange using Amberlyst (15 % wet).

<i>Sample</i>	<i>23 Na [He]</i>	<i>101 Ru [He]</i>
	<i>Conc. [mg L⁻¹]</i>	<i>Conc. [mg L⁻¹]</i>
<i>Before Amberlyst</i>	522.54	28.28
	532.10	28.15
<i>After Amberlyst</i>	47.96	23.12
	47.45	23.26

A post-reaction protocol was developed to separate the products from the metal ions (Figure 2-14), in order to remove the metal ions without losing organic substrate/products. A ternary mixed-solvent solution of water-acetonitrile–ethyl acetate was used³⁷. Firstly, after quenching the reaction with sodium sulphate, the solid materials precipitated (sodium iodate),³⁸ formed during the reaction, were filtered and washed with sodium hydroxide. This would convert the carboxylic acids (benzoic acid is sparingly soluble in water at room temperature) into their sodium salts. Diluted hydrochloric acid was then used to acidify this solution to convert the salt back to carboxylic acid prior to extracting them using ethyl acetate. Therefore the upper phase is useful for qualitative purpose by GC-MS (Figure 2-15). ICP of both phases was also analysed showing better results than in the case of Amberlyst®, especially for the Ru (see Table 2-4).

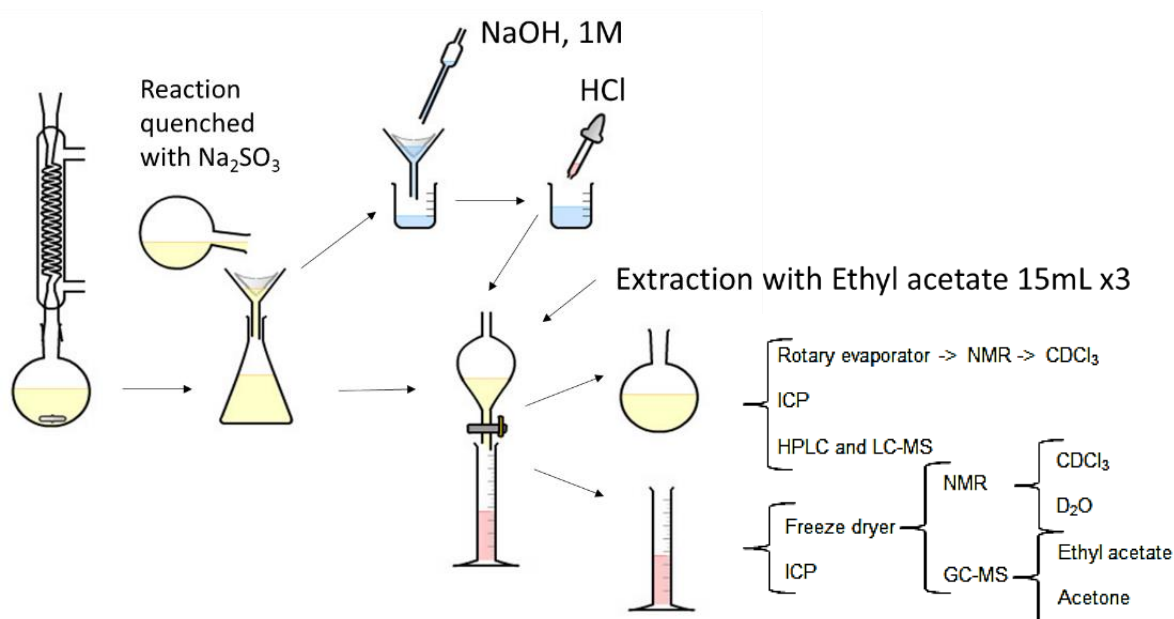


Figure 2-14. Post-reaction protocol. Diagram obtained by Chemix® 2.0

Table 2-4 ICP analysis of the organic and aqueous phases after the extraction with ethyl acetate

Sample Name	23 Na [He]		101 Ru [He]	
	Conc. [mg/L]	Conc. RSD	Conc. [mg/L]	Conc. RSD
Organic phase	31	4.23	0.14	4.96
Aqueous phase	4546	1.59	88	7.22

Table 2-5 ICP analysis of the different extraction make in a typical RICO reaction.

Sample Name	23 Na (mg/L)	101 Ru (mg/L)
Lower phase	14055.7	92.9
1 st Ext.	154.7622	0.3164
2 nd Ext.	16.93125	0.0122
3 rd Ext.	6.50486	0.0052

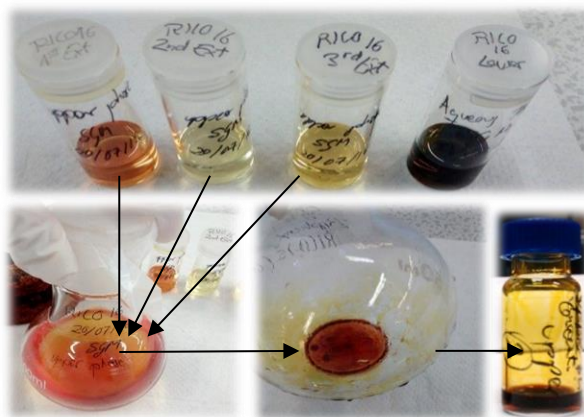


Figure 2-15. Sample preparation of the organic phase sample for GC-MS and thin layer chromatography proposes.

Once the ICP confirmed an excellent separation of metal ions, to avoid damage to the HPLC column, it was crucial to see if there was an organic compound remaining in the aqueous (lower) phase. It was proved with a control experiment (without catalyst or sodium) that no organic compounds are remaining in the aqueous lower phase after 3 extractions with 15 mL of ethyl acetate. These “blank” experiments using biphenyl and benzoic acid standards without any NaOH or catalyst confirmed that after 3 or 4 extractions with 15 mL of ethyl acetate (Figure 2-16). Most of the organic compounds are extracted in during the first extraction; nevertheless, for all the reactions, the extraction process was carried out three times with waiting time in between extraction of half an hour. Besides, a sample of the lower phase was analysed by NMR, confirming no presence of organic compounds in the aromatic region.

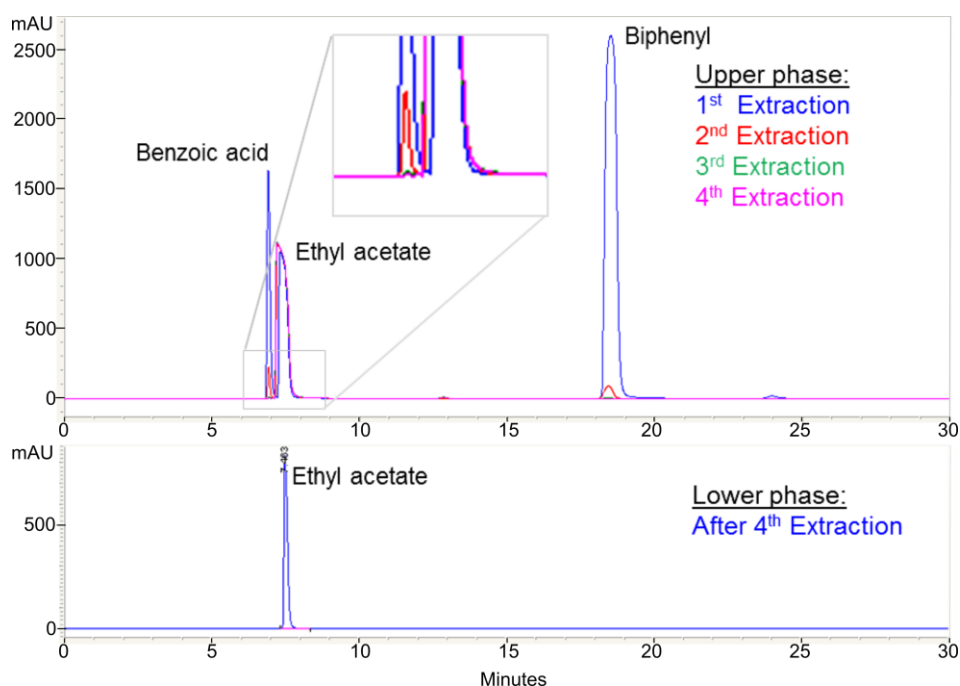


Figure 2-16 HPLC chromatogram for a blank reaction after several extractions.

This experiment confirms that the post reaction protocol developed to separate the products from the metal ions using a ternary mixed-solvent solution of water-acetonitrile–ethyl acetate is an effective method to quantify the product and study the catalytic system.

2.3.3 Analytical Techniques

- **Gas Chromatography coupled with Mass Spectroscopy**

Gas Chromatography coupled with mass spectroscopy (GC-MS) is a technique used to both separate and identify unknown molecules present in a sample. Every GC-MS set-up is readied with a library of reference data to aid the identification process. Firstly, the sample is sent through a GC column where the compounds are separated base in polarity. These separated products are then directed through the ionisation chamber of the MS system (electron ionisation was used). This gas-phase ion is produced and separated using a mass analyser (this separation corresponds to the mass to charge ratio). A detector then collects and registers the ions as they pass through.

All GC-MS samples were prepared by dissolving the concentrated in the vacuum (5-10 mg) in ethyl acetate (1 mL) and then syringe filtered (0.45 μm PTFE filter) and poured into a vial. Any GC-MS analyte was sent through a Waters GCT premier instrument fitted with an Agilent HP-5MS column. The choice of carrier gas was helium (flow rate, 1 mL.min⁻¹), and the temperature range of the instrument was between 40 °C-280 °C.

- **Nuclear magnetic resonance spectroscopy**

Nuclear magnetic resonance spectroscopy (NMR) is a powerful analytical technique widely used for identification and structural analysis of organic compounds. This technique is based on the physical phenomenon of resonance transition between levels of energy. The atomic nuclei are placed in an external magnetic field and are subjected to electromagnetic radiation with a specific frequency. The nuclei can absorb energy. The absorption signals are detected as resonance peaks. Any nuclei may be characterised by a nuclear spin quantum number I (multiples to $\frac{1}{2}$). Spinning nuclei has angular moment P , applying a static magnetic field, B_0 , traces a circular path about the applied field, results in its precession around B_0 with the rate corresponding to the Larmor frequency. The angular velocity describes this rate of precession³⁹.

$$\omega = -\gamma \cdot B_0 \quad (23)$$

where,

- ω is the Larmor frequency
- γ is the magnetic ratio of nuclei
- B_0 is the static magnetic field strength along the z -direction

The frequency of the radiation for the energy absorption depends on the type of nucleus (characteristic of ^1H , ^{13}C , etc.), on the chemical environment of the nucleus and the spatial location in the electromagnetic fields, if it is not uniform.⁴⁰ The relative sensitivities of the different isotopes ^1H , ^{13}C , ^{31}P can be derived by the Boltzmann regime.⁴¹ Among the nuclei, ^1H is clearly the most sensitive (Table 2-6).

Table 2-6 Nuclear properties of the selected isotopes

Isotope	Abundance (%)	Relative Sensitivity	Absolute Sensitivity
^1H	99.98	1.00	1.00
^{31}P	100.00	0.0664	0.0664
^{13}C	1.11	0.0159	0.00018

Where relative sensitivity at an equal number of spins and constant B_0 , while absolute sensitivity is the relative sensitivity corrected for natural abundance. Adapted from Ref. ^{39,41}

All NMR spectra were obtained using a Bruker DPX 500 MHz instrument. The data were processed and assessed using both TopSpin3.5 and/or MetraNova software. To prepare the samples for NMR, first, the solvent from the reaction must be removed by evaporation via freeze dryer or in vacuum using a rotary evaporator. The sample preparation differs depending on the substrate employed in the reaction and the kind of experiment. The solvents used were deuterated chloroform (CDCl_3) and deuterated water (D_2O) for the small model compounds, such as biphenyl and bibenzyl; 0.8 mL of acetone- d_6 and 0.088 mL of D_2O for the full dissolution of the β -O-4' polymer and just CDCl_3 in the case of the hexamer. For qualitative analysis, the dry material (ca. 20 mg) was re-dissolved in 1 mL the corresponding deuterated solvent and transferred to the NMR tube. In contrast for quantitative analysis, the dry material was added into the NMR tube, its weight was recorded, and then 0.5 mL of the adequate deuterated solvent was added. Also an internal standard of tetramethylsilane (TMS)⁴² (sealed off in a thin glass thread-like tube) was carefully introduced into the NMR tube, to keep constant the TMS concentration for quantification purposes.

- ^1H NMR

^1H NMR spectroscopy was applied for both qualitative and quantitative analyses. For quantitative analysis, the integrations of selected chemical shifts were measured and then referenced relative to the TMS peak. For instance, the calibration for the hexamer was

calculated by first dissolving three different known masses of the substrate (10.8 mg, 20.5 mg, and 30.3 mg) in CDCl_3 (0.5 mL), using the same TMS's insert for all the samples. These samples were run through the NMR instrument (16 scans proton NMR method) and the relative areas for the desired proton environments were achieved from the integration of the resulting spectra. A plot representing of moles (x-axis) against the relative area (y-axis) was gathered using this data. The response factor was attained for each proton environment of interest in the hexamer molecule.

Figure 2-17 shows one example of one of the calibrations obtained, with the proton signal at 4.18 ppm being at the focus. Here, a response factor (gradient) of 44887 was obtained, and the R^2 coefficient is very close to equal 1 (0.99884), suggesting that regression line fits almost perfectly.

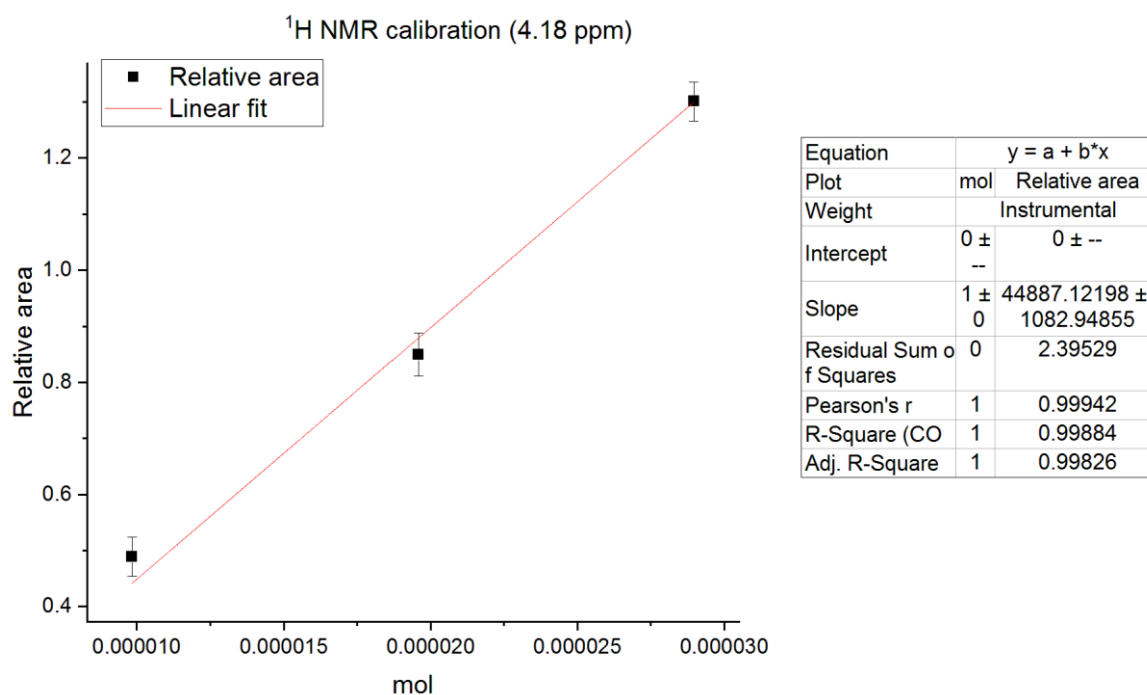


Figure 2-17 Calibration of the chemical shift ($\delta = 4.18$ ppm) in moles of the hexamer. Also displayed is the equation of the trend line with the response factor (gradient) and the R^2 value obtained using Origin® 9.0.

A response factor is required for the quantification and in this case is defined as:

$$\text{Response Factor (RF)} = \frac{\text{difference in relative area}}{\text{difference in moles}} \quad (24)$$

Once the response factor for all the chemical shift (δ) of interest was obtained, the samples after RICO reaction, which contains unknown moles of the started material were analysed. Hence potential percentage cleavages of each inter-unit linkage were also resolved.

To estimate the potential percentage cleavage is required the number of moles of the starting hexamer substrate, the moles of the products and the moles of the product used in the NMR sample. Then, the actual number of moles of the hexamer within the sample can be calculated using the response factor. This can then be scaled up to the total moles of hexamer in the total product mass. Finally, the percentage of cleavage can be worked out using the following equation 25. *Table 2-7* represents one example of how all the data obtained is put together in order to calculate the potential percentage cleavage. This example shows the data collected from the products after a 30 minutes RICO reaction.

$$\text{Potential cleavage (\%)} = \frac{(\text{Starting moles of Hexamer}) - (\text{moles of Hexamer after RICO}) * 100}{(\text{Starting moles of Hexamer})} \quad (25)$$

Table 2-7 $^1\text{H-NMR}$ areas integrated for the estimation of the potential cleavage (%) using the data obtained from the products obtained after the oxidation of the hexamer model compound using RICO.

<i>RF</i>	<i>Area (rel)</i>	<i>δ (ppm)</i>	<i>Moles of NMR sample ($\times 10^{-6}$)</i>	<i>Moles of dry products ($\times 10^{-5}$)</i>	<i>Potential % cleavage</i>
-	1	0	-	-	-
44867	0.2598	4.19	5.79	3.24	80.3
52254	0.2395	4.98	4.58	2.56	84.4
62206	0.4112	5.09	6.61	3.70	77.5

The chemical shifts (δ) at 0, 4.19, 4.98 and 5.09 represent the TMS, β -O-4' (β), β -O-4' (α) and β -5' proton environments respectively.

- *Heteronuclear single quantum correlation spectroscopy ($^1\text{H-}^{13}\text{C HSQC}$)*

Heteronuclear single-quantum correlation spectroscopy is a two-dimensional (2D-NMR) experiment that detects heteronuclear correlations where the nuclei are separated by one bond; hence identifying directly connected nuclei.⁴³

- *Heteronuclear multiple bond correlation (^1H - ^{13}C HMBC)*

Heteronuclear multiple-bond correlation is another type of 2D-NMR technique used that detects correlations between two different nuclei (^1H and ^{13}C) of which are separated by 2-4 bonds;⁴³ hence HMBC tuned through inverse detection. HMBC suffers from the breakthrough from 1-bond correlations, which are not detected by using this method.

HSQC and HMBC methods were also used for quantification during the project. This was carried out using the same procedures and principles as the ^1H NMR quantification. One additional step, however, is before integrating the TMS signal; it is required to calibrate the axis and set the parameters both to zero.

- *^{31}P NMR*

Phosphorylation reaction of lignin model compounds and preparation of samples for ^{31}P -NMR was done using different chlorophosphate reagents in a round bottom flask inside the fume hood at room temperature and atmospheric pressure.

For quantitative analysis 40 mg of hexamer or the dry material after the reaction was accurately weighed and dissolved in 400 μL of a solvent mixture of pyridine and CDCl_3 (1.6:1, v/v). 200 μL of the internal standard N-hydroxynophthalimide (11.4 mg mL^{-1}) in the solvent mixture and 50 μL of a stock solution of relaxation agent (11.4 mg mL^{-1} of $\text{Cr}(\text{acac})_3$ in 5 mL of the solvent mixture) was added to the NMR tube. Typically in lignin analysis, a 25-s pulse delay is considered appropriate for quantitative ^{31}P -NMR.⁴⁴ However, for the hexamer lignin model compound, it has been proved enough to use $d_1 = 5$ s, after confirmation of no change of signal for a range between 5 s and 15 s. The mixture was phosphorylated with 100 μL of 2-chloro-1,3,2-dioxaphospholane (DP) or its sterically hindered analogue 2-chloro-4,4,5,5-tetramethyl-1,3,2-dioxaphospholane (TMDP) depending on the OH groups to investigate. DP is better to distinguish between primary and secondary alcohols of the phenyl chains, carboxylic and guaiacyl phenolic hydroxyls, while TMDP is better to distinguish between guaiacyl and syringyl.⁴⁴

Because the amount of internal standard used is known, the amount of OH can be used to stoichiometrically determinate the amount of each specific OH on the NMR tube. The integration of the ^{31}P signals is used to quantify the amount of OH according to:

$$\text{Moles of compound with OH} = \frac{\text{area of compound with OH}}{\text{area of IS}} \times \text{moles IS} \quad (26)$$

- **Advanced Polymer Chromatography**

Gel permeation chromatography (GPC) is the preferred technique used for characterising polymers, mostly to determine their molar weight distribution. For this thesis, an Advanced Polymer Chromatography (APC) instrument from Waters Corporation was employed. APC system is an improved version of the conventional GPC technique. The main difference between both systems is that in the APC the column operates under high backpressure (up to 15,000 psi), which allows short analysis times, higher resolution and requires less solvent. It is based on a column packed with rigid porous beads with a continuous solvent flow. The beads quite often contain highly cross-linked polystyrene (with the correct pre-sizes, often 10-10⁵ nm). The principle is that as a polymer solution flows through the column, the solvent will go through the beads as well as around them. Larger molecules will not be able to be held by the pores in the beads, and therefore will remain in the solvent flowing around the beads first. Meanwhile, smaller molecules can pass through the pores and will maintain in the solvent; hence, their flow will be held back. As a result, larger molecules will pass through the column relatively quick, whereas the smaller molecules will take longer to pass through the column (*Figure 2-18-A and B*). The principles of separation are the simple relationship between the molecular weight (M_w) and elution volume (V_e), where the effective separation range will be above a limit all the compounds are eluted at V_0 and under a limit where all compounds are eluted at V_t (*Figure 2-18-C*).

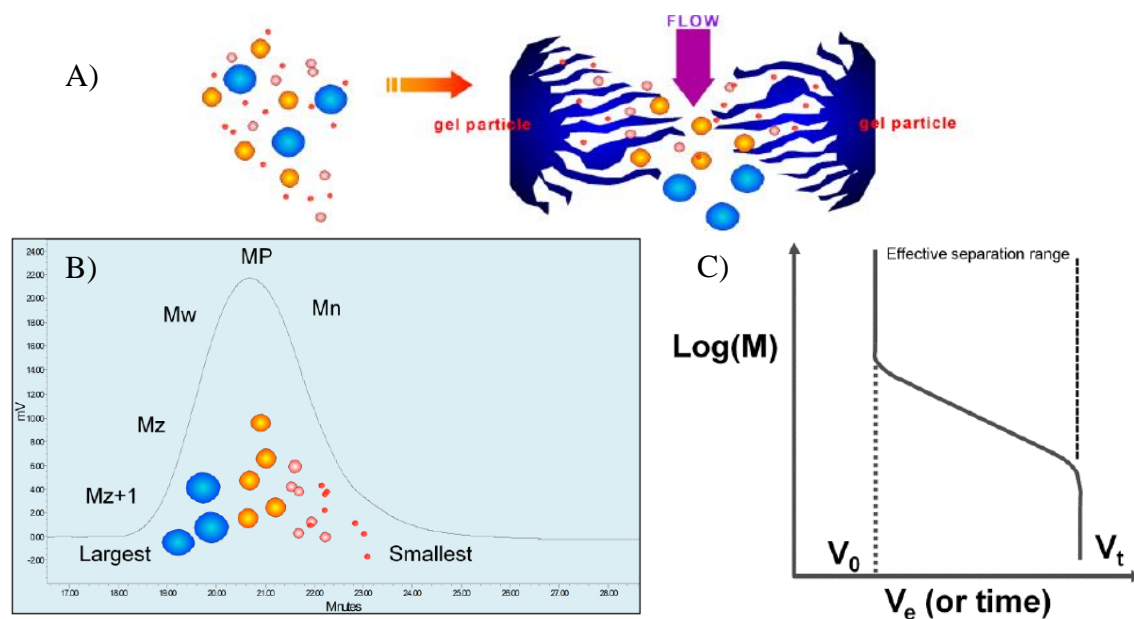


Figure 2-18 A) Separation mechanism of the size exclusion occurring in the APC column. B) The particle distribution on the chromatogram and C) Principles of separation plot. Copyright © Waters Corporation, 2018.

The polymeric sample, once it is injected into the solvent stream, will pass through the column and then it will meet a refractive index (RI) detector. In the RID the sample is compared with the solvent stream as a reference.^{45,46}

All APC samples were run on the Waters Acquity Advanced Polymer XT instrument. The instrument was calibrated to correlate the molecular weight to the elution volume or retention time of the sample, using commercial well-characterised Polystyrene solutes standards from Waters in THF, which is the preferred standard for organic size exclusion chromatography analysis. The three narrow standards of Polystyrene (labelled as their vial colour as black, blue and green) with a range of known molecular weight composition was analysed via refractive index (RI) detector. The known molecular weight was introduced in the Empower 2 software to work out the calibration as follow: black standard: 66000, 21500, 4920, 2280 Da, blue standard 44200, 15700, 3470, 1250 Da, and green standard: 28000, 9130 Da. Each sample run involved a 10 μL injection volume, a flow rate of 0.8 mL min^{-1} and followed a 7-minute method. The sample was run at a temperature of 45 $^{\circ}\text{C}$ and sent through a set of 3 columns (400 x 150 mm) with pore sizes of 45, 125 and 200 \AA . The results of these injections are represented in *Figure 2-19*.

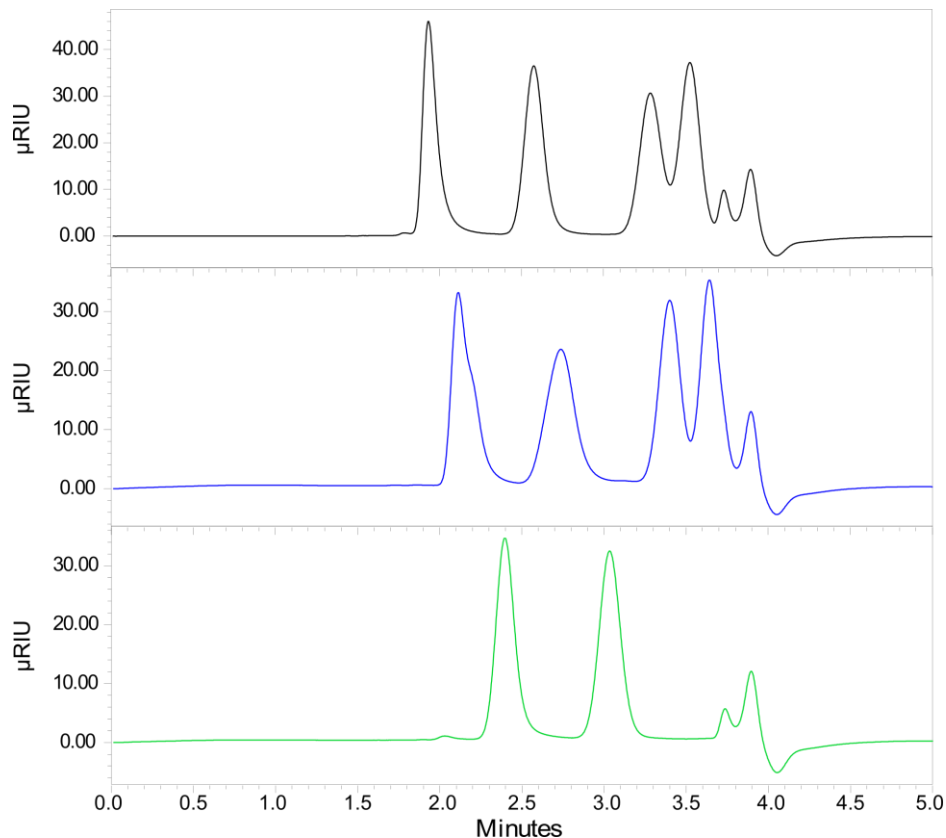


Figure 2-19 APC chromatogram of the calibration from top to bottom: black, blue and green narrow polystyrene standard samples in THF.

The calibration curve resulting log M versus retention time (or volume) could be fit to a polynomial equation, usually a third or fifth order, with the limitation that any small change in retention time outside the linear region will introduce a significant error in the determination of the molecular weight. In this case, the equation resulting for a fit order 3 as show the calibration plot and its data are summarised in *Figure 2-20* and *Table 2-8*.

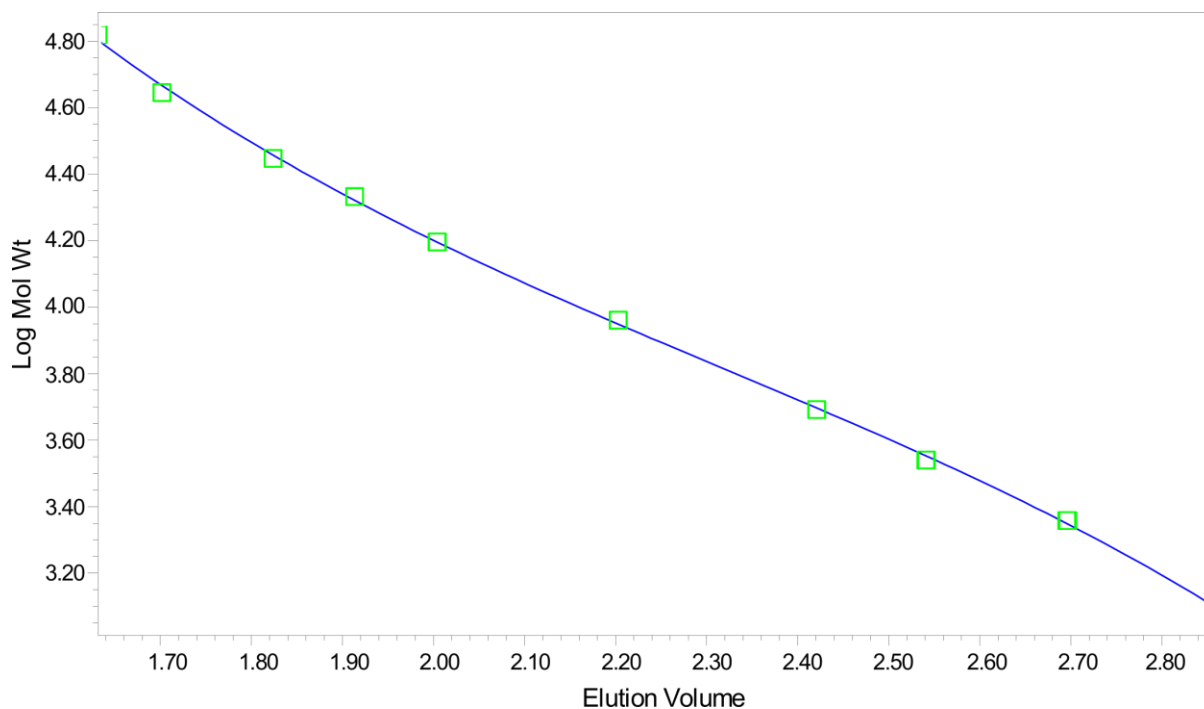


Figure 2-20 GPC polystyrene standard calibration curve, obtained using Empower2TM GPC software. The available molecular weight range is from 1250 up to 66000 Da. Fit order 3 parameters A: $1.406612e+001$, B: $-1.096512e+001$, C: $4.233476e+000$, D: $-6.086168e-001$, R: 0.999765, R²: 0.999530, V₀: 1.631452 and V_t: 2.859115.

Once the standards are analysed to probe the quality of the calibration, a white sample was injected as a broad sample to confirm if the instrument gives the result expected. For the characterisation of our material, GPC samples were prepared by dissolving the dry product (10 mg) in HPLC grade THF (2 mL). The samples were left overnight to be sure of complete dissolution. This solution was then filtered through a 0.2 μm syringe filter. In the same way than for the calibration, each sample run involved a 10 μL injection volume, a flow rate of 0.8 mL min^{-1} and followed a 7-minute method. The sample was run at a temperature of 45 $^{\circ}\text{C}$ and sent through a set of 3 columns (400 x 150 mm) with pore sizes of 45, 125 and 200 \AA . Moreover, the refractive index (RI) detector was used.

Table 2-8 GPC Calibration Table

	<i>Retention Time</i>	<i>Mol Wt</i>	<i>Log Mol Wt</i>	<i>Calculated Weight</i>	<i>Residual</i>
	(min)	(Daltons)		(Daltons)	%
1	3.263	66000	4.819544	63350	4.184
2	3.263	66000	4.819544	63417	4.073
3	3.263	66000	4.819544	63398	4.104
4	3.403	44200	4.645422	46457	-4.858
5	3.403	44200	4.645422	46436	-4.814
6	3.404	44200	4.645422	46390	-4.721
7	3.648	28000	4.447158	28667	-2.328
8	3.647	28000	4.447158	28691	-2.409
9	3.648	28000	4.447158	28669	-2.332
10	3.826	21500	4.332438	20965	2.553
11	3.827	21500	4.332438	20936	2.692
12	3.827	21500	4.332438	20957	2.589
13	4.008	15700	4.1959	15694	0.035
14	4.007	15700	4.1959	15701	-0.006
15	4.009	15700	4.1959	15672	0.176
16	4.406	9130	3.960471	8893	2.661
17	4.406	9130	3.960471	8883	2.775
18	4.406	9130	3.960471	8892	2.673
19	4.842	4920	3.691965	4973	-1.068
20	4.841	4920	3.691965	4979	-1.178
21	4.842	4920	3.691965	4976	-1.122
22	5.083	3470	3.540329	3566	-2.684
23	5.082	3470	3.540329	3569	-2.78
24	5.081	3470	3.540329	3575	-2.928
25	5.391	2280	3.357935	2236	1.983
26	5.394	2280	3.357935	2226	2.427
27	5.392	2280	3.357935	2232	2.173
28	5.717	1250	3.09691	1255	-0.378
29	5.718	1250	3.09691	1252	-0.19
30	5.718	1250	3.09691	1252	-0.193

- **Inductively coupled plasma mass spectroscopy**

Inductively coupled plasma mass spectrometry (ICP-MS) is an extremely sensitive technique. It is mainly used for heavy metal elemental analysis and directly measure trace element at very low concentrations (down to parts per quadrillion for some elements).⁴⁷ The instrument is equipped with a nebuliser, spray chamber and a plasma torch with a quartz outer body and sapphire injector. The samples are disseminated into hot argon carrier gas and derived to the plasma torch. Then a rapidly oscillating electromagnetic field passes on high kinetic energies to the ions and electrons contained in the sample. The effective temperatures of the plasma of

approximately 10,000 °K⁴⁸. All the analytes in a sample are ionised to individually charged gas ions. After this high-temperature process, the ions generated are sent through ion optics into a high vacuum, room temperature mass analyser and are measured for abundance and mass to charge ratio.⁴⁵

All the samples submitted for ICP-MS analysis were liquid samples taken straight after the RICO reaction. Both organic and aqueous phases after the solvent extraction process were submitted to the Mass Spectrometry Laboratory service of Cardiff University for full quantitative analysis. The samples were run on the Agilent Technologies 7900 ICP-MS system, complemented with an Agilent Integrated Autosampler.

- ***Fourier Transform Infra-Red Spectroscopy***

Infra-red (IR) spectroscopy is a vibrational spectroscopy technique. It is used for the identification of functional groups and structural analysis of both organic and inorganic products within a solid as well as liquid sample. Also, FTIR can also be used for measuring bond lengths and force constants of small molecules. For the measured, the sample is exposed to infrared radiation. The radiation must interact with the electric field occasioned by the change in the electrical permanent dipole moment (μ) of the molecule due to vibration to absorb IR radiation.

Molecules possess several vibrational modes depending on the number of atoms, N. The degrees of vibrational modes observed for non-linear and linear molecules are $3N - 6$ and $3N - 5$ vibrational modes respectively. The difference is due to the absence of rotation about the molecular axis in the linear molecule.⁴⁹ The types of molecular vibrations or modes are classified as stretching (change in the bond length along the line of the bond) and bending (change of bond angle). Every bond or functional group requires a different frequency of vibration for the IR absorption. Therefore, characteristic peaks are observed for each one, creating a molecular fingerprint of the sample. All IR samples were carried out using an Agilent Technologies Cary 630 FTIR instrument.

- ***High-performance liquid chromatography***

HPLC samples were prepared by transferring the sample (~10 mg) into a glass vial and dissolving it in acetonitrile (1 mL). The resulting solution was then filtered using a 0.45 μ m syringe filter and poured into an HPLC vial. The instrument used in this case is an Agilent 1200 Series HPLC fitted with a Diode Array Detector (DAD) UV detector that displays the retention

time of a compound depending on the wavelength of absorbance of the compounds. Every sample was run through a Poroshell 120 SB-C18 4.6 x 150 mm, 2.7 μm column. The Poroshell 120 packing has a solid core of 1.7 μm in size with a porous outer layer 0.5 μm thick and a total particle size of 2.7 μm . The particles have a nominal surface area of 120 $\text{m}^2 \text{g}^{-1}$ and a controlled pore size of 120 \AA . The mobile phase was made up of HPLC grade water (with dissolved phosphoric acid, 85 wt. %) and HPLC grade acetonitrile at a flow rate of 0.5 mL min^{-1} . The method used a solvent gradient, which included 30 % water and 70 % acetonitrile with a stop time of 27 minutes and posts time of 5 minutes. An injection volume of 10 μL was applied, and a constant temperature of 30 $^\circ\text{C}$ was withheld.

- ***Thin layer chromatography and Column chromatography***

Thin layer chromatography (TLC) monitoring by a UV light using a UV lamp to find the ratios of different solvent able to separate the products present in the products obtained after 2 h of RICO reaction of the hexamer.

0.77 mg of high-purity grade Silica gel, with pore size 60 \AA and 200-400 mesh particle size from Sigma Aldrich was employed to pack a Pasteur pipette that was used as a column. 24 mg of hexamer's oxidation products were mixed with 24 mg of silica, dissolved in ethyl acetate and dry under vacuum to prepare the sample to load the column.

The polarity of the eluents used in the column chromatography was increased in the order Hexane > Ethyl acetate > Acetonitrile > Methanol. Starting with pure Hexane to pack the silica properly, followed of [hexane: ethyl acetate] in increasing ratio of ethyl acetate such as [1:1], [1:2], [1:3], [1:9] and [0:1]. Then a mix of [ethyl acetate: acetonitrile] with ratio [1:1] was added, followed by just acetonitrile and then pure methanol to remove the remaining products still visible with brown colour in the column.

The fractions that showed the same products according to the TLC were combined and concentrated under vacuum in the rotary evaporator to remove all the solvent. It was dissolved in Ethyl acetate to take an aliquot for the GC-MS analysis. The remaining sample was dry under vacuum again and dissolved in deuterated chloroform for NMR studies.

2.4 References

1. Luo, W.; Sankar, M.; Beale, A. M.; He, Q.; Kiely, C. J.; Bruijninx, P. C. A.; Weckhuysen, B. M., *Nat. Commun.* **2015**, *6* (1), 6540.
2. Sankar, M.; He, Q.; Morad, M.; Pritchard, J.; Freakley, S. J.; Edwards, J. K.; Taylor, S. H.; Morgan, D. J.; Carley, A. F.; Knight, D. W.; et al., *ACS Nano* **2012**, *6* (8), 6600–6613.
3. Rosen, A., *Stud. Surf. Sci. Catal.* **1999**, *124* (C), 163–183.
4. Perry, R. .; Perry, S.; Green, D. .; Maloney, J., *Perry's Chemical Engineers' Handbook, 7th Ed.*; 1997.
5. Cao, E.; Sankar, M.; Firth, S.; Lam, K. F.; Bethell, D.; Knight, D. K.; Hutchings, G. J.; McMillan, P. F.; Gavriilidis, A., *Chem. Eng. J.* **2011**, *167* (2–3), 734–743.
6. Hill, C. G.; Wiley, J.; Charles, G. *An Introduction to Chemical Engineering Kinetics & Reactor Design*; John Wiley & Sons, Inc.: The University of Wisconsin, 1977.
7. Hilal, A. A. Microstructure of Concrete. In *High Performance Concrete Technology and Applications*; InTech, 2016; pp 3–24.
8. Niemantsverdriet, J. W. Microscopy and Imaging. In *Spectroscopy in Catalysis*; Wiley-Blackwell, 2007; pp 179–216.
9. Palisaitis, J. *Electron Energy Loss Spectroscopy of III-Nitride Semiconductors Electron Energy Loss Spectroscopy of III-Nitride Semiconductors Justinas Palisaitis*; 2015.
10. MacArthur, B. K. E., *Johnson Matthey Technol. Rev.* **2017**, *60* (2), 117–131.
11. Li, Z. Scanning Transmission Electron Microscopy Studies of Mono- and Bimetallic Nanoclusters. In *Metal Nanoparticles and Nanoalloys*; Johnston, R. L., Wilcoxon, J. P., Eds.; Frontiers of Nanoscience; Elsevier, 2012; Vol. 3, pp 213–247.
12. Niemantsverdriet, J. W. Photoemission and Auger Spectroscopy. In *Spectroscopy in Catalysis*; Wiley-Blackwell, 2007; pp 39–83.
13. Andoni, a. A Flat Model Approach to Ziegler-Natta Olefin Polymerization Catalysts, Eindhoven University of Technology, 2009.
14. Leofanti, G.; Padovan, M.; Tozzola, G.; Venturelli, B., *Catal. Today* **1998**, *41* (1–3), 207–219.
15. Thommes, M.; Kaneko, K.; Neimark, A. V.; Olivier, J. P.; Rodriguez-Reinoso, F.; Rouquerol, J.; Sing, K. S. W., *Pure Appl. Chem.* **2015**, *87* (9–10), 1051–1069.
16. Sing, K. S. W., *Pure Appl. Chem.* **1982**, *54* (11).
17. Anovitz, L. M.; Cole, D. R., *Rev. Mineral. Geochemistry* **2015**, *80* (1), 61–164.
18. Giesche, H., *Advances in Process Measurements for the Ceramic Industry*. 1999, pp 69–86.
19. Ismail, I. M. K., *Langmuir* **1992**, *8* (2), 360–365.
20. Hwang, N.; Barron, A. R. BET Surface Area Analysis of Nanoparticles. In *Nanomaterials and Nanotechnology*; 2011.
21. Lónyi, F.; Valyon, J., *Microporous Mesoporous Mater.* **2001**, *47* (2–3), 293–301.
22. Rakić, V.; Damjanović, L. Temperature-Programmed Desorption (TPD) Methods. In *Calorimetry and Thermal Methods in Catalysis*; Auroux, A., Ed.; Springer Berlin Heidelberg: Berlin, Heidelberg, 2013; pp 131–174.
23. Jin, F.; Fan, Y. C.; Wu, G.; Yuan, M., *React. Kinet. Mech. Catal.* **2018**, *123* (2), 517–527.
24. Farahani, S. H.; Alavi, S. M.; Falamaki, C., *RSC Adv.* **2017**, *7* (54), 34012–34022.

25. Zou, B.; Ren, S.; Ye, X. P., *ChemSusChem* **2016**, 9 (23), 3268–3271.
26. Supamathanon, N.; Wittayakun, J.; Prayoonpokarach, S.; Supronowicz, W.; Roessner, F., *Quim. Nova* **2012**, 35 (9), 1719–1723.
27. Zhang, Y.; Su, Q.; Wang, Z.; Yang, Y.; Xin, Y.; Han, D.; Yang, X.; Wang, H.; Gao, X.; Zhang, Z., *Chem. Eng. Technol.* **2008**, 31 (12), 1856–1862.
28. Bao, Q.; Zhu, W.; Yan, J.; Zhang, C.; Ning, C.; Zhang, Y.; Hao, M.; Wang, Z., *RSC Adv.* **2017**, 7 (82), 52304–52311.
29. Chow, Y. K.; Dummer, N. F.; Carter, J. H.; Williams, C.; Shaw, G.; Willock, D. J.; Taylor, S. H.; Yacob, S.; Meyer, R. J.; Bhasin, M. M.; et al., *Catal. Sci. Technol.* **2017**, 8, 154–163.
30. Mitchell, M. B. *Fundamentals and Applications of Diffuse Reflectance Infrared Fourier Transform (DRIFT) Spectroscopy*; 1993; pp 351–375.
31. Colthup, N. B.; Daly, L. H.; Wiberley, S. E. *Introduction to Infrared and Raman Spectroscopy*; Academic Press, 1990.
32. Hooijschuur, J. H.; Verkaaik, M. F. C.; Davies, G. R.; Ariese, F., *Geol. en Mijnbouw/Netherlands J. Geosci.* **2016**, 95 (2), 141–151.
33. El-Said, W. A.; Cho, H.-Y.; Choi, J.-W. SERS Application for Analysis of Live Single Cell. In *Nanoplasmonics - Fundamentals and Applications*; InTech, 2017; Vol. i, p 13.
34. Gilles, R.; Mukherji, D.; Hoelzel, M.; Strunz, P.; Toebbens, D. M.; Barbier, B., *Acta Mater.* **2006**, 54 (5), 1307–1316.
35. Lancefield, C. S.; Ojo, O. S.; Tran, F.; Westwood, N. J., *Angew. Chem. Int. Ed. Engl.* **2015**, 54 (1), 258–262.
36. Forsythe, W. G.; Garrett, M. D.; Hardacre, C.; Nieuwenhuyzen, M.; Sheldrake, G. N., *Green Chem.* **2013**, 15 (11), 3031.
37. Akahashi, N. T.; Ashimoto, M. H.; Sukagoshi, K. T., *Japan Soc. Anal. Chem.* **2013**, 29, 665–667.
38. Carlsen, P. H. J.; Katsuki, T.; Martin, V. S.; Sharpless, K. B., *J. Org. Chem.* **1981**, 46 (19), 3936–3938.
39. Glasel, J. A.; Deutscher, M. P. *Introduction to Biophysical Methods for Protein and Nucleic Acid Research*; Academic Press, 1995.
40. James, T. L. *Fundamentals of NMR*; Department of Pharmaceutical Chemistry, University of California: San Francisco, CA 94143-0446 U.S.A. 1.1, 1998; pp 1–31.
41. Lindon, J. C.; Tranter, G. E.; Koppenaal, D. W. *Encyclopedia of Spectroscopy and Spectrometry*, 3rd Editio.; Academic Press, 2017.
42. Hoffman, R. E., *Magn. Reson. Chem.* **2006**, 44 (6), 606–616.
43. Claridge, T. D. W. *High-Resolution NMR Techniques in Organic Chemistry*; Elsevier, 2016.
44. Pu, Y.; Cao, S.; Ragauskas, A. J., *Energy Environ. Sci.* **2011**, 4 (9), 3154.
45. Waters 2414 Refractive Index Detector Operator's Guide 715003806 / Revision A. 2012.
46. Young, R. J.; Lovell, P. A. *Introduction to Polymers*; Springer US: Boston, MA, 1991.
47. Nasirian, H.; Nasirian, Z.; Sadeghi, S. M. T., *Int. J. Entomol. Res.* **2014**, 47.
48. Batsala, M.; Chandu, B.; Sakala, B.; Nama, S.; Domatoti, S. Inductively coupled plasma mass spectrometry. *IJRPC* 2012 (3).
49. Harris, D. C., *J. Mol. Struct.* **1980**, 62, 301.

CATALYTIC CONVERSION OF BIOMASS

CHAPTER 3. RUTHENIUM BASED BIMETALLIC CATALYSTS FOR SELECTIVE GLYCEROL HYDROGENOLYSIS.

S. Guadix-Montero
CARDIFF UNIVERSITY | CARDIFF CATALYSIS INSTITUTE

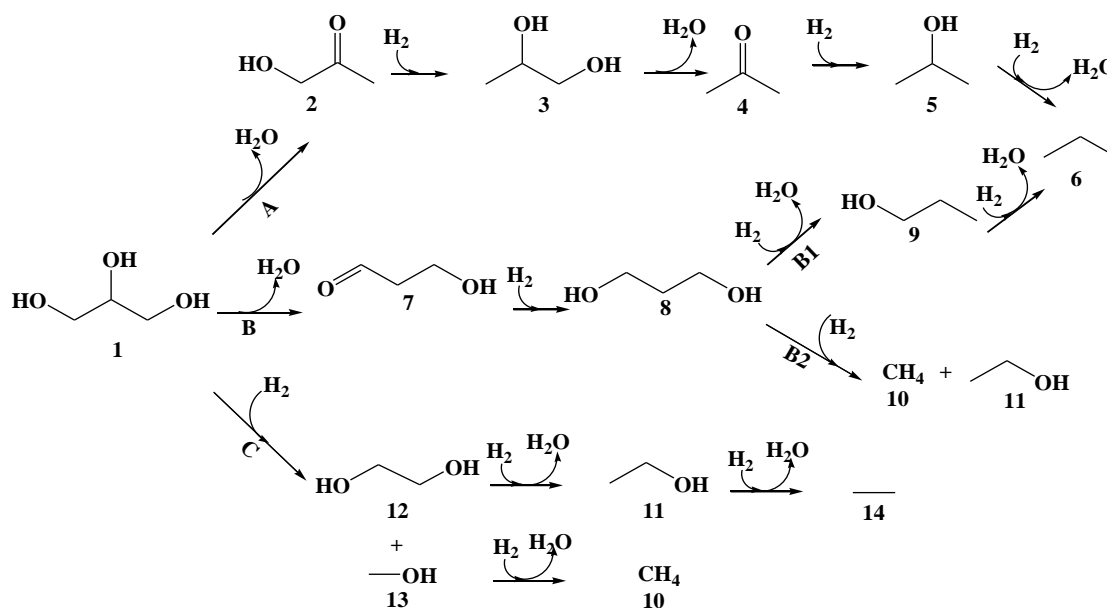
Contents

3	Ruthenium-based bimetallic catalyst for selective glycerol hydrogenolysis.....	116
3.1	Introduction.....	116
3.1.1	Batch reactor.....	118
	• Catalytic activity.....	118
	• Energy profiles.....	123
	• Kinetic studies.....	126
	• Role of heat treatment and metal oxidation state study.....	134
3.1.2	Continuous fixed bed reactor.....	140
	• Effect of the in-situ reduction in the fixed bed reactor.....	142
3.1.3	Catalyst characterisation by electron microscopy.....	144
3.2	Conclusions.....	148
3.3	References.....	150

3 Ruthenium-based bimetallic catalyst for selective glycerol hydrogenolysis

3.1 Introduction

Hydrogenolysis of organic compounds is the breaking of intermolecular bonds using H_2 to form C-H and H-X. This process is an important strategy to valorise biorenewable feedstock. It is an alternative to the conventional fossil fuel-based feedstock leading to the production of fine chemicals and fuels as a green and sustainable process.^{1,2} Glycerol is a saturated compound generated as a by-product of biodiesel production. It has a high O/C ratio and, hence, the hydrogenolysis is the preferred strategy to transform this bulk material, identified by the US DoE, into high-value compound(s).³ Several valorisation routes such as selective oxidation or hydrogenolysis, dehydration and many others have been reported on glycerol conversion.⁴⁻⁸ Among these routes, hydrogenolysis of glycerol to C3 chemicals, such as propanediols (PDOs) has received considerable attention owing to their huge commercial importance.^{6,9-11} 1,2-propanediol (1,2-PDO) is the raw material for the industrial production of unsaturated polyester resins, food additives, paints, cosmetics, liquid detergents, print ink, plasticisers, antifreeze, de-icing and as heat transfer fluid.^{12,2} Currently, PDOs are produced either by a chlorohydrin process or a hydroperoxide process involving propylene oxide derived from fossil fuel-based feedstock.^{13,14} Hence, the development of an active, selective and stable catalyst to produce propanediols *via* the hydrogenolysis of glycerol is crucial to the development of novel green and sustainable processes. *Scheme 3-1* shows different hydrogenolysis pathways of glycerol: dehydration (paths **A** and **B**) and C-C bond cleavage (pathway **C**). Note that 1,3-Propanediol (1,3-PDO) is the most attractive target in the conversion of glycerol due to its high price and large demands.^{9,15} However, this commodity is generated through the 3-hydroxypropionaldehyde (3-HPA), which is an unstable intermediate of the dehydration pathway **B**, and the reaction may proceed to further hydrogenation.



Scheme 3-1. Schematic representation of the glycerol hydrogenolysis reaction pathways, A) Dehydration, B) Dehydration and C) Degradation. Compounds are labelled as: 1) glycerol, 2) acetol, 3) 1,2-propanediol, 4) acetone, 5) 2-propanol, 6) propane, 7) 3-hydroxypropanaldehyde, 8) 1,3-propanediol, 9) 1-propanol, 10) methane, 11) ethanol, 12) ethylene glycol, 13) methanol, 14) ethane. Adapted from Ref.^{16, 17}

For the hydrogenolysis of glycerol, many transition metal (Ru, Rh, Re, Pt, Pd, Ir, Ag, Cu, Co and Ni) catalysts have been reported.^{7,18–20} During this reaction, the selectivity of PDOs is controlled by the selectivity of C-O bond cleavage over C-C bond cleavage. Disruption of the C-C bond leads to the formation of in C2 (ethylene glycol, ethanol) and C1 (methanol and methane) products. For different metals, the selectivity of C-O bond cleavage follows the order Ru < Rh < Pt < Pd < Cu.²¹ However, the reverse order has been reported for the hydrogenolysis via the C-C bond cleavage as follows Ru ≈ Cu ≈ Ni > Pt > Pd¹⁷ or Ru >>> Rh > Pt > Pd.^{16,22} Hence it is challenging to design a catalyst that could achieve the maximum activity with the highest PDOs selectivity. Non-noble metal catalyst such as Cu suffer of deactivation during glycerol hydrogenolysis, reason why Ru is preferred over Cu. Deactivation is attributed to Cu sintering.²³

Since Sinfelt *et al.* first introduced the use of bimetallic catalysts for reforming reactions,^{24,25} several research groups have developed many bimetallic catalysts for a variety of organic transformations.^{26–29} Addition of second metal to a primary metal to form bimetallic nanoparticles can hugely influence the catalytic properties such as activity, selectivity and/or stability of supported monometallic catalysts.^{30,31} Hutchings and co-workers have reported the

superiority of bimetallic AuPd catalysts for several reactions including direct synthesis of hydrogen peroxide,³² solvent-free oxidation of primary alcohols³³ and selective oxidation of glycerol.³⁴ For instance, Falcone *et al.* reported the beneficial nature of the bifunctional bimetallic PtRe catalyst to increase the selectivity of 1,3-PDO.³⁵ Initially, these authors improved the rate of glycerol hydrogenolysis, adding HCl for the monometallic 8 wt. % Pt/SiO₂ catalyst. This resulted in an increase of the turnover frequency (TOF) from $4.2 \times 10^{-6} \text{ s}^{-1}$ to $5.5 \times 10^{-5} \text{ s}^{-1}$ at very low conversion. However, after the incorporation of Re, a TOF of 0.0105 s^{-1} was observed using the bimetallic catalyst with HCl. For the same reaction, Sun *et al.* reported that adding Zn to Pd/ZrO₂ catalyst, the catalytic activity could be increased substantially.²¹ For instance, the turnover rate of monometallic Pd/m-ZrO₂ catalyst was of $11.1 \text{ mol}_{\text{glycerol}} (\text{mol}_{\text{surfacePd}} \cdot \text{ks})^{-1}$ and by adding Zn to this catalyst, this turnover rate was increased to $119.5 \text{ mol}_{\text{glycerol}} (\text{mol}_{\text{surfacePd}} \cdot \text{ks})^{-1}$. More recently, Luo *et al.* reported that for the hydrogenolysis of levulinic acid (LA) to *gamma*-valerolactone (GVL) bimetallic AuPd catalyst (TOF 0.1 s^{-1}) to be several folds more active than the monometallic Au and Pd catalysts (Au, TOF 0.004 s^{-1} and Pd, TOF 0.005 s^{-1}).³⁶ In the same work, the authors further stated that by adding Pd to Ru the most active and unselective Ru/TiO₂ catalyst could be transformed to a slightly less active, but highly selective catalyst. These authors proposed that Pd metal selectively poisons or blocks the most active (unselective) sites of monometallic Ru catalysts.³⁶

For the conversion of glycerol to PDOs, the critical challenge is to develop an active and selective catalyst for C-O bond cleavage.³⁷ In this chapter is described how Ru-based bimetallic catalysts are reducing the C-C bond cleavage during glycerol hydrogenolysis. PdRu and PtRu supported on TiO₂ were tested in different reactor configuration, both batch and fixed bed reactors to study their relative stabilities. Based on spectroscopic and microscopic characterisation data of the monometallic and bimetallic catalysts, a structured activity correlation has been attempted in this chapter.

3.1.1 *Batch reactor*

- *Catalytic activity*

The catalysts tested were prepared using a modified impregnation method. This method is preferred for controlling the metal particle size as well as the composition of the bimetallic particles.³⁸ Monometallic Pd, Ru, Pt and bimetallic PdRu, PtRu nanoparticles supported on TiO₂ catalysts were prepared with a 2 wt.% metal loading. For bimetallic catalysts, a 1:1 molar ratio of the two metals was established. Moreover, the two monometallic catalysts were physically mixed, i.e. Pt+Ru and Pd+Ru. In order to maintain equal metal loadings as the

bimetallic catalyst, the same number of metals mols was used. For physically mixed catalyst, two monometallic catalysts were loaded as follows: Pt+Ru (0.3209 g of 2 wt.% Pt/TiO₂ + 0.1647 g of 2 wt.% Ru/TiO₂) and Pd+Ru (0.1735g of 2 wt.% Pd/TiO₂ + 0.1647g of 2 wt.% Ru/TiO₂). All these catalysts were tested for the hydrogenolysis of glycerol with glycerol to metal molar ratio equal to [1:0.005]. *Figure 3-1* shows the catalytic results are of the reaction conditions were fixed at 800 rpm, 165 °C, under 20 bar of H₂ pressure for 16 h. *Figure 3-1A* represent the selectivity product distribution based carbon content C1, C2 and C3 of the compound molecule, while *Figure 3-1B* exhibit the yield obtained for each catalyst. Blank reactions corresponding to the hydrogenolysis of glycerol without catalysts were also carried out under the same conditions.

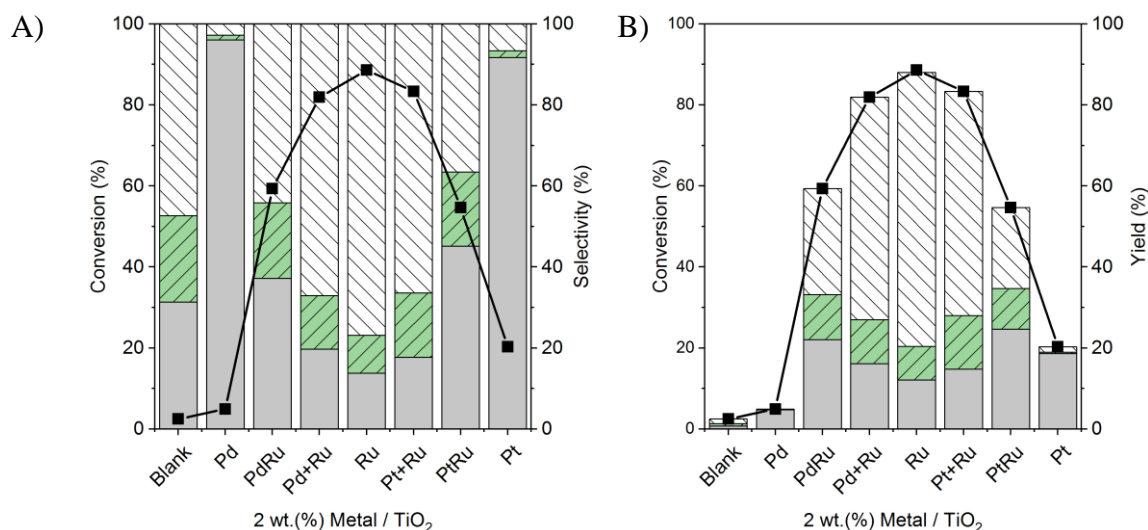



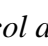

Figure 3-1 Comparison of catalytic activities of supported monometallic and bimetallic (2 wt. % Pd, Pt, Ru, PdRu, and PtRu on TiO₂) nanoparticles for the hydrogenolysis of glycerol in an autoclave batch reactor. Note that PdRu and PtRu correspond to the bimetallic nanoparticles, while Pd+Ru and Pt+Ru correspond to physically mixed two monometallic catalysts. Conversion of glycerol (-■-). A) Selectivity and B) Yield of products classified as C1 () methanol, methane and carbon dioxide), C2 () ethanol, ethylene glycol and ethane), C3 () acetol, 1,2-propanediol, acetone, 2-propanol, propane, 1,3-propanediol and 1-propanol). Reaction conditions: temp: 165 °C; time: 16 h; p_{H2}: 20 bar, stirring speed: 800 rpm; glycerol to metal molar ratio [1: 0.005].

Figure 3-1 shows that for the blank reactions no products are formed in a significant amount, less than 2 % of glycerol conversion. As expected, this result confirms that an active metal site of the catalyst is needed to promote the reaction. For the catalytic reactions, the data visibly

indicate that the activity of monometallic catalysts for the hydrogenolysis activity follows the trend Ru \gg Pt $>$ Pd. This is in good agreement with the previous reports.^{9,22} The glycerol conversion achieved was of 89, 20 and 5 %, respectively. However, the selectivity into C3 products seems to follow the reverse order. Above 90 % of C3 selectivity for both Pd and Pt and only 14 % for the Ru monometallic was reached. The cleavage of the C-O bond of glycerol produces C3 useful bulk chemicals, (acetol, 1,2-propanediol, acetone, 2-propanol, propane, 1,3-propanediol and 1-propanol).¹² Although the mechanism route (C), through C-C bond cleavage, leads to degradation products such as C2 products (ethanol, ethylene glycol and ethane) and even formation of C1 products (methanol, methane and carbon dioxide).³⁹

When Pd or Pt monometallic catalyst are mixed physically with the monometallic Ru catalyst, the selectivity into C3 increases (from 14 % to *c.a.* 20 % in both cases). Though it is when the bimetallic catalysts are used a two-fold increase in C3 selectivity was achieved, around 37 % and 45 % for bimetallic PdRu and PtRu catalysts respectively. *Table 3-1* and *Table 3-2* reports the selectivity and the carbon mass balance data of the different products obtained in these experiments are explained in detail later on. Roy *et al.* proposed the synergistic effect of the admixture 5 wt. % Pt and Ru catalysts supported on Al₂O₃ over individual Pt and Ru catalyst for glycerol hydrogenolysis (under 14 bar of N₂ atmosphere and without gaseous H₂).⁴⁰ In this work, the authors concluded that the optimum glycerol conversion and C3 product selectivity were obtained with 1:1 Ru: Pt admixture catalyst.

Ru monometallic gave the highest yield to degradation products (C1+C2) (*ca.* 75 %), which is followed by the physically mixed catalyst (66-68 %). However, both bimetallic catalysts decrease by half the C-C bond cleavage, reporting only 30 and 37 % of C1+C2 yield (see *Table 3-1* and *Figure 3-1*). It is evident that the bimetallic catalysts are more selective towards C-O bond cleavage (C3 compounds). These C3 products are mainly 1,2-PDO with selectivity equally to 50 % of the total products.

In contrast, the physical mixture of Ru+Pd and Ru+Pt catalysts functioned like Ru monometallic catalyst. Indeed, it is much closer to the latter than to their corresponding nanoalloy catalyst. This fact is expected since both Pd and Pt monometallic were significantly less active than Ru monometallic catalyst. In the admixture, a fraction of Ru is substituted by either Pd or Pt monometallic to keep the total metal loading, which could be the reason for the slight decrease in conversion. This behaviour is in agreement with the previous work for the case of PtRu/C by Maris *et al.*⁴¹

The predominant pathway that takes place when Ru monometallic catalyst was used could be: 1) pathway **C**, glycerol degradation via C-C bond cleavage; 2) pathway **B2**, which also leads to the C-C bond cleavage after dehydration of glycerol to 3-hydroxypropionaldehyde and hydrogenation to 1,3-PDO (see *Scheme 3-1*). The almost full conversion of glycerol was achieved because of the gas products formation. Compounds such as methane, ethane, propane and CO₂ are obtained, which is in agreement with the literature when using various Ru catalyst.⁴²⁻⁴⁴

On the other hand, Pd and Pt monometallic catalyst on TiO₂ gave conversions of *ca.* 5 % and 20 %, respectively, and low 1,2-PDO yield. Nevertheless, they gave a higher percentage of liquid products (*ca.* 86-97 % of carbon balance in liquid phase products, see *Figure 3-2*). In this respect, it has been reported that 3 wt. % Pt/TiO₂ catalyst is highly selective through C3 products, achieving a 62 % and 75 % under 60 bar of N₂ and H₂ pressure respectively and 210 °C.⁴⁵

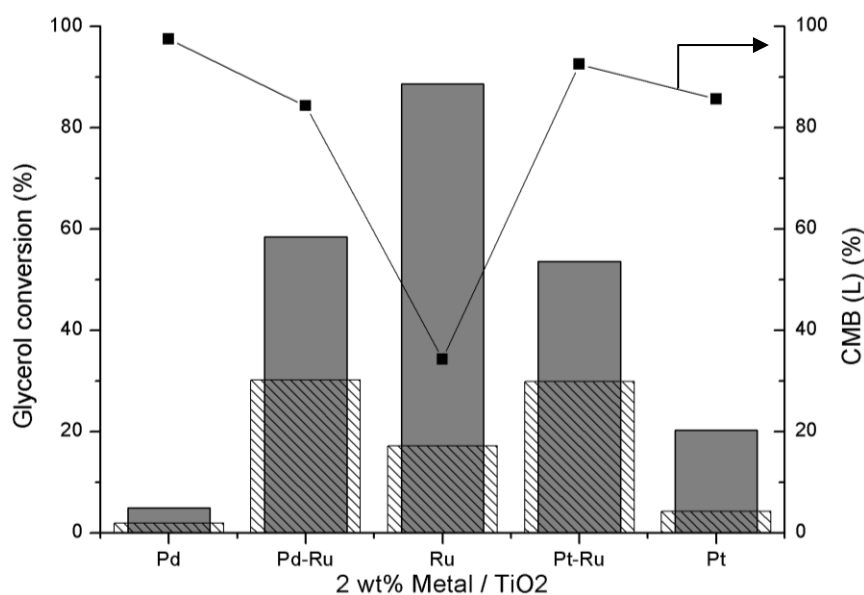


Figure 3-2 Comparison of the glycerol conversion (■) vs yield of 1,2-PDO (▨) and carbon mass balance of liquid products (-■-) of the 2 wt. % PdRu, Ru, PtRu on TiO₂. Reaction carried out in a batch autoclave for 16 h at 165 °C, 20 bar H₂, 800 rpm, with a molar ratio glycerol vs metal in the catalyst of [1:0.005].

Based on the result presented in this work, bimetallic catalysts are the best choice for this reaction. These nanoalloy catalysts gave a relatively high glycerol conversion, typically above 50 % in both cases (PdRu and PtRu). Moreover, using bimetallic, the C-C bond cleavage was suppressed (approx. 50 % less than the monometallic Ru). Consequently, bimetallic catalysts

produce an improvement in the yields for C3 products (Summarised in *Table 3-1* and *Table 3-2*).

Table 3-1 Conversion, selectivity data and yield base on the C1, C2, C3 products

2 wt. % metal	Conversion (%)	Selectivity (%)			Yield (%)			Total Carbon Mass Balance (%)
		C1	C2	C3	C1	C2	C3	
Blank	2	47	21	31	1	1	1	97
Pd	5	3	1	96	0	0	5	98
PdRu	58	44	19	37	26	11	22	100
Pd+Ru	82	67	13	20	55	11	16	67
Ru	89	77	9	14	68	8	12	81
Pt+Ru	83	66	16	18	55	13	15	69
PtRu	54	37	18	45	20	10	25	100
Pt	20	7	2	92	1	0	19	86

*Selectivity of products labelled as C1 (methanol, methane and carbon dioxide), C2 (ethanol, ethylene glycol and ethane), C3 (acetol, 1,2-propanediol, acetone, 2-propanol, propane, 1,3-propanediol and 1-propanol). Note that PdRu and PtRu correspond to the bimetallic nanoparticles, while Pd+Ru and Pt+Ru correspond to physically mixed two monometallic catalysts. Reaction conditions: temp: 165 °C; time: 16 h; p_{H₂}: 20 bar; stirring speed: 800 rpm; glycerol to metal molar ratio: [1:0.005].

Table 3-2 Conversion, selectivity and carbon mass balance of liquid products

2 wt. % metal	Conversion (%)	Products Selectivity (%)													CMB(L) (%)
		Acetone	MeOH	EtOH	2-PO	1-PO	Acetol	1,2-PDO	EG	1,3-PDO	CO ₂	CH ₄	C ₂ H ₆	C ₃ H ₈	
Blank	2	0	0	4	0	0	19	30	17	0	17	9	3	2	99
Pd	5	3	0	1	0	10	5	80	0	0	1	0	0	0	97
PdRu	58	0	1	3	2	4	0	50	13	1	0	22	4	1	84
Pd+Ru	82	1	2	1	6	1	1	28	10	0	0	42	6	1	44
Ru	89	0	1	1	1	0	0	26	6	0	2	53	7	2	34
Pt+Ru	83	0	2	7	7	1	1	25	8	0	0	42	6	2	44
PtRu	54	0	1	6	8	9	0	46	8	0	0	17	4	2	93
Pt	20	0	1	1	15	10	1	69	0	0	2	0	0	1	86

*Selectivity of products labelled as: Acetone, Methanol (MeOH), Ethanol (EtOH), 2-Propanol (2-PO), 1-Propanol (1-PO), Acetol, 1,2-Propanediol (1,2-PDO), Ethylene glycol (EG) and 1,3-Propanediol (1,3-PDO), CO₂, Methane (CH₄), Ethane (C₂H₆), Propane (C₃H₈). Note that PdRu and PtRu correspond to the bimetallic nanoparticles, while Pd+Ru and Pt+Ru correspond to physically mixed two monometallic catalysts. Reaction conditions: temp: 165 °C; time: 16 h; p_{H₂}: 20 bar; stirring speed: 800 rpm; glycerol to metal molar ratio: [1:0.005].

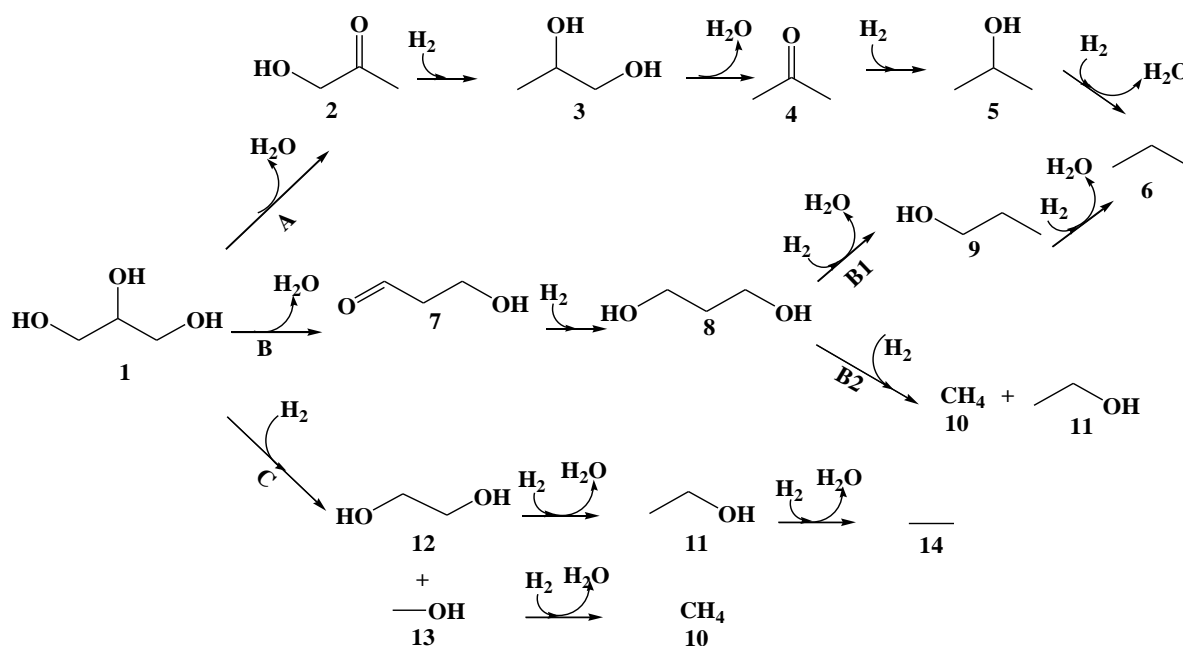
The catalytic activities results are within an experimental error limit of $\pm 5\%$, (determined from the standard deviation of 5 reactions tested). This shows a good reproducibility of both the catalyst preparation and catalyst testing.

- **Energy profiles**

To understand the catalytic behaviour of bimetallic systems and the energetically favourable reaction pathway, computational studies were done for this system. This study focuses on linking structure and energy using approximated solutions to the electronic Schrödinger equation.⁴⁶ Thanks to the knowledge in this field of our collaborator Dr A. Roldan from Cardiff University, it has been found the relative energies of the species along with the mechanisms in *Scheme 3-1*. *Figure 3-3* shows the thermodynamic energy profiles obtained for both alloys and pure Ru catalyst for both hcp and fcc structures. Ru is generally stable in hcp form; despite of its meta-stability Ru nanoparticles can be found also in fcc. The initial state corresponds to an initial “gas phase” and clean surface, used as a reference. It is important to evaluate how strong the molecules interact with the surface in the next step. For the model it was considered nanoparticles of at least 2 nm and therefore TiO₂ effect is insignificant in the electronic structure of the nanoparticles. The nanoparticles were simulated as extended surfaces, to discard the low coordinated sites.

The computed energy profiles for both alloys and pure Ru (fcc) are similar. The result further suggests that the dehydration pathway **B** involving the intermediate 3-hydroxypropanaldehyde is favoured (see *Scheme 3-1*). Note that **B1** is not shown because it proceeds through an endothermic path compared to **B2**. Despite, the hydrogenation of 3-hydroxypropanaldehyde (7) is endothermic and hinders pathway **B**. It was not detected in solution, according to the energy profile, it could be strongly adsorbed. Indeed, the next step of pathway **B** requires of high energy, reason why it is unlikely to occur. Thus, while pathway **B** is preferable in situations of energy conservation, pathways **A** and **C** are downhill and therefore competing with **B**. The products found to correspond to the downhill routes (mainly pathways **A** and **C**). Indeed, the surface intermediate 1,3-propanediol (8) from pathway **B** has higher relative energy than 1,2-propanediol and ethanol from pathways **A** and **C**, (see *Figure 3-3*).

Pure Ru nanoparticles may grow in hcp structure (as the bulk). It was also studied the effect of the crystal structure and found that Ru-hcp largely stabilises acetol, following a pathway more favourable than **B**, pathway **C**.



Scheme 3-1. Schematic representation of the glycerol hydrogenolysis reaction pathways, A) Dehydration, B) Dehydration and C) Degradation. Compounds are labelled as: 1) glycerol, 2) acetol, 3) 1,2-propanediol, 4) acetone, 5) 2-propanol, 6) propane, 7) 3-hydroxypropanaldehyde, 8) 1,3-propanediol, 9) 1-propanol, 10) methane, 11) ethanol, 12) ethylene glycol, 13) methanol, 14) ethane. Adapted from Ref.^{16, 17}

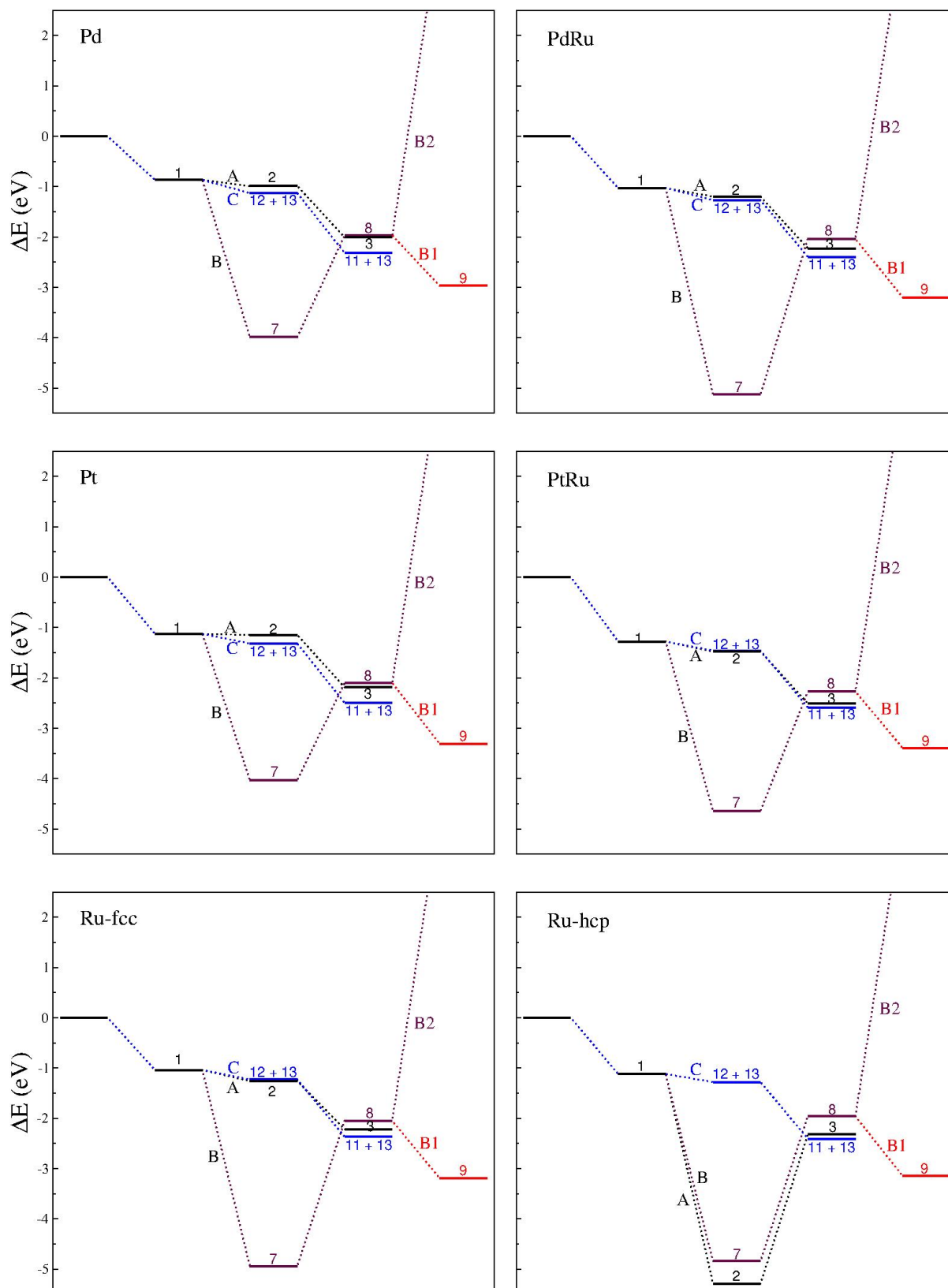


Figure 3-3 Energy profiles for the dehydration (A and B) and C-C cleavage (C) mechanisms on Pd and PdRu (top), Pt and PtRu (centre) and Ru both fcc and hcp (down). Numbers inset indicates the adsorbed species according to Scheme 3-1.

- **Kinetic studies**

Kinetic studies of the monometallic Ru and bimetallic PdRu and PtRu catalysts were performed in the batch reactor. *Figure 3-4* presents the results in terms of conversion, total carbon mass balance (including all liquid and gas products labelled as CMB(L+G)).

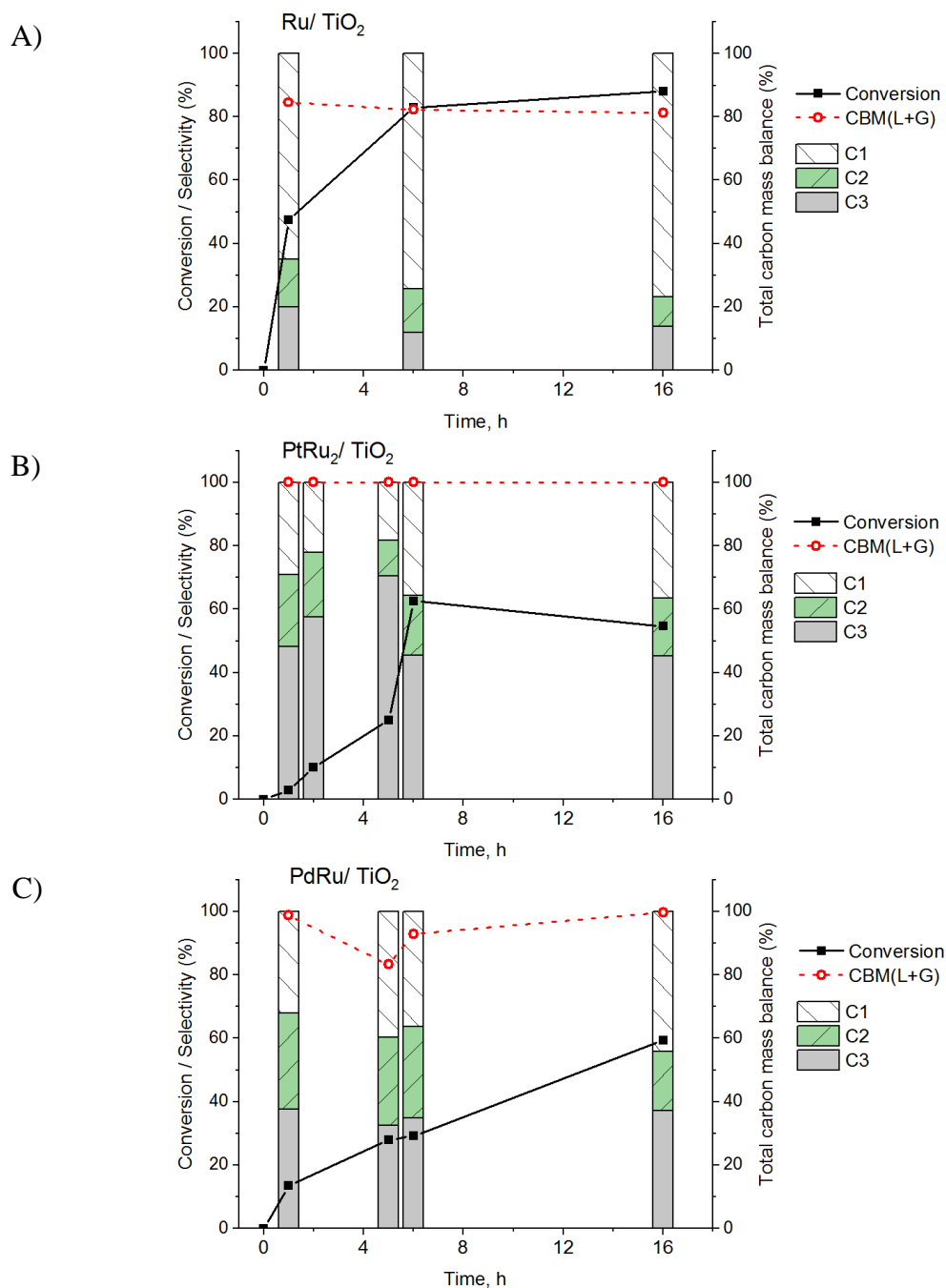


Figure 3-4 Kinetic studies for the 2 wt % of A) Ru, B) PtRu, and C) PdRu supported in TiO₂ at 165 °C; p_{H₂}: 20 bar; 800 rpm; glycerol to metal molar ratio of [1:0.005]. Conversion, total carbon mass balance (L+G) and selectivity of products labelled as C1 (methanol, methane and carbon dioxide), C2 (ethanol, ethylene glycol and ethane), C3 (acetol, 1,2-propanediol, acetone, 2-propanol, propane, 1,3-propanediol and 1-propanol).

Figure 3-5 illustrates the gas phase composition, with an apparent increase in methane selectivity with time. Detailed individual product distributions for these reactions are presented in Table 3-3.

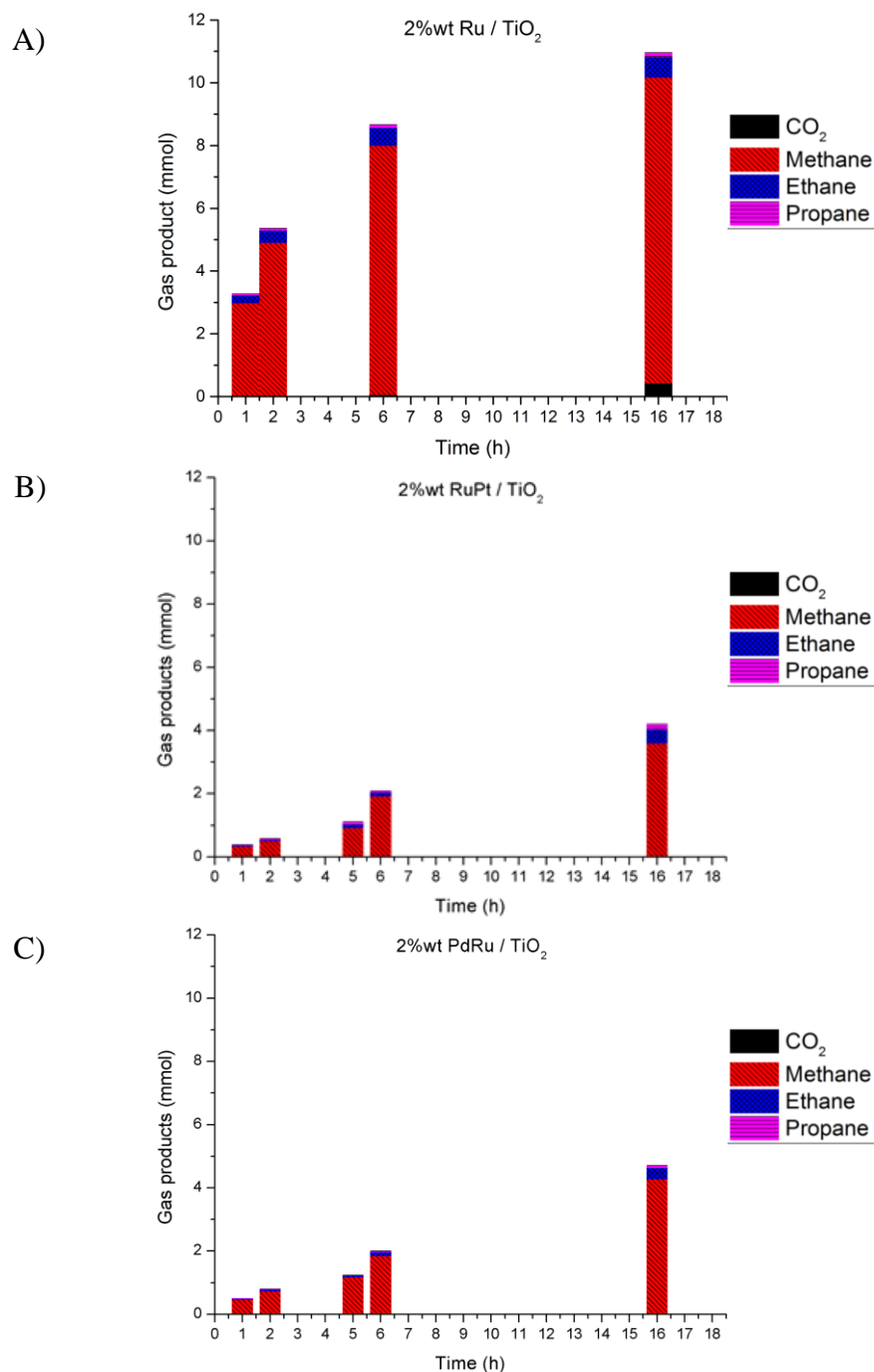


Figure 3-5 Time online results of the gas phase product distribution at the different reaction times tested for the 2 % wt. A) Ru, B) PtRu and C) PdRu on TiO₂ catalyst. Reaction carried out in a batch autoclave at 165 °C, 20 bar H₂, 800 rpm, with a glycerol vs metal molar ratio of [1:0.005].

Table 3-3 Product distribution and carbon mass balance of liquid product CMB (L) versus total carbon mass balance CMB (L+G).

2% wt. Metal	Time (h)	Conversion	Products Selectivity (%)													CMB(L) (%)	CMB(L+G) (%)
			Acetone	MeOH	EtOH	2-PO	1-PO	Acetol	1,2-PDO	EG	1,3-PDO	CO ₂	CH ₄	C ₂ H ₆	C ₃ H ₈		
Ru	1	47	0	3	5	2	7	0	26	8	2	0	39	7	2	68	84
	6	83	0	2	2	1	1	0	21	11	0	0	51	7	2	41	82
	16	88	0	1	1	1	0	0	26	6	0	2	53	7	2	36	81
PtRu	1	3	0	1	3	4	10	0	39	16	11	0	12	2	2	98	100
	2	10	0	1	3	4	11	0	44	13	13	0	9	2	2	97	100
	5	25	0	0	1	16	13	0	42	6	11	0	7	2	2	97	100
	6	45	0	1	5	4	11	0	40	10	8	0	16	3	2	87	100
	16	55	0	1	6	8	9	0	46	8	0	0	17	4	2	81	100
PdRu	1	13	0	1	2	2	7	0	40	25	5	0	14	2	1	96	99
	5	28	2	2	0	9	5	0	34	27	0	0	19	2	1	80	83
	6	29	0	2	1	0	7	0	44	26	0	0	17	2	1	89	93
	16	59	0	1	3	2	4	0	50	13	1	0	22	4	1	82	100

The results show that the monometallic Ru/TiO₂ catalyst displayed the highest glycerol conversion of 47 % in only 1 h, and over 80 % in 6 hours (*Figure 3-4*). However, most of the products are in gas-phase (selectivity CH₄: 51 %; 1,2-PDO: 21 %; EG :11 % and C₂H₆: 7 %). This would agree with the downhill pathways **C** in Ru-hcp. Among the liquid products, 1,2-PDO is the most selective product (*ca.* 26 % at 1 and the same at 16 hours of reaction). It is followed by EG with a selectivity of 11 % at 6 hours but decreasing to 6 % at 16 h. From 1 to 16 h, the CMB(L) decreases from *ca.* 75 % down to 35 %, because of the formation of gaseous products. This effect is shown in *Figure 3-5-A*. This data suggests that very quickly, monometallic Ru catalyst promotes C-C bond cleavage *via* pathway **C** (*Scheme 3-1*). At early reaction time, the EG is dehydrated to ethane, and also the methanol is converted to CH₄. The last one represents approximately 85 % of the gaseous products at each reaction time and more than 50 % of total selectivity after 6 h.

The incorporation of the second metal (Pt or Pd) to Ru catalyst increased substantially the selectivity towards C-O cleavage. The bimetallic catalysts suppressed the C-C cleavage resulting in an increase in the yields of C3 products. Shastri *et al.* proposed that a similar phenomenon could be explained with a geometric dilution effect of the active Ru surface ensembles by inactive Au in their RuAu/SiO₂ catalyst.⁴⁷ Other authors have worked under this hypothesis for RuAu,⁴⁸ RuCu^{49,50} and RuRe systems.⁵¹ Salazar *et al.* reported that the

incorporation of Cu into Ru-base catalyst supported on TiO₂ increases the 1,2-PDO selectivity from 48 to 69 %. This was accompanied by a decrease in EG selectivity from 41 to 25 %. They achieved conversions of glycerol between 19 and 10 % using as reaction conditions: 20 wt. % aqueous glycerol solution, T = 200 °C; H₂ pressure = 2.5 MPa; 0.6 g of catalyst; during reaction time: 1 h. RuRe bimetallic catalysts possess less selectivity to degradation products than Ru monometallic catalysts due to the synergistic effect of Ru and Re on TiO₂ revealed by Ma *et al.* In this case, the bimetallic catalyst showed higher activity, with 36 % conversion for the RuRe/TiO₂ and only a 6% for the Ru/TiO₂. This is due to the observation that the Re component improves the dispersion of Ru on the support.⁵¹ Deposition of Au or Pt onto carbon supported Ru catalyst to form the bimetallic for glycerol hydrogenolysis was investigated by Maris *et al.* However, they obtained similar product distribution than those of Ru monometallic catalyst. Their RuPt/C catalyst was yielding to methane and ethylene glycol over 1,2-PDO without effect to the catalytic activity under neutral pH conditions. Nevertheless, they found that the RuPt/C was more stable than the Ru/C catalyst.⁴¹

Pt-based catalysts are the favourite choice for hydrogenation reactions⁵² as well as for aqueous phase reforming.⁵³ Indeed, it has been reported to be effective for glycerol hydrogenolysis, where Pt metal sites catalyse acetol hydrogenation to 1,2-PDO.^{54,55} For example, Barbelli *et al.* reported that PtSn/SiO₂ was more active than the Pt monometallic showing good selectivity of 1,2-PDO (84 %) but still low conversion (16 %), which leads to a 13.4 % yield. They attributed this improvement to the higher electronic density of Pt in the bimetallic. This could lead to a favourable site for the adsorption of the C–OH group and subsequent C–O cleavage occurs.³⁷ In this work, using the PtRu/TiO₂ catalyst and the previous reaction conditions, *ca.* 45 % of conversion after 6 hours of reaction and 54% in 16 h was obtained. The selectivity is, among the liquid products, *ca.* 46 % to 1,2-PDO suggesting promotion of the hydrogenolysis reaction (1,2-PDO yield equal to 25 %). The selectivity to 1,3-PDO at lower reaction times is also higher for the bimetallic catalyst than for pure Ru (*ca.* 10-13 % at short reaction times), showing a potential promotion of the reaction pathway **B** (*Scheme 3-1*). This is also supported by the production of 1-propanol upon further dehydration of propanediol, with a value of approximately 10 % throughout each reaction time. EG shows a decreasing selectivity with time from 15 % to 7.5 %. While ethanol, produced from the C–C cleavage of 1,3-propanediol, pathway **B2**, has around 5 % of selectivity. Despite, PtRu produces a higher percentage of C3 compounds than the monometallic Ru/TiO₂ catalyst; it still produces C2 and C1 products. The

gas product concentration is increasing with longer reaction times, as confirmed by the gas phase product distribution in *Figure 3-5-B*.

On the other hand, bimetallic catalysts containing Pd have shown good catalytic performance for many applications. For instance, Pd is widely used for the reduction of carbonyl compounds (from aliphatic aldehydes and ketones to the corresponding alcohols),⁵⁶ CO oxidation and glycerol hydrogenolysis, such as Pd-M (M=Co, Fe, Zn or Ni).⁵⁷ Jiang *et al.* thoroughly investigated PdNi catalyst for glycerol hydrogenolysis.⁵⁸ However, it was leading to the production of EG (45.4 % of glycerol conversion in 6 h of reaction). In the work presented here, using the bimetallic PdRu/TiO₂ catalyst, the glycerol conversion was *ca.* 60 % after 16 h. However, for this reaction, the CMB (L) is between 80-85 %, which is much higher than that observed for the monometallic Ru/TiO₂ catalyst (34 %). Among the liquid products, the selectivity towards 1,2-PDO increases from 44 % in 6 h to 50 % after 16 h (*ca.* 30 % yield). This suggests that the promotion of the dehydration reaction correspond to pathway **A** (*Scheme 3-1*), again following a downhill path from the energy profile obtained (see *Figure 3-3*). As confirmed by the energy profiles, pathway **A** is thermodynamically favourable to form the acetol intermediate before its hydrogenation to propanediol. However, this intermediate is generally found only in small amounts.^{59,60} 25 % of EG selectivity was reached upon 1, 2 or 6 h. After 16 h that it shows a decrease to 13 %. The selectivity of 1-PO also decreases from 7 % in 1 h to 4 % in 16 h, due to further hydrogenation of the products. The CMB-L (%) is between 80-90 %. In conclusion, PdRu bimetallic catalyst produces significantly more liquid products than the monometallic Ru catalyst, in a similar way than the bimetallic PtRu/TiO₂, as shown in *Figure 3-5-C*. Therefore, bimetallic catalysts are more selective towards the formation of C3 compounds (a two-fold increase in yield) than monometallic catalysts. Besides, bimetallic catalysts are generally more resistant to deactivation than their monometallic counterparts.³⁰

In this work, the reusability of the bimetallic catalysts was also investigated. Stability is one of the most critical properties of heterogeneous catalysts along with its activity and selectivity. It is probably one of the best characteristics because a reusable catalyst makes it suitable for use in industry from an economic point of view. Since Ru catalyst have been shown stable against leaching, many Ru-based catalysts have been used for hydrogenation reactions.^{30,61} For reusability studies, the bimetallic catalysts were recovered from the reaction mixture. The catalyst was washed with acetone to remove any possible adsorbed products and dried

overnight in an oven at 120 °C. Further treatment under static air at 120 °C for 1 h was employed before the 1st reuse experiment. Using this method, 2nd and 3rd reuse were performed. *Figure 3-6* presents the reusability results.

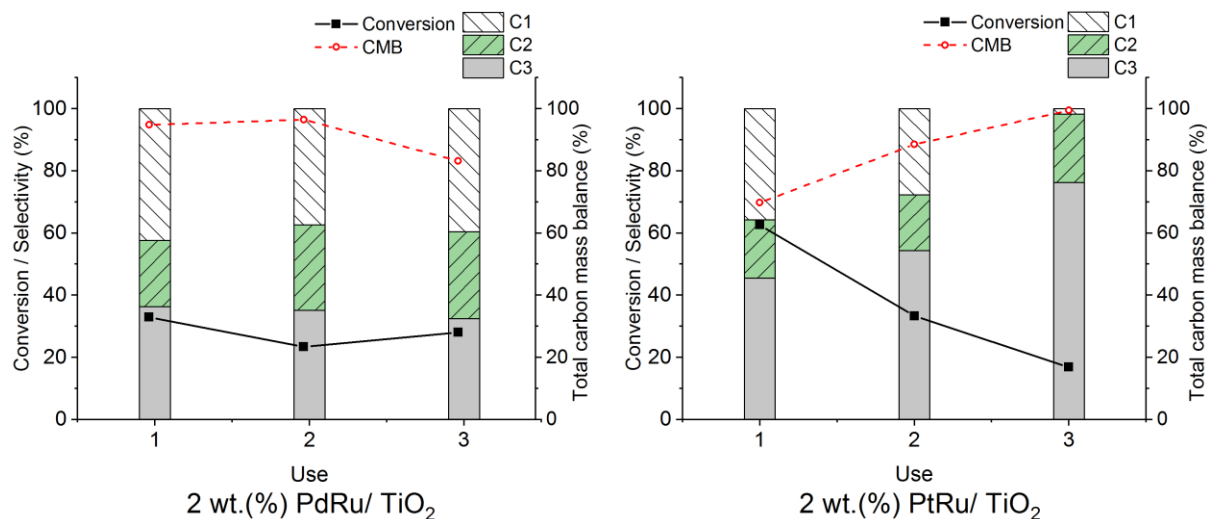


Figure 3-6 Reusability study for the bimetallic catalysts. PdRu/TiO₂ catalyst was run for 5 hours of reaction each use (left-hand side), while PtRu/TiO₂ catalyst was run for 6h of reaction each use (right-hand side).

These results clearly indicate that the PtRu nanoalloy catalysts deactivate, whereas PdRu remains stable. Jiang *et al.* prepared a RuCu bimetallic catalyst supported on modified bentonite, resulting in a stable catalyst able to run 5 cycles of glycerol hydrogenolysis without loss of activity.⁶² Using iron oxide species, bimetallic Ru-based catalysts also show excellent stability.⁶³ Maris *et al.* found PtRu more stable than Ru monometallic supported on carbon, even though the activity showed was similar.^{41,64} In contrast, the authors also investigated how Au tend to migrate off from RuAu bimetallic. This migration was forming agglomeration on the carbon under hydrogenolysis of glycerol aqueous reaction conditions.⁴¹ For instance, in the oxidation of glycerol, Pd monometallic deactivates quickly while the bimetallic with Au shows far better stability.⁶⁵ In the work presented here, the stability of the monometallic catalyst was not considered, because of the low C3 selectivity obtained.

Common reasons for the deactivation of supported metal catalysts are (1) leaching of the active metal component; (2) sintering of metal nanoparticles; and/or (3) irreversible adsorption of products (poisoning).⁶⁶ Understanding the mode of deactivation of these catalysts is crucial to the design reactivation strategies.^{66,67} Thermo Gravimetric Analyses (TGA) was performed to study the adsorption of products on the spent catalyst (*Figure 3-7*).

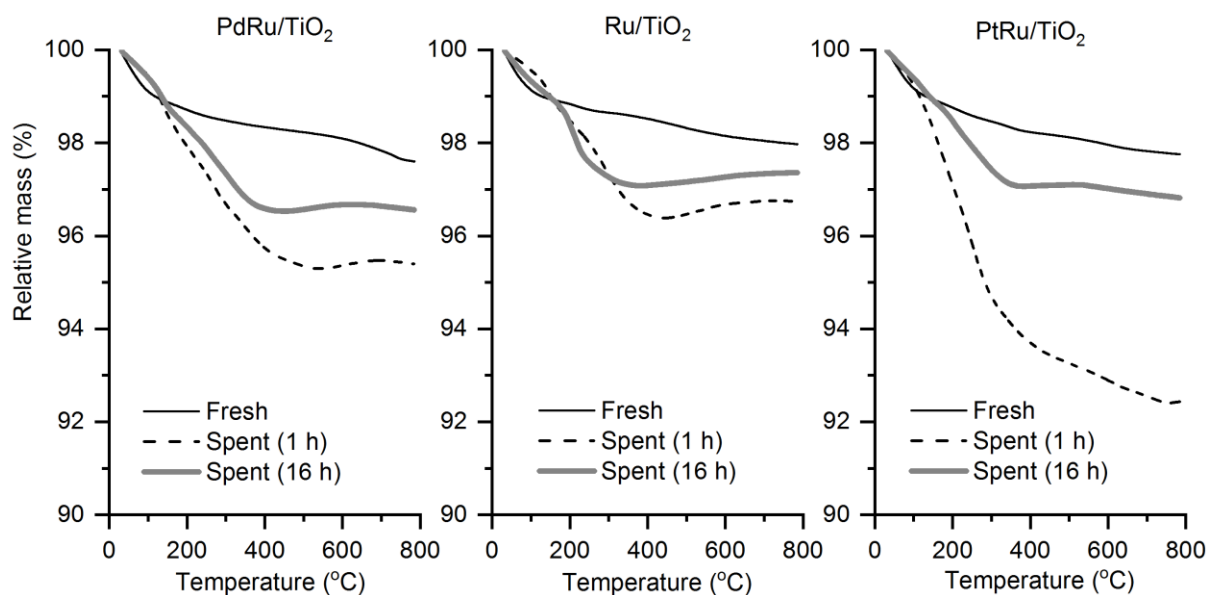


Figure 3-7 TGA data of different catalysts measured under an inert atmosphere. Fresh (thin black line), spent catalyst after 1 h of reaction (dotted line) and spent catalyst after 16 h of reaction (thick grey line). Heat-treatment conditions: air flow at 50.0 mL min^{-1} , heat from $30 \text{ }^{\circ}\text{C}$ to $800 \text{ }^{\circ}\text{C}$ at $5.00 \text{ }^{\circ}\text{C min}^{-1}$.

The TGA results show that the relative mass losses for all the spent catalysts for 16 h are less than 4 %. This suggests that no products were deposited onto the catalyst surface upon 16 h reaction. The behaviour is similar to that of the fresh catalysts. This mass loss around $100\text{--}200 \text{ }^{\circ}\text{C}$ could be attributed to the removal of H_2O and CO_2 . However, when the catalyst was used only for 1 h of reaction, TGA showed a slightly more significant mass loss around $300 \text{ }^{\circ}\text{C}$ in all the cases. This mass loss could be due to the adsorption of 3-hydroxypropanaldehyde. According to the energy profile (see Figure 3-3), this compound could be strongly adsorbed on the catalyst. However, still, in the case the spent PtRu/TiO₂ catalyst for 1 h, which exhibits the most significant relative mass loss is quite low ($< 8 \%$) (see Figure 3-7). This fact presents an exciting prospect for the principles of green chemistry and industrial use, where the long life of a catalyst is desired.⁶⁸

Then, TGA of the fresh and spent catalyst after the 3rd use was also performed. Figure 3-8 shows the TGA results and the differential thermogravimetry curve (DTG). A more significant relative mass loss is again observed for the PtRu in comparison with the PdRu on TiO₂. However, still, in this case, the relative mass loss is too low to be considered significant ($< 5\%$).

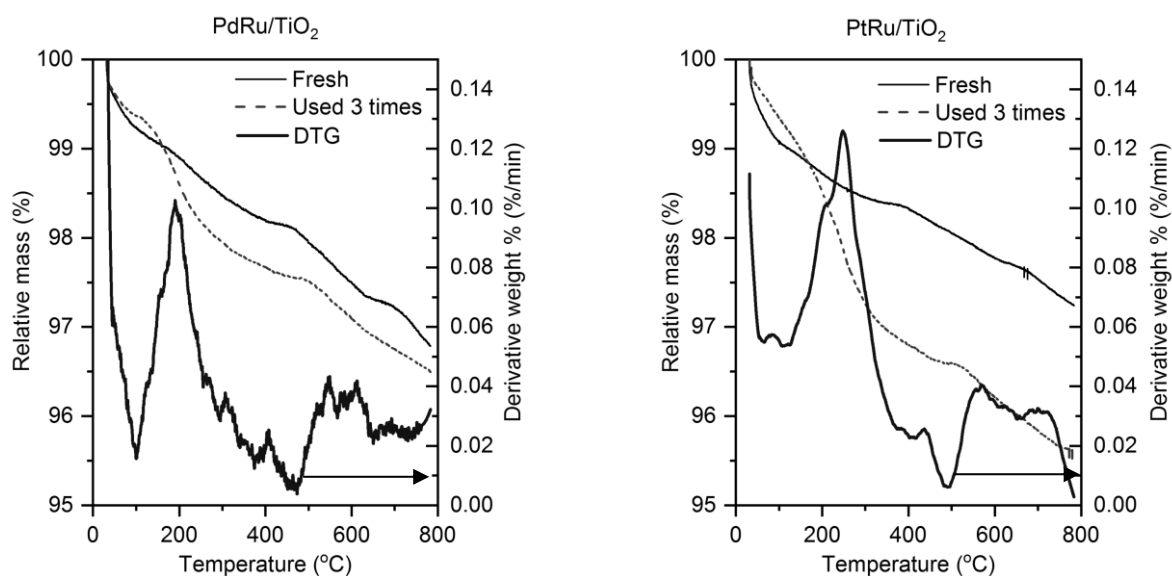


Figure 3-8 TGA results, including the 1st derivative of the catalyst used 3 times. Heat-treatment conditions: air flow at 50.0 mL min⁻¹, heat from 30 °C to 800 °C at 5.00 °C min⁻¹.

After thermal studies, the reaction mixture was analysed by ICP to study the leaching of metal components (Table 3-4). The results confirm that no leaching is occurring during the reactions.

Table 3-4 Metal content in the reaction mixture after the reusability studies

PtRu/TiO ₂	101 Ru [He]			195 Pt [No Gas]		
	Conc. [mg/l]	Conc. RSD	Leaching, %	Conc. [mg/l]	Conc. RSD	Leaching, %
1 st Use	0.03746933	0.96	0.026	0.00937251	7.54	0.003
	0.03704508	0.84		0.00984654	9.91	
	0.03769737	2.75		0.00921601	9.52	
2 nd Use	0.00917314	5.72	0.003	0.00127744	8.28	0.001
	0.00929257	6.39		0.00137023	9.02	
	0.00935511	3.64		0.00157082	17.78	
3 rd Use	0.00483935	5.89	6.5 · 10 ⁻⁵	0.00194706	10.13	1.5 · 10 ⁻⁵
	0.0050022	5.89		0.00205155	5.86	
	0.00478021	3.58		0.00209257	9.62	

• **Role of heat treatment and metal oxidation state study**

Another essential feature of supported metal catalyst is the oxidation state of the active metal. The oxidation states of Ru, Pt or Pd in all monometallic and bimetallic catalysts were manipulated by employing different heat treatments. The materials were analysed using XPS to determine its role on the catalytic activity. The catalysts were either reduced (R) or first reduced and then calcined (R+C) before testing them under optimised reaction conditions. *Figure 3-9-A* illustrates the catalytic results and liquid product distribution, while and *Figure 3-9-B* the gas product obtained.

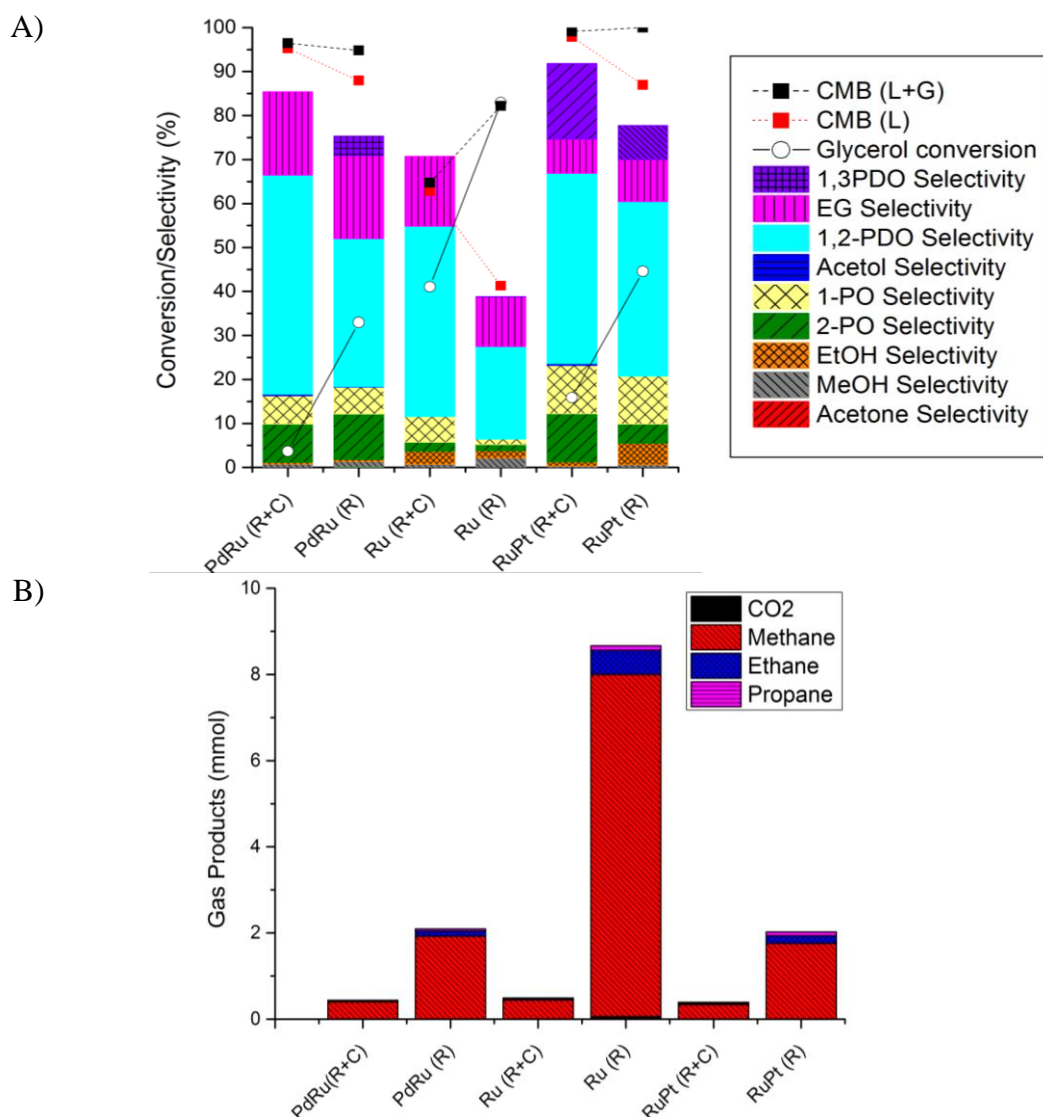


Figure 3-9 Effect of the catalyst heat treatments: Reduced only catalyst (R) or reduced + calcined (R+C) for PdRu, Ru and PtRu supported on TiO₂ catalyst. R = Reduction at 400 °C for 4 hours under 5 % H₂/Ar; C = Calcination at 300 °C for 2 hours under static air. Reaction carried out for 6 h in a batch autoclave at 165 °C, 20 bar H₂, 800 rpm, with a molar ratio

glycerol vs metal in the catalyst of [1:0.005]. A) Conversion, liquid product normalised selectivity, carbon mass balance of the liquid products and carbon mass balance, including the liquid and gas product. B) Gas phase product distribution at different reaction times tested.

From the above catalyst comparison, we can see that all the reduced only catalysts exhibit better catalytic activity than the reduced and calcined catalyst (around 30 % more of glycerol conversion). However, this rise in the conversion is accompanied by the production of more gaseous products. As shown in *Figure 3-9-A*, the carbon mass balance of the liquid products always increases for those catalysts that have been first reduced and then calcined in an oxidising atmosphere. The previous hypothesis was confirmed by the quantification of the gas phase products, *Figure 3-9-B*.

The oxidation state of the metals on the supported catalysts was studied by XPS for the fresh catalysts. Analysis of both reduced-only (R) and reduced and calcined (R+C) catalysts was performed. The primary XPS regions of the elements employed are Pd 3d, Ru 3d and Pt 4f. *Figure 3-10*, *Figure 3-11* and *Figure 3-12* show the fitting peaks of the different XPS spectra obtained. Quantitative analysis of the supported catalyst obtained from the regions described above is presented in *Table 3-5*. All spectra levels were aligned with the C 1s characterised by the binding energy of 284.4 eV as in previous works.^{69–71}

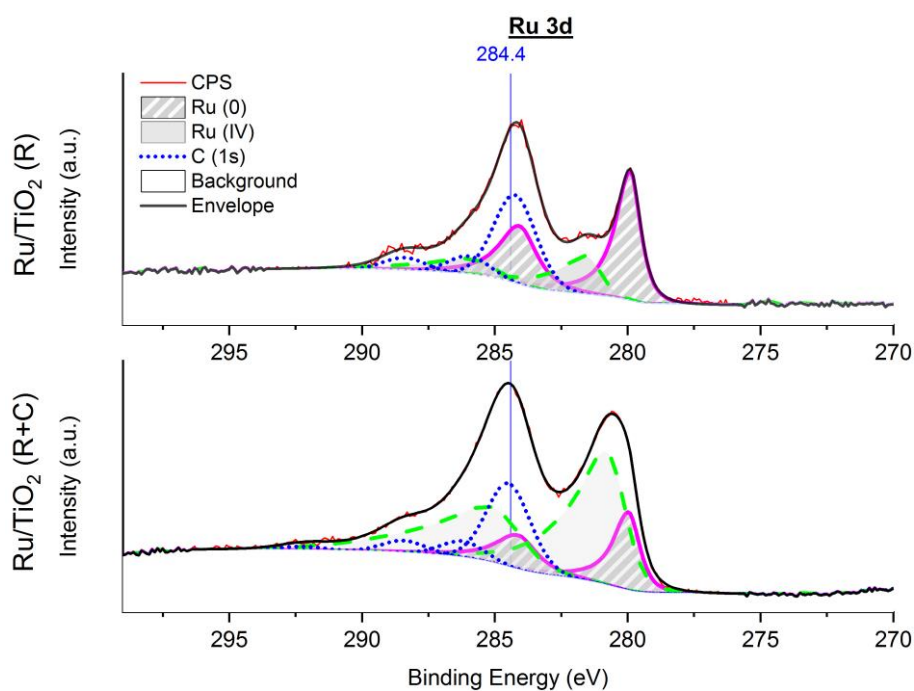


Figure 3-10 Fitted Ru(3d) spectra for Ru/TiO₂ (R) top and (R+C) bottom. The fits are described in the text.

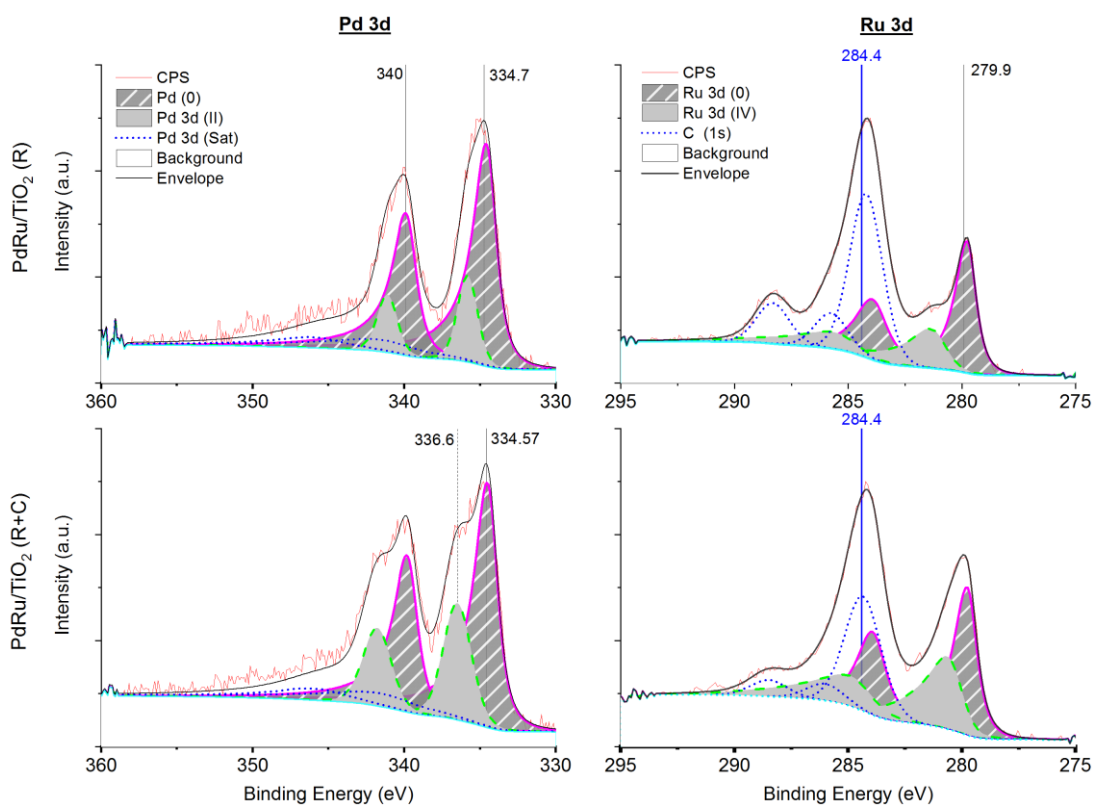


Figure 3-11 Fitted Pd(3d) left panels and Ru(3d) right panels for the PdRu/TiO₂ (R) top and PdRu/TiO₂ (R+C) bottom. The fits are described in the text.

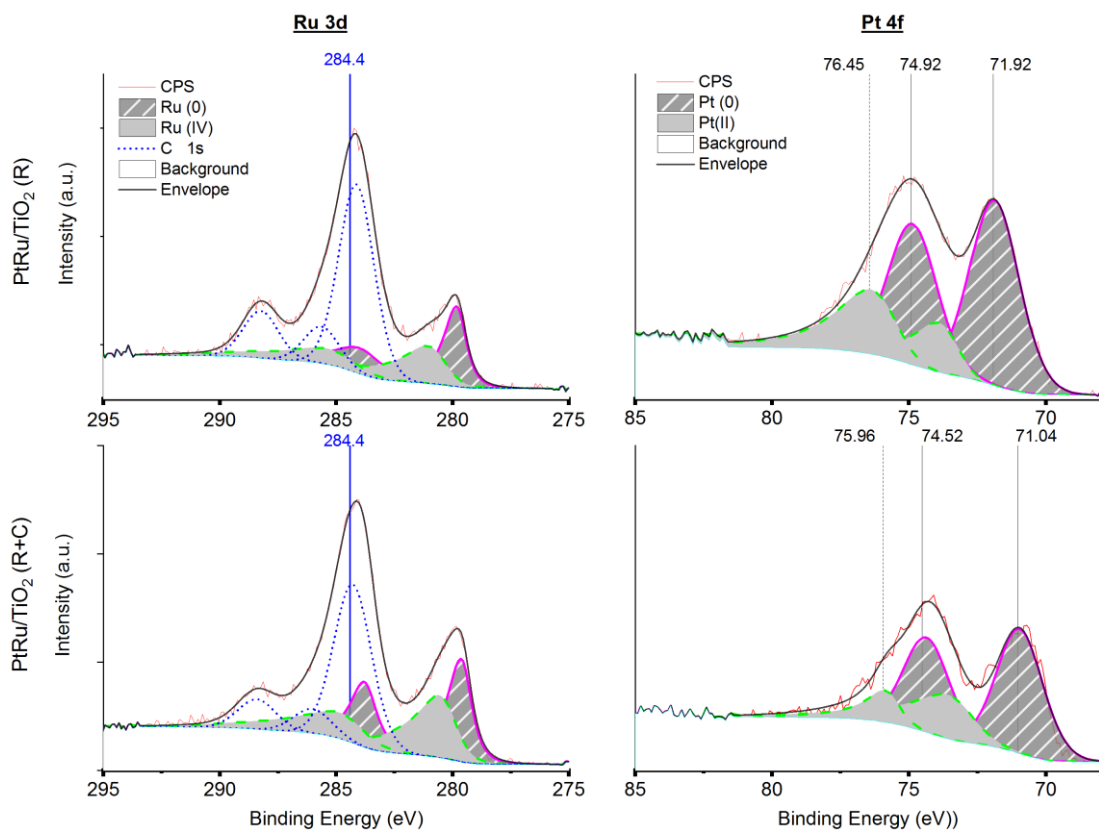


Figure 3-12 Fitted Ru(3d) left panels and Pt(4f) right panels for the PtRu/TiO₂ (R) top and PtRu/TiO₂ (R+C) bottom. The fits are described in the text.

To resolve the Ru 3d region, it was necessary to take into account that there are overlapping regions for C1s.⁷² The binding energies of common chemical states for Ru can be found in the literature fitted using: 1st) a pair of peaks for Ru metal (Ru⁰) found at 280.2 eV and 284 eV for 3d_{5/2} and 3d_{3/2} respectively; 2nd) a pair of doubles for RuO₂ (Ru⁴⁺) at low binding energy 280.7 eV for 3d_{5/2} and 285 eV for 3d_{3/2}; and 3rd) another pair of oxides at high binding energy 282.5 eV and 287 eV.^{73,72,74} *Figure 3-10* shows that the results obtained in are in good accordance with the literature values.

In *Figure 3-11*, the comparison of the Ru catalyst reduced only Ru/TiO₂(R) versus the reduced and calcined (R+C), shows an increase in the Ru oxide species on the catalyst surface. The relative percentages of the different metal species are summarised in

Table 3-6. The binding energies of common chemical states for Pd 3d are for 2 pairs of doubles. In the case of the 3d_{5/2} the binding energy is 335.2 eV for Pd metal (Pd⁰), and 336.7 eV for the native oxide (Pd²⁺).^{75,74} The spectrum also shows a pair corresponding to satellites. The presence of satellites has been previously reported and studied in detail by Pillo *et al.*^{76,74} The spectra in *Figure 3-11* are in good accordance with the binding energy reported previously in the literature, and no significant shift is observed regarding the reduced only and the reduced and calcined catalyst ($\Delta E \approx -0.2$ eV), same for the Ru 3d.

Finally, in the case of the PtRu/TiO₂ catalyst (*Figure 3-12*), the binding energies of common chemical states for the region Pt 4f could be resolved in 2 or even 3 pairs of doubles. In the case of 4f_{7/2} are 71.0 eV for Pt metal (Pt⁰), 72.4 eV PtO (Pt²⁺) and 74.9 for PtO₂ (Pt⁴⁺), while for the 4f_{5/2} are 74.7 eV for Pt metal (Pt⁰), 76.3 eV PtO (Pt²⁺) and 77.9 for PtO₂ (Pt⁴⁺).^{75,77-79} The spectrums in *Figure 3-12* is in good accordance with the literature, detecting both Pt metal peaks with binding energy at 71.9 and 74.9 eV, in the catalyst reduce under H₂/Ag flow at 400 °C.

In addition, it can be observed a negative shift of the Pt_{7/2} and the Pt_{5/2} signal of Pt⁰ species, when the reduced catalyst is also calcined in air ($\Delta E \approx -0.88$ eV and -0.40 eV respectively). Electron transfer could occur, leading the Pt with electron-rich status. Previous reports suggest that the free electron transfer into Pt may also take place due to interactions metal-support with TiO₂.⁸⁰ However, no shift was observed on the Ti 2p, 458.5 eV, which suggest that Ti are close

to the lattice oxygen as Ti^{4+} of TiO_2 .^{81,82} In the same way, no shift was obtained in the O 1s constant at 529.78 eV.

Nevertheless, when Pt and Ru are forming a bimetallic alloy, it has been reporting that the Pt 4f suggests that the contact with RuO_2 induces a change in the state of the bulk Pt.⁸² Herein the evidence of the growth of the RuO_2 along the TiO_2 surface after calcination at 400 °C is clear. Consequently, the electronic changes shifts suggest the alloy formation when compared with the monometallic Ru and Pt binding energy reported in the literature.⁸³ Quantitative analysis of the Pd 3d, Ru 3d and Pt 4f binding energy regions for these catalysts obtained from XPS analysis are shown in

Table 3-6.

Table 3-5 Quantitative analysis of the supported platinum catalysts obtained from the XPS spectra

Catalyst, 2%wt. Metal/ TiO_2	Ti % At. Conc.	O % At. Conc.	Pd % At. Conc.	Ru % At. Conc.	Pt % At. Conc.
<i>PdRu (R)</i>	30.35	68.04	0.85	0.76	-
<i>PdRu (R+C)</i>	29.93	69.01	0.51	0.55	-
<i>Ru (R)</i>	30.20	67.85	-	1.94	-
<i>Ru (R+C)</i>	29.98	69.07	-	0.94	-
<i>PtRu (R)</i>	30.16	68.81	-	0.66	0.37
<i>PtRu (R+C)</i>	29.84	69.07	-	0.35	0.74

Table 3-6 Relative concentration of the oxidation species on the catalyst surface from XPS

Catalyst, 2%wt. Metal/ TiO_2	Pd 3d (0) % Conc.	Pd 3d Sat % Conc.	Pd 3d (II) % Conc.	Ru 3d (0) % Conc.	Ru 3d (IV) % Conc.	Pt 4f (0) % Conc.	Pt4f (II) % Conc.
<i>PdRu (R)</i>	70.8	14.6	14.6	67.3	32.7	-	-
<i>PdRu (R+C)</i>	62.2	12.2	25.6	58.9	41.1	-	-
<i>Ru (R)</i>	-	-	-	69.7	30.3	-	-
<i>Ru (R+C)</i>	-	-	-	26.4	73.6	-	-
<i>PtRu (R)</i>	-	-	-	60.6	39.4	68.9	31.1
<i>PtRu (R+C)</i>	-	-	-	51.6	48.4	70.2	29.8

Temperature programmed reduction (TPR) is used to study the redox behaviour of supported metal catalysts. This method can also be used to identify the correct reduction temperature for these supported metal catalysts *Figure 3-13*.

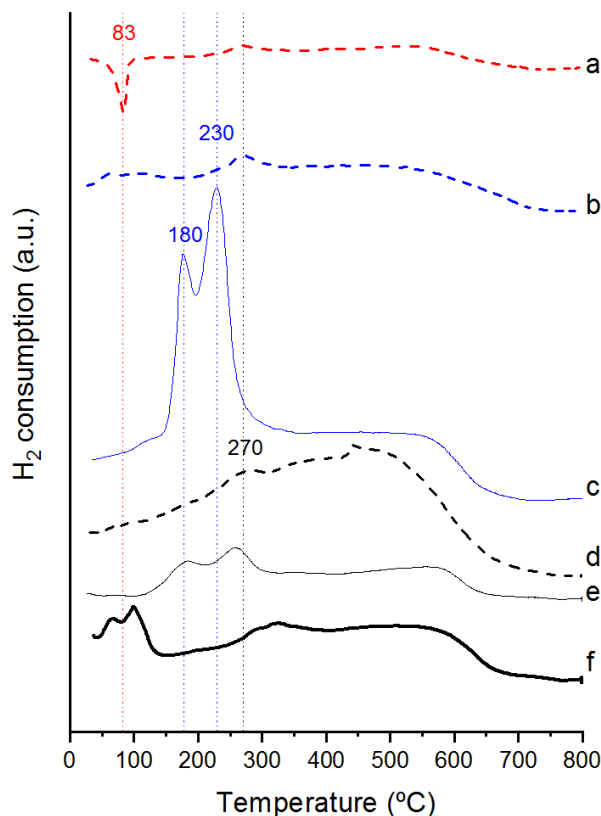


Figure 3-13 Temperature programmed reduction (H_2 -TPR) profile of the catalysts: a) Pd/TiO_2 (R); b) Ru/TiO_2 (R); c) Ru/TiO_2 (R+C); d) $PdRu/TiO_2$ (R); e) $PdRu/TiO_2$ (R+C); f) $PdRu/TiO_2$ (fresh)

The TPR profile of the fresh (dried-only) PdRu catalyst *Figure 3-13(f)* showed that 400 °C is the optimum reduction temperature. This only dried catalyst (f), also shows how PdO species reduce at low temperature (ca. 100 °C). The TPR profile of the reduced only Pd (R) catalyst exhibits a negative peak at 83 °C, *Figure 3-13(a)*. These peaks represent the decomposition of Pd hydride, which releases H_2 .⁸⁴

The reduced only Ru (R) catalyst shows one small peak around 270 °C, *Figure 3-13(b)*. Conversely, the Ru-(R+C) shows two separate peaks at 180 and 230 °C, assigned to the reduction of Ruthenium oxides (RuO_x)⁷⁴ *Figure 3-13(c)*. These two overlapping reduction peaks are related to the 2-steps for the reduction of the $RuCl_3$ precursor (firstly from Ru^{3+} to Ru^{2+} and secondly from Ru^{2+} to Ru^0).⁸⁵ In fact, the separation of these peaks depends on how

fast these two reduction steps are taking place, hence the reducibility of the metal is affected by the nature of the support. These results state that the catalysts (R+C) consume more amount of H₂ than the (R) catalyst, which is due to the presence of oxide species on the catalyst surface, as expected. The same, but with less intensity, occurs between the PdRu (R) and (R+C) catalysts, *Figure 3-13(d)* and (e), respectively. In the bimetallic catalysts, the metal loading of Ru decreases by the half; thus, there is less amount of RuO_x. These results are in good accordance with the XPS results discussed earlier.

Thus the H₂ consumption acquired at a higher temperature for these samples can be attributed to the partial reduction of the TiO₂.⁸⁶ Whereas peaks about 350 °C, are related to a reduction of surface capped oxygen of TiO₂.^{87,88} Consequently, the reduction temperature of the catalysts must be at 400 °C or higher to ensure that the support has not a partial reduction. This could produce the formation of oxygen vacancies and Ti³⁺. It has been reported that this phenomenon could be occurring at the interface between the support (anatase TiO₂) and the Ru, acting as Lewis base.⁸⁹

3.1.2 *Continuous Fixed Bed Reactor*

Depending on the application or production scale, different reactor designs may be considered. In general, batch reactors are employed for small-scale production because of its simple operation, among other reasons. In contrast, Continuous-flow reactors such as Continuous-Stirred Tank Reactor (CSTR), Packed-Flow Reactors or Packed-Bed Reactor (tubular) are more applicable in processes where large amounts of products are required. However, its operation is more complicated, as more variables can affect the overall performance, such as undesired thermal gradients, poor temperature control, channelling, etc.^{90, 91}

For this reason, this section focuses on the study of the performance of the previous catalysts in a continuous flow system. The studies on a fixed-bed reactor were performed at the Dalian Institute of Chemical-Physic (DICP) facilities, (see the experimental set-up in *Chapter 2, section 2.2.2.*). The results obtained from the continuous flow system were compared with those obtained from the autoclave batch reactor. The continuous fixed-bed reactor was also used to study the effect of reducing catalyst *in-situ*.

Weight hourly space velocity (WHSV) was taken into account since the weight of catalyst was kept always same, 0.5 g in all reactions. To maintain the molar ratio between the metal on the catalyst and the reactant, the variation in the flow of glycerol solution per hour changed the

WHSV. Which gives a WHSV within a range between 2 to 3.2 h⁻¹, depending on the catalyst used. *Figure 3-14* shows the catalytic activity and the liquid product selectivity obtained in the fixed bed reactor for both monometallic and bimetallic catalyst supported on TiO₂.

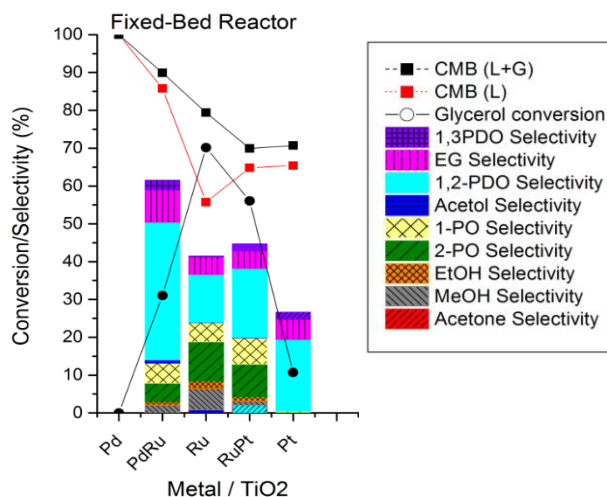


Figure 3-14 Liquid products distribution, selectivity obtained with the different 2 wt. % metal supported on TiO₂ catalyst. Reaction carried out in a fixed-bed reactor at 165 °C, 20 bar H₂, with a glycerol vs metal molar ratio in the catalyst of [1:0.005] for 20 h.

The tendency for the activity of all the catalyst was similar to the one obtained from the batch reactors — a significant increase of the liquid phase product when bimetallic catalysts were attained (*Figure 3-14*). The catalysts have slightly more activity in the flow reactor (30-35 % of conversion) compared to the batch reactor for the case of the PdRu (25-30 %). For the bimetallic PtRu catalyst, a slight increase in activity, from 45 % of glycerol conversion in the batch to 56 % in the flow reactor, was also observed. Regarding product distribution, 1,2-PDO is the primary liquid product for the PdRu catalyst. In the case of the reaction with PdRu/TiO₂, the missing of carbon mass balance was around 10 % in all the samples taken, while for the Ru and PtRu catalyst it was more significant (*Figure 3-15*).

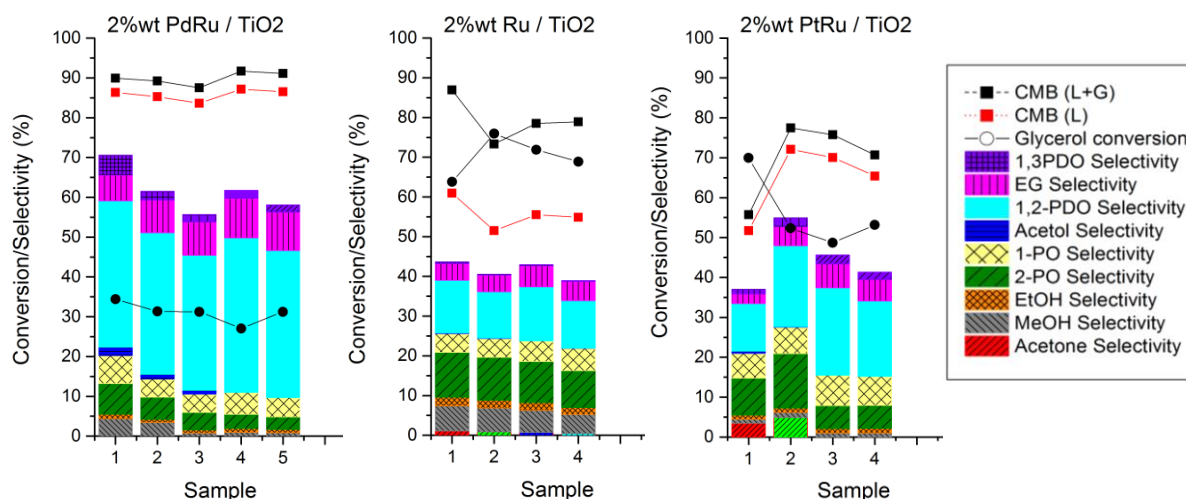


Figure 3-15 Catalytic activity of the PdRu, Ru and PtRu catalysts on TiO₂ samples were taken every hour until reach stable conversion in the fixed-bed reactor at 165 °C, 20 bar H₂, with a glycerol vs metal molar ratio in the catalyst of [1:0.005].

- **Effect of the *in-situ* reduction in the fixed bed reactor**

All the catalysts tested previously were reduced *ex-situ*. The heat treatment was carried out in a furnace under 5 % v/v H₂ in Argon at 400 °C for 4 h with a heating temperature ramp of 10 °C min⁻¹. The fixed bed reactor allowed us to reduce the catalyst *in-situ* using 99 % pure H₂ at 400 °C for 4h. The effect of *in-situ* reduction on the catalytic properties of PtRu/TiO₂ catalyst is presented in Figure 3-16. The *in-situ* reduced PtRu catalyst showed a lower conversion compared to the same catalyst reduced *ex-situ*. Figure 3-16 also shows an enhancement in the 1-3 PDO selectivity. The main difference between these two treatments is that the catalyst reduced *ex-situ* could be passivated in air at room temperature after reduction. Indeed, this is part of the catalyst heat pre-treatment that for instance, Zhao *et al.* reported after the *ex-situ* reduction of their Pt/ W-containing catalyst for this reaction.^{92,93} More investigation needs to be carried out to understand this interesting behaviour with this bimetallic catalysts.

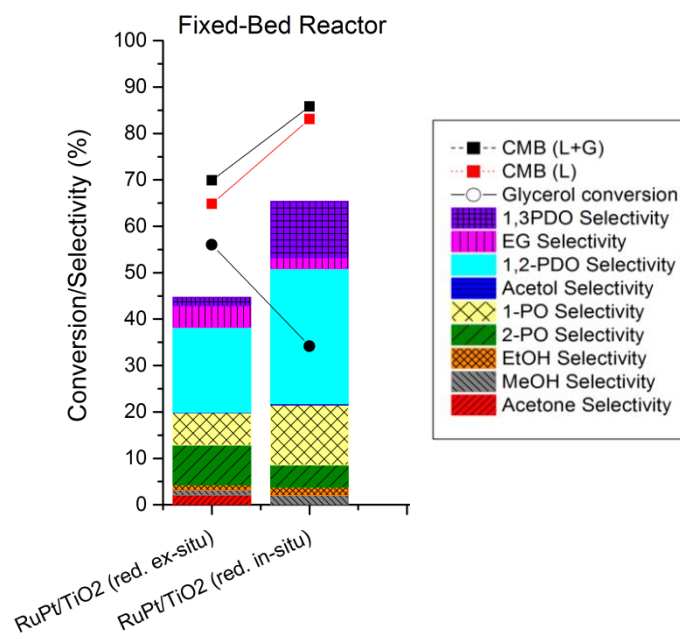


Figure 3-16 Reduction *ex-situ* vs reduction *in-situ* comparison. Reaction carried out in a fixed-bed reactor at 165 °C, 20 bar H₂, with a glycerol vs metal molar ratio in the catalyst of [1:0.005] for 20 h (steady state reaction).

3.1.3 Catalyst characterisation by electron microscopy

Detailed information of the three catalysts tested in both reactors was obtained from SEM and STEM. SEM images show well-dispersed nanoparticles with spherical morphology, *Figure 3-17*.

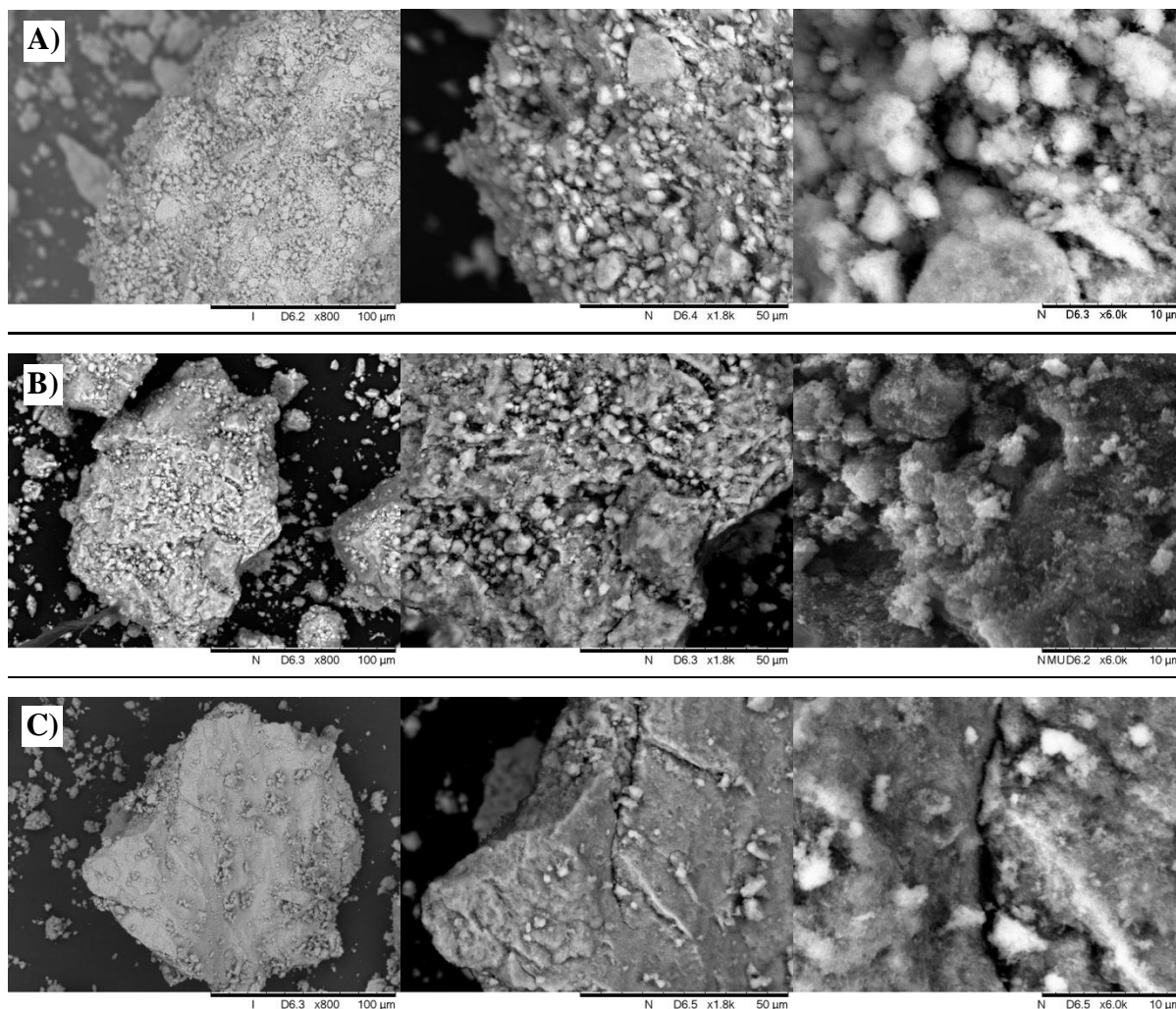


Figure 3-17. Selected Scanning Electron Microscopy Images of A) 2 wt. % Ru/TiO₂; B) 2 wt. % PdRu/TiO₂; C) 2 wt. % PtRu/TiO₂. Scale bar shows increasing magnification from left to right 100, 50 and 10 μm.

From the SEM-EDX mapping in *Figure 3-18*, as an approach of qualitative chemical composition and its elemental distribution. An overall view of each catalyst can be seen in the top row. Whereas selected elements Pd, Ru and Pt, are shown in the bottom row to distinguish clearly the metal distribution.

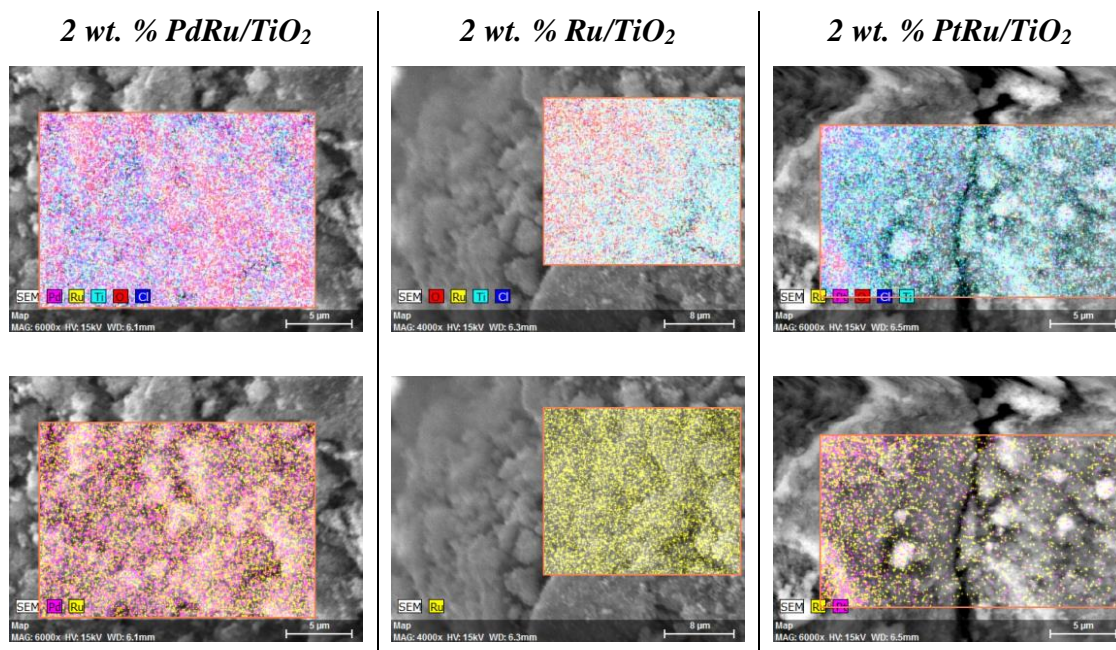


Figure 3-18 EDX - Elemental mapping by SEM. Top row: including Pd or Pt (magenta), Ru (yellow), Ti (cyan), O (red) and Cl (blue). Bottom row: including just Pd or Pt (magenta) and Ru (yellow). Scale bar represents 5 μm .

The images show the homogeneous distribution of the metal atoms of PdRu and Ru catalysts. High dispersion was found within all the areas sampled. A well-dispersed metal on the catalyst is vital for high catalytic activity. In that sense, it correlates well with the high conversion rates observed, especially for the Ru catalysts. The bimetallic PtRu catalyst presents a metal dispersion not as good as the PdRu catalyst.

Fresh and used Pd, PdRu, Ru catalysts supported on TiO_2 were characterised by Scanning Transmission Electron Microscopy (STEM) to estimate the particle size distribution and metal composition.

Selected micrograms of the catalyst and the size distribution histograms are shown in Figure 3-19. Pd monometallic catalyst present the highest particle sizes, up to 19 nm, with a mean size of 4 nm (STEM microgram a). However, when Pd is co-impregnated with Ru to form the bimetallic catalyst, the mean particle size decreases to 2 nm (microgram b), being the biggest particle found around 3.9 nm. Ru monometallic catalyst also presents a mean particle size of 2 nm (microgram c).

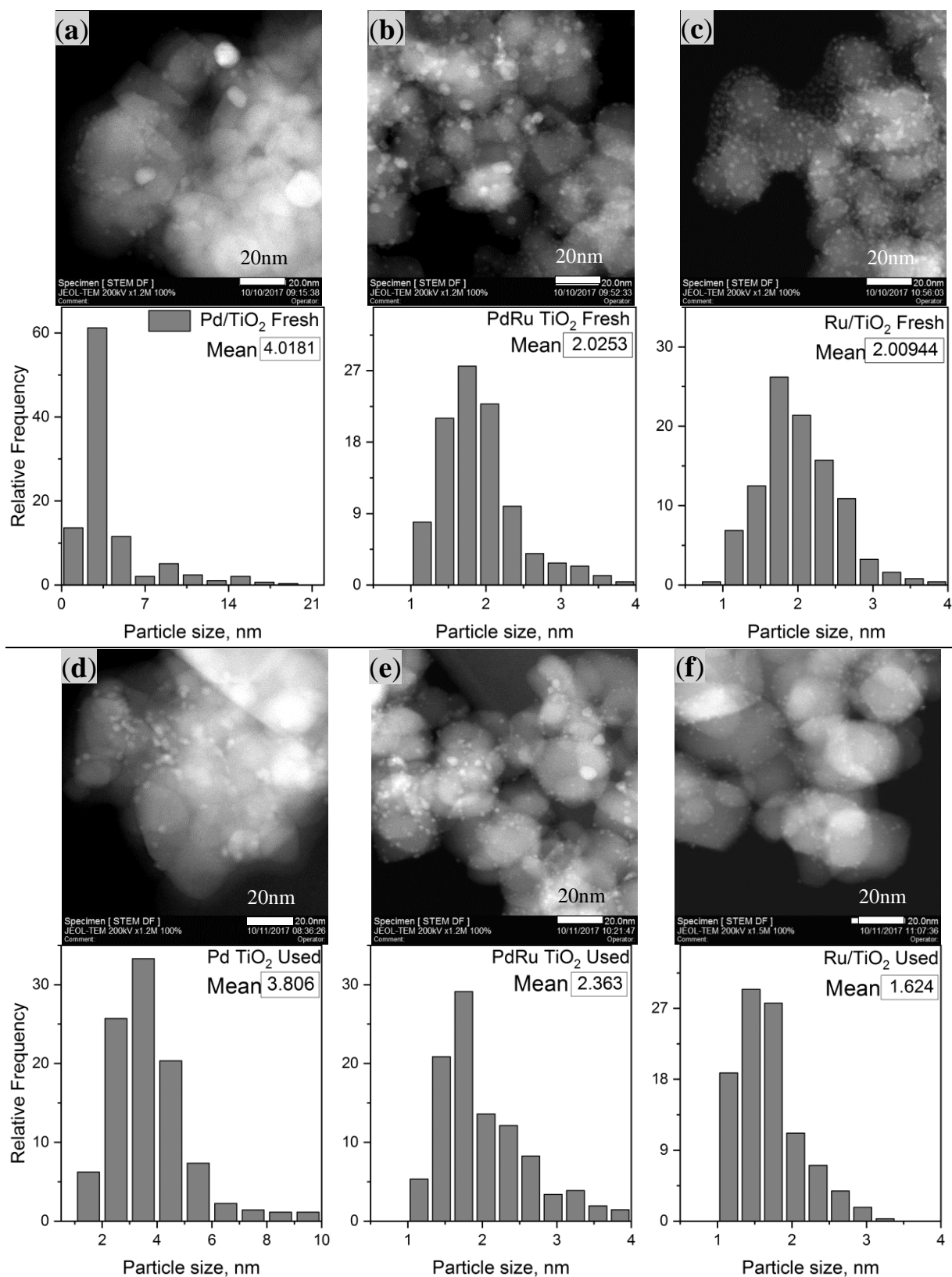


Figure 3-19 STEM HAADF micrographs and particle size distribution of the catalyst: Top row: fresh (a) Pd/TiO₂, (b) PdRu/ TiO₂ and (c) Ru/ TiO₂; Bottom row: micrographs of the catalyst after 1st Reuse (d) Pd/TiO₂, (e) PdRu/ TiO₂ and (f) Ru/ TiO₂. The scale bars represent 20.0 nm.

From *Figure 3-19*, it is evident that there is no significant particle size difference between the three fresh catalysts after the reaction (d, e and f micrograms). Also, no apparent change in the nature of the support was observed after the reaction. The reused catalyst showed an insignificant particle size variation. The results show slightly smaller and fewer particles in the case of the monometallic Pd (mean particle size reduced a 5 %, from 4.01 to 3.8 nm) and Ru (mean particle size reduced about 18%, from 2 to 1.64 nm). Whereas the spent bimetallic PdRu seems to be very similar to the fresh (mean particle size increased a 12%, from 2.02 to 2.3nm). The most active monometallic Ru catalyst also has the most uniform particle size distribution. However, it shows fewer particles in the spent catalyst with the same particle sizes. Elemental mapping by EDX-STEM of the catalysts was performed at several broad and punctual areas. An example of the spectra taken of each bimetallic catalyst is shown in the *Appendix (7.1)*. The analysis confirms that the bigger nanoparticles in the bimetallic are Pd-rich, while the small particles contain equal amounts of Ru and Pd. On the other hand, selected micrograms of the Pt catalyst and the size distribution histograms are shown in *Figure 3-19*. Pt monometallic catalyst presents a mean particle size of < 2 nm (STEM microgram a). The PtRu bimetallic catalyst has even smaller mean particle size 1.6 nm (STEM microgram b).

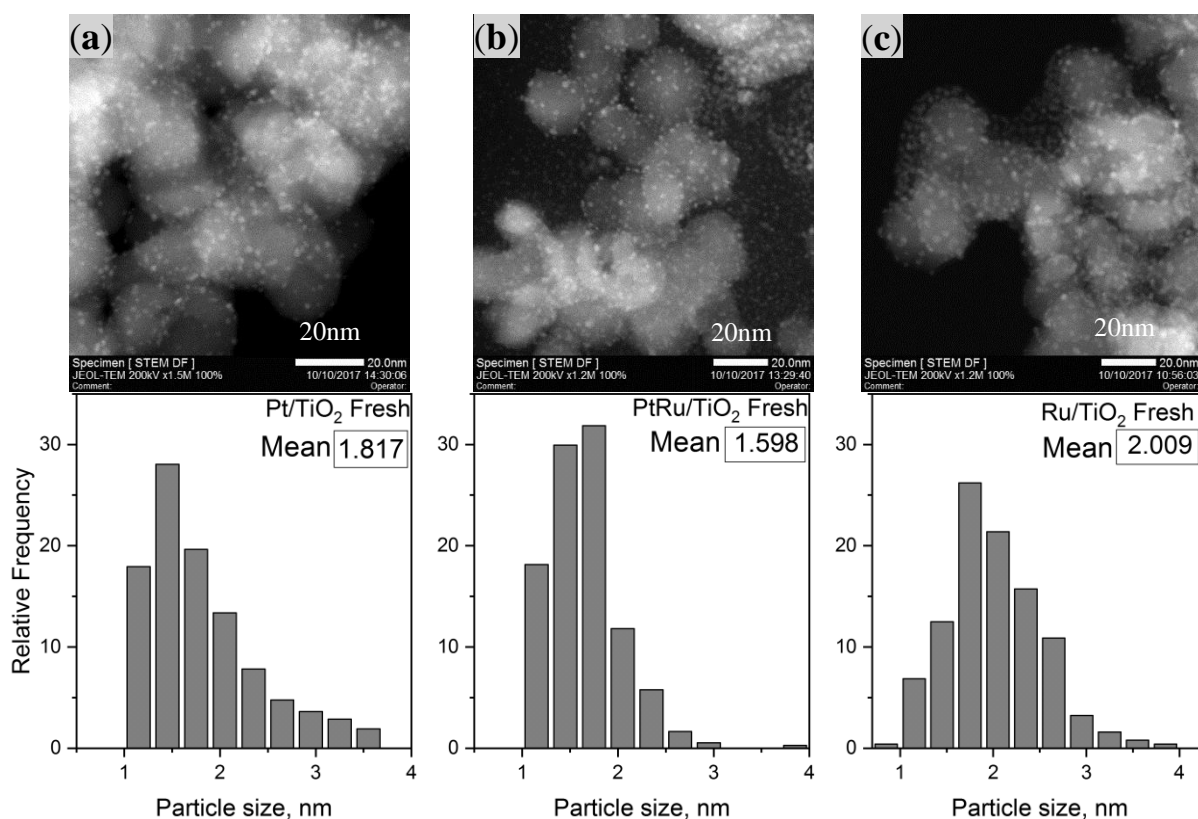


Figure 3-20 STEM HAADF micrographs and particle size distribution of the Fresh a) Pt, b) PtRu and c) Ru on TiO₂ catalyst. The scale bars represent 20 nm.

STEM analysis for this post catalysis bimetallic catalyst was performed. *Figure 3-21* shows selected HAADF and BF images of the fresh and spent catalyst after the 3rd use.

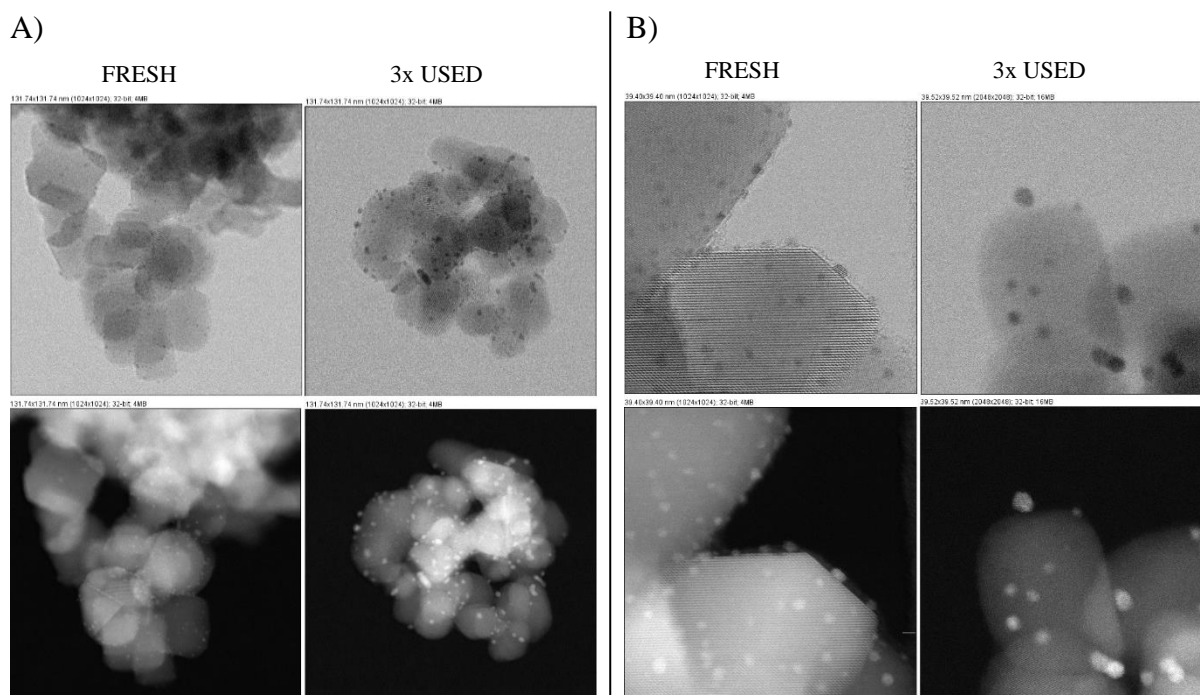


Figure 3-21 STEM BF(top row) and HAADF(bottom row) micrographs of the 3 x times used PtRu on TiO₂ catalyst.. Zoom boxes scaled A) 131.74 x 131.74 nm B) 39.52 x 39.52 nm

The results show some metal particle agglomeration. Indeed, the particle size distribution of the post catalysis samples increased around 29 % (from 1.6 in the fresh catalyst to 2.25 nm of main particle size). The metal agglomeration implicates a loss of active surface via structural modification of the catalyst. Therefore, it seems that the sintering of the small metal nanoparticles is the main reason for the catalyst deactivation observed for the PtRu/TiO₂ catalyst in this reaction.

3.2 Conclusions

This work shows how bimetallic catalyst can control the selectivity towards C3 products, using relatively low temperatures (165 °C) in presence of H₂.

Among the metals (Ru, Pd, and Pt monometallic and bimetallic combinations) supported on TiO₂-P25, bimetallic catalyst gave the best activity/selectivity results. Both, the Ru monometallic catalyst and the admixture (Pd+Ru or Pt+Ru) give the highest activity. However, an increase in the formation of the C1 and C2 products was obtained due to further hydrogenolysis. It was confirmed by microscopy studies that Ru monometallic showed the best

metal dispersion of small nanoparticles (*ca.* 2 nm). The presence of nanoalloys, supported by EDX analysis, is required to achieve better C3 products yields, which is in correspondence with the energy profiles obtained.

Despite both bimetallic catalysts having similar activity, PdRu/TiO₂ seems to be the best catalyst for the hydrogenolysis of glycerol in both kind of reactor configurations used in this work. Furthermore, it is a stable catalyst that can be reused several times without losing any activity. On the contrary, PtRu/TiO₂ deactivates under the reaction conditions. After performing TGA experiments for the fresh and spent catalyst, significant product adsorption on the catalyst was discarded. Also, metal leaching was not found in the reaction mixtures analysed by ICP. However, changes in the particle size of this catalyst were observed. After the third time that the catalyst was used for the glycerol hydrogenation reaction, an increase of almost a 30 % in the mean particle size was obtained by STEM measurements. This indicated that catalyst sintering could be the reason why PtRu/TiO₂ deactivates.

It is found that the metal oxidation states present on the catalyst can be affected by the activation process. Results confirmed that the reduction of the catalyst above 400 °C is required. The presence of a high percentage of metal oxides leads to the C-C bond cleavage mechanism pathway C. However, *in-situ* reduction in the fixed flow reactor with pure H₂, does not exhibit higher activity on the catalyst as expected. XPS analysis of the spent *in-situ* reduced catalyst would be recommended elucidating the metal oxidation state of this catalyst.

In general, the hydrogenolysis of glycerol performed in a fixed flow reactor gave a higher reaction rate than in an autoclave batch reactor; however, the selectivity to 1,2-PDO was much higher. Moreover, the higher 1,3-PDO yield was obtained in this kind of configuration for the PtRu/TiO₂ catalyst. Nevertheless, to improve the selectivity of 1,3-PDO, it is suggested that the catalyst should have high hydrogenation activity for the intermediate 3-HPA, Pt is the more recommended metal and Brønsted acid sites are needed.

3.3 References

1. *Catalytic Hydrogenation for Biomass Valorization*; Rinaldi, R., Ed.; Energy and Environment Series; Royal Society of Chemistry: Cambridge, 2014.
2. Martin, A.; Armbruster, U.; Gandarias, I.; Arias, P. L., *Eur. J. Lipid Sci. Technol.* **2013**, *115* (1), 9–27.
3. Werpy, T.; Petersen, G. *Top Value Added Chemicals from Biomass: Volume I -- Results of Screening for Potential Candidates from Sugars and Synthesis Gas*; Golden, CO (United States), 2004.
4. Zhou, C.-H. (Clayton); Beltramini, J. N.; Fan, Y.-X.; Lu, G. Q., *Chem. Soc. Rev.* **2008**, *37* (3), 527–549.
5. Talebian-Kiakalaieh, A.; Amin, N. A. S.; Hezaveh, H., *Renew. Sustain. Energy Rev.* **2014**, *40*, 28–59.
6. Wang, Y.; Zhou, J.; Guo, X., *RSC Adv.* **2015**, *5* (91), 74611–74628.
7. Lee, C. S.; Aroua, M. K.; Daud, W. M. A. W. A. W.; Cognet, P.; Pérès-Lucchese, Y.; Fabre, P.-L. L.; Reynes, O.; Latapie, L., *Renew. Sustain. Energy Rev.* **2015**, *42*, 235–244.
8. Sivasankaran, C., *J. Environ. Biol.* **2016**, *37* (January), 1539–1543.
9. Nakagawa, Y.; Tomishige, K., *Catal. Sci. Technol.* **2011**, *1* (1), 179–190.
10. Gilkey, M. J.; Xu, B., *ACS Catal.* **2016**, *6* (3), 1420–1436.
11. Shen, L.; Haufe, J.; Patel, M. K.; Science, G., *Gr. Sci. Technol. Soc.* **2009**, No. June, 41.
12. Sun, D.; Yamada, Y.; Sato, S.; Ueda, W., *Appl. Catal. B Environ.* **2016**, *193*, 75–92.
13. Pandhare, N. N.; Pudi, S. M.; Biswas, P.; Sinha, S., *Org. Process Res. Dev.* **2016**, *20* (6), 1059–1067.
14. Yadav, G. D.; Chandan, P. A.; Tekale, D. P., *Ind. Eng. Chem. Res.* **2012**, *51* (4), 1549–1562.
15. Samudrala, S. P.; Kandasamy, S.; Bhattacharya, S., *Sci. Rep.* **2018**, *8* (1), 7484.
16. Miyazawa, T.; Kusunoki, Y.; Kunimori, K.; Tomishige, K., *J. Catal.* **2006**, *240* (2), 213–221.
17. Chheda, J. N.; Huber, G. W.; Dumesic, J. A., *Angew. Chemie - Int. Ed.* **2007**, *46* (38), 7164–7183.
18. Johnstone, R. a. W.; Wilby, A. H.; Entwistle, I. D., *Chem. Rev.* **1985**, *85* (2), 129–170.
19. Wang, S.; Yin, K.; Zhang, Y.; Liu, H., *ACS Catal.* **2013**, *3* (9), 2112–2121.
20. Jiang, T.; Kong, D.; Xu, K.; Cao, F., *Appl. Petrochemical Res.* **2016**, *6* (2), 135–144.
21. Sun, Q.; Wang, S.; Liu, H., *ACS Catal.* **2017**, *7* (7), 4265–4275.
22. van Ryneveld, E.; Mahomed, A. S.; van Heerden, P. S.; Friedrich, H. B., *Catal. Letters* **2011**, *141* (7), 958–967.
23. Rajkhowa, T.; Marin, G. B.; Thybaut, J. W., *J. Ind. Eng. Chem.* **2017**, *54*, 270–277.
24. Sinfelt, J. H., *Acc. Chem. Res.* **1977**, *10* (1), 15–20.
25. Sinfelt, J. H. *Bimetallic Catalysts: Discoveries, Concepts, and Applications*; Exxon Monographs Series; Wiley, 1983.
26. Shibasaki, M.; Yamamoto, Y. *Multimetallic Catalysts in Organic Synthesis*; Wiley, 2006.
27. Yu, W. Y.; Mullen, G. M.; Flaherty, D. W.; Mullins, C. B., *J. Am. Chem. Soc.* **2014**, *136* (31), 11070–11078.
28. Croy, J. R.; Mostafa, S.; Hickman, L.; Heinrich, H.; Cuenya, B. R., *Appl. Catal. A Gen.*

- 2008**, 350 (2), 207–216.
29. Guadix-Montero, S.; Alshammari, H.; Dalebout, R.; Nowicka, E.; Morgan, D. J.; Shaw, G.; He, Q.; Sankar, M., *Appl. Catal. A Gen.* **2017**, 546, 58–66.
 30. Sankar, M.; Dimitratos, N.; Miedziak, P. J.; Wells, P. P.; Kiely, C. J.; Hutchings, G. J., *Chem. Soc. Rev.* **2012**, 41 (24), 8099.
 31. Gao, F.; Goodman, D. W., *Chem. Soc. Rev.* **2012**, 41 (24), 8009–8020.
 32. Crole, D. A.; Freakley, S. J.; Edwards, J. K.; Hutchings, G. J., *Proc. R. Soc. London A Math. Phys. Eng. Sci.* **2016**, 472 (2190).
 33. Enache, D. I.; Edwards, J. K.; Landon, P.; Solsona-Espriu, B.; Carley, A. F.; Herzing, A. A.; Watanabe, M.; Kiely, C. J.; Knight, D. W.; Hutchings, G. J., *Science*. **2006**, 311 (5759), 362–365.
 34. Dodekatos, G.; Abis, L.; Freakley, S. J.; Tüysüz, H.; Hutchings, G. J., *ChemCatChem* **2018**, 10 (6), 1351–1359.
 35. Falcone, D. D.; Hack, J. H.; Klyushin, A. Y.; Knop-gericke, A.; Schlögl, R.; Davis, R. J.; Schlo, R.; Davis, R. J.; Schlögl, R.; Davis, R. J., *ACS Catal.* **2015**, 5 (10), 5679–5695.
 36. Luo, W.; Sankar, M.; Beale, A. M.; He, Q.; Kiely, C. J.; Bruijninx, P. C. A.; Weckhuysen, B. M., *Nat. Commun.* **2015**, 6 (1), 6540.
 37. Bond, G. C., *Platin. Met. Rev.* **1957**, 1 (3), 87–93.
 38. Hutchings, G. J.; Kiely, C. J., *Acc. Chem. Res.* **2013**, 46 (8), 1759–1772.
 39. Miyazawa, T.; Koso, S.; Kunimori, K.; Tomishige, K., *Appl. Catal. A Gen.* **2007**, 318 (3), 244–251.
 40. Roy, D.; Subramaniam, B.; Chaudhari, R. V., *Catal. Today* **2010**, 156 (1–2), 31–37.
 41. Maris, E. P.; Ketchie, W. C.; Murayama, M.; Davis, R. J., *J. Catal.* **2007**, 251 (2), 281–294.
 42. Vasiliadou, E. S.; Lemonidou, A. A., *Org. Process Res. Dev.* **2011**, 15 (4), 925–931.
 43. Li, B.; Wang, J.; Yuan, Y.; Ariga, H.; Takakusagi, S.; Asakura, K., *ACS Catal.* **2011**, 1 (11), 1521–1528.
 44. Vasiliadou, E. S.; Heracleous, E.; Vasalos, I. A.; Lemonidou, A. A., *Appl. Catal. B Environ.* **2009**, 92 (1–2), 90–99.
 45. Delgado, S. N.; Yap, D.; Vivier, L.; Especel, C., *J. Mol. Catal. A Chem.* **2013**, 367, 89–98.
 46. Vinet, L.; Zhedanov, A., *J. Phys. A Math. Theor.* **2011**, 44 (8), 085201.
 47. Shastri, A. G.; Schwank, J., *J. Catal.* **1985**, 95 (1), 271–283.
 48. Villa, A.; Chan-Thaw, C. E.; Campisi, S.; Bianchi, C. L.; Wang, D.; Kotula, P. G.; Kübel, C.; Prati, L., *Phys. Chem. Chem. Phys.* **2015**, 17 (42), 28171–28176.
 49. Salazar, J. B.; Falcone, D. D.; Pham, H. N.; Datye, A. K.; Passos, F. B.; Davis, R. J., *Appl. Catal. A Gen.* **2014**, 482, 137–144.
 50. Liu, H.; Liang, S.; Jiang, T.; Han, B.; Zhou, Y., *Clean - Soil, Air, Water* **2012**, 40 (3), 318–324.
 51. Ma, L.; He, D., *Top. Catal.* **2009**, 52 (6–7), 834–844.
 52. Sipponen, M. H.; Farooq, M.; Koivisto, J.; Pellis, A.; Seitsonen, J.; Österberg, M., *Nat. Commun.* No. 2018, 1–7.
 53. Chen, G.; Li, W.; Chen, H.; Yan, B., *J. Zhejiang Univ. Sci. A* **2015**, 16 (6), 491–506.
 54. Villa, A.; Manzoli, M.; Vindigni, F.; Chinchilla, L. E.; Botton, G. A.; Prati, L., *Catal. Letters* **2017**, 147 (10), 2523–2533.

55. Gandarias, I.; Arias, P. L.; Requies, J.; Güemez, M. B.; Fierro, J. L. G., *Appl. Catal. B Environ.* **2010**, *97* (1–2), 248–256.
56. Musolino, M. G.; Busacca, C.; Mauriello, F.; Pietropaolo, R., *Appl. Catal. A Gen.* **2010**, *379* (1–2), 77–86.
57. Musolino, M. G.; Scarpino, L. A.; Mauriello, F.; Pietropaolo, R., *ChemSusChem* **2011**, *4* (8), 1143–1150.
58. Jiang, T.; Huai, Q.; Geng, T.; Ying, W.; Xiao, T.; Cao, F., *Biomass and Bioenergy* **2015**, *78* (130), 71–79.
59. Sheldon, R. A., *J. Mol. Catal. A Chem.* **2016**, *422*, 3–12.
60. Hirunsit, P.; Luadthong, C.; Faungnawakij, K., *RSC Adv.* **2015**, *5* (15), 11188–11197.
61. Huang, Q.-Q.; Yu, W.-Q.; Luo, X.-L.; Gao, J.; Xu, J., *Asian J. Org. Chem.* **2018**, *7* (10), 2039–2044.
62. Jiang, T.; Zhou, Y.; Liang, S.; Liu, H.; Han, B., *Green Chem.* **2009**, *11* (7), 1000–1006.
63. Li, B.; Wang, J.; Yuan, Y.; Ariga, H.; Takakusagi, S.; Asakura, K., *ACS Catal.* **2011**, *1*, 1521.
64. Maris, E. P.; Davis, R. J., *J. Catal.* **2007**, *249* (2), 328–337.
65. Prati, L.; Villa, A.; Porta, F.; Wang, D.; Su, D., *Catal. Today* **2007**, *122* (3–4), 386–390.
66. Argyle, M.; Bartholomew, C., *Catalysts* **2015**, *5* (1), 145–269.
67. Moulijn, J. A.; van Diepen, A. E.; Kapteijn, F. Deactivation and Regeneration. In *Handbook of Heterogeneous Catalysis*; Wiley-VCH Verlag GmbH & Co. KGaA: Weinheim, Germany, 2008.
68. Anastas, P.; Eghbali, N., *Chem. Soc. Rev.* **2010**, *39* (1), 301–312.
69. Venezia, A. M., *Catal. Today* **2003**, *77* (4), 359–370.
70. Mosbæk, S.; Gusenleitner, S.; Hauschild, D.; Graber, T.; Ehm, D.; Tougaard, S.; Reinert, F., *Surf. Sci.* **2013**, *616*, 161–165.
71. Larichev, Y. V.; Shlyapin, D. A.; Tsyrl'nikov, P. G.; Bukhtiyarov, V. I., *Catal. Letters* **2008**, *120* (3–4), 204–209.
72. Elmasides, C.; Kondarides, D. I.; Grünert, W.; Verykios, X. E., *J. Phys. Chem. B* **1999**, *103* (25), 5227–5239.
73. Morgan, D. J., *Surf. Interface Anal.* **2015**, *47* (11), 1072–1079.
74. Paoli, E. A.; Masini, F.; Frydendal, R.; Deiana, D.; Schlaup, C.; Malizia, M.; Hansen, T. W.; Horch, S.; Stephens, I. E. L.; Chorkendorff, I., *Chem. Sci.* **2015**, *6* (1), 190–196.
75. Singh, R. K.; Rahul, R.; Neergat, M., *Phys. Chem. Chem. Phys.* **2013**, *15* (31), 13044–13051.
76. Pillo, T.; Zimmermann, R.; Steiner, P.; Hüfner, S., *J. Phys. Condens. Matter* **1997**, *9*, 3987–3999.
77. Chen, D.; Li, Y.; Liao, S.; Su, D.; Song, H.; Li, Y.; Yang, L.; Li, C., *Sci. Rep.* **2015**, *5* (April 2014), 1–9.
78. Chang, Y.; Yuan, C.; Li, Y.; Liu, C.; Wu, T.; Zeng, B.; Xu, Y.; Dai, L., *J. Mater. Chem. A* **2017**, *5* (4), 1672–1678.
79. Zhang, G.; Yang, D.; Sacher, E., *J. Phys. Chem. C* **2007**, *111* (2), 565–570.
80. Lewera, A.; Timperman, L.; Roguska, A.; Alonso-vante, N., *J. Phys. Chem.* **2011**, *115*, 20153–20159.
81. Huang, H.; Leung, D. Y. C., *J. Catal.* **2011**, *280* (1), 60–67.
82. Zhang, T.; Wang, S.; Chen, F., *J. Phys. Chem. C* **2016**, *120* (18), 9732–9739.
83. Alayoglu, S.; Nilekar, A. U.; Mavrikakis, M.; Eichhorn, B., *Nat. Mater.* **2008**, *7* (4),

- 333–338.
84. Hao, Y.; Li, M.; Cárdenas-Lizana, F.; Keane, M. A., *Catal. Struct. React.* **2015**, *1* (3), 132–139.
 85. Álvarez-Rodríguez, J.; Rodríguez-Ramos, I.; Guerrero-Ruiz, A.; Gallegos-Suarez, E.; Arcoya, A., *Chem. Eng. J.* **2012**, *204–206*, 169–178.
 86. Ekou, T.; Ekou, L.; Vicente, A.; Lafaye, G.; Pronier, S.; Especel, C.; Marécot, P., *J. Mol. Catal. A Chem.* **2011**, *337* (1–2), 82–88.
 87. González, C. A.; Ardila, A. N.; De Correa, C. M.; Martínez, M. A.; Fuentes-Zurita, G., *Ind. Eng. Chem. Res.* **2007**, *46* (24), 7961–7969.
 88. Zhang, C.; He, H.; Tanaka, K., *Appl. Catal. B Environ.* **2006**, *65* (1–2), 37–43.
 89. Hernandez-Mejia, C.; Gnanakumar, E. S.; Olivos-Suarez, A.; Gascon, J.; Greer, H. F.; Zhou, W.; Rothenberg, G.; Raveendran Shiju, N., *Catal. Sci. Technol.* **2016**, *6* (2), 577–582.
 90. Buelna, G.; Ulutagay-Kartin, M.; Nenoff, T. M., *Chem. Eng. Commun.* **2006**, *193* (5), 606–619.
 91. Richardson, R. C. *Design of Fixed Bed Catalytic Reactors*; Iowa State University, Ed.; 1963.
 92. Zhao, X.; Wang, J.; Yang, M.; Lei, N.; Li, L.; Hou, B.; Miao, S.; Pan, X.; Wang, A.; Zhang, T., *ChemSusChem* **2017**, *10* (5), 819–824.
 93. Wang, J.; Zhao, X.; Lei, N.; Li, L.; Zhang, L.; Xu, S.; Miao, S.; Pan, X.; Wang, A.; Zhang, T., *ChemSusChem* **2016**, *9* (8), 784–790.

CATALYTIC CONVERSION OF BIOMASS

CHAPTER 4. ROLE OF SUPPORT IN GLYCEROL HYDROGENOLYSIS

Contents

4	Role of support in glycerol hydrogenolysis	157
4.1	Introduction.....	157
4.2	Catalytic activity	159
4.3	Catalyst characterisation	164
4.3.1	Analysis of the textural properties of the catalysts.	164
4.3.2	Elemental analysis and oxidation state species of the catalysts.....	167
4.3.3	The surface chemistry and structure of the supported catalyst for glycerol hydrogenolysis	175
4.3.4	Effect of catalysts acidity on hydrogenolysis of glycerol.....	185
4.4	Conclusions.....	188
4.5	References.....	190

4 Role of support in glycerol hydrogenolysis

4.1 Introduction

Among the different roles of supports, the most important ones are dispersing the active phase of the catalyst, increasing metal surface area and improving the catalytic performance through interactions between the metal and support.¹ In general, using a heterogeneous catalyst, the reaction rate is accelerated because the reactant chemisorbs on the active surface and the reactions occur on the surface of the catalyst. Typically, the role of a metal is to activate the substrate and/or reactant(s), while one of the roles of support is to disperse the metal and to stabilise them. Highly dispersed supported metal nanoparticles provide an increased metal surface accessibility for the reactant(s) to adsorb. Therefore, the larger the dispersion, the higher the number of active sites resulting in higher activity. The support properties, such as morphology, surface area, pore volume and pore size distribution also play an essential role in enhancing catalyst stability and performance. In addition, the acidic or basic properties of the support are important to make the catalyst behave as a multifunctional catalyst. Understanding the relationship between the support and the activity is crucial to design a tailor-made catalyst for any given reaction.

For glycerol hydrogenolysis, the role of the support has been studied mainly for materials such as activated carbon, Al₂O₃ and SiO₂.^{2,3} Monometallic Ru-based catalyst has been widely reported for glycerol hydrogenolysis supported over many supports such as SiO₂, Al₂O₃, activated carbon, graphite, carbon nanotubes (CNT), KL zeolites.^{3,4} For example, SiO₂ shows lower thermal stability than Al₂O₃, but it has stronger metal-support interaction. It has been reported that for monometallic Ru catalyst carbon is more suitable than Al₂O₃ and SiO₂.³ Delgado *et al.* also compared Al₂O₃ with Al₂O₃-SiO₂ and TiO₂ as support for this reaction. Among all of them, TiO₂ leads to the best performance. It favours the maintenance of the carbonaceous chain of glycerol without breaking the C-C bond.⁵

As reported in Chapter 3, the hydrogenation of glycerol can be promoted by combining two metals in a bimetallic catalyst. However, the dehydration step preceding the hydrogenolysis of glycerol is catalysed by the acid sites of the material.⁶ In this regard, catalysed bifunctional system is convenient for this hydrogenolysis reaction, as mentioned in the introduction Chapter 1.⁷ Zeolites are versatile, cheap, and they can be easily modified.⁸⁻¹¹ They have been used extensively for dehydration of glycerol showing excellent catalytic activity for the selective production of acrolein.¹¹ However, their use for hydrogenolysis is more limited to the vapour

phase reaction.¹² Pt monometallic and bimetallic Pt-Cu/Mordenite was employed to catalyse the vapour phase reaction of glycerol hydrogenolysis, where the bimetallic phase-support interaction was found crucial.¹³ The total acidity of bimetallic was higher than the corresponding monometallic, suggesting that the acid strength of catalysts due to the zeolite material plays an essential function in this reaction.

One of the main challenges of using zeolites for aqueous phase reaction is the insufficient hydrothermal stability of zeolites. In general, in vapour phase reactions, little damage is caused. However, under liquid phase conditions degradation or even structural collapse of the zeolites framework can occur.^{14,15} Many factors such as dealumination and desilication can contribute to the weakness of these materials in a hot aqueous medium.¹⁴⁻¹⁷ The reaction at high-temperatures in water leads to the hydrolysis of the Si-O-Si or/and Al-O-Si bond, which lead to the removal of a certain number of hydroxylated Al or Si species from the framework. It has been reported that it depends on the hydrophilic or hydrophobic character of the zeolite surface and also on the number of defect sites in the framework.^{15,18} For instance, it has been found that in basic medium ZSM-5 zeolites partially dissolve, but the Al content can decrease the dissolution rate.^{19,20} The pore size and arrangement are also essential factors in determining their stabilities.¹⁸ For instance, monometallic Ru catalyst supported on a modified HY type zeolite was reported by Jin *et al.* in aqueous phase glycerol hydrogenolysis reaction.¹⁶ They found that treating the support with HCl increases the BET surface area and the number of strong acid sites due to partial dealumination. However, when HY zeolites are treated with NaOH; instead, it suffered desilication resulting in lower conversion. Lin *et al.* reported a sequential two-layer catalytic system in a fixed-bed reactor for the hydrogenolysis of glycerol in the liquid phase.²¹ This catalytic system was based on a first acidic H- β zeolite layer followed by a Ni/Al₂O₃ catalyst layer in the packed bed.

Besides the reaction routes, it is important to notice that the support material can influence the metal particle size. The reason is that this could also influence the number of active sites available. In this regard, the incorporation of a second metal forming bimetallic catalysts could help to disperse the metal better on the support. But also, it could help to stabilise the bimetallic NPs avoiding particles agglomeration and sintering, that is the case of RuFe on the CNT surface.²²

As mentioned in Chapter 1, another strategy to improve catalytic activity is the modification of the support. The use of a noble metal catalyst with a low-valent metal oxide such as Re or

W could form metallic bonds. This was proved to selectively favour a reaction route over the other, with an observed increase in the production of 1,3-PDO.³ However it has also been reported that an excess of these oxide species on the catalyst support can block the active sites.²² In the case of ReOx, the catalyst acidity was crucial. Recently, it was reported that the surface W density controls the formation of polytungstates, which are species that exhibits weak Brønsted acidity, which is required to produce 1,3-propanediol selectively.^{23,24}

Based on the *state-of-the-art* of glycerol hydrogenolysis, the simultaneous presence of a noble metal and acid sites can favour the formation of C3 products.^{25,26} To improve the catalyst performance for glycerol hydrogenolysis, the bimetallic system based on ruthenium and palladium was selected to study the role of the acidity of the supports. This chapter aims to investigate the oxidation properties and acidity of supported PdRu catalysts and mainly, how the support material affects these properties. The use of an appropriate support was investigated, and the attention turned on zeolites. After investigating their catalytic performance, it was also compared with other metal oxides of interest such as SiO₂ and Al₂O₃, and a novel modification of TiO₂ doped with W, (Ti_{0.9}W_{0.1}O₂).

Characterisation of the representative catalysts is also presented in this chapter. One of the principal challenges in catalysis is to identify the active site of a catalyst for a specific reaction. This chapter combines insights from basic structural characterisation techniques with their catalytic activities, specifically the formation of C3 products, to arrive at a structure-activity correlation.

4.2 Catalytic activity

The catalysts were prepared using the same synthesis methodology used in Chapter 3, *i.e.* modified wet impregnation, described in Chapter 2. All the catalysts were then tested for the glycerol hydrogenolysis reaction. The activity of the supported catalysts was obtained under mild reaction conditions, fixed at 165 °C, 20 bar H₂, 800 rpm; using a glycerol to metal molar ratio of [1:0.005]. The results are shown in *Figure 4-1*. The product distribution obtained with each catalyst is summarised in *Table 4-1* and *Table 4-2* for 5 and 16 h of reaction, respectively.

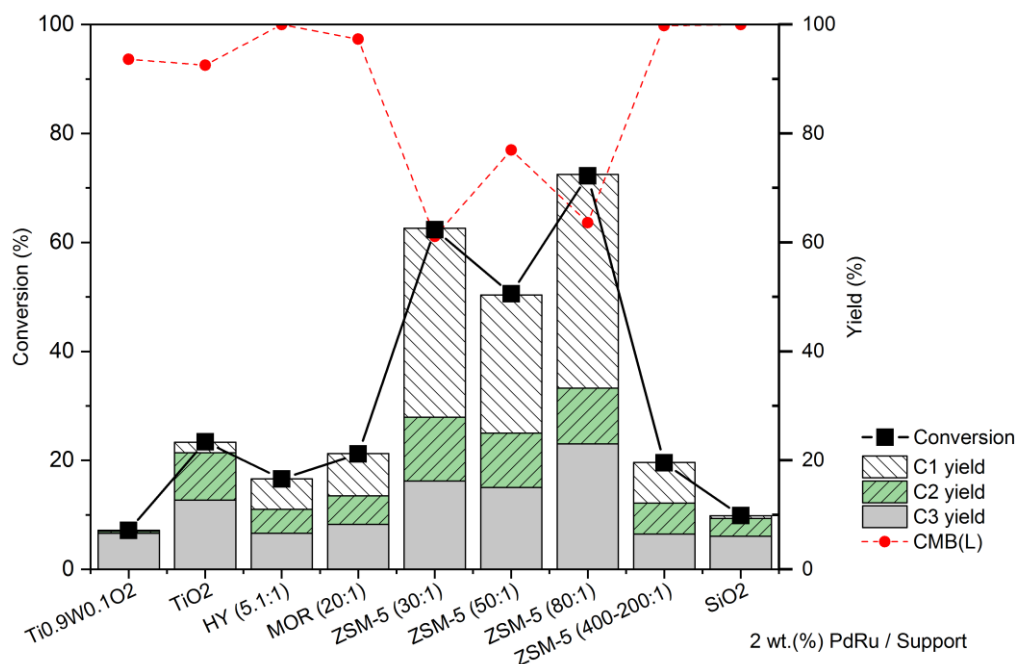


Figure 4-1 Effect of the support on the activity and selectivity using a 2 wt.% PdRu/support catalyst tested using as a molar ratio 1: 0.005 glycerol-metal and reaction conditions of 165 °C, 20 bar H₂, 800 rpm. Conversion (■), carbon mass balance (L) (---●---) and yield of products labelled as C1 (▨), C2 (▤), C3 (▥).

Table 4-1 Effect of the supports on the catalytic performance of the PdRu bimetallic catalyst for Glycerol Hydrogenolysis. Product distribution and carbon mass balance of liquid product CMB (L) versus total carbon mass balance CMB (L+G).

Entry	Conversion	Products Selectivity (%)													CMB(L) (%)	CMB(L+G) (%)
		Acetone	MeOH	EtOH	2-PO	1-PO	Acetol	1,2-PDO	EG	1,3-PDO	CO ₂	CH ₄	C ₂ H ₆	C ₃ H ₈		
1	7	0	0	1	0	10	1	82	3	0	0	3	1	0	94	96
2	23	0	2	0	9	5	0	33	26	4	0	11	9	2	93	96
3	17	0	2	0	9	5	0	22	25	1	0	31	2	3	98	100
4	21	0	1	0	11	5	0	17	22	1	0	35	3	5	97	100
5	62	0	2	0	8	3	0	9	14	0	0	54	5	6	61	81
6	51	0	1	0	8	2	0	14	15	1	0	49	5	5	77	96
7	72	0	1	0	7	2	0	17	9	0	0	53	5	6	64	92
8	20	0	2	0	10	3	0	16	27	1	0	37	2	3	98	100
9	10	0	2	1	0	9	0	53	31	0	0	3	1	0	99	100

2 wt. % PdRu supported on 1) Ti_{0.9}W_{0.1}O₂, 2) TiO₂, 3) HY (5.1:1), 4) MOR (20:1), 5) ZSM-5 (30:1), 6) ZSM-5 (50:1), 7) ZSM-5 (80:1), 8) ZSM-5 (400-200:1), 9) SiO₂. Reaction conditions 165 °C; pH₂: 20 bar, 800 rpm, 5h; glycerol to the metal molar ratio of [1:0.005]

The results obtained shows that the activity was different, indicating the choice of support is crucial for this reaction. Among all the supports, ZSM-5 (entries 5, 6 and 7) exhibits the higher conversion at the same reaction time, but a lower selectivity to liquid products, as evidenced from the carbon mass balance for liquid products CMB (L) in *Figure 4-1*. Varying the Si/Al ratios (30:1, 50:1, 80:1) of the ZSM-5 zeolite, the results illustrates a reasonably high activity in terms of conversion. This improvement in conversion is based on significant production of gases phase products such as CH₄, *via* C-C bond cleavage. *Figure 4-2* shows the results of the iso-conversion activity tests of the supported catalyst. This chart allows us to contrast the catalytic data by comparing the product selectivity obtained by the different catalysts tested. PdRu/TiO₂ gives a 1,2-PDO selectivity of 50 % at iso-conversion conditions (*ca.* 50 %), while PdRu/ZSM-5 (50:1) only achieved *ca.* 15 % (see *Figure 4-2-A*). Major product for this catalyst CH₄ with a selectivity of 49 %; producing about 15 % of EG and 8 % of 2-PO selectivity.

In contrast, for the other two types of zeolites tested, PdRu/HY (Entry 3) and PdRu/MOR (Entry 4), the conversion was similar to that of PdRu/TiO₂ catalyst *ca.* 20 %. However, the product distribution in the case of Mordenite as support suggests that this catalyst promotes C-C cleavage. (see *Figure 4-2-B*). Mordenite zeolite has been used for glycerol hydrogenolysis in the gas phase because of the strong metal-support interaction and the appropriate acidity of the support. Priya *et al.* achieve high conversion (94.9 %) and excellent yield of 1,3-PDO (48.6 %), using monometallic 2 wt. % Pt/Mor.¹² They also tested a bimetallic catalyst of Pt-Cu/Mor for this reaction with an increased metal loading (2 wt. % for the Pt and 5 wt. % for Cu). This addition of Cu improved the selectivity to 1,3-PDO up to 58.5 % at 90 % of conversion.²⁷ Their catalysts were also prepared by wet impregnation method although these results were obtained under very different reaction conditions and their catalyst was calcined instead of reduced after impregnation. Herein, at conversions *ca.* 20 %, PdRu/TiO₂ is the most selective catalyst for 1,2-PDO (33 %) compared to PdRu/MOR (17 %), PdRu/ZSM5-200:1 (16 %) or PdRu/Al₂O₃ (19 %). All of them produced a significant amount of EG (between 22-36 %). However, PdRu/TiO₂ is the one that generates lesser CH₄ (11 %) compared to other supports (33-37 %). For the gas phase dehydration of glycerol, it has been reported that zeolites with different Si:Al ratios follow the order MOR [20:1] > ZSM-5 [23:1] > HY [5.1:1].^{9,27} Based on the results presented here, to the activity follows the order ZSM-5 >> MOR [20:1] > HY[5.1:1].

Entry 1 in *Figure 4-1* corresponds to the results obtained with PdRu over a TiO₂ support that contains 10 % of tungsten doping resulting in Ti_{0.909}W_{0.091}O₂, support synthesised by Dr A. Folli from Cardiff University.²⁸ For simplicity, this support was labelled as Ti_{0.9}W_{0.1}O₂. This

PdRu/Ti_{0.9}W_{0.1}O₂ catalyst gave the best selectivity to 1,2-PDO, followed by the SiO₂ (Entry 9) and TiO₂ supported catalyst (Entry 2). However, the conversion of glycerol for entries 1 and 9 was below 10 %. It has been reported that the presence of moderate strength of Lewis acidity leads to good 1,2-PDO selectivity.²⁹ SiO₂ has been used widely for this reaction, giving an excellent 1,2-PDO selectivity for the bimetallic Ru-Re catalyst.³⁰ In this case, the synergetic contribution of the Re oxide (acid sites) to the Ru metal sites on the pre-reduced Ru-Re/SiO₂ led to its high activity (51 % of conversion and 25 % selectivity) using quite high metal loading (9 wt. %). At low conversion levels (*ca.* 15 %), *Figure 4-1-C* shows that the selectivity towards 1,2-PDO follows the other PdRu/Ti_{0.9}W_{0.1}O₂ (49 %) > PdRu/TiO₂ (40 %) > PdRu/HY (22 %).

An exciting outcome is that the highest selectivity to 1,2-PDO (82 %) and the lowest selectivity of EG (3 %) were obtained using the PdRu bimetallic system over the Ti_{0.9}W_{0.1}O₂ support, even though the conversion achieved was *ca.* 7 % (*Figure 4-2-D*). Compared to PdRu/SiO₂ (1,2-PDO selectivity 42 %), the selectivity to EG was also insignificant, (28% for the PdRu/SiO₂) vs (3 % for PdRu/Ti_{0.9}W_{0.1}O₂). 1-propanol is also obtained, it is possibly produced from 1,2-PDO (see *Scheme 3-1* reported in Chapter 3). The production of 1-PO from hydrogenolysis of 1,2-PDO was previously reported.³¹ In general, under mild conditions, it is challenging to reach both, high conversion of glycerol and high selectivity of 1,2-PDO, because in the liquid phase reaction conditions it is common to find the conversion of 1,2-PDO into propanol or even propane at longer reaction times.^{3,32,33} Besides this catalyst also shows the higher selectivity to propane over 16 h of reaction (*Table 4-2* and *Figure 4-2-C*). Chau *et al.* reported that HSiW/Al₂O₃ supported catalysts are shown high selectivity to 1-PO, proposing an economical production of green and sustainable 1-PO from glycerol hydrogenolysis.³⁴

The activities of PdRu supported on metal oxides such as PdRu/Ti_{0.9}W_{0.1}O₂, PdRu/SiO₂ and PdRu/Al₂O₃, achieved low conversions around 12, 22 and 7 % after 16 h of reaction respectively (*Table 4-2*). Overall, the results indicate that TiO₂, which gives around 55 % of conversion and 50 % of 1,2-PDO selectivity seems to be the better option.

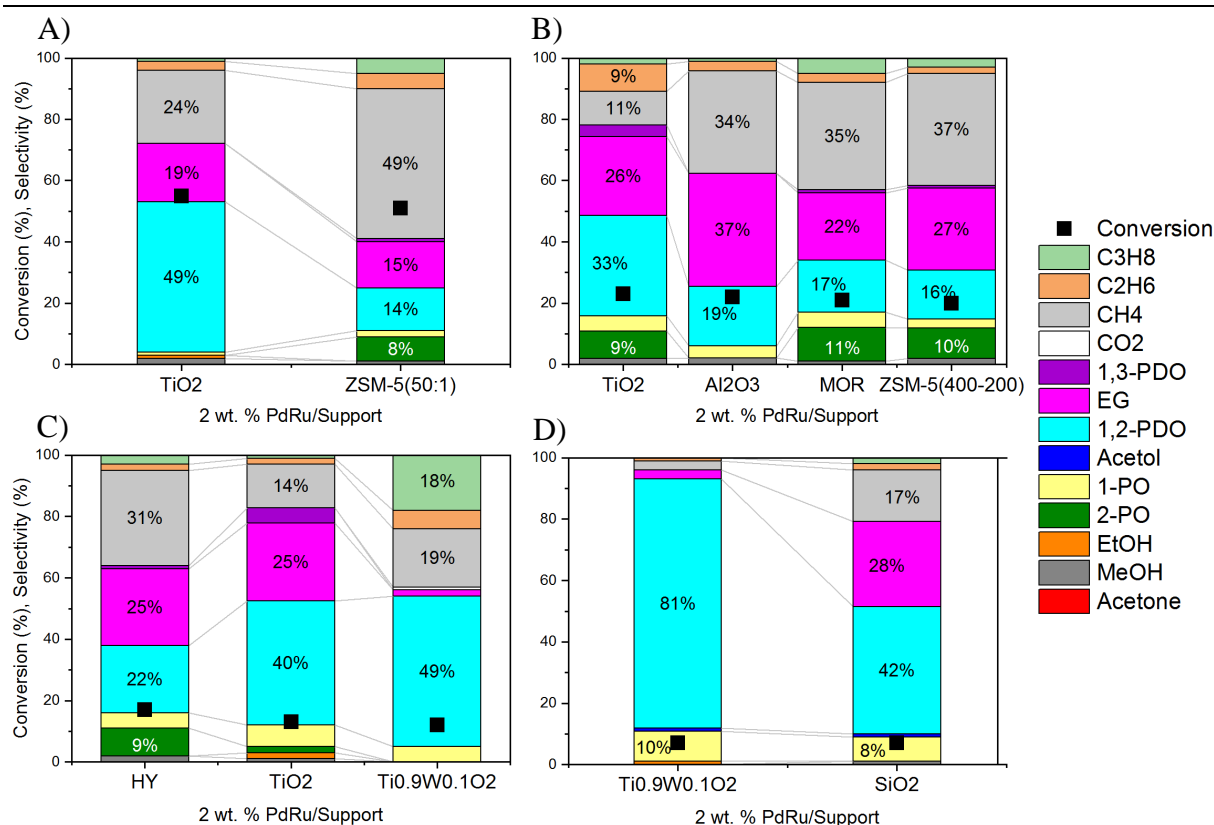


Figure 4-2 Distribution of the hydrogenolysis products at iso-conversion values (■) of A) 50-55 %, B) 20-25 %, C) 15-20 % and D) 5-10 %. Using 2 wt. % PdRu/support catalyst tested using as a molar ratio 1: 0.005 glycerol-metal and reaction conditions of 165 °C, 20 bar H₂, 800 rpm.

Table 4-2 Effect of the supports on the catalytic performance of the PdRu bimetallic catalyst for Glycerol Hydrogenolysis. Product distribution and carbon mass balance of liquid product CMB (L) versus total carbon mass balance CMB (L+G).

Entry	Conversion	Products Selectivity (%)													CMB(L) (%)	CMB(L+G) (%)
		Acetone	MeOH	EtOH	2-PO	1-PO	Acetol	1,2-PDO	EG	1,3-PDO	CO ₂	CH ₄	C ₂ H ₆	C ₃ H ₈		
1	12	0	0	0	0	5	0	49	2	0	1	19	6	18	96	101
2	55	0	2	1	0	1	0	49	19	0	0	24	3	1	72	83
3	89	0	1	1	0	4	1	26	10	0	0	38	13	7	31	56
4	22	0	2	0	0	4	0	19	36	0	0	33	3	1	86	93
5	7	0	1	0	0	8	1	42	28	0	0	17	2	2	64	98

2 wt. % PdRu supported on 1) Ti_{0.9}W_{0.1}O₂, 2) TiO₂, 3) ZSM-5 (80:1), 4) Al₂O₃, 5) SiO₂. Reaction conditions 165 °C; pH₂: 20 bar, 800 rpm, 16h; glycerol to the metal molar ratio of [1:0.005].

4.3 Catalyst characterisation

4.3.1 *Analysis of the textural properties of the catalysts.*

The surface area, pore volume and pore size distribution of the support play an important role in dispersing the active metal of the catalyst.³⁵ *Figure 4-3* shows the adsorption-desorption isotherms of the different supported catalysts used in this study. The characteristic zeolites adsorption isotherms are a combination of Type I and Type IV(a) curves, according to the IUPAC classification (see Chapter 2, *Section 2.2.4*). These results are in agreement with the literature for this kind of materials.³⁶ Type I isotherm is typical for microporous materials, where the uptake rises sharply at a shallow relative pressure (P/P_0) due to the microporous filling. Type IV(a) isotherm is representative of mesoporous materials, showing a small hysteresis loop that could be associated with pore filling and emptying when occurs capillary condensation.³⁷ It is no present in the case of the bimetallic supported on Mordenite.

On the other hand, the nitrogen adsorption isotherm for the metal oxide catalysts is a Type IV isotherm (*Figure 4-3*). The curves show, in accordance with the literature, that the capillary condensation is accompanied by hysteresis for the bimetallic supported on TiO_2 ³⁸ and SiO_2 ³⁹ and very reduced loop in the case of the Al_2O_3 .⁴⁰ The shape of hysteresis loops observed is corresponding to the H3 identify by the IUPAC classification. H3 hysteresis loop could be observed since the pore network consists of macropores which are not entirely filled with pore condensate.³⁷

According to the shapes of the isotherms obtained for all the zeolites samples, the sharp adsorption increases, filling of micropores is done for P/P_0 below 0.1. Beyond that point, the quantity adsorbed outside the micropores is minimal in comparison. A weak hysteresis loop can be observed at high P/P_0 near 0.8. This corresponds with the filling of the mesopores, due to interparticle voids in the zeolites.⁴¹ The comparison of the different zeolites tested can be observed in the following overlap plot (*Figure 4-4*). This plot shows that the BET specific surface area and total pore volume are much lower for the PdRu/ZSM 30:1 than for the PdRu/MOR, while for the rest of zeolite-based catalysts the difference is not so significant in term of surface area.

Isotherm Summary

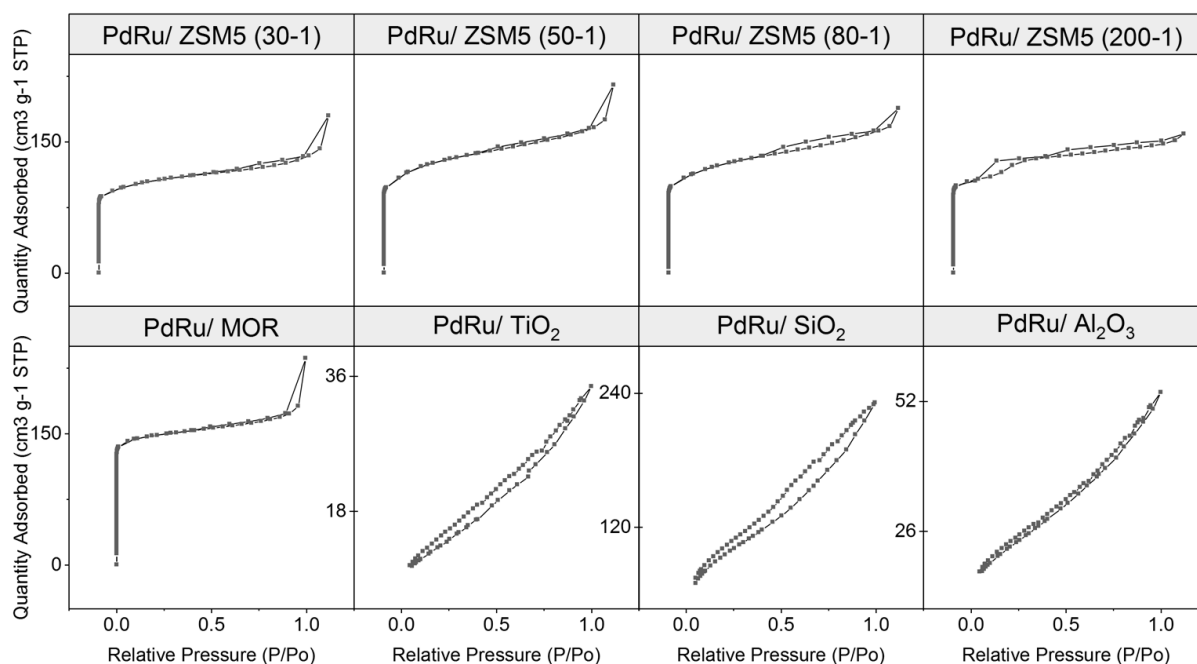


Figure 4-3 Isotherm of the supported 2 wt. % PdRu bimetallic catalysts. PdRu/ZSM5 and PdRu/MOR catalysts are showing a combination of Type I and Type IV(a) curves. PdRu/metal oxides such as TiO₂, SiO₂ and Al₂O₃ present Type IV isotherm.

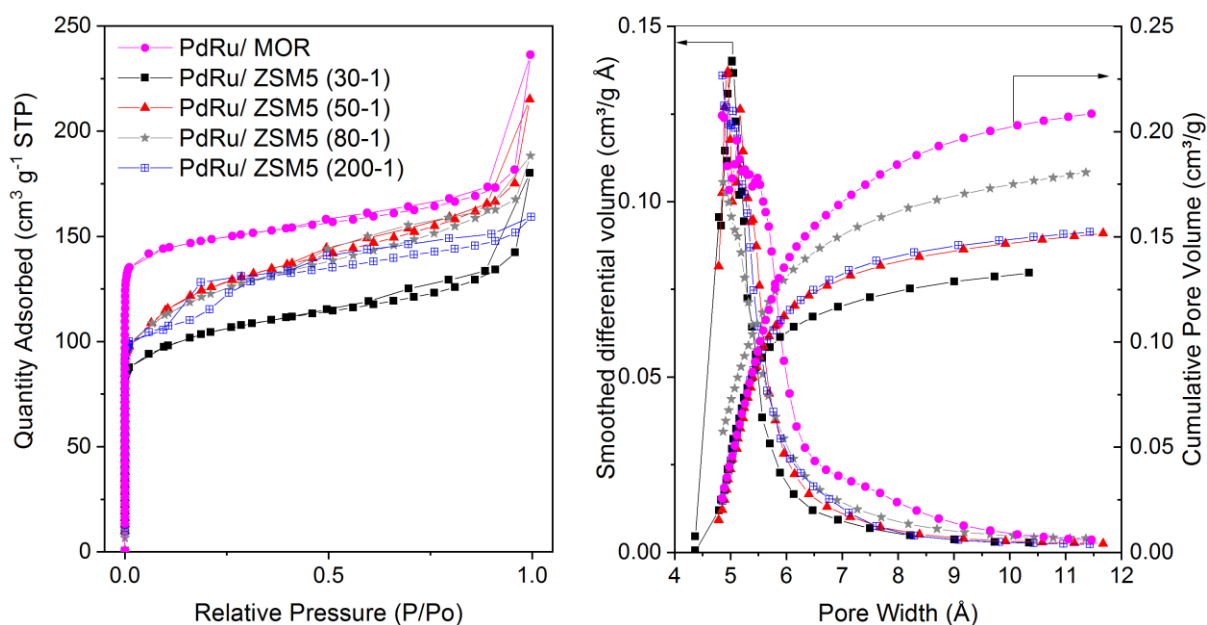


Figure 4-4 Adsorption-desorption isotherms (left-hand site) and Horvath-Kawazoe differential and cumulative pore volume plot (right-hand site) for the PdRu/zeolites analysed on the 3-Flex instrument. The pore size distribution was calculated using a cylinder pore geometry (Saito-Foley).⁴²

The specific surface area was determined using the BET (Braunauer-Emmett-Teller), model. The micropore volume and specific surface area of micropores were calculated using the t-plot analysis micropore volume. The results are summarised in *Table 4-3* and *Table 4-4*.

Table 4-3 BET, t-Plot and Horvath-Kawazoe summary for zeolites before and after impregnation of a 2 wt. % PdRu catalyst.

<i>Metal/ Support</i>	<i>SiO₂: Al₂O₃ molar ratio</i>	<i>Surface area, m²/g</i>	<i>C</i>	<i>Micro- pore vol. cc/g</i>	<i>Micro- pore area, m²/g</i>	<i>External surface area, m²/g</i>	<i>Max. pore volume, cc/g</i>	<i>Median pore width, Å</i>
<i>PdRu/MOR</i>	20:1	531	114808	0.202	466	65	0.209	5.6
<i>Calcined ZSM-5</i>	30:1	406	7533	0.139	319	87	0.143	5.4
<i>PdRu/ZSM5</i>	30:1	378	13140	0.091	207	171	0.135	5.2
<i>Calcined ZSM-5</i>	50:1	445	8404	0.157	385	87	0.158	5.5
<i>PdRu/ZSM5</i>	50:1	425	9557	0.132	283	142	0.151	5.3
<i>Calcined ZSM-5</i>	80:1	457	7785	0.147	336	121	0.161	5.5
<i>PdRu/ZSM5</i>	80:1	426	19771	0.127	285	141	0.157	5.3
<i>Calcined ZSM-5</i>	200:1	423	56713	0.030	80	344	0.150	5.5
<i>PdRu/ZSM5</i>	200:1	427	60632	0.038	105	322	0.150	5.3

Table 4-4 BET and t-Plot results of metal oxides before and after impregnation of a 2 wt. % PdRu catalyst.

<i>Support Catalyst</i>	<i>Surface area, m²/g</i>	<i>Micropore vol. cc/g</i>	<i>Micropore área, m²/g</i>	<i>External surface area, m²/g</i>	<i>Total pore volume, cc/g</i>	<i>Radius, Å</i>
<i>TiO₂</i>	66	0.000	0	66	0.430	166.7
<i>PdRu/TiO₂</i>	47	0.002	3	43	0.051	256.6
<i>Al₂O₃</i>	113	0.000	0	113	0.723	167.6
<i>PdRu/Al₂O₃</i>	79	0.007	13	65	0.078	235.6
<i>PdRu/SiO₂</i>	332	0.031	65	266	0.333	167.9

In the case of the calcined zeolites, the surface areas are in general higher than that reported by the supplier. For instance, the commercial H-Mordenite is supposed to have a surface area of 500 m²/g, and the ZSM-5 for the Si/Al ratios of [50:1] and [80:1] a surface area of 425 m²/g. For zeolites with ratios [30:1] and [400-200:1] the expected surface area was 400 m²/g.

Furthermore, the surface areas decreased after metal incorporation. The difference in the surface area of the calcined zeolite and the impregnated catalyst was at *ca.* 5-7 % as shown in *Table 4-3*. This effect was noticed for all the ZSM-5 zeolites, with exception to the ZSM-5 with ratio [400-200:1], which does not show any significant change.

In the case of the mesoporous materials (metal oxides), the surface area was reduced by *c.a.* 30 % after the impregnation with 2 wt. % metal loading on the support (*Table 4-4*). PdRu-loaded samples showed a change in the textural properties. Both surface area and total pore volume of the different catalyst were decreased after the metal impregnation. These can be attributed to the partial occupation of the catalyst pores by PdRu nanoparticles, which is supported by the micropore volume analysis.⁴³

The catalyst with the highest surface area is PdRu/MOR (531.42 m²g⁻¹), which gave a glycerol conversion around 20 % in 5 h. The supported PdRu/ZSM-5 gave a higher conversion, with a surface area around 100 m²g⁻¹ inferior to the PdRu/Mor. This study shows that surface area alone is not affecting the catalytic activity, and hence, other structural properties must be studied to arrive at a structure-activity correlation.

4.3.2 *Elemental analysis and oxidation state species of the catalysts*

The surface compositions of the catalyst were determined by XPS analysis, measured with *CasaXPS*® (*Table 4-5*). Meanwhile, quantitative analysis of the supported PdRu catalysts obtained from MP-AES was also evaluated to determinate the actual metal loading of the bimetallic catalysts, which were prepared with equimolar ratio and a total metal loading equal to 2 wt. % in all cases.

Table 4-5 Quantitative analysis of the surface composition of the supported PdRu catalyst obtained from XPS spectra

	<i>Pd</i>	<i>Ru</i>	<i>Ratio Ru/Pd</i>
<i>Catalyst</i>	% Conc.	% Conc.	%
<i>PdRu/Al₂O₃</i>	0.3	0.32	1.1
<i>PdRu/SiO₂</i>	0.11	0.1	0.9
<i>PdRu/TiO₂</i>	0.6	0.49	0.8
<i>PdRu/ZSM5 (200:1)</i>	0.11	0.08	0.7
<i>PdRu/ZSM5 (30:1)</i>	0.07	0.05	0.7
<i>PdRu/ZSM5 (50:1)</i>	0.08	0.1	1.3
<i>PdRu/ZSM5 (80:1)</i>	0.04	0.02	0.5
<i>PdRu/MOR (20:1)</i>	0.2	0.25	1.3
<i>PdRu/HY (5.1:1)</i>	0.05	0.07	1.4

Although XPS gives a general idea about the catalyst surface composition, quantitative elemental analysis using different techniques such as ICP or MP-AES is also recommended to study the bulk composition. The analysis of the Ru/Pd ratio and the metal loadings determined by MP-AES analysis are summarized in *Table 4-7*.

Several batches of PdRu/TiO₂ were analysed to confirm the reproducibility of the catalyst synthesis. In general, the catalyst loading seems to be slightly higher than the expected 2 wt.% (average of 2.32 wt. % \pm 0.14). These differences between the expected value and the measured are due to experimental errors during the catalyst preparation or the analysis itself. MP-AES also confirmed the reproducibility of catalysis synthesis. Different batches (1-4) for the PdRu/TiO₂ catalysts were analysed, and the results obtained are very similar (*Table 4-6*). As can be seen, the metal loading values of Pd and Ru were close to the nominal values in all cases, revealing the equal molar ratio of Pd to Ru dispersed on the different supports.

Table 4-6 Quantitative analysis of the supported PdRu catalyst obtained from MP-AES analysis. Measurements obtained with selected wavelengths (340.46 nm for Pd and 349.89 nm for Ru).

2 wt. % PdRu/ Support	Catalyst Weight, mg	Pd, ppm	Pd, %	Ru, ppm	Ru, %	Metal loading %	Ru/Pd % Ratio	Ru/Pd Molar Ratio
<i>TiO₂ -1</i>	25.7	3.04	1.18	3.26	1.27	2.45	1.07	1.13
<i>TiO₂ -2</i>	25.5	2.6	1.02	3.08	1.21	2.23	1.18	1.25
<i>TiO₂ -3</i>	26.2	2.61	0.99	3.00	1.15	2.14	1.15	1.21
<i>TiO₂ -4</i>	25.5	2.94	1.15	3.16	1.24	2.39	1.07	1.13
<i>MOR (20:1)</i>	26.4	2.75	1.04	3.54	1.34	2.38	1.29	1.36
<i>ZSM5 (50:1)</i>	26.6	3.08	1.16	2.68	1.01	2.17	0.87	0.92
<i>ZSM5 (80:1)</i>	26.5	3.41	1.29	3.01	1.14	2.42	0.88	0.93
<i>ZSM5 (30:1)</i>	27.9	3.08	1.10	3.95	1.41	2.52	1.28	1.35
<i>ZSM (200:1)</i>	28.2	3.54	1.26	2.42	0.86	2.11	0.68	0.72
<i>HY (5.1:1)</i>	23.4	2.45	1.05	3.04	1.30	2.35	1.24	1.31

Nevertheless, the values differ quite significantly between the molar ratios obtained from the XPS and the MP-AES. The reason is that XPS is analysing the surface of the catalyst with a penetration depth between 1-10 nm.^{44,45} On the contrary, the MP-AES is reporting the total metal loading, after the microwave-assisted digestion of the catalysts in aqua regia, as described in Chapter 2, section 2.2.4. The catalyst composition was also characterised by Energy Dispersed X-ray analysis in both SEM and TEM. The results are summarised in Table 4-7.

Table 4-7. Catalyst composition comparison obtained from EDX and XPS.

Catalyst,								
2 wt. % PdRu/Support	Technique		Ti wt. %	O wt. %	Al wt. %	Si wt. %	Ru wt. %	Pd wt. %
TiO₂	<i>SEM</i>	*	49	48	-	-	0.95	0.6
	<i>TEM</i>		60	39	-	-	0.95	0.41
	<i>XPS</i>		57	41	-	-	1.11	0.92
SiO₂	<i>XPS</i>		-	63	-	36	0.10	0.11
Al₂O₃	<i>XPS</i>		-	58	41	-	0.33	0.31

Mordenite	<i>SEM</i>	*	-	55	4.05	39	0.65	0.56
	<i>TEM</i>	1	-	59	2.20	39	0.08	0.13
		2	-	59	3.47	37	0.47	0.32
		3	-	54	2.52	41	1.11	1.12
	<i>XPS</i>		-	63	2.31	34	0.21	0.26
ZSM5-30:1 Include Na	<i>SEM</i>	*		64	2.17	33	0.29	0.34
	<i>TEM</i>	1	-	59	2.18	37	0.71	0.53
		2**	-	51	2.66	45	0.19	0.22
		3	-	53	2.42	43	0.80	0.71
	<i>XPS</i>		-	63	1.50	36	0.05	0.07
ZSM5-50:1	<i>SEM</i>	*		60	1.51	38	0.57	0.60
	<i>TEM</i>	1	-	60	1.35	38	0.39	0.49
		2	-	60	1.30	37	0.59	0.48
		3	-	60	1.36	38	0.34	0.52
	<i>XPS</i>		-	63	1.25	36	0.10	0.08
ZSM5-80:1	<i>SEM</i>	*		53	1.71	43	0.76	1.06
	<i>TEM</i>	1	-	60	0.90	38	0.17	0.53
		2	-	60	0.87	38	0.79	0.60
		3	-	61	0.89	37	0.03	0.59
	<i>XPS</i>		-	63	0.64	36	0.02	0.04
ZSM5-200:1	<i>SEM</i>	*		51	0.62	34	1.40	1.29
	<i>TEM</i>	1	-	50	0.27	46	2.88	1.13
		2	-	54	0.25	44	0.45	1.16
		3	-	52	0.22	47	0.60	0.43
	<i>XPS</i>		-	62	2.25	36	0.25	0.20
HY	<i>SEM</i>	*		62	0.99	36	0.42	0.45
	<i>TEM</i>	1	-	57	0.98	40	0.97	0.96
		2*	-	56	2.12	33	5.30	2.95
		3**	-	60	0.04	38	0.64	0.73
	<i>XPS</i>		-	63	0.76	36	0.07	0.07

The elemental analysis performed by EDX-TEM samples marked by * represents that the chemical composition showed some traces of *Cl or **Na on the catalyst.

The sum of all the components detected for each catalyst should be equal to 100 %. In the case of the SEM-EDX results summarised in *Table 4-7*, the difference to complete 100 % is because of the presence of Cl. This element was selected during the analysis because it could be remaining on the catalyst because chloride precursors were used during the catalyst synthesis (See the elemental mapping in *Appendix 7.2*).

Note that for all the XPS results that are shown in *Table 4-7* were normalised due to the presence of the C (1s) signal from the adhesive tape, which was used as a reference setting the peak for all the samples to 284.4 eV.

The XPS results show a significant proportion of the presence of Pd (II) on the catalyst surface of all the PdRu/ZSM-5 catalysts (*Figure 4-5*) and the PdRu/Al₂O₃. However, PdO is not detected by XPS on the catalyst surface of PdRu/MOR, PdRu/HY or PdRu/SiO₂. In the case of the ZSM-5 [80:1], the most active catalyst, the Pd (0) represents 52 % of the Pd species while the Pd (II) is 48 %, being detected also some Satellite from XPS analysis (*Table 4-8*). In the case of the PdRu/ZSM-5 [50:1], the percentage of Pd (II) is smaller *ca.* 26 %. These results present a behaviour similar to the PdRu/TiO₂ (R) catalyst (discussed in Chapter 3). The relationship between the strong metal-support interaction and the catalytic performance was previously reported in for Pd-M bimetallic catalyst.⁴⁶ They conclude that one possible explanation of the Pd effect is the promotion of retro-aldol reaction which is the key to the high selectivity of EG.⁴⁶ In this case, the product that has been enhanced is CH₄, which comes for the further reduction of EG. Nevertheless, the signal-to-noise ratio is very low making challenging to make any solid conclusion.

Table 4-8 Relative concentration of different oxidation states of Ru and Pd in the supported PdRu catalyst surface derived from XPS spectra

Catalyst, 2 wt. % Metal	Pd 3d (0) % Conc.	Pd 3d (II) % Conc.	Ru 3d (0) % Conc.	Ru 3d (IV) % Conc.
<i>PdRu/MOR</i>	100	0	100	0
<i>PdRu/ZSM5 (50:1)</i>	74	26	100	0
<i>PdRu/ZSM5 (80:1)</i>	52	48	83	17

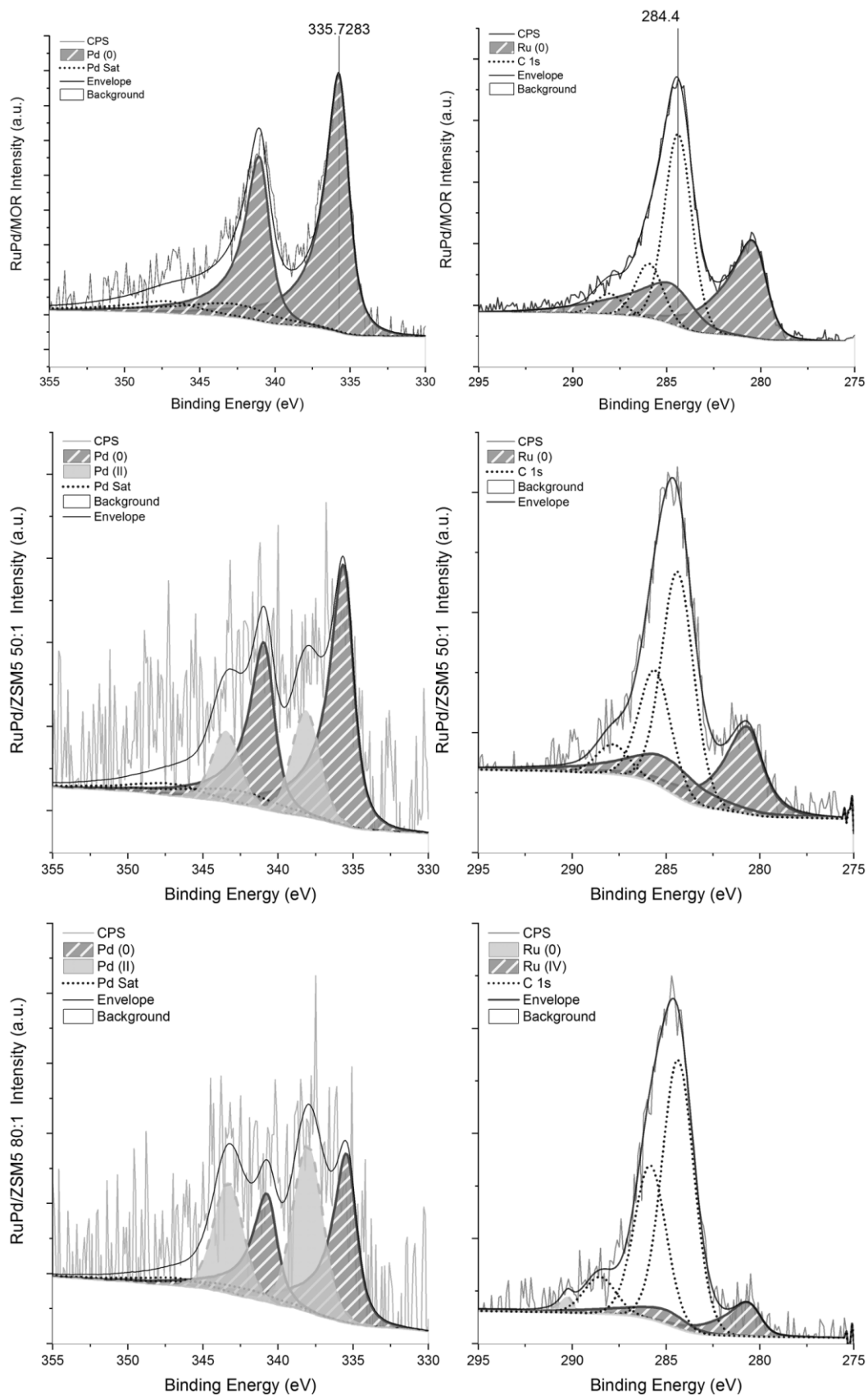


Figure 4-5 XPS spectrum of 2 wt. % PdRu/Mordenite and 2 wt. % PdRu/ZSM5 with Si/Al ratios corresponding to (50:1) and (80:1) catalyst comparison.

Many areas were analysed and selected SEM and TEM micrographs of the supported bimetallic catalysts are presented in *Figure 4-6* and *Figure 4-7*. The images reveal dispersed spherical nanoparticles of the metals. The results indicate good dispersion of the Pd and Ru on the different zeolites.

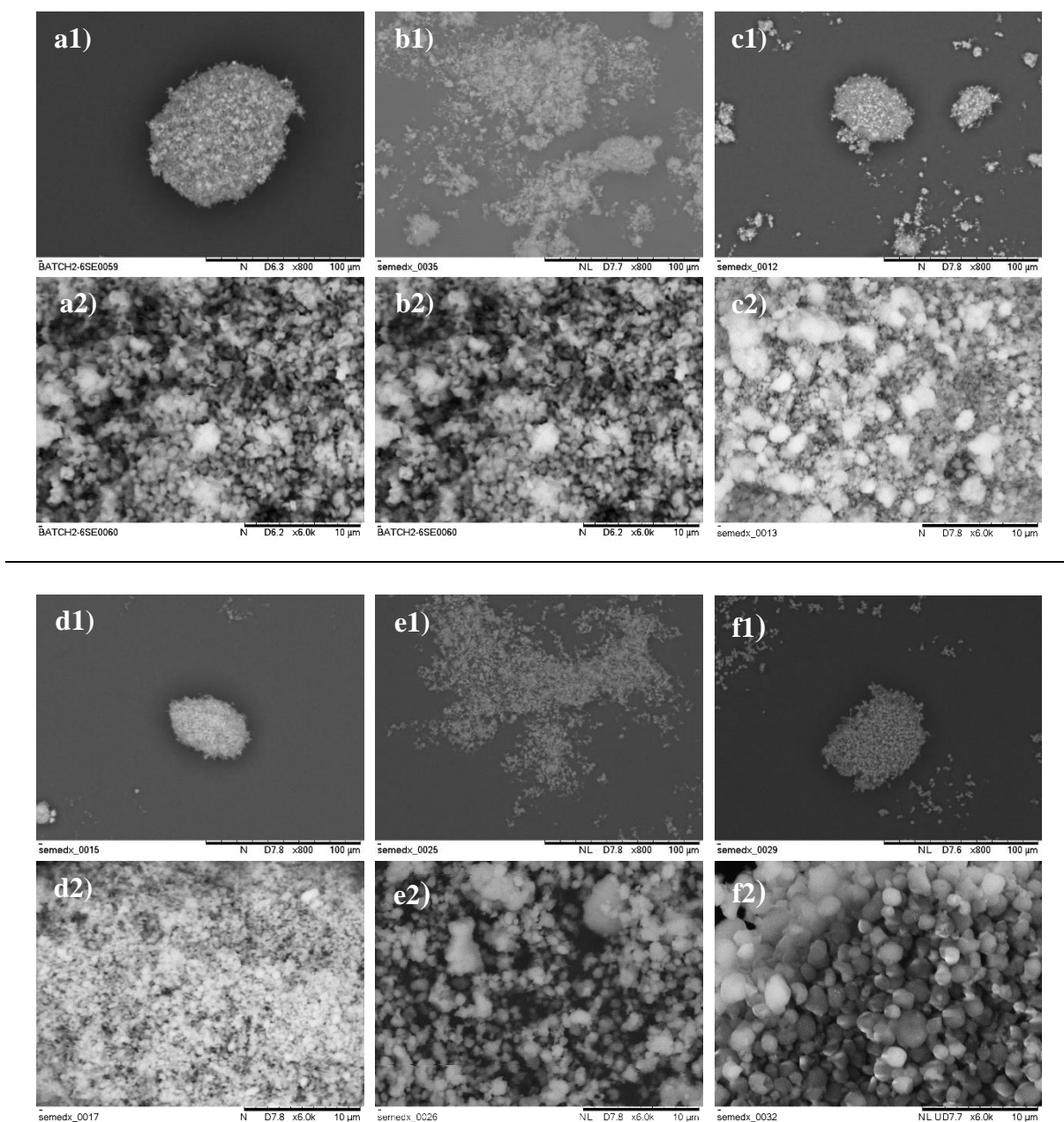


Figure 4-6 SEM images of the supported PdRu catalysts. Top-1 scale bar 100 μm. Bottom-2 scale bar 10 μm. a) HY (5.1:1), b) MOR (20:1), c) ZSM5 (30:1), d) ZSM5 (50:1), e) ZSM5 (80:1), f) ZSM5 (200-400:1)

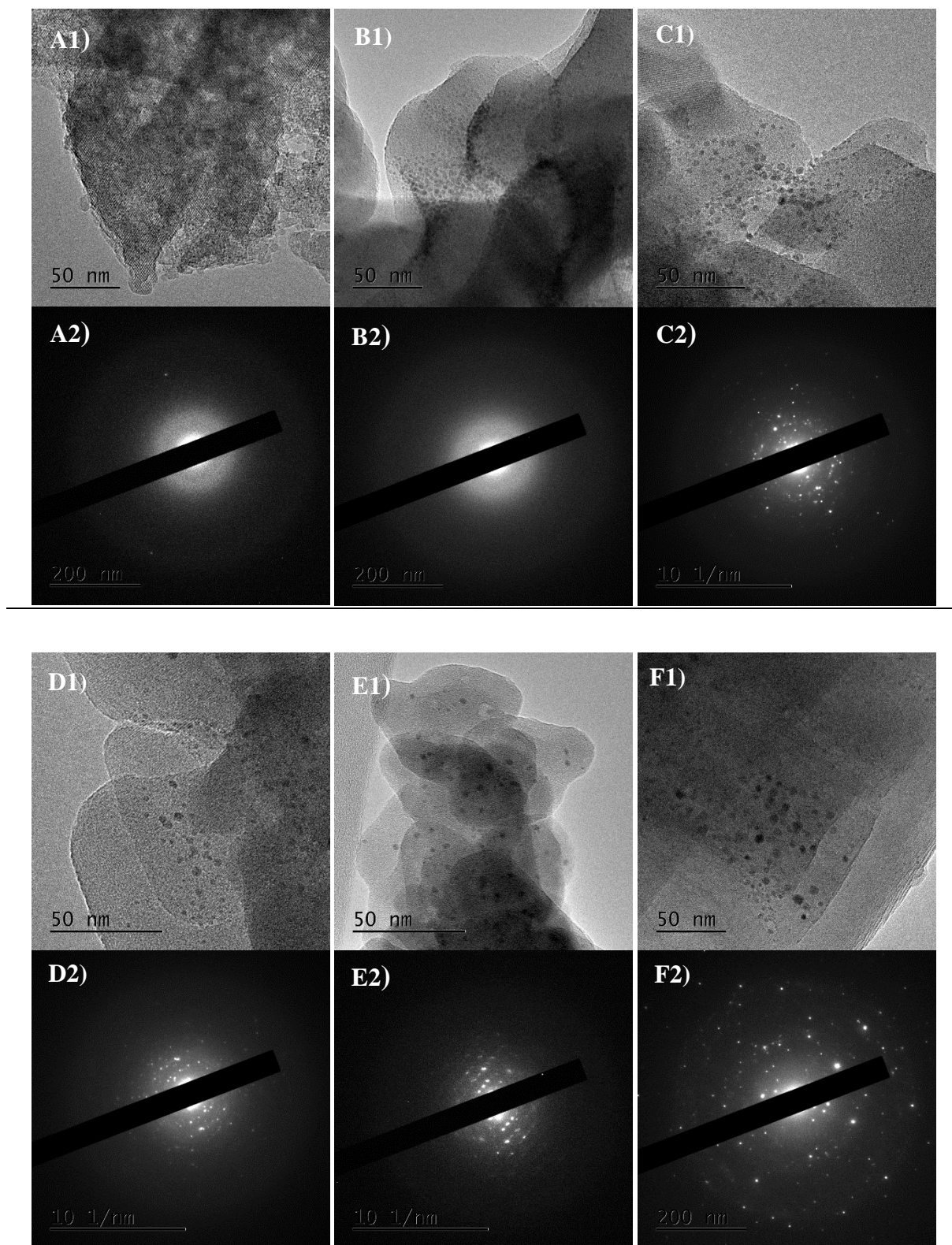


Figure 4-7 1) TEM images of the supported PdRu catalysts (Scale bar 50 nm) and 2) SAED patterns. A) HY (5.1:1), B) MOR (20:1), C) ZSM5 (30:1), D) ZSM5 (50:1), E) ZSM5 (80:1), F) ZSM5 (200-400:1).

Selected area electron diffraction (SAED) patterns showed continuous ring-like patterns for both HY (A2-*Figure 4-7*) and Mordenite (B2-*Figure 4-7*) supported catalyst. These patterns indicate that the catalysts have finer nanoparticle size and weaker crystallinity than the ZSM5 catalysts. ZSM5 zeolites with different Si/Al ratios show more evident and speckled patterns (C2, D2, E2 and F2 -*Figure 4-7*).

4.3.3 *The surface chemistry and structure of the supported catalyst for glycerol hydrogenolysis*

The use of the modified impregnation method by addition of metal precursors on the support for the catalyst preparation seems to be a simple process. However, and especially in the case of bimetallic metal impregnation over zeolites, this process can be complicated due to the formation of metal nanoparticles either inside or outside the zeolite pores.^{43,47,48} Since both, the catalyst synthesis and the reaction were carried out in hot aqueous solution; it becomes imperative to study the impact of these processes on the stability of these materials. XRD, Raman spectroscopy, TGA and leaching studies using ICP-MS of the catalysts tested were performed.

The structure of the catalyst was elucidated using X-ray powder diffraction of the starting material (zeolite after calcination). Using this method, the hydrothermal stabilities of the catalysts were studied. The official IUPAC nomenclature for microporous materials classify these materials by their framework type, using a 3 letter code.⁴⁹ ZSM-5 present a framework type MFI, which is a three-dimensional medium (10-ring) pore size system. Mordenite has a one-dimensional large (12-ring) pore system (MOR). Same pore size has HY zeolite, which presents a faujasite (FAU) type framework. Experimental XRD data obtained for the ZSM-5, Mordenite and HY zeolites were compared to the reference patterns of each different zeolitic frameworks, MFI, MOR, FAU respectively (See *Appendix 7.3*).⁴⁹ Characteristic reflections corresponding to each framework pattern were found in all XRD patterns for the calcined samples. These plots show good accordance with the reference pattern obtained from the literature.⁵⁰ A comparison of the XRD patterns of three catalyst stages (calcined, fresh and used) are presented in *Figure 4-8*.

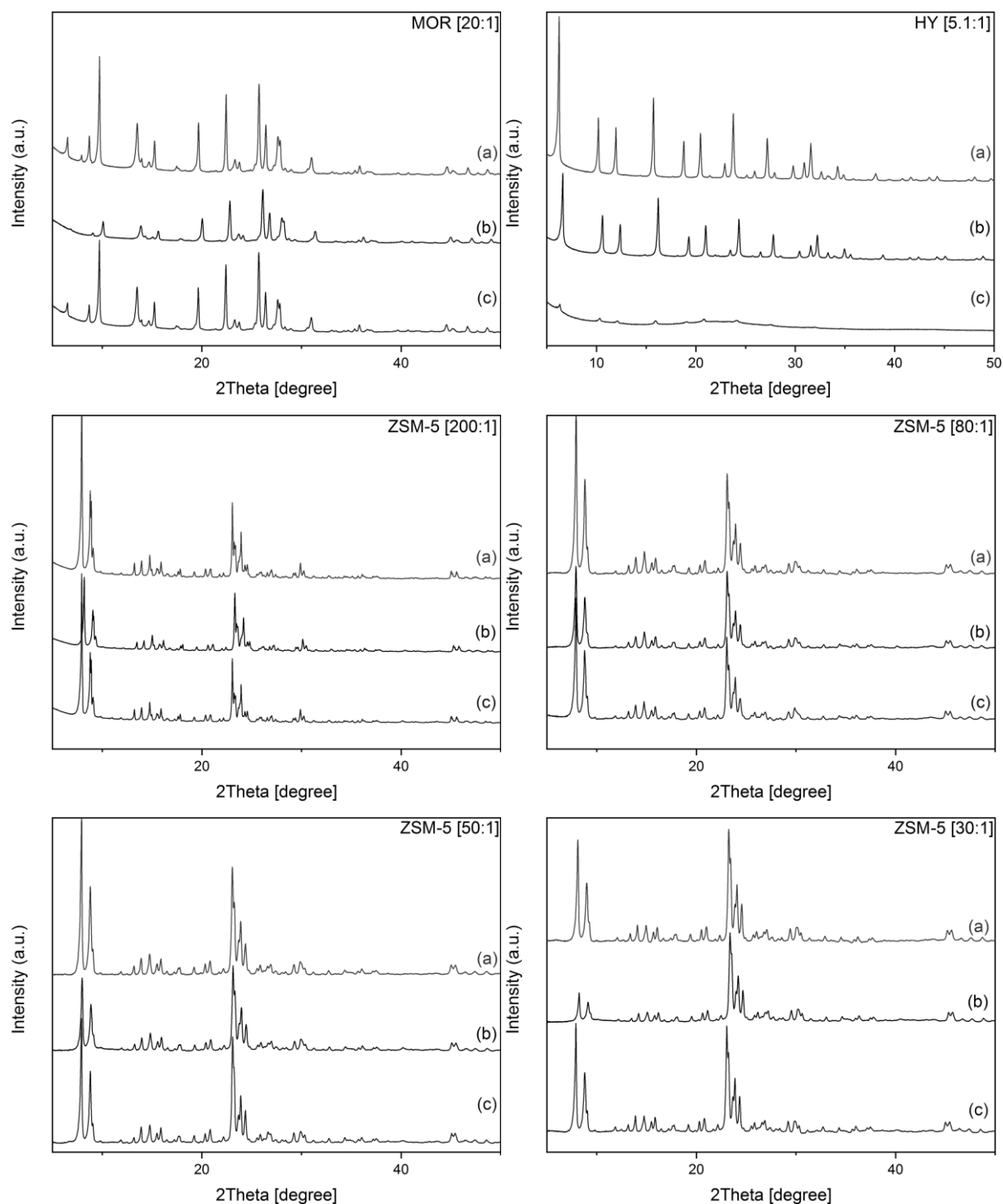


Figure 4-8 XRD spectrum of the a) calcined b) fresh and c) spent catalysts

All ZSM-5 and the MOR materials exhibit no significant changes in the zeolite framework.⁴⁷ This indicates that their zeolite basic framework structure remains the same after the metal impregnation and even after the reaction without suffering any structural damage. This observation is expected since using this catalyst preparation method, the metal cations are not incorporated into the zeolite framework, but at the external surface or even inside the pores of

the zeolite, as mentioned earlier.⁵¹ On the other hand, HY zeolite seems to have degraded after the reaction (*Figure 4-8*).

The fact that the structure also remains for the used samples indicates that ZSM-5 and MOR have good hydrothermal stability under the reaction conditions used. However, different relative intensities of the reflections can be observed. The XRD peak intensity depends on the crystallinity and the morphology.⁵² In general, the result shows that the crystallinity of the zeolites increases with the Si/Al ratio,⁵³ which is in a good agreement with the SAED patterns showed earlier in *Figure 4-7*.

The diffraction peaks decrease in amplitude upon the metal loading in the fresh zeolite-based catalysts, when compared to the calcined material. This is attributed mainly to a decrease in the crystallinity and an effect of the absorption coefficient of X-ray radiation.⁵⁴⁻⁵⁶ HY zeolite presents a weak spectrum for the used catalyst, after the reaction, reducing its crystallinity by *ca.* 85 % of its original level. This is in agreement with Dimitrijevic *et al.* who reported the degradation of the Zeolite Y (FAU type) between 403-473 K, losing around 60 % of its crystallinity into the amorphous matter and kaolinite.¹⁷

Catalyst preparation method affects the crystallinity, which alters the intensity of the diffraction peaks.⁵⁶ For instance, the ion-exchange method decreases the intensity of the XRD pattern, and this relative loss of crystallinity is proportional to the number of ion-exchanges performed.⁵⁷ While using wet impregnation, the higher the metal loading, the higher the loss of zeolite crystallinity.⁵⁵ This could be associated with the formation of the amorphous phase due to the increase of defects in the framework.⁵⁸

The effect of the metal loading by impregnation on the morphology of the zeolites could vary depending on the metal employed, acting differently in case of bimetallic.⁵⁷ Previous studies carried out by Hutchings and co-workers reported that monometallic Ru or Pd impregnated on ZSM-5 did not show a decrease in the XRD peak intensity.⁴⁷ However, using bimetallic PdRu, the decrease in the diffraction peak intensity and surface area is evident. Besides crystallinity loss, this could also be attributed to the effect of the species loaded on the ZSM-5, result of the higher absorption coefficient of Ru compounds for the X-ray radiation.^{56,59,60} It has also been reported that the reduction peak intensity at low diffraction angles ($2\theta^\circ$ between 0-15°) is assigned to the incorporation of non-framework species (*e.g.* metal nanoparticles) into the channels of the material, rather than to breakdown of the framework of the zeolites.⁶¹

Regarding the metal species on the catalyst, the size of the metal nanoparticle can affect the intensity of the peaks.⁵⁶ It is well known that XDR technique has limitations in detecting particles lower than *ca.* 2 nm and in such a low metal loading, due to the need for a long-range atomic order.^{62–65} Many authors reported that weak peak of crystalline phase correspond to good dispersion and small crystallite size of the component.^{59,66–68} The mean particle size of the PdRu/TiO₂ catalysts is 2 nm, as described in Chapter 3. However, isolated big bright nanoparticles were always found to be palladium rich according to TEM and SEM - EDX for PdRu/TiO₂ and PdRu/ZSM5 catalyst (see *Figure 4-9*). *Table 4-9* shows the EDX quantification for Ru and Pd composition. Two different zones were observed on the bimetallic PdRu/ZSM5 catalyst: 1) Area A, which was predominant on the whole sample, and 2) Area B, containing the bright spots observed in SEM.

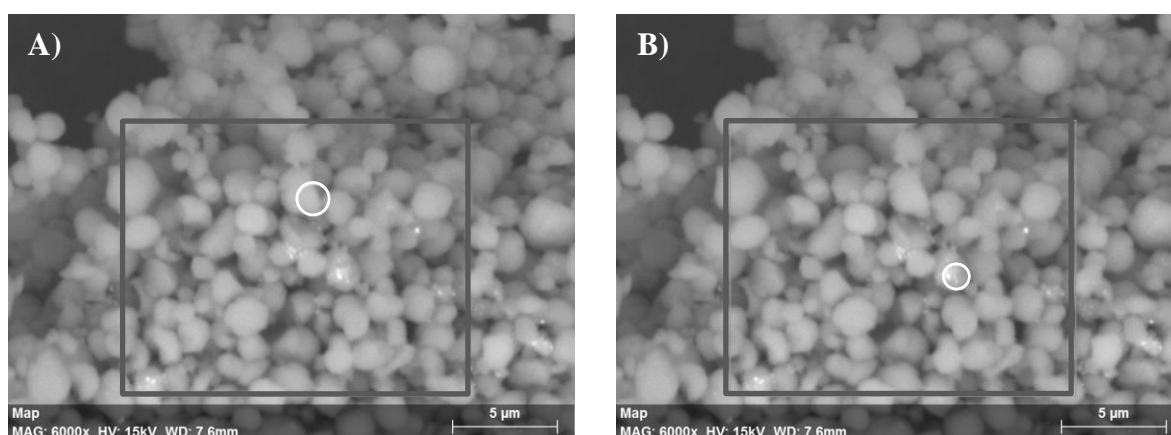


Figure 4-9 SEM of the 2 wt. % PdRu/ZSM-5 (400-200:1) highlighted with a circle, the area analysed by EDX. Area A) without bright spot and Area B) containing bright spots. Scale bar is 5 μ m in both images.

Table 4-9 Pd and Ru quantification for the fresh 2 wt. % PdRu/ZSM-5 (400-200:1) by SEM-EDX

<i>Element</i>	<i>Area A</i>			<i>Area B</i>		
	<i>norm. C (wt. %)</i>	<i>Atom. C (wt. %)</i>	<i>Error (%)</i>	<i>norm. C (wt. %)</i>	<i>Atom. C (wt. %)</i>	<i>Error (%)</i>
<i>Palladium</i>	0.94	1.22	0.23	1.88	0.28	0.10
<i>Ruthenium</i>	1.19	1.54	0.30	0.02	0.00	0.00

The results show that in the case of the spectrum area A, the composition is equal for ruthenium and or palladium, suggesting a homogeneous distribution of both metals on the support. However, in the spectrum area B, focused on the bright spot, Pd is found with a superior composition (1.88 wt. %), while Ru was found in lesser quantity (0.02 wt. %) detected.

Therefore, the biggest particles are palladium-rich nanoparticles. Indeed, the XRD data for these catalysts, PdRu/TiO₂ and PdRu/ZSM-5, shows a reflection at $2\theta^\circ$ equal to 40.1° . This peak corresponds to the metallic Pd[111], with a face-centred cubic structure.^{47,63} Figure 4-10 shows a clear example of the PdRu/ZSM-5 (80:1).

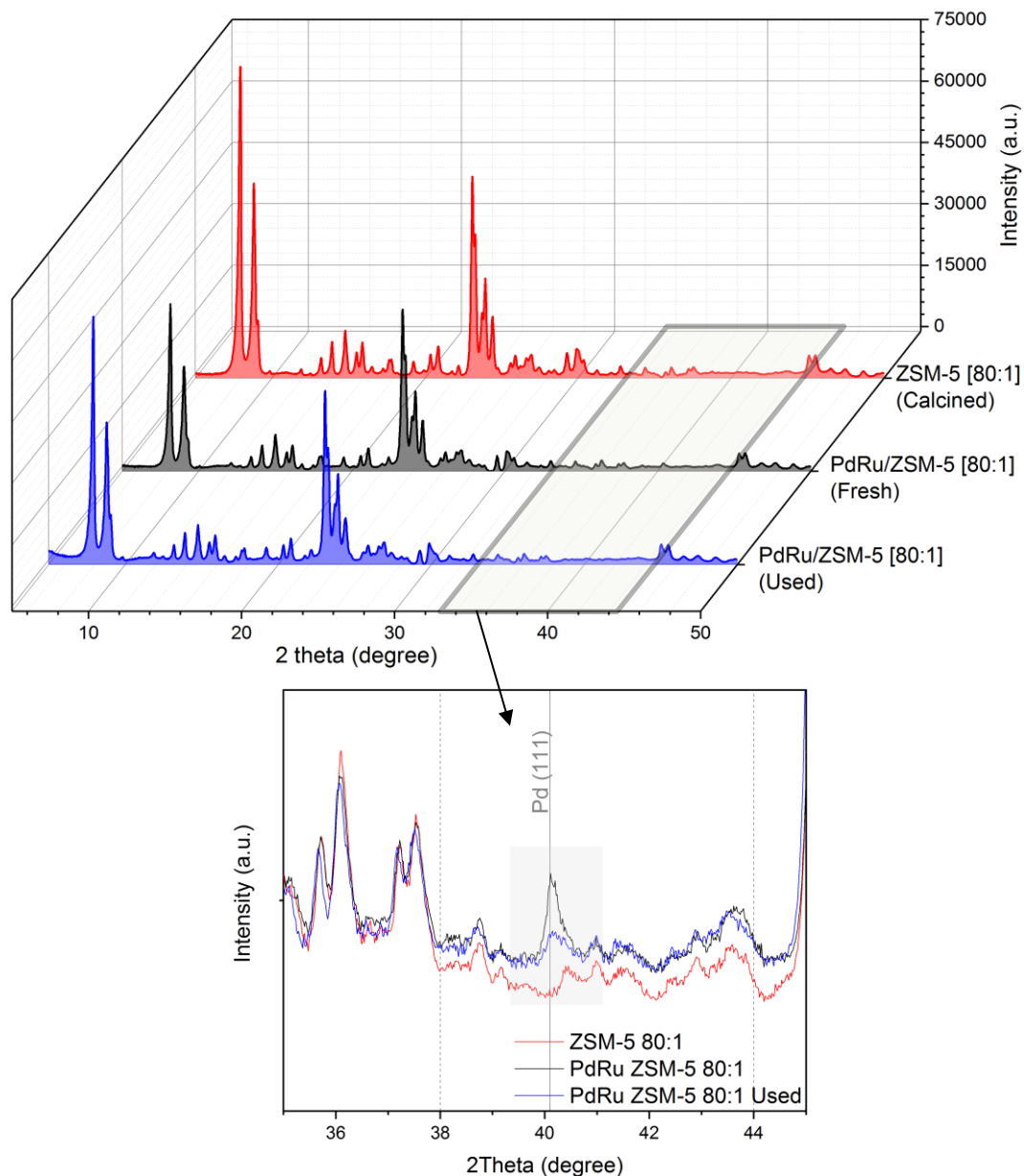


Figure 4-10 XRD spectrum of the calcined, fresh and spent 2 wt. % PdRu/ZSM-5 (80:1) catalyst. Zoom for $2\theta^\circ$ between $35-45^\circ$ where the vertical solid line refers to Pd (111) diffraction peak and the vertical dotted lines refer to Ru (002) and (101) at 38 and 44° , respectively.

Regarding Ru species present on the catalysts, Ru metal reflection should be at 2θ 38° and 44° for the [002] and [101] respectively.^{57,69} On the other hand, metal oxide RuO₂ identified by XPS data in these catalysts, should give reflections at 2θ 28° [100] or 35° [101].⁵⁷ Nevertheless, these crystalline diffraction phases were not detected by XRD. As mentioned earlier, this

indicates that the Ru is well dispersed on the support.^{36,59} It is also remarkable how in the used catalyst, the Pd [111] diffraction line presents a weaker relative intensity (see the zoomed plot in *Figure 4-10*). This suggests that the possibility of either Pd leaching or re-dispersion of the metal nanoparticles.^{70,71} The same was observed in the case of PdRu/TiO₂ (*Figure 4-11*). The diagnostic reflection the XRD pattern of TiO₂ reveals [100] reflections at 2θ 25.32° and 27.45° due to the presence of both anatase and rutile, respectively.⁷² The relative proportions of the crystalline titania phases are approximately 80 % anatase and 20 % rutile, concordant with the phase composition of the widely used TiO₂.⁷³

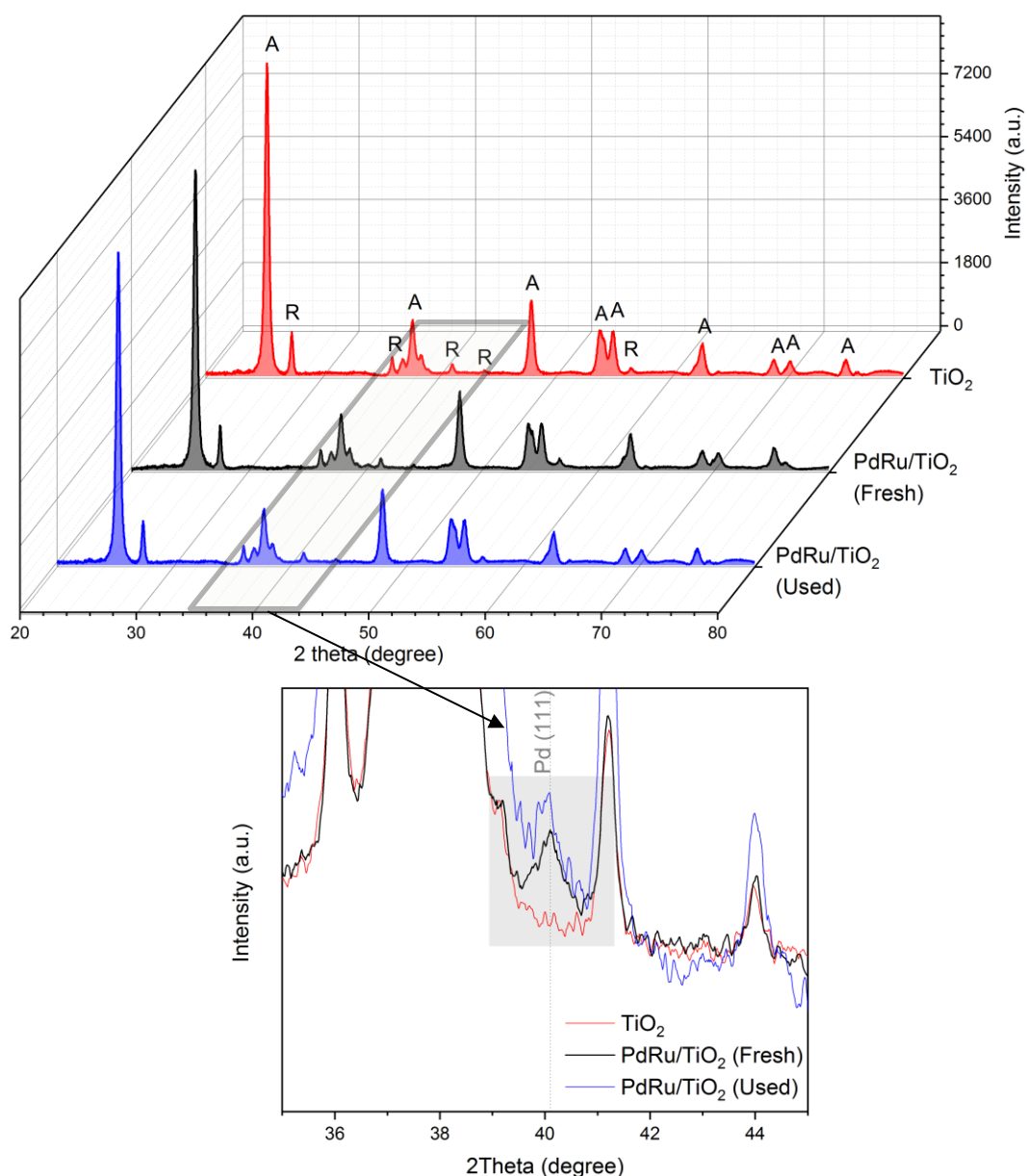


Figure 4-11 XRD spectrum of the calcined, fresh and spent 2 wt. % PdRu/TiO₂ catalyst. Zoom for 2θ° between 35-45° where the vertical line refers to Pd (111) diffraction peak.

To confirm Pd leaching during the reaction, the reaction mixture, after the separation of solid catalyst, was analysed by inductively coupled plasma (ICP) method. The amount of metals detected in the reaction mixture by ICP are given in *Figure 4-12*.

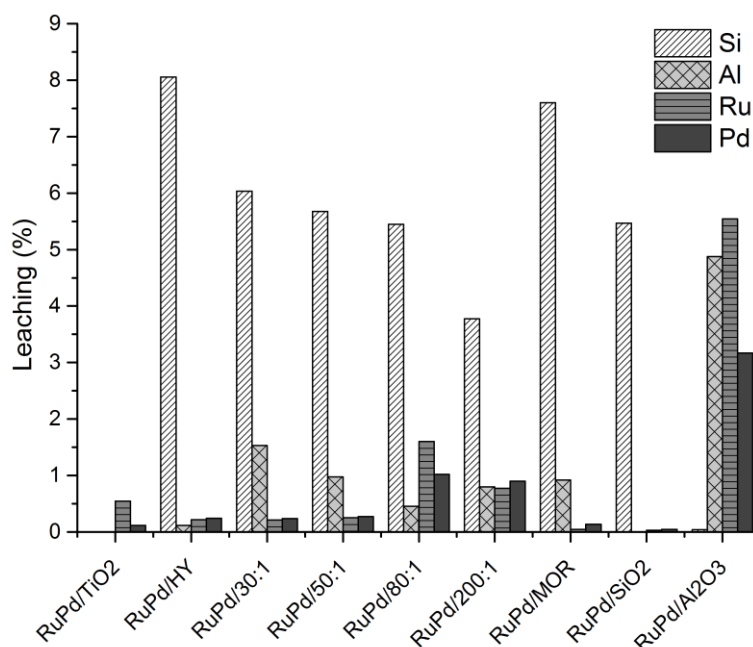


Figure 4-12 Leaching study by the analysis of reaction mixtures by ICP – MS.

The leaching study shows less than 8 % of Si leaching for all the zeolites used under reaction conditions. Significant PdRu leaching was only observed in the case of Al₂O₃ catalyst. After the PdRu/Al₂O₃ the higher leaching observed (less than 1.5 % of Ru and about 1 % of Pd) for the PdRu/ZSM-5 catalyst with 80:1 molar ratio of Si:Al. However, no significant Pd leaching was observed for PdRu/ZSM-5 and PdRu/TiO₂ catalyst. One hypothesis could be that the small leaching percentage corresponds to metal nanoparticles on the catalyst surface/edges; remaining the metal in the pores of the support. In this way, by changing the surface, the XRD diffraction pattern after reaction shows intensities more similar to the original calcined material (before impregnation). On the other hand, there is a possibility that the metal might have leached into the solution during reaction but deposited back on to the support when the reaction mixture was cooled.⁷⁴ In this way, the loss of the diffraction of Pd [1,1,1] could be due to the re-dispersion of metal to form smaller particles.⁷¹ Indeed, the STEM of the PdRu/TiO₂ after reaction showed a more homogeneous metal distribution, as reported in Chapter 3.

Raman spectroscopy was also used to characterise the structural changes of the catalyst. However, conventional Raman of zeolites shows fluorescence phenomena interference, which originates from impurities, organic species and defect sites.⁷⁵ Ultraviolet (UV)-Raman spectroscopy shows characteristic peaks of zeolites avoiding the strong background fluorescence which mainly occurs in the visible range of the spectrum.⁷⁶⁻⁷⁹ *Figure 4-13* shows that the results obtained for the different framework types are in good agreement with the known chemistry of these zeolites. For the ZSM-5 Raman shifts at 294 cm^{-1} , 378 cm^{-1} and 440-470 cm^{-1} bands were observed. These bands are associated with the bending mode of 6, 5 and 4-membered rings, respectively. It also shows a band at 800 cm^{-1} , which is associated with symmetric stretching. On the contrary, the bands at 975, 1028 and 1086 cm^{-1} are associated with asymmetric stretching vibrations of Si-O bonds.^{80,81} The features observed for Mordenite, at 240 cm^{-1} , 405 cm^{-1} , 470-482 cm^{-1} correspond to the 8, 5 and 4-membered rings, respectively. The feature at 820 cm^{-1} is associated with symmetric stretching.

Broad features are observed in the case of the HY zeolite at 305 and 500 cm^{-1} . All the calcined zeolites present a significant change in the Raman intensity after impregnation. This is in good agreement with the results of XRD discussed above. In general, the Raman intensity signals is proportional to the increase/decrease of structural order.⁸⁰ Therefore it is sensitive to any Si/Al ratio change. Especially for the PdRu/HY after the reaction, it can be noticed a decrease in intensity that could be due to the Si leaching. Nevertheless, Raman intensity is also quite sensitive to sample thickness and analyte concentration.⁷⁸ Notice that for the supported ZSM5 and MOR catalyst, there are prominent bands at 1400 cm^{-1} (D band) and 1620 cm^{-1} (G band), which could relate to carbon from coke formation.^{79,82} One possible origin of carbon in the fresh catalyst, before the reaction, could be because of the structure directing agent (quaternary ammonium salts) in zeolites that has to burn off during calcination.

No apparent strong features associated with the metallic Pd-Ru particles were detected since metallic bonds are not Raman active. A rising background dominates the spectra to a more significant Raman shift. This could be indicating electronic fluorescence from transition metal ions contained in the catalyst, more specifically, to oxidised Pd species (Pd^{4+}).⁸³ To compare these data, the background was subtracted. Overall, the result exhibits the existence of high bimetal dispersion over the support.⁸⁴

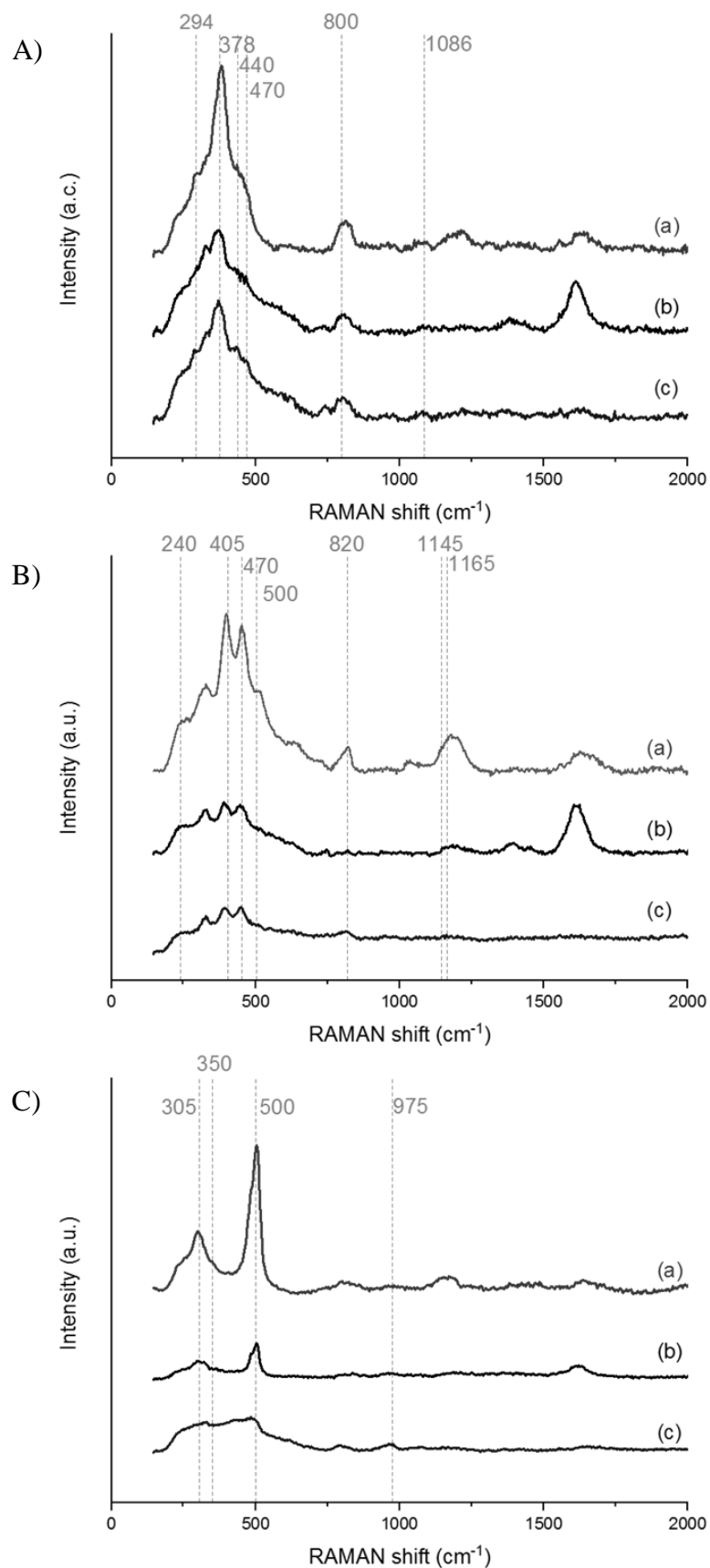


Figure 4-13 UV-Raman spectra of calcined zeolites (a), fresh (b), and used (c) 2 wt. % PdRu catalyst supported on A) ZSM5; B) MOR and C) HY zeolites. (244 nm laser excitation)

Finally, the fresh and the spent catalyst were analysed by thermogravimetric analysis (TGA). From the TG thermograms represented in *Figure 4-14*, can be observed that < 10 wt. % weight loss for the fresh and spent catalyst was obtained below 200 °C. These results also establish the evidence that no coke formation was deposited on the spent catalysts during the reaction since coke degrades around 500 °C.⁶

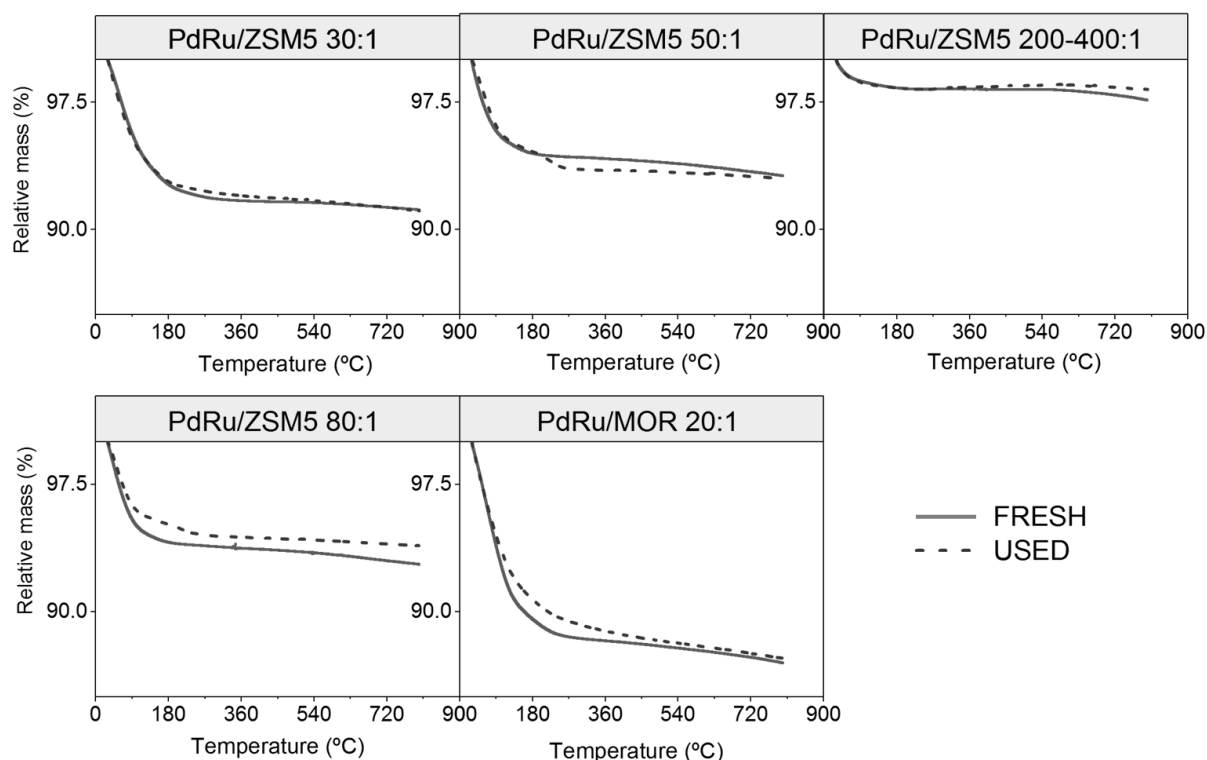


Figure 4-14 Thermogravimetric analysis of the bimetallic zeolite-based catalyst before reaction (fresh) and after reaction (used).

Despite all the characterisation described above regarding the catalyst surface; it can be concluded that both surface area and pore volume, for this reaction does not seem to have a significant influence on the activity or selectivity, since no trend has been found to correlate this relationship. The next step is to investigate the influence of acidity ion the catalytic activity.^{7,85,86} It has been reported that selectivity can be tuned by modifying the acid sites on the catalyst for many reactions.⁸⁷ Specifically for Ru-based catalyst supported on zeolites, an enhancement of the hydrogenolysis activity to favour the selectivity toward 1,2-PDO *via* formation of the intermediate acetol on acid sites has been shown.⁴

4.3.4 Effect of catalysts acidity on hydrogenolysis of glycerol.

Relative acid site density of the samples was determined by ammonia temperature-programmed desorption (NH₃-TPD). The acidic strength of the material can be estimated by the temperature at which the chemisorbed ammonia desorption occurs; the higher the desorption temperature, the stronger the relative acid site strength. The acidity density (NH₃ μmol g⁻¹) was quantified for all the catalyst tested (see *Appendix 7.4* for the NH₃-TPD plots). The results show very good correlation for all the cases, $R^2 > 0.99$. The goodness of fit of the statistical model show similar sum of squares values across all the samples, which estimates the error. The same order of magnitude for the Chi-Square value across all the catalyst was obtained. *Figure 4-15* presents a comparison of the acid sites density present in each PdRu catalyst. The data was estimated using the response factor obtained from the NH₃ calibration and the Chi-Square goodness of fit test described in Chapter 2, *section 2.2.4*.

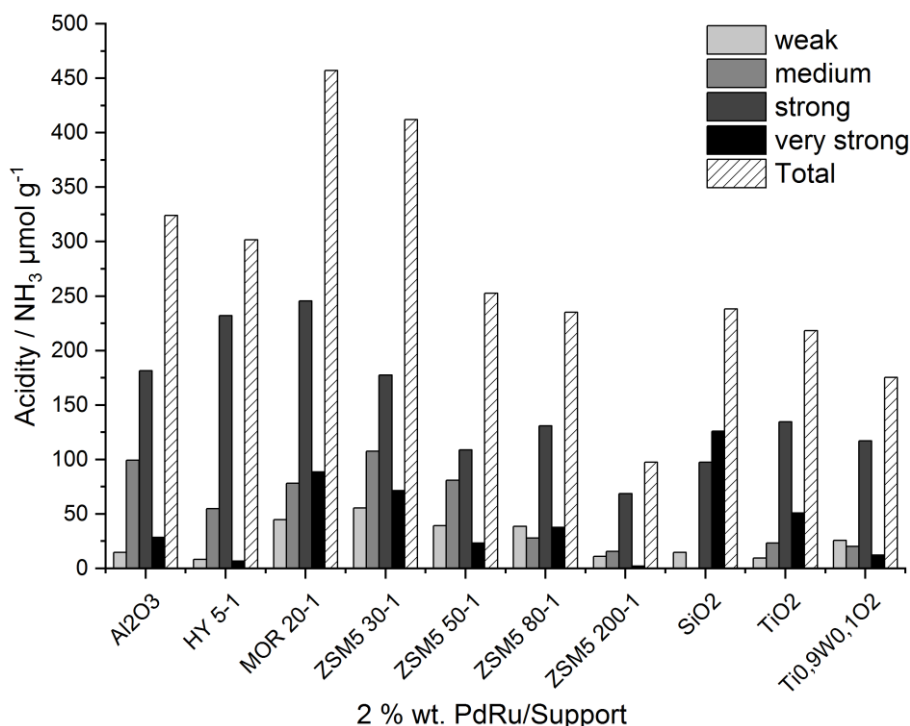


Figure 4-15 Acid site density distribution of the different bimetallic PdRu catalysts tested for the hydrogenolysis of glycerol

The more acidic supported catalyst was PdRu/MOR followed by the PdRu/ZSM-5, zeolites with a molar ratio of Si/Al of 20:1 and 30-1 respectively, considering the total acidity of the catalyst.

For both kinds of zeolites, Lewis and Brønsted acidity was monitored as a function of the temperature through a pyridine desorption experiment, using DRIFTS. For the determination of the different acid sites, this study was focussed on the frequency range from 1600 to 1400 cm^{-1} . In this region, the pyridine absorbance on a Brønsted acid site is observed at a band at 1540 cm^{-1} , which correspond with the C-C bond vibration of the pyridinium ion.⁸⁷ On the other hand, the pyridine absorption on a Lewis acid site is shown on the band at 1450 cm^{-1} , while the band at 1490 correspond with both acid sites, Brønsted and Lewis.¹³

It is commonly observed that the addition of metal into the silica framework produce on the one hand a decrease in the amount of the Brønsted site, which was also supported by DRIFTS for these materials. This phenomenon could be due to the metal introduction into the pores. On the other hand, it produces an increase in the Lewis sites, where the metal site could act as a Lewis site by accepting electron pairs from pyridine. *Figure 4-16* shows two different FTIR spectra of pyridine adsorbed on a) ZSM-5 and b) MOR zeolites (from 30-575 °C). It can be seen how the peaks reduce their intensity along with the temperature increases until no pyridine remains absorbed at 300 °C. *Figure 4-16-a* compares the nature of the acid sites of the most active ZSM-5 (80-1) with the most acid support Mordenite.

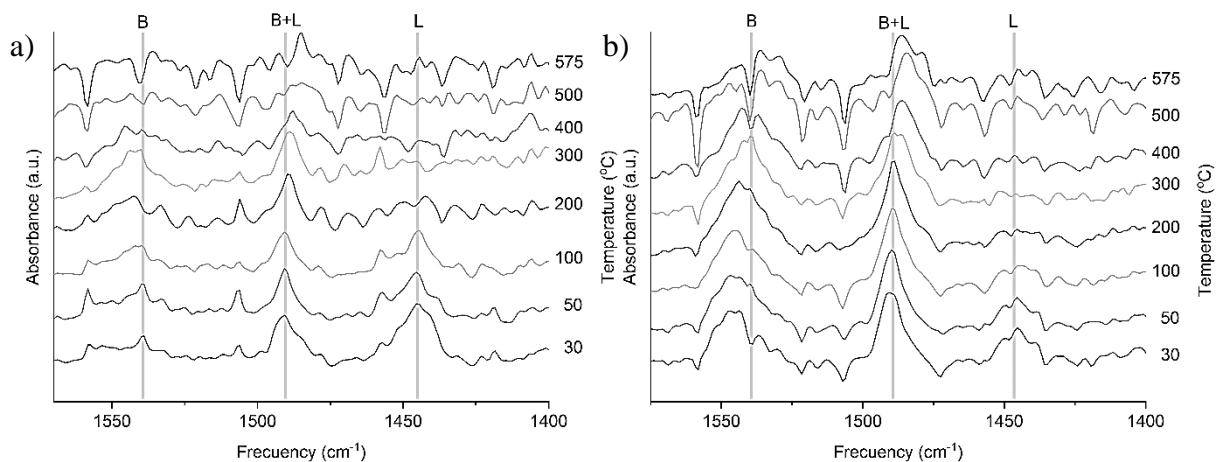


Figure 4-16 FTIR spectra of pyridine adsorbed on the materials recorded between 30-575 °C. a) ZSM-5 (80:1), b) Mordenite (20:1).

The results indicate that MOR has more Brønsted sites than Lewis, and the ZSM-5 presents the opposite. Yoda *et al.* studied the reaction pathways for the dehydration of glycerol over H-ZSM-5, confirming that different kind of acid sites lead to different reaction pathways.⁸ Lewis acid sites are useful for the dehydration pathway **A** (See Scheme 3-1 in Chapter 3). Lewis sites attack the 1st hydroxyl group to form 1,2-PDO via acetol. On the contrary, Brønsted acid sites favour the mechanism pathway **B**, interacting with the 2nd hydroxyl group of glycerol (*Scheme*

3-1 Chapter 3).^{2,8,88} This could be the main reason why the PdRu/ZSM-5 catalyst with low Si/Al ratio promotes a high conversion of glycerol with highest 1,2-PDO yields than PdRu/MOR catalyst.

The Pyridine adsorbed spectra of the Mordenite shows more significant Brønsted acidity peaks than the ZSM-5 zeolite. This agrees with the NH₃ desorption results, where the 2 peaks at low temperature are attributed to weak Brønsted and Lewis sites, and the peaks above 450 °C is assigned to strong Brønsted acid sites. Mordenite was the material with a higher desorption peak at the higher temperature, labelled here as very strong acidity. Studying how the acidic properties influence on the catalytic activity is vital.

Regarding the effect of the acid site on the catalytic activity, *Figure 4-17* shows a volcano curve correlation between the relatively strong acid sites and the activity of the PdRu nanoparticles supported on zeolites.

This relationship leads to a volcano-type dependence of the catalytic activity. The plot shows a maximum of activity around 40 NH₃ μmol g⁻¹ of very strong and 130 NH₃ μmol g⁻¹ of strong acid sites for the PdRu/ZSM-5 (80:1), with a conversion of glycerol above 75 %. It is important to note that the catalyst supported on TiO₂, which has the best performance suppressing the C1 products, contains the same amount of strong acid sites. This is in agreement with Patri and co-workers. These author reported a similar tendency where intermediate acidity of TiO₂ showed the best results for their AuPt bimetallic catalysts: (AuPt/TiO₂) > (AuPt/MCM41 ≥ AuPt/ SiO₂) > (AuPt/H-Mordenite > AuPt/S-ZrO₂).²⁹

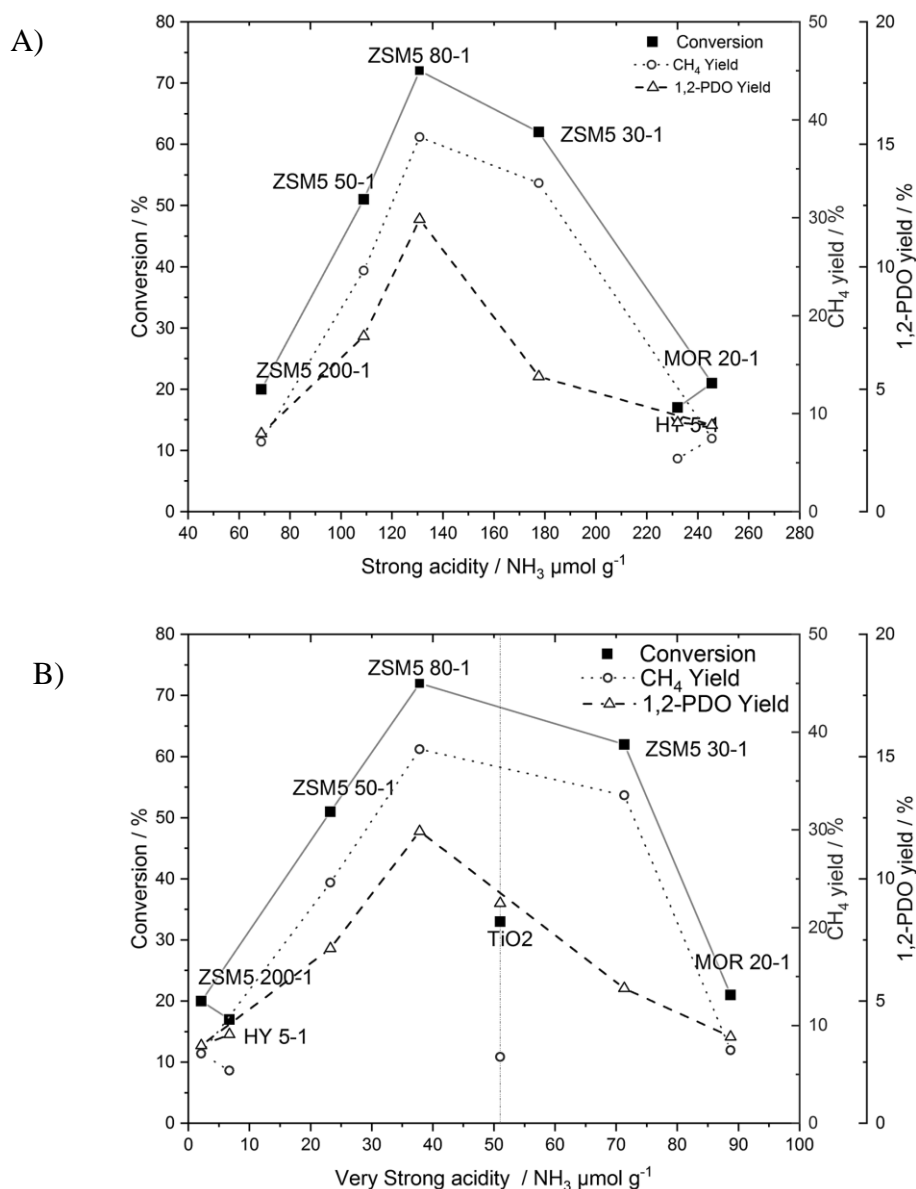


Figure 4-17 Volcano plot correlation between activity (conversion (■), CH₄ yield (○) and 1,2-PDO yield (△)) vs A) strong acidity sites estimated from ammonia desorption peak 3; and B) the very strong acidity sites obtained from ammonia desorption peak 4 (See Appendix).

4.4 Conclusions

Hydrogenolysis of glycerol by bimetallic PdRu catalyst was investigated with a series of metal oxides and several zeolitic supports. The catalysts were prepared by a modified impregnation method and tested under the same reaction conditions for comparison. Several characterisation techniques were used to study the stability of the zeolites in the hot aqueous medium during the catalyst synthesis and the hydrogenolysis reaction.

This study of the textural properties of the catalyst shows that both surface area and total pore volume decrease after the metal impregnation. In the case of the zeolites, the reduction of the

surface area is between 5-7 %. For the mesoporous material (metal oxides) the decrease is more significant *ca.* 30 %. These can be attributed to the partial occupation of the catalyst pores by PdRu nanoparticles, which is supported by the micropore volume analysis.

As expected, zeolites present different catalytic behaviour depending on structure and composition (Si:Al ratio). It was interesting to find that the bimetallic PdRu over ZSM-5 behaves more like Ru monometallic than the bimetallic PdRu/TiO₂. XPS data proved that the catalyst had mainly Ru metallic and Pd was found as both metal and oxide species on the catalyst.

Hydrothermal stabilities of the zeolites were investigated during metal impregnation and reaction conditions. Both XRD and UV-Raman spectroscopy proved that the framework of the support did not suffer structural changes for any ZSM5 or MOR catalyst. Their morphology was preserved after impregnation and the reaction conditions. However, HY zeolite shows evident degradation after the reaction.

SEM, TEM with coupled EDX analysis, confirmed the highly dispersed spherical PdRu alloy nanoparticles on the different support. However, it was found Pd-rich bigger nanoparticles in all the PdRu/ZSM5 and PdRu/TiO₂ catalyst. This was also confirmed by XRD where Pd [1,1,1] reflection was found on the fresh catalyst.

Conclusions can be drawn from the study that the support clearly affects the catalyst activity. ZSM-5 with Si:Al ratio of 30:1, 50:1 and 80:1 give the highest activity. However, this structure has nearly all Lewis acidity, and very few Brønsted acid sites were present as shown by the pyridine DRIFTS. Therefore, these catalyst yield, more 1,2-PDO than 1,3-PDO. However, it was interesting to find that the main product was CH₄ instead.

It was found that the strong acidity of these materials correlates with their activity showing a volcano plot. Among the supports, the catalyst supported TiO₂ possesses a moderate acidity and catalyst activity that promotes the yield to 1,2-PDO avoiding the formation of C1 products. The simultaneous presence of bimetallic noble metals and moderate density of strong acid sites favour the yield to C3 products.

Studies on a PdRu/Ti_{0.9}W_{0.1}O₂ catalyst shows an improvement in the PdRu/TiO₂ catalytic performance regarding 1,2-PDO selectivity. More investigation into the role of this W doped TiO₂ catalyst and characterisation needs to be done for this bimetallic system.

4.5 References

1. Misono, M. Mixed Oxides as Catalyst Supports. In *Studies in Surface Science and Catalysis*; Elsevier, 2013; Vol. 176, pp 157–173.
2. Falcone, D. D.; Hack, J. H.; Klyushin, A. Y.; Knop-gericke, A.; Schlögl, R.; Davis, R. J.; Schlo, R.; Davis, R. J.; Schlögl, R.; Davis, R. J., *ACS Catal.* **2015**, *5* (10), 5679–5695.
3. Nakagawa, Y.; Tomishige, K., *Catal. Sci. Technol.* **2011**, *1* (1), 179–190.
4. Gallegos-Suarez, E.; Guerrero-Ruiz, A.; Rodriguez-Ramos, I.; Arcoya, A., *Chem. Eng. J.* **2015**, *262*, 326–333.
5. Delgado, S. N.; Yap, D.; Vivier, L.; Especel, C., *J. Mol. Catal. A Chem.* **2013**, *367*, 89–98.
6. Martin, A.; Armbruster, U.; Gandarias, I.; Arias, P. L., *Eur. J. Lipid Sci. Technol.* **2013**, *115* (1), 9–27.
7. Kusunoki, Y.; Miyazawa, T.; Kunimori, K.; Tomishige, K., *Catal. Commun.* **2005**, *6* (10), 645–649.
8. Yoda, E.; Ootawa, A., *Appl. Catal. A Gen.* **2009**, *360* (1), 66–70.
9. Kim, Y. T.; Jung, K. D.; Park, E. D., *Appl. Catal. A Gen.* **2011**, *393* (1–2), 275–287.
10. Zou, B.; Ren, S.; Ye, X. P., *ChemSusChem* **2016**, *9* (23), 3268–3271.
11. Lin, X.; Lv, Y.; Qu, Y.; Zhang, G.; Xi, Y.; Phillips, D. L.; Liu, C., *Phys. Chem. Chem. Phys.* **2013**, *15* (46), 20120–20133.
12. Priya, S. S.; Bhanuchander, P.; Kumar, V. P.; Dumbre, D. K.; Periasamy, S. R.; Bhargava, S. K.; Lakshmi Kantam, M.; Chary, K. V. R., *ACS Sustain. Chem. Eng.* **2016**, *4* (3), 1212–1222.
13. Shanthi Priya, S.; Bhanuchander, P.; Pavan Kumar, V.; Bhargava, S. K.; R Chary, K. V.; Priya, S. S.; Bhanuchander, P.; Kumar, V. P.; Bhargava, S. K.; Chary, K. V. R., *Ind. Eng. Chem. Res.* **2016**, *55* (16), 4461–4472.
14. Prodinge, S.; Shi, H.; Eckstein, S.; Hu, J. Z.; Olarte, M. V.; Camaioni, D. M.; Derewinski, M. A.; Lercher, J. A., *Chem. Mater.* **2017**, *29* (17), 7255–7262.
15. Zhang, L.; Chen, K.; Chen, B.; White, J. L.; Resasco, D. E., *J. Am. Chem. Soc.* **2015**, *137* (36), 11810–11819.
16. Jin, S.; Xiao, Z.; Li, C.; Williams, C. T.; Liang, C., *J. Energy Chem.* **2014**, *23* (2), 185–192.
17. Dimitrijevic, R.; Lutz, W.; Ritzmann, A., *J. Phys. Chem. Solids* **2006**, *67*, 1741–1748.
18. Müller, M.; Harvey, G.; Prins, R., *Microporous Mesoporous Mater.* **2000**, *34* (2), 135–147.
19. Čimek, A.; Subotić, B.; Šmit, I.; Tonejc, A.; Aiello, R.; Crea, F.; Nastro, A., *Microporous Mater.* **2002**, *8* (3–4), 159–169.
20. Sano, T.; Nakajima, Y.; Wang, Z. B.; Kawakami, Y.; Soga, K.; Iwasaki, A., *Microporous Mater.* **1997**, *12* (1–3), 71–77.
21. Lin, X.; Lv, Y.; Xi, Y.; Qu, Y.; Phillips, D. L.; Liu, C., *Energy & Fuels* **2014**, *28* (5), 3345–3351.
22. Li, B.; Wang, J.; Yuan, Y.; Ariga, H.; Takakusagi, S.; Asakura, K., *ACS Catal.* **2011**, *1* (11), 1521–1528.
23. García-Fernández, S.; Gandarias, I.; Tejido-Núñez, Y.; Requies, J.; Arias, P. L., *ChemCatChem* **2017**, *9* (24), 4508–4519.
24. Zhou, W.; Luo, J.; Wang, Y.; Liu, J.; Zhao, Y.; Wang, S.; Ma, X., *Appl. Catal. B Environ.* **2019**, *242* (September 2018), 410–421.

25. Chaminand, J.; Djakovitch, L. auren.; Gallezot, P.; Marion, P.; Pinel, C.; Rosier, C., *Green Chem.* **2004**, *6* (8), 359–361.
26. Al Ameen, A.; Mondal, S.; Pudi, S. M.; Pandhare, N. N.; Biswas, P., *Energy and Fuels* **2017**, *31* (8), 8521–8533.
27. Priya, S. S.; Bhanuchander, P.; Kumar, V. P.; Bhargava, S. K.; Chary, K. V. R., *Ind. Eng. Chem. Res.* **2016**, *55* (16), 4461–4472.
28. Bloh, J. Z.; Folli, A.; Macphee, D. E. ., *J. Phys. Chem. C* **2014**, *118* (36), 21281–21292.
29. Villa, A.; Manzoli, M.; Vindigni, F.; Chinchilla, L. E.; Botton, G. A.; Prati, L., *Catal. Letters* **2017**, *147* (10), 2523–2533.
30. Alayoglu, S.; Nilekar, A. U.; Mavrikakis, M.; Eichhorn, B., *Nat. Mater.* **2008**, *7* (4), 333–338.
31. Liu, H.; Liang, S.; Jiang, T.; Han, B.; Zhou, Y., *Clean - Soil, Air, Water* **2012**, *40* (3), 318–324.
32. Sun, D.; Yamada, Y.; Sato, S.; Ueda, W., *Appl. Catal. B Environ.* **2016**, *193*, 75–92.
33. Sun, D.; Yamada, Y.; Sato, S., *Appl. Catal. A Gen.* **2014**, *487*, 234–241.
34. Mai, C. T. Q.; Ng, F. T. T., *Org. Process Res. Dev.* **2016**, *20* (10), 1774–1780.
35. Liu, J.-Y.; Zheng-Song, Q.; Huang, W.-A.; Yang, L.; Ding-Ding, S., *J. Chem. Pharm. Res.* **2014**, *6* (4), 850–857.
36. Cruz-Cabeza, A. J.; Esquivel, D.; Jiménez-Sanchidrián, C.; Romero-Salguero, F. J., *Materials (Basel)*. **2012**, *5* (1), 121–134.
37. Thommes, M.; Kaneko, K.; Neimark, A. V.; Olivier, J. P.; Rodriguez-Reinoso, F.; Rouquerol, J.; Sing, K. S. W., *Pure Appl. Chem.* **2015**, *87* (9–10), 1051–1069.
38. Castro, C. A.; Jurado, A.; Sissa, D.; Giraldo, S. A., *Int. J. Photoenergy* **2012**, *2012*, 1–10.
39. Rafigh, S. M.; Heydarinasab, A., *ACS Sustain. Chem. Eng.* **2017**, *5* (11), 10379–10386.
40. Mokhtar, W. N. A. W.; Bakar, W. A. W. A.; Ali, R.; Kadir, A. A. A., *Arab. J. Chem.* **2018**, *11* (8), 1201–1208.
41. Huang, Z.; Su, J.; Guo, Y.; Su, X.-Q.; Teng, L.-J., *Chem. Eng. Commun.* **2009**, *196* (9), 969–986.
42. Meshcheryakova, I. D.; Kashcheeva, T. P.; Rutkovskii, M. L., *Prot. Met.* **1975**, *11* (1), 36–37.
43. Viswanadham, N.; Saxena, S. K.; Kumar, M., *Pet. Sci. Technol.* **2011**, *29* (4), 393–400.
44. van Ravensteijn, B. G. P.; Schild, D. J.; Kegel, W. K.; Klein Gebbink, R. J. M., *ChemCatChem* **2017**, *9* (3), 440–450.
45. Botelho do Rego, A. M.; Ferreira, L. F. V. 4. Photonic and Electronic Spectroscopies for the Characterization of Organic Surfaces and Organic Molecules Adsorbed on Surfaces. In *Experimental Methods in the Physical Sciences*; Academic Press, 2001; pp 269–354.
46. Jiang, T.; Huai, Q.; Geng, T.; Ying, W.; Xiao, T.; Cao, F., *Biomass and Bioenergy* **2015**, *78* (130), 71–79.
47. Conte, M.; Lopez-Sanchez, J. A.; He, Q.; Morgan, D. J.; Ryabenkova, Y.; Bartley, J. K.; Carley, A. F.; Taylor, S. H.; Kiely, C. J.; Khalid, K.; et al., *Catal. Sci. Technol.* **2012**, *2* (1), 105–112.
48. Lai, Y.; Vesper, G., *Catal. Sci. Technol.* **2016**, *6* (14), 5440–5452.
49. McCusker, L. B.; Olson, D. H.; Baerlocher, C. *Atlas of Zeolite Framework Types*, 6ed ed.; Elsevier, 2007.

50. Treacy, M. M. J.; Higgins, J. B. J. B. *Collection of Simulated XRD Powder Patterns for Zeolites*; Elsevier, 2001.
51. Fricke, R.; Kosslick, H.; Lischke, G.; Richter, M., *Chem. Rev.* **2000**, *100* (6), 2303–2406.
52. Van Steen, E.; Callanan, L. H.; Claeys, C. Recent Advances in the Science and Technology of Zeolites and Related Materials. In *Studies in Surface Science and Catalysis*; Elsevier: South Africa, 2004; p 724.
53. Držaj, B.; Hočevár, S.; Pejovnik, S. *Zeolites : Synthesis, Structure, Technology, and Application : Proceedings of an International Symposium*; Elsevier, 1985.
54. Serrano, D. P.; Escola, J. M.; Sanz, R.; Garcia, R. A.; Peral, A.; Moreno, I.; Linares, M., *New J. Chem* **2016**, *40*, 4206.
55. Fillipe A. C. G.; Araújo, D. R.; Silva, J. C. M.; Macedo, J. L. de; Ghesti, G. F.; Dias, S. C. L.; Dias, J. A.; R.Filho, G. N., *J. Braz. Chem. Soc.* **2011**, *22* (10), 1894–1902.
56. Yang, Y.; Zhang, H.; Yan, Y., *R. Soc. open Sci.* **2018**, *5* (3), 171731.
57. Anggoro, D. D.; Hidayati, N.; Buchori, L.; Mundriyastutik, Y., *Bull. Chem. React. Eng. Catal.* **2016**, *11* (1), 75.
58. Vjunov, A.; Fulton, J. L.; Camaioni, D. M.; Hu, J. Z.; Burton, S. D.; Arslan, I.; Lercher, J. A., *Chem. Mater.* **2015**, *27*, 3533–3545.
59. Rauscher, M.; Kesore, K.; Mönnig, R.; Schwieger, W.; Tißler, A.; Turek, T., *Appl. Catal. A Gen.* **1999**, *184* (2), 249–256.
60. Gullikson, E. M. *X-Ray Data Booklet. Mass Absorption Coefficients*; 1993; Vol. 54.
61. Gong, T.; Qin, L.; Lu, J.; Feng, H., *Phys. Chem. Chem. Phys* **2016**, *18*, 601.
62. Warlimont, H.; Martienssen, W. Material for Solid Catalysts. In *Handbook of Materials Data*; Springer, 2018; p 1140.
63. Wojcieszak, R.; Genet, M. J.; Eloy, P.; Ruiz, P.; Gaigneaux, E. M., *Society* **2010**, 16677–16684.
64. Marinkovic, N.; Sasaki, K.; Adzic, R., *Zast. Mater.* **2016**, *57* (1), 101–109.
65. Kumar, C. S. S. R. *X-Ray and Neutron Techniques for Nanomaterials Characterization*; Springer, 2019.
66. Cao, J.-L.; Wang, Y.; Zhang, T.-Y.; Wu, S.-H.; Yuan, Z.-Y., *Appl. Catal. B Environ.* **2008**, *78* (1–2), 120–128.
67. Zou, Z.-Q.; Meng, M.; Guo, L.-H.; Zha, Y.-Q., *J. Hazard. Mater.* **2009**, *163*, 835–842.
68. Li, X.; Wang, L.; Xia, Q.; Liu, Z.; Li, Z., *Catal. Commun.* **2011**, *14* (1), 15–19.
69. Fukuda, K.; Sato, J.; Saida, T.; Sugimoto, W.; Ebina, Y.; Shibata, T.; Osada, M.; Sasaki, T., *Inorg. Chem.* **2013**, *52* (5), 2280–2282.
70. Sarioglan, S., *Platinummetalsreview* **2013**, *57* (4), 289–296.
71. Zhao, F.; Shirai, M.; Ikushima, Y.; Arai, M., *J. Mol. Catal. A Chem.* **2002**, *180* (1–2), 211–219.
72. Swanson, H. E.; Mc Murdie, H. F.; Morris, M. C.; Evans, E. H. Standar X-Ray Diffraction Powder Patterns. In *National Bureau of Standard Monograph*; 1969; Vol. 25, p 188.
73. Hampel, B.; Kovács, G.; Czekes, Z.; Hernádi, K.; Danciu, V.; Ersen, O.; Girleanu, M.; Focşan, M.; Baia, L.; Pap, Z., *ACS Sustain. Chem. Eng.* **2018**, *6* (10), 12993–13006.
74. Gruber-Woelfler, H.; Radaschitz, P. F.; Feenstra, P. W.; Haas, W.; Khinast, J. G., *J. Catal.* **2012**, *286* (9), 30–40.
75. Jin, S.; Feng, Z.; Fan, F.; Li, C., *Catal. Letters* **2015**, *145* (1), 468–481.

76. Li, C.; Wu, Z. Microporous Materials Characterized by Vibrational Spectroscopies. In *Handbook of Zeolite Science and Technology*; CRC Press, 2003.
77. Auerbach, S. M.; Carrado, K. A.; Dutta, P. K. *Handbook of Zeolite Science and Technology*; CRC Press, 2003.
78. Fan, F.; Feng, Z.; Sun, K.; Guo, M.; Guo, Q.; Song, Y.; Li, W.; Li, C.; Fan, F.; Feng, Z.; et al., *Angew. Chem. Int. Ed* **2009**, *48*, 8743–8747.
79. Fan, F.; Feng, Z.; Li, C., *Acc. Chem. Res.* **2010**, *43* (3), 378–387.
80. Yu, Y.; Xiong, G.; Li, C.; Xiao, F.-S. S., *Microporous Mesoporous Mater.* **2001**, *46* (1), 23–34.
81. Fan, F.; Feng, Z.; Li, C., *Chem. Soc. Rev* **2010**, *39*, 4794–4801.
82. Karge, H. G.; Weitkamp, J. *Characterization II*; Springer, 2007.
83. Cao, E.; Sankar, M.; Firth, S.; Lam, K. F.; Bethell, D.; Knight, D. K.; Hutchings, G. J.; McMillan, P. F.; Gavriilidis, A., *Chem. Eng. J.* **2011**, *167* (2–3), 734–743.
84. Ajayi, B. P.; Rabindran Jermy, B.; Abussaud, B. A.; Al-Khattaf, S., *J. Porous Mater.* **2013**, *20* (5), 1257–1270.
85. Bressel, A.; Donauer, T.; Sealy, S.; Traa, Y., *Microporous Mesoporous Mater.* **2008**, *109* (1–3), 278–286.
86. Foo, G. S.; Wei, D.; Sholl, D. S.; Sievers, C., *ACS Catal.* **2014**, *4* (9), 3180–3192.
87. Chow, Y. K.; Dummer, N. F.; Carter, J. H.; Williams, C.; Shaw, G.; Willock, D. J.; Taylor, S. H.; Yacob, S.; Meyer, R. J.; Bhasin, M. M.; et al., *Catal. Sci. Technol.* **2017**, *8*, 154–163.
88. Du, H.; Chen, S.; Wang, H.; Lu, J., *Chinese J. Catal.* **2017**, *38* (7), 1237–1244.

CATALYTIC CONVERSION OF BIOMASS

CHAPTER 5. CATALYTIC CLEAVAGE OF C-C INTER-UNIT LINKAGES IN LIGNIN MODEL COMPOUNDS

S. Guadix-Montero
CARDIFF UNIVERSITY | CARDIFF CATALYSIS INSTITUTE

Contents

5	Catalytic cleavage of C-C inter-unit linkages in lignin model compounds	197
5.1	Introduction.....	197
5.2	Carbon-carbon bond cleavage in dimeric model compounds using RICO.....	198
5.2.1	Oxidative cleavage of 5-5' inter-unit linkage in biphenyl.	199
	• Effect of the oxidant in the oxidation of biphenyl.....	204
	• Investigation of the RICO reaction mechanism of biphenyl towards phenylgloxal..	207
5.2.2	Oxidative cleavage of β -1' inter-unit linkage in bibenzyl	210
5.3	Carbon-carbon bond cleavage in complex lignin model compounds using RICO. Towards lignin depolymerisation	215
5.3.1	Oxidative cleavage of C-C bond in β -O-4' lignin model polymer.	215
5.3.2	Oxidative cleavage of different inter-unit linkages in a hexamer model compound	219
	• Kinetic studies and potential inter-unit cleavage quantification	221
	• Oxidation products identification.	234
5.4	Conclusions.....	239
5.5	References.....	241

5 Catalytic cleavage of C-C inter-unit linkages in lignin model compounds.

5.1 Introduction

Depolymerisation of lignin to smaller molecular weight compounds is a very promising reaction. It can potentially generate value-added products, especially aromatics and functionalised aromatics.¹ Aromatics compounds can be used for the sustainable production of high-value fine chemicals, and fuels.² To achieve the full potential of lignin valorisation *via* depolymerisation reactions is necessary to the development of new technology. This would allow integrating the process within the biorefinery. Depolymerisation of lignin can be either catalytic or non-catalytic. In both cases, it involves the breaking of C-O and C-C inter-unit linkages present in lignin. Depolymerisation techniques can be oxidative, reductive or redox-neutral. Typically, the oxidative depolymerisation reaction results in aromatic acids, aldehydes and occasionally aliphatic acids via the opening of the aromatic ring.³ The challenge in designing these strategies is to get the desired product(s) in high selectivity. Breaking specific inter-unit linkages selectively would avoid complex separation processes.

To design strategies for the selective cleavage of inter-unit linkages, it is a common practice to use lignin model compounds. They are used to avoid the complexities such as the presence of impurities and heterogeneous structures involved in using the real lignin.^{4,5} These model compounds contain specific kind of inter-unit linkages that are present in lignin. A few examples of such model compounds, representing different inter-unit linkages in lignin, that are typically used in the literature, are presented in *Figure 1-9* (Chapter 1). Lignin model compounds are beneficial to study the kinetics and mechanism of the cleavage reactions. They are also useful for understanding the mechanisms in designing catalysts able to break the inter-unit linkages. However, translating the catalytic results from these model compounds to real lignin is not a straight-forward process. Due to the presence of substituents and other functionalities severely complicate the depolymerisation reactions. It is important to highlight that these lignin model compounds (*Figure 1-9*) reduce the complexities involved in dealing with compounds with many different functionalities. Therefore, model compounds are a good starting point for initial catalyst development.

In this Chapter Ruthenium Ion Catalysed Oxidation (RICO) chemistry is applied for the cleavage of inter-unit linkages in lignin model compounds in an effort to depolymerise lignin. This work reiterates the research challenges to achieve the C-C bond scission during lignin depolymerisation (see our review published recently for further details).¹ In this chapter, there is also a description of the challenges in the qualitative and quantitative analyses of the products obtained. Also, the methodology for the estimation of the potential C-C bond cleavage using quantitative 2D-NMR and ³¹P-NMR techniques is presented.

5.2 Carbon-carbon bond cleavage in dimeric model compounds using RICO

Among the inter-unit linkages present in lignin, C-C linkages are stronger and hence are more recalcitrant than the C-O linkages. Most of the reported literature focus on the breaking of C-O inter-unit linkages. The C-O linkage has a bond dissociation enthalpy BDE around 54-72 kcal/mol.⁶ Almost all the C-C bond breaking reported in the literature are related to the C_α-C_β bond cleavage of the β-O-4' lignin linkage (BDE 75-80 kcal/mol) rather than stronger C-C linkages such as 5-5' (BDE 115-118 kcal/mol).^{7, 8}

RICO is a useful methodology for the oxidative cleavage of C-C in alkyl-substituted polyaromatics compounds.⁹ Therefore, oxidation of several lignin model compounds (see structures in *Figure 5-1*) that represent some of the different inter-unit linkages present in lignin was studied *via* RICO (explained in detail in Chapter 1 *section 1.3.3*). The first step is to start with simple dimeric compounds such as biphenyl and bibenzyl for the 5-5' and β-1' inter-unit linkage, respectively. As mentioned in Chapter 1 (*section 1.3.2*) 5-5' and β-1' linkages are highly refractory. They typically survive during all commercially practised delignification processes (*e.g.* kraft lignin pulping process).¹⁰ In particular, C₅-C_{5'} bonds are very stable during alkaline and/or kraft pulping.¹¹ The order of the Bond Dissociation Energy (BDE) is as follows; C_α-O < C_β-O < C_α-C_β (β-1') < C_α-C_β (β-O-4') < C₄-O < O-C₅ < C_α-C₁ < C₅-C_{5'}.¹² Therefore, if we initially focus on breaking the C₅-C_{5'}, the cleavage of the rest of the inter-unit linkages should be more accessible. To prove this hypothesis, on other model compounds used was a β-ether-type lignin-like model polymer, for the oxidative cleavage of C₄-O and C_α-C_β in the β-O-4' inter-unit linkage.

Further studies have been done on a more complex model compound. This compound is a hexamer which contains not only β-O-4' and the 5-5' linkages, but also the benzofuran ring (β-5' linkage).

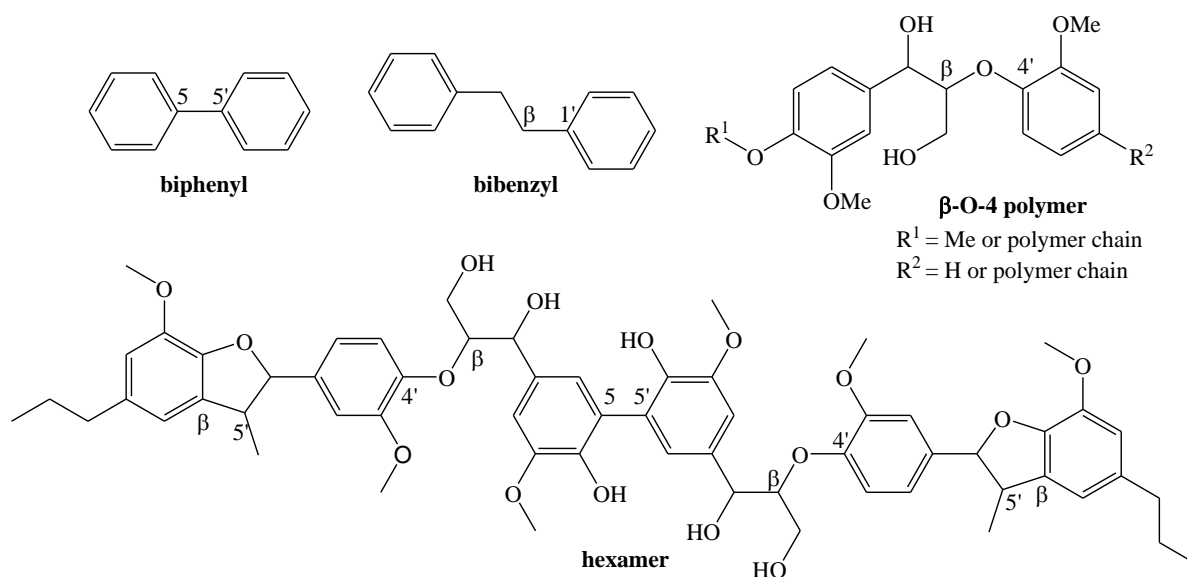


Figure 5-1 Lignin model compounds/polymers employed in this chapter.

This chapter aims at developing a catalytic system to break the most difficult inter-unit linkages present in lignin using appropriate model compounds. After optimising the reaction conditions for these model compounds, the long-term objective is to translate this system for the depolymerisation of real lignins.

5.2.1 Oxidative cleavage of 5-5' inter-unit linkage in biphenyl.

The 5-5' aryl-aryl C-C bond linkages are present in original wood, and indeed it is found in lignin as the second-most abundant linkage. Its frequency is between a 20-25 % of the total phenylpropane units in softwoods lignin and around 3-9 % in hardwoods lignin.¹³ Therefore, its rupture is of high importance for the valorisation of lignin to produce monomeric platform aromatics. A significant part of the compounds found in soil contains biphenyl, which comes from natural lignin, what suggest that nature does not degrade it easily by its own. Therefore, it is evident that biphenyl degradation leads to the goal of lignin depolymerisation. Bacterial degradation of biphenyls has been widely studied since there are soil bacteria which are biphenyl degraders.¹⁴ Several mechanisms of microbial biphenyl degradation have been studied (e.g. *S. paucimobilis* and *S. cereveace*).^{13,15} Moreover, degradation of phenolic biphenyl model compounds was also attempted by a fungus (e.g. white-rot *Phanerochaete chrysosporium*). This fungus did not achieve the biphenyl cleavage, nevertheless it affords some C-C bond cleavage, being the C_α-C₁ cleavage the major degradative reaction.¹⁶

Nevertheless, using chemical methods, the biphenyl 5-5' inter-unit linkage cleavage through lignin model compounds has been a target to attempt for decades with not much progress.^{16,}

^{17,18} Catalytically, aqueous phase reforming seems to be the most appropriate approach for the breaking of this strong bond. However, the reaction conditions of this process are far from being considered as mild, since H₂SO₄, at least 29 bar He, 225 °C is required in the presence of 1 % Pt/Al₂O₃ as the catalyst.¹⁹

One of the advantages of using RICO chemistry is that the reactions are carried out under mild conditions, typically at room temperature (22 °C) and atmospheric pressure. A non-phenolic biphenyl was used as a simple analogue of 5-5' lignin carbon bond. As described previously in Chapter 2, *section 2.1.2.*, the reactions were conducted in a round bottom flask in a monophasic solvent system (2:1 acetonitrile and deionised water). The optimisation of the reaction conditions involves the adjustment of the substrate: oxidant: catalyst molar equivalences from [1:8:0.1] to [1:2.67:0.03] in this case. After the reaction, the mixture was always quenched using Na₂SO₃. Then, the post reaction protocol was followed until the separation of the organic phase was completed (see *section 2.1.2.*). The organic phase was then concentrated in vacuum and re-dissolved in different solvents with several polarity values. Solvents such as ethyl acetate (A), acetone (B), o-xylene (C) and hexane (D) were used to be analysed by GC-MS (*Figure 5-2*).

Using biphenyl (8) as a substrate, the main product observed by GC-MS was benzoic acid (6) followed by phenylglyoxal (5). This clearly indicates the cleavage of the 5-5' bond *via* the opening of one of the aromatic rings. On the other hand, products such as toluene (2), o-xylene (3) and benzaldehyde (4) were also suggested by GC-MS. *Table 5-1* summarises all the compounds suggested by GC-MS.

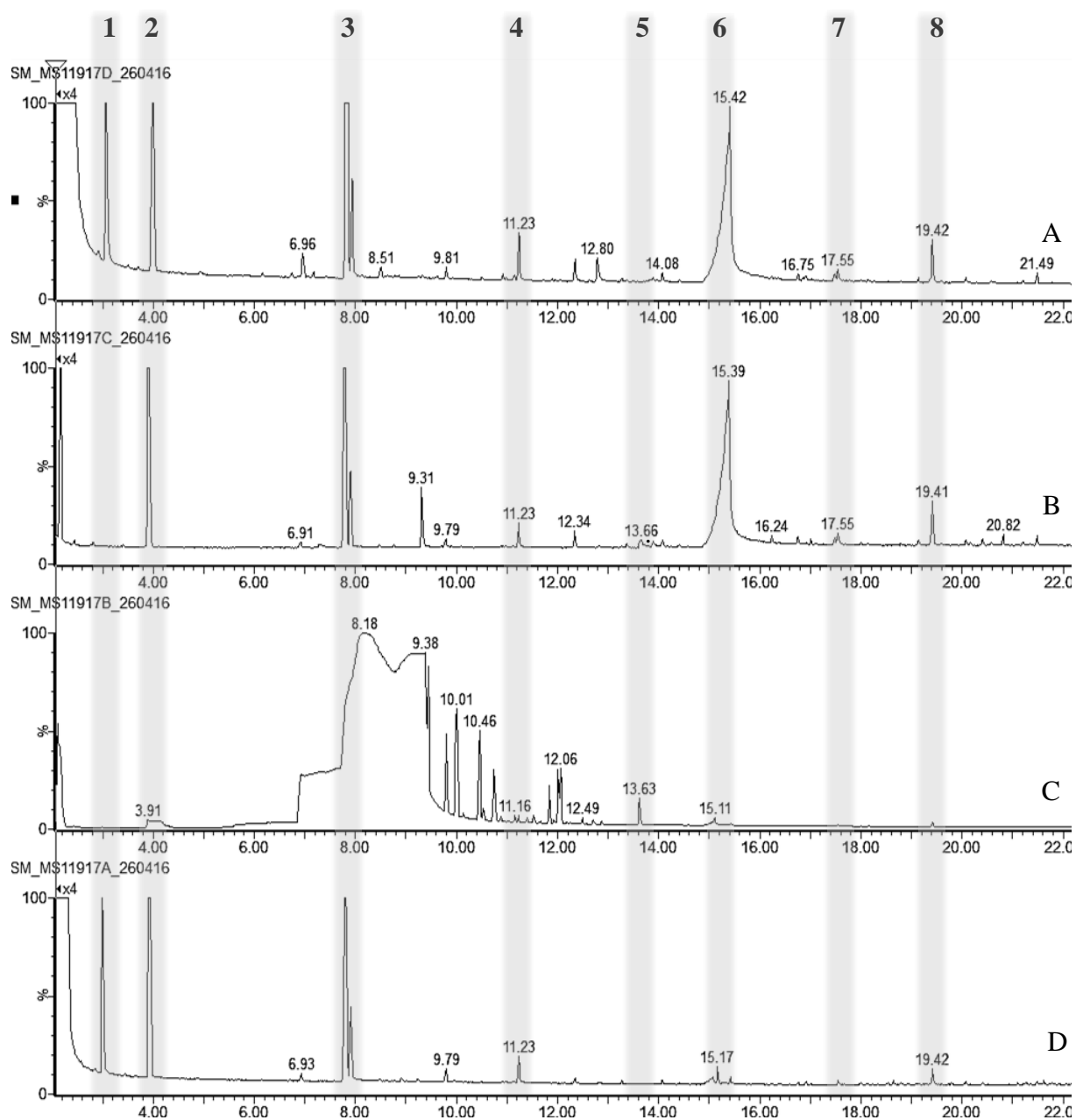
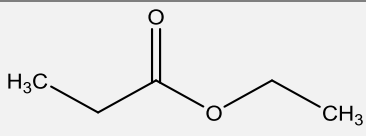
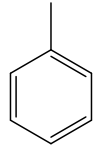
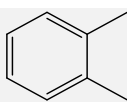
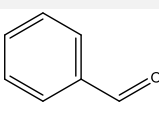
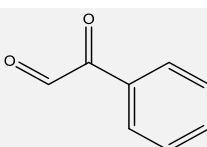
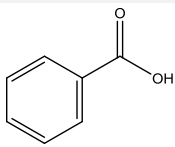
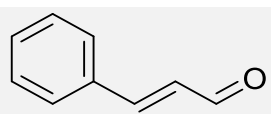
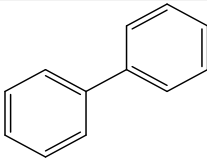
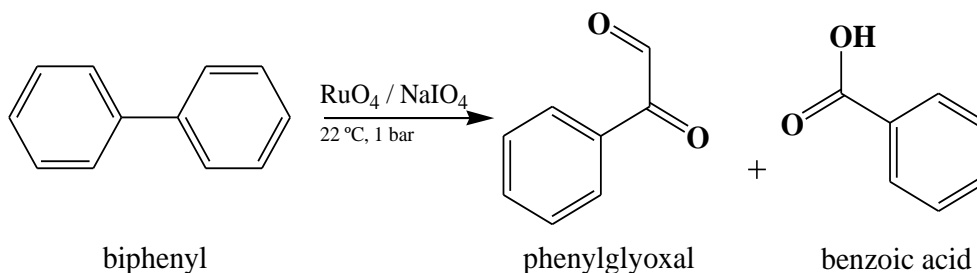


Figure 5-2 GC-MS chromatogram of highly concentrated reaction mixtures in ethyl acetate (A), Acetone (B), O-xylene (C) and Hexane (D)

Table 5-1: Oxidation products of Biphenyl found from GC-MS (Figure 5-2)

Compound Number	Retention time	Compound	Molecular Formula	Structure
1	3.01	Ethyl Propionate	C ₄ H ₈ O ₂	
2	3.91	Toluene	C ₇ H ₈	
3	7.75	o-Xylene	C ₈ H ₁₀	
4	11.23	Benzaldehyde	C ₇ H ₆ O	
5	13.66	Phenylglyoxal	C ₈ H ₆ O ₂	
6	15.17	Benzoic acid	C ₇ H ₆ O ₂	
7	17.55	Cinnamaldehyde	C ₉ H ₈ O	
8	19.42	Biphenyl	C ₁₂ H ₁₀	

Commercial standards of the products suggested by GC-MS were injected in the reverse phase HPLC to identify and quantify them in the reaction mixture. The HPLC method for quantitative analysis of the reaction mixture was optimised to get good separation. To calculate conversion and product selectivity a standard calibration of biphenyl, benzoic acid and phenylglyoxal were carried out.



Scheme 5-1 Oxidative cleavage of 5-5' linkage in biphenyl using RICO chemistry.

The formation of the compounds such as benzoic acid, is a result of the strong oxidising ability of RuO₄ which opens one of the aromatic rings *via* the formation of a cyclic ruthenium(VI)diester.²⁰ Indeed, as described in the Introduction Chapter 1, *section 1.2.3.*, RICO reactions on aromatic compounds lead to the formation of carboxylic acid products.²¹

The RICO of biphenyl is effective at short reaction times, 4 h being the optimum reaction time. Catalytic results are reported as the on-line time evolution of products and substrate conversion (*Figure 5-3*). The results show that *ca.* 30 % of biphenyl is converted in 4 h of reaction. This is of great importance, considering the strength of the 5-5' bond. Indeed, only a few works previously reported the cleavage of this bond. Zakzeski *et al.* succeeded in the 5-5' bond cleavage obtaining methylguaiacol and guaiacol (only 7 and 12 % yield) in 1.5 hours. The authors employed aqueous phase reforming using a 1 % Pt/Al₂O₃ catalyst and harsher reaction conditions (i.e. H₂SO₄, high pressure, 29 bar He and 225 °C).¹⁹ However, the model compound that these authors used to test the 5-5' bond cleavage was fully functionalised; this could make it more accessible to the oxidation than biphenyl. Indeed, the most abundant compound that they obtained was the result of the hydrolysis of one or both methoxy-groups (in 42 % and 9 % yield, respectively).

From the products calibrated, the selectivity towards benzoic acid was above 80 % at *ca.* 30 % of biphenyl conversion with a carbon mass balance of *ca.* 80 % considering the two main products produced (benzoic acid and phenylglyoxal) and the unreacted substrate at 4 h of RICO reaction.

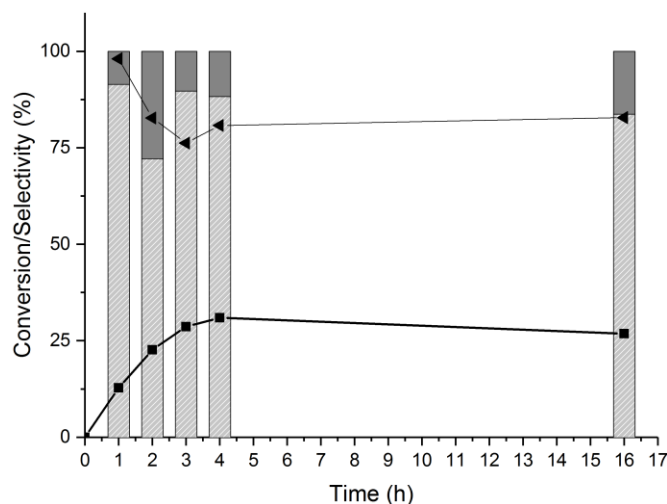
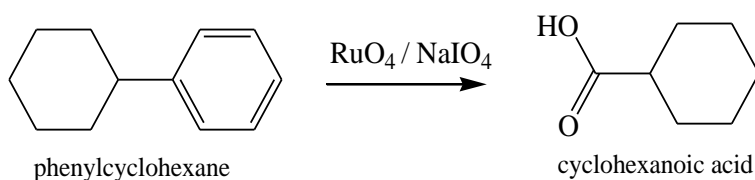


Figure 5-3. Time online of the RICO reaction for biphenyl with a molar ratio of substrate, oxidant and catalyst of [1:2.67:0.03]. Biphenyl conversion (-■-), carbon mass balance (-◄-), the selectivity of benzoic acid (▨) and selectivity of phenylglyoxal (■). 75 mg Biphenyl, 280 mg NaIO_4 and 0.23 mL of $\text{RuCl}_3 \cdot x\text{H}_2\text{O}$ stock solution. 30 mL of reaction solvent mixture of 2:1 Acetonitrile-deionise water, at 22 °C, 1 atm.

From the results presented in this section, RICO of biphenyl demonstrates the successful cleavage of C-C bond cleavage under mild reaction conditions (22 °C and atmospheric pressure). Oxidative degradation of benzene rings has been reported using ruthenium tetraoxide (RuO_4) as a strong oxidant for the synthesis of carboxylic acids. For example, phenylcyclohexane was converted into cyclohexanoic acid using catalytic amounts of RuO_4 , with sodium periodate as the co-oxidant (Scheme 5-2).^{22,23} Production of aldehydes from aromatics instead to carboxylic acids was observed in the oxidation of olefins by Yang *et al.* via the formation of ruthenium (VI) diester as possible intermediate. This intermediate yielded keto aldehyde directly and cis-diol by hydrolysis.²⁴



Scheme 5-2 Oxidation of aromatic rings into carboxylic acid using. RuO_4 .²²

- **Effect of the oxidant in the oxidation of biphenyl**

In order to increase the conversion of biphenyl without modifying the mild reaction parameters such as temperature or pressure, different molar equivalences of substrate, oxidant and catalyst

were investigated. As a result, there is a vast improvement in the conversion of biphenyl from 30 % to 70 %. Benzoic acid and phenylglyoxal were found as products in all these reactions, indicating the C-C scission. However, these processes also present a decrease in their carbon mass balances (sometimes by 50 %) as the concentration of oxidant increases (*Figure 5-4*). The C mass balance decreases probably because it is further oxidase to unknown products.

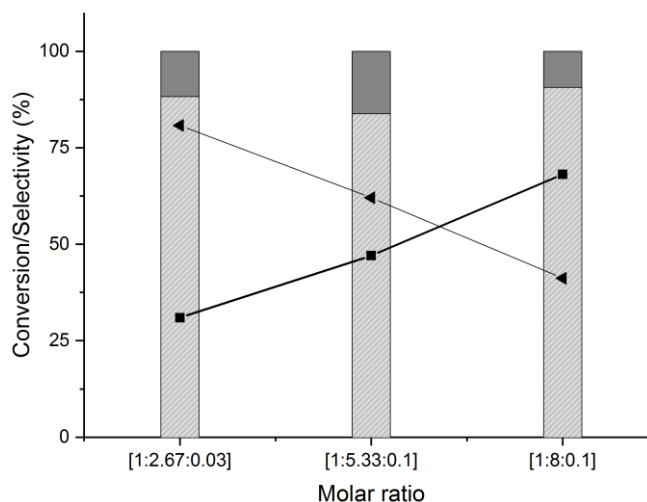


Figure 5-4 Oxidant effect after 4 hours of RICO reaction for biphenyl at 22 °C and 1 atm with a molar equivalences of [1:2.67:0.03], [1:5.33:0.01] and [1:8:0.01]. Biphenyl conversion (-■-), carbon mass balance (-◄-), the selectivity of benzoic acid (▨) and selectivity of phenylglyoxal (■).

Efforts have been made to understand the reasons behind the missing carbon mass for the reaction mixtures when a higher amount of NaIO_4 was used. This reaction shows the precipitation of large quantities of iodate.²⁵ The solid precipitate was washed with an aqueous NaOH solution and then analysed. This step was incorporated in the post-reaction protocol mainly to recover any possible solid carboxylic acids. Since benzoic acid is a white crystalline solid, slightly soluble in water, it could remain easily in the filter paper at room temperature. Addition of a 1 M solution of sodium hydroxide would dissolve it entirely producing sodium benzoate. Then, this basic solution was neutralised using diluted hydrochloric acid and the resultant solid precipitate was analysed by NMR and IR techniques. The results showed no presence of organic compounds in the solid precipitate, indicating that the loss of carbon mass balance should be due to a different reason. The gas phase of the reaction with substrate:oxidant:metal of [1:8:0.01] was analysed by GC, however, no CO_2 was obtained.

The organic phase of the previous reactions using different substrate:oxidant:metal molar ratio ([1:2.67:0.03] [1:5.33:0.01] and [1:8:0.01]), were concentrated in vacuum, using a rotary evaporator. They are labelled as Reaction Mixture-1 (RM-1), Reaction Mixture-2 (RM-2) and Reaction Mixture-3 (RM-3), respectively. The concentrated samples were analysed by GC-MS using ethyl acetate as solvent. The results suggested that cinnamaldehyde and trans-cinnamic acid (17.98 min and 20.21 min of retention time respectively) are the new products obtained, (7 and 9 peaks in *Figure 5-5*) in the case of RM-2 and RM-3. In addition to the previous, relatively small quantities of phenylacetaldehyde (13.1 min) and phenylmaleic anhydride (22.85 min) were produced.

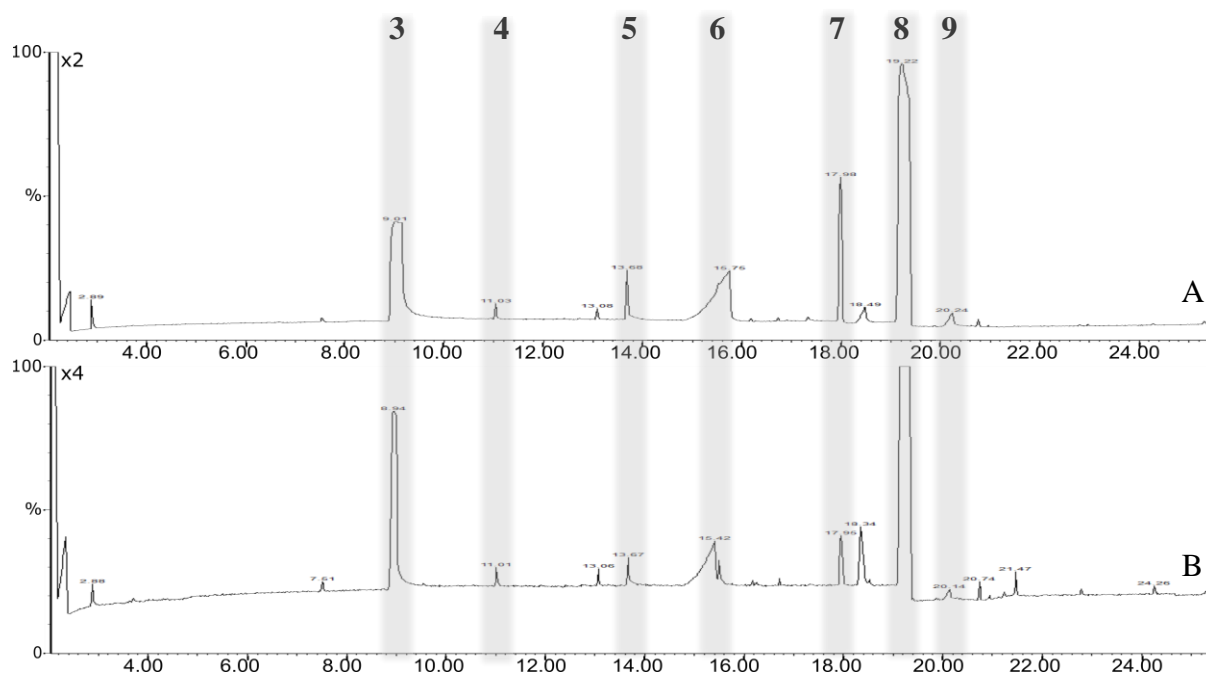


Figure 5-5 GC-MS spectrum of highly concentrated sample in ethyl acetate of RICO reaction mixtures for biphenyl after 4 hours at 22 °C and 1 atm with a molar ratio of (A) [1:8:0.01] RM-3 and (B) [1:5.33:0.01] RM-2.

Thin layer chromatography (TLC) was performed to identify the products in the reaction mixtures, by comparing with the commercial standards from *Sigma Aldrich*. *Figure 5-6-A* shows the developed for TLC plate under UV light using an eluent mixture containing Ethyl Acetate: Hexane with a volume ratio of [1:9] as the mobile phase. In *Figure 5-6-A* spots from left to right correspond to benzaldehyde, cinnamaldehyde, phenylglyoxal, phenylacetaldehyde, RM-2 [1:5.33:0.01], and RM-3 [1:8:0.01], respectively. In this case, the cinnamaldehyde and the benzaldehyde spots are at the same level, and this spot is present in both reaction mixtures. The separation between cinnamaldehyde and benzaldehyde was found using a solvent ratio of [0.75:9.25] for the eluent. *Figure 5-6-B* shows, from left to right, the spotting of benzoic acid,

cinnamaldehyde, benzaldehyde, RM-3 [1:2.67:0.03] concentrated in vacuum (*), and just after quenching the reaction, RM-1 [1:5.33:0.01], and RM-2 [1:8:0.01]. In the same way, *Figure 5-6-B* illustrates that there is a match with cinnamaldehyde in two of the four reaction mixtures tested, coinciding with the higher amount of oxidant added to the reaction. This technique shows tentative evidence of the presence of benzoic acid, which is confirmed by GC-MS and HPLC studies. On the contrary, benzaldehyde was not found in any of the reaction mixtures.

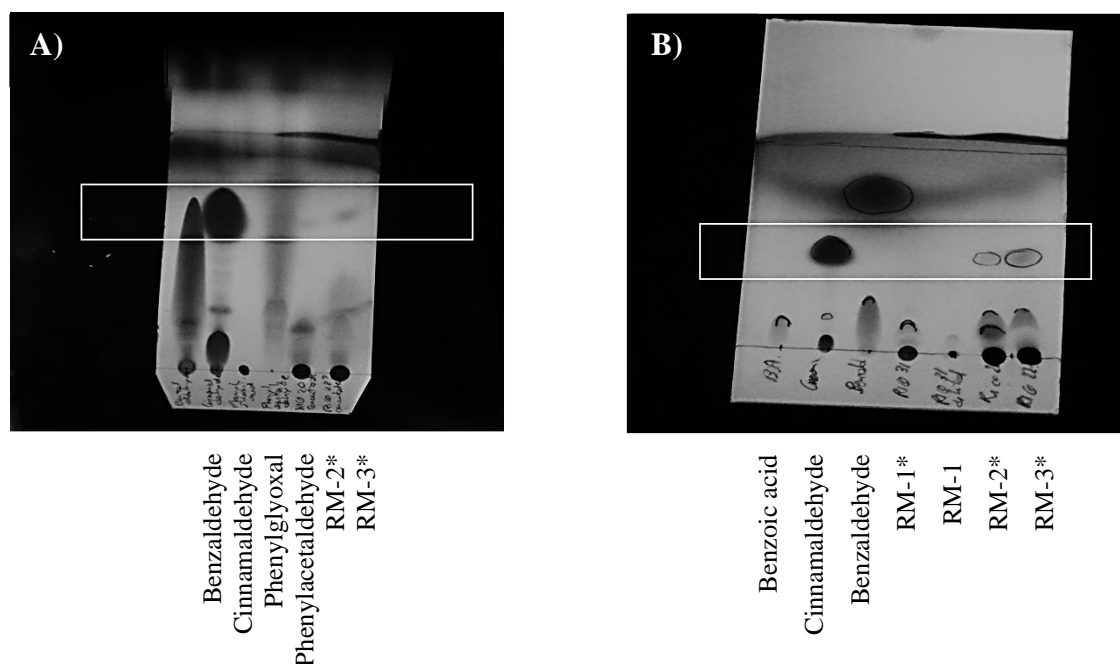


Figure 5-6 Thin layer chromatogram under UV light using as mobile phase A) Ethyl Acetate: Hexane [1:9] and B) Ethyl Acetate: Hexane [0.75:9.25] Reaction mixtures concentrated in a vacuum are labelled ().*

Finally, a prominent peak area of an unknown compound was also found to increase among the amount of oxidant in the product mixtures (RM-2 and RM-3) in the HPLC chromatogram. The peak visible with a maximum of absorbance around 274 nm has a retention time of around 14.5 min.

- ***Investigation of the RICO reaction mechanism of biphenyl towards phenylglyoxal***

Computational studies on the mechanism for the RuO₄ catalysed the oxidation of biphenyl was investigated in collaboration with Dr David Willock, Alhaji Mala and Jiangpeiyun Jin (Cardiff University) using Advanced Research Computing at Cardiff (ARCCA).

Computational methods were used to investigate the mechanism of the formation of phenylglyoxal through oxidation of biphenyl with ruthenium tetroxide. Density functional

theory (DFT) was employed in calculating the energy corresponding to the reaction. Hybrid functionals are a class of approximations to the exchange-correlation energy functional in DFT. In this case, the commonly used version of the hybrid functionals (B3LYP) was employed.²⁶ By analysing the energy calculated by Gaussian09,12 it predicts which of the theoretical pathways for forming phenylglyoxal through the [3+2] addition of ruthenium tetroxide and biphenyl is the most efficient one. *Figure 5-7* shows the different mechanisms depending on the position where the RuO₄ is added on a double bond of biphenyl to form a ruthenium (VI) compound adduct, leaving intact the unreacted aromatic ring, to produce phenylglyoxal.

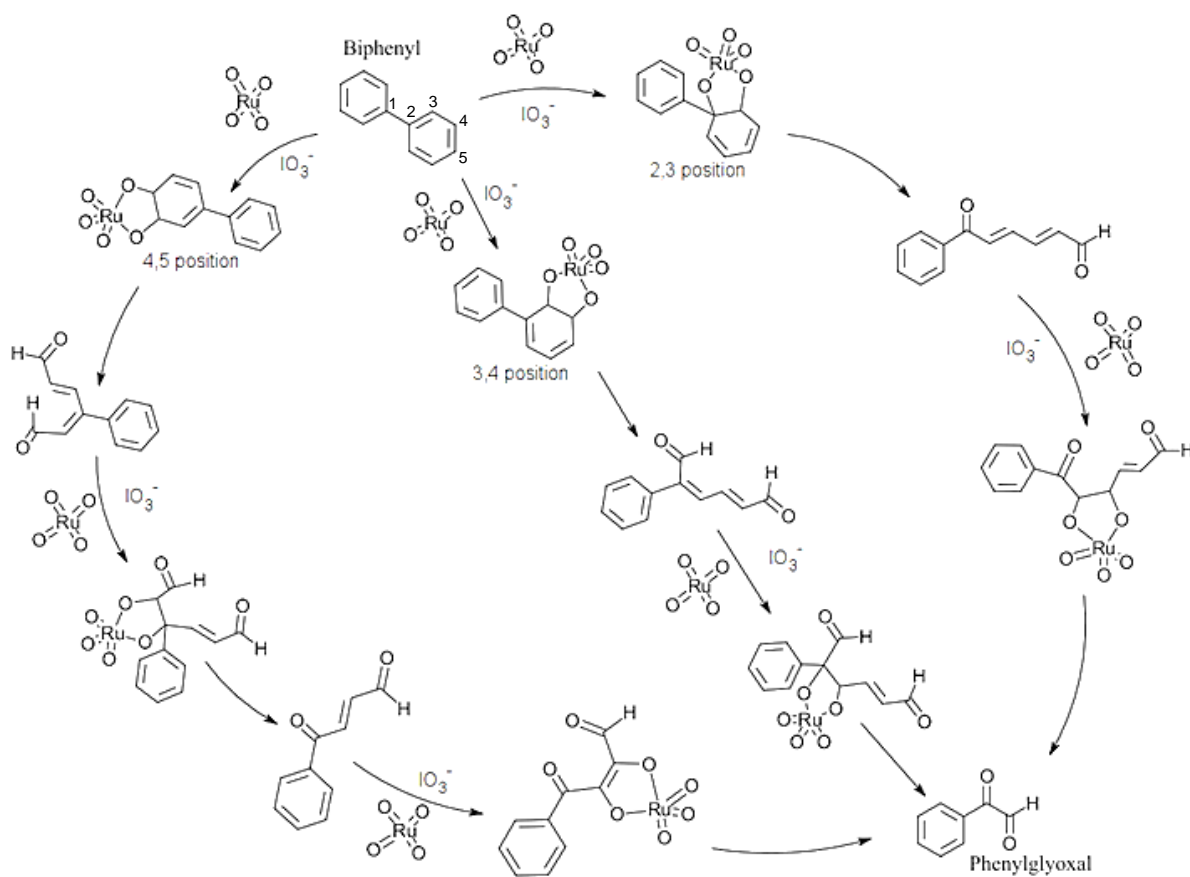


Figure 5-7 Proposed mechanism for the oxidation of biphenyl using ruthenium tetroxide, with IO₃⁻ to oxidise Ru (IV) to the Ru (VIII) oxidation state.

As the proposed mechanism shows, two steps of [3+2] additions take place for the formation of phenylglyoxal on the (2, 3) and (3, 4) positions of biphenyl (see *Figure 5-7*). However, in the case of the (4, 5) position a total of 3 steps of [3+2] additions are necessary. The first [3+2] additions of RuO₄ Ru (+8) to the double bond of biphenyl on all the three possible positions are slightly exothermic since their enthalpy changes are within -7 kcal mol⁻¹. However, among the three positions studied, the adduct formed on the (3, 4) position had the lowest binding

energy ($-8.58 \text{ kcal mol}^{-1}$), which makes this position the most favourable one. Nevertheless, the (4, 5) position is the second more favourable, since it is only $1.12 \text{ kcal mol}^{-1}$ higher than the (3, 4) position. Therefore, the selectivity of ruthenium tetroxide on these two positions is not suggested by the calculated data. Indeed, the small difference in energy barrier calculated suggests that factors such as the solvent effect in the reaction need to be considerate. Comparing monophasic against the biphasic solvent system could be a good approach when using in RICO chemistry.²⁷ In the case of the less favourable position studied (2, 3) might be affecting the proximity of unreacted side (phenyl group), which could have a stronger interaction with the RuO_4 on this position. Thus, it is required more energy for the formation of the adduct on the $\text{C}_5\text{-C}_{5'}$ bond or (1, 2) position. Once the [3+2] adduct is formed, the re-oxidation of RuO_2 (+4) to the RuO_4 (+8) oxidation state takes place thanks to the reduction of IO_4^- to IO_3^- which ensures that ruthenium has a stronger oxidising power. Another observation obtained from this work was that the activation energy of the reaction of the RuO_5 adduct is lower than that of the RuO_4 adduct, increasing the rate of the reaction.

Studies on the mechanistic pathways to produce benzoic acid from biphenyl using RuO_4 are currently underway. As mentioned before, to the exemption of benzoic acid and phenylglyoxal, no additional significant products were present. The incomplete mass balance obtained (especially in those reactions with a high ratio of IO_4^-), could be attributed to unstable products, polymerisation or other reactions of radical intermediates, as have been reported in previous work using RICO or with other lignin model compounds.^{28,29}

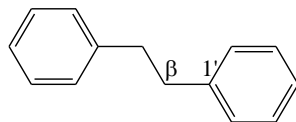
In summary, this work confirmed RICO chemistry is a potential tool for the oxidative cleavage of the 5-5' inter-unit linkage, opening one of the aromatic rings in the refractory structure of biphenyl to form a valuable aromatic product such as carboxylic acids. These results motivated us to study the performance of this catalytic system using other dimer model compounds. For instance, to investigate the effect on the RuO_4 on a model which contains an aliphatic chain between the aromatic rings, such as bibenzyl, something familiar in lignin structure. This would help us to understand RICO chemistry and its application for lignin depolymerisation.

5.2.2 Oxidative cleavage of β -1' inter-unit linkage in bibenzyl

β -1' inter-unit linkage in lignin is relatively uncommon (7-9 % in wood lignin).³⁰ However, it is present in both softwood and hardwood native lignin.³¹ The β -1' inter-unit linkage can be coupling at the C_α in its side chain through α -O- α linkage to form a cyclic structure called Spirodienone units (see the structure reported in *Table 1-1*, Chapter 1). This unit is the predominant form of this linkage in native lignin. Indeed, recent studies have proposed this structure to be a precursor for acyclic β -1' linkages in lignin.³²

The cleavage of β -1' linkage is more straightforward than trying to break the 5-5' linkage. Indeed, it has been intensively investigated previously due to this reason (see *Chapter 1, section 1.3.2.*).

The work carried out in this thesis shows evidence of the cleavage of this inter-unit linkage in the nonphenolic bibenzyl as a model compound using RICO chemistry (*Scheme 5-3*). Employing a molar ratio of substrate: oxidant: metal of [1:8:0.1] the conversion increased rapidly until it reaches a plateau at *ca.* 25 %. The substrate conversion reaches 21 % in just about 2 hours of reaction and then it plateaus (*Figure 5-8*). This plateau could be because of the complete consumption of the active component (RuO_4).



Scheme 5-3 β -1' inter-unit linkage in bibenzyl model compound

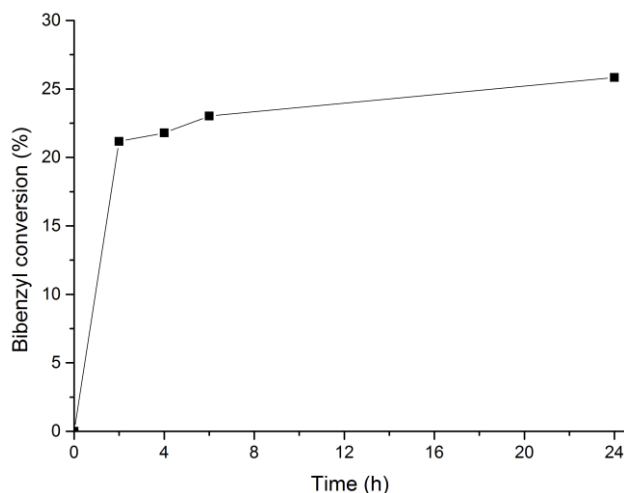


Figure 5-8 Time online studies for the conversion of bibenzyl (-■-) at 22 °C, 1 atm, the molar ratio of substrate: oxidant: metal of [1:8:0.1].

GC-MS analysis of the reaction mixture was performed after drying the samples under vacuum, using a freeze dryer. The samples were re-dissolved in a solvent with different polarities such as ethyl acetate (A), hexane (B) and acetone (C) (Figure 5-9). Table 5-2 shows a list of the suggested products by GC-MS.

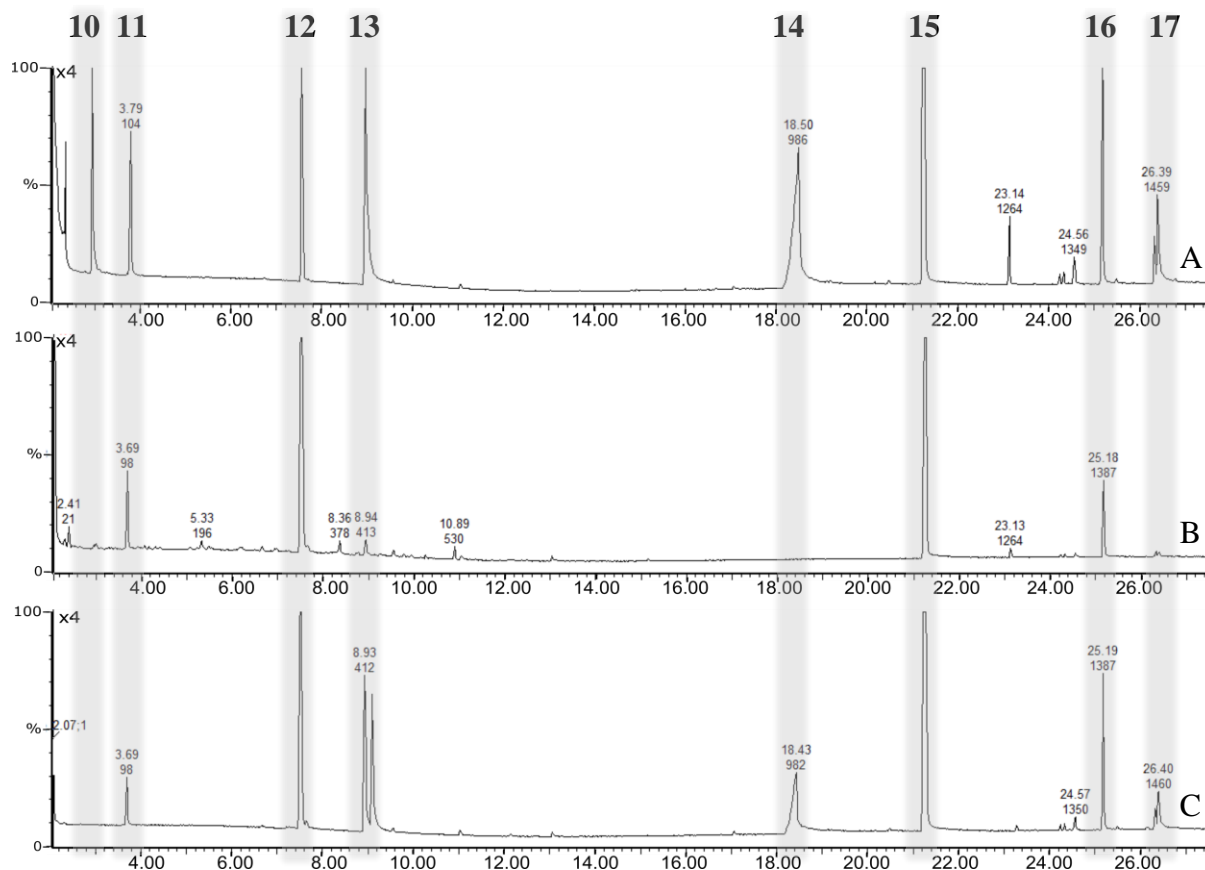
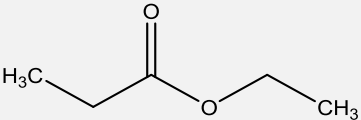
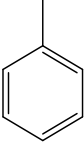
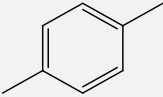
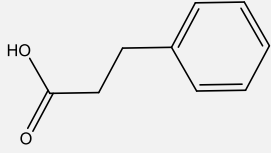
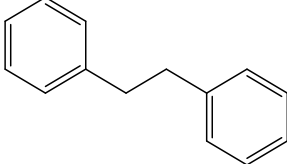
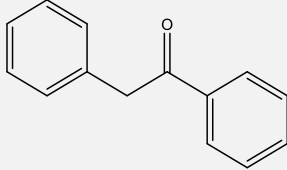
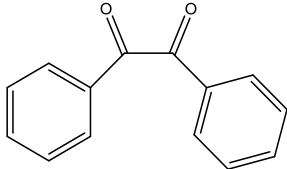


Figure 5-9 GC-MS chromatogram of a highly concentrated sample in ethyl acetate (A), hexane (B) and acetone (C)

Similar to biphenyl oxidation, ethyl propionate, an ester which is more likely to be a derivative of the ethyl acetate solvent is observed (10). This analysis confirmed the C-C cleavage at the aromatic ring and also showed evidence of its further oxidation to form hydrocinnamic acid (14).

On the other hand, an interesting outcome is that 2-phenyl acetophenone (16) and benzyl (17) show oxidation to form a ketone with C-C inter-unit bond intact. Benzyl (17) is not present in the sample dissolved in hexane (spectrum B), but this is not discarded since this compound is not soluble in this solvent. Therefore, evidence of the formation of the products was investigated using different techniques such as LC-MS and NMR.

Table 5-2: Oxidation products of Bibenzyl found from GC-MS

Compound Number	Retention time	Compound	Molecular Formula	Structure
10	2.35	Ethyl Propionate	C ₄ H ₈ O ₂	
11	3.79	Toluene	C ₇ H ₈	
12	7.52	p-Xylene	C ₈ H ₁₀	
13	8.94	Iodine		
14	18.50	Phenylpropanoic acid (or Hydrocinnamic acid)	C ₉ H ₁₀ O ₂	
15	21.23	Bibenzyl	C ₁₄ H ₁₄	
16	25.18	Diphenyl-ethanone (or 2-Phenyl acetophenone)	C ₁₄ H ₁₂ O	
17	26.32	Diphenyl-ethanedione (or Benzyl)	C ₁₄ H ₁₀ O ₂	

However, after a few trial experiments and NMR analyses, it was found that the concentration of the substrate was too low as looking at the number of signals in its ¹H NMR spectrum of the sample after the reaction, any peaks found, if any, were very small. Initially, the *substrate: oxidant: catalyst* molar ratio was [1:8:0.1]. Therefore, the concentration of substrate in the reaction was increased to a [3:8:0.1] molar equivalences, which showed peaks that may have been insignificant baseline peaks in the previous spectrum. In this case, carboxylic acids are also formed. Identified by GC-MS as hydrocinnamic acid and benzoic acid. Besides, ketones at the aliphatic chains have been detected, such as 2-phenylacetone and benzyl. The spectra in Figure 5-10 show the analysis of the starting material, bibenzyl in CDCl₃ (spectrum-3), and the

dried products obtained after 4 h of RICO reaction dissolved in different deuterated solvents D_2O (spectrum-2) and $CDCl_3$ (spectrum-1). Spectrum-2 shows a new peak at approx. 8.4 ppm, in the aromatic region between 7.3 and 7.2 ppm and in the aliphatic region around 2.2-3 ppm. Therefore, there must be some product which involves the CH_2 groups in the bibenzyl. D_2O is a polar solvent, the compound dissolved should also be polar, i.e. possibly an oxygenated compound. Bibenzyl is not soluble in D_2O , reason why it is not present in this spectrum. In the last spectrum, the dry products were dissolved in $CDCl_3$. The results presented in spectrum-1 shows new environments in the aromatic region approximately 7.94, 7.48 and 7.37 ppm. These peaks, along with the peak at 4.22 ppm (aliphatic protons), could be assigned to the 2-phenylacetophenone. Indeed, this compound was clearly identified using LC-MS (See *Appendix*), showing a higher molecular weight than the reactant, which is 182.261.

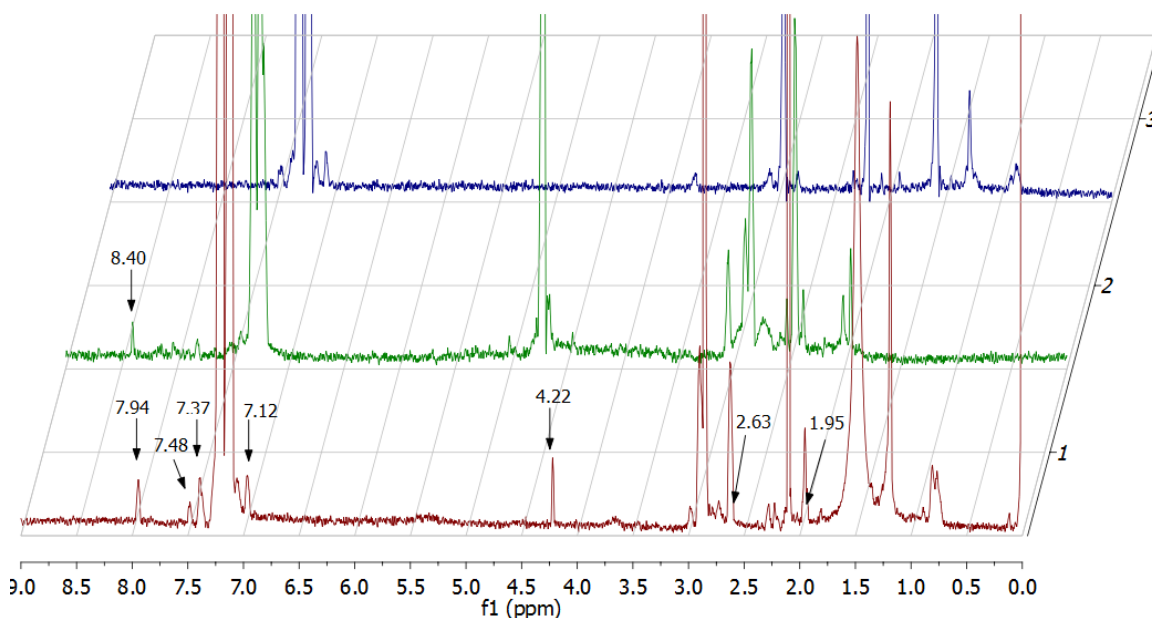
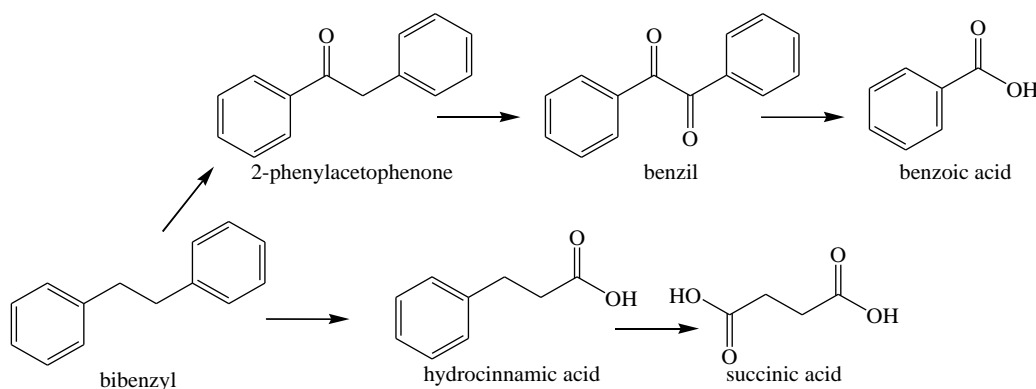


Figure 5-10: 1H NMR spectra comparison of the bibenzyl in $CDCl_3$ (3), reaction products in D_2O (2), and reaction products in $CDCl_3$ (1) after 4 hours of RICO reaction at 22 °C and 1 atm, with a molar ratio of [3:8:0.1].

In order to effectively disentangle these products at this stage, a new analytical method reverse phase HPLC, was necessary. The products identified using commercial standards were benzoic acid, hydrocinnamic acid (**14**) and 2-phenyl acetophenone (**16**). A new peak was observed with the same retention time of succinic acid in the HPLC (see *Appendix 7.5*). However, ethyl acetate also comes out at that retention time. Therefore, more investigation needs to be done to

confirm this product. Nevertheless, this product is mechanistically possible from the further oxidation of hydrocinnamic acid, as shown in the proposed mechanism in *Scheme 5-4*.



Scheme 5-4 Proposed mechanistic pathway for the oxidation of bibenzyl using RICO

As reported in the published review,¹ using oxidative routes, the cleavage of β -1' linkage has been achieved in excellent yields. In general, oxidation reactions give a mixture of C-H and C-C bond cleavage products, such as benzaldehydes. Hanson *et al.* performed oxidation of β -1' linkage using vanadium complexes as homogeneous catalysts. The author demonstrated that the reaction solvent plays an important role in the selectivity of the products.³³ In their work, changing the reaction solvent from DMSO- d_6 to Pyridine- d_5 , the main product becomes benzoic acid instead of benzaldehyde, achieving almost complete conversion of the phenolic lignin model compound. Nevertheless, the oxidation proceeds with a first step by the formation to ketones on the free OH present in the C_α position.

In general, the model compounds used in the literature are highly substituted. Sedai *et al.* also confirmed that the incorporation of a phenolic functionality to the model compound change the reactivity of the catalyst drastically. In their case, this was producing a different kind of C-C bond cleavage. The phenolic model compound enhances the production of ketones, and dehydrated ketones, here derivatives of benzoic acid were also found.³⁰

The fact that the model compounds used in this thesis have a total lack of substituents make them more challenging. Even though it is established that RuO₄ is expected to be added on the double bond of one of the aromatic ring of the model compound, and the aliphatic hydroxyl groups could not affect much, it would be worth it to try RICO chemistry using highly substituted model compounds. In this way, the difference in performances between phenolic and nonphenolic reactants in term of the yield of the desired products could be studied.

5.3 Carbon-carbon bond cleavage in complex lignin model compounds using RICO. Towards lignin depolymerisation

The results showed in previous sections of this thesis indicate that RICO chemistry breaks C-C bonds of non-functionalised dimer model compounds, such as biphenyl and bibenzyl, which make this technique very potent for lignin depolymerisation. RICO was tested with a synthetic lignin-like polymer (G-type lignin model polymer) to investigate if this catalytic system is valid also for a very well-known functionalized phenolic model compound. This polymer is representing the β -O-4' linkage in lignin, which consists of an ether with aliphatic hydroxyl groups from the C_α and the C_γ of the propyl chain and methoxy functionalities.

5.3.1 Oxidative cleavage of C-C bond in β -O-4' lignin model polymer.

The β -aryl ether units are by far the most frequent type of linkage in softwood and hardwood lignin, representing more than 50 % of the structure of native lignin.³⁴ For this reason, from the last few years, researches have focused their attention on the cleavage of this inter-unit linkage. The aryl-alkyl ether bonds are the weakest bond. Indeed, it is susceptible to biodegrading reactions and during alkaline delignification processes. On the contrary, the cleavage of the ether bond occurs in pulping and bleaching processes, although, its C_α - C_β bond is more stable.³⁵

The substrate used in this section was synthesized by our collaborators Prof. Nick Westwood and Dr Chris Lancefield from The University of St. Andrews.^{36,37} It is a β -O-4' model polymer with only guaiacyl (G) sub-units.

The synthesis of the polymer is described in detail in Chapter 2, *Section 2.3.1.* of this thesis. Briefly, it involves the synthesis of the monomer Ethyl 2-(4-formyl-2-methoxyphenoxy) acetate firstly, *via* alkylation reaction of vanillin and ethyl bromoacetate, followed by an aldol reaction with the vanillin derivative 4-hydroxy-3-methoxy benzaldehyde and its further reduction with NaBH_4 and MeOH.³⁸

The G-polymer was formed by the incorporation of several reduced monomers, approximately seven β -O-4' units long. Therefore, it is a heptamer with 8 aromatic units, and it has a molecular weight of 1571.63 Da (*Figure 5-11*). The polymer is purified after its reduction.

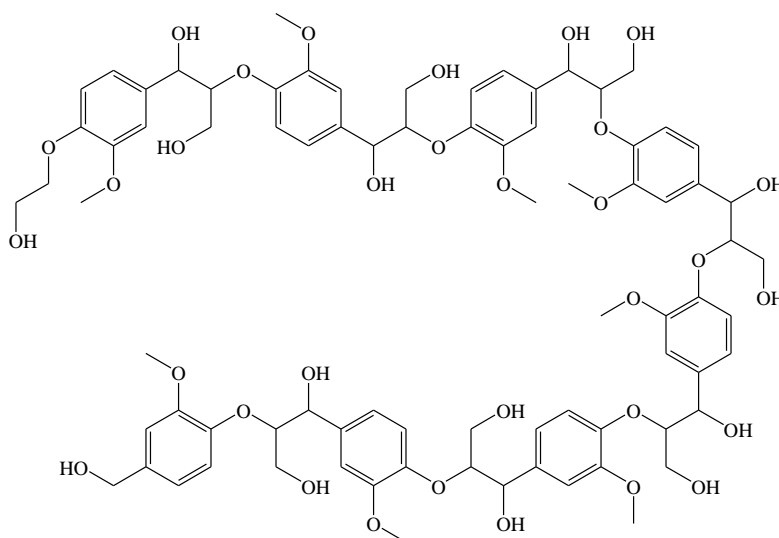


Figure 5-11 G-polymer structure provided by St. Andrews University

To perform a RICO reaction using this model as a substrate, it was necessary to change the solvent system. The G-only β -O-4' polymer is not soluble in acetonitrile or water. In general, to dissolve polymers, solvents such as THF, dioxane or acetones are used. However, none of these are suitable for the RICO reaction, and alcohols were used for solubility test. The sample was not soluble at room temperature in ethanol, but it was completely soluble in methanol. Therefore, methanol was used as the solvent for this reaction, with the addition of the oxidant NaIO_4 in miscible deionised water. 2-dimensional NMR techniques, such as the Heteronuclear Single-Quantum Correlation (HSQC) experiment, was used for the analysis of the reaction mixture. Table 5-3 shows the chemical shift of the $\delta\text{C}/\delta\text{H}$ (ppm) assigned to the starting material using 2D-HSQC.

Table 5-3 Experimental chemical shift for 2D [$^1\text{H};^{13}\text{C}$] HSQC NMR assigned for the β -O-4' model

Linkage/unit	Chemical shift of the peak $\delta\text{C}/\delta\text{H}$ (ppm)
Methoxy groups	55/3.7
Benzyl alcohol group	64/4.4
End group (EG)	61/3.8 & 71/3.9
β -O-4' ($A\gamma$)	61/3.5
β -O-4' ($A\alpha$)	71.9/4.9
β -O-4' ($A\beta$)	85/4.3
Guaiacyl (G2)	111/7.5 & 111/7.6
Guaiacyl (G6)	124.5/7.75

Figure 5-12 illustrates the partial 2D-HSQC corresponding to the aromatic region of the starting material of the heptamer. The H-C environments for the α and β and γ carbon within the β -O-4' linkage can be observed in blue as A(G-G). The environments corresponding to the benzyl alcohol and end groups of the polymer are shown coloured in purple. In addition, the yellow area represents the methoxy group present in the structure.

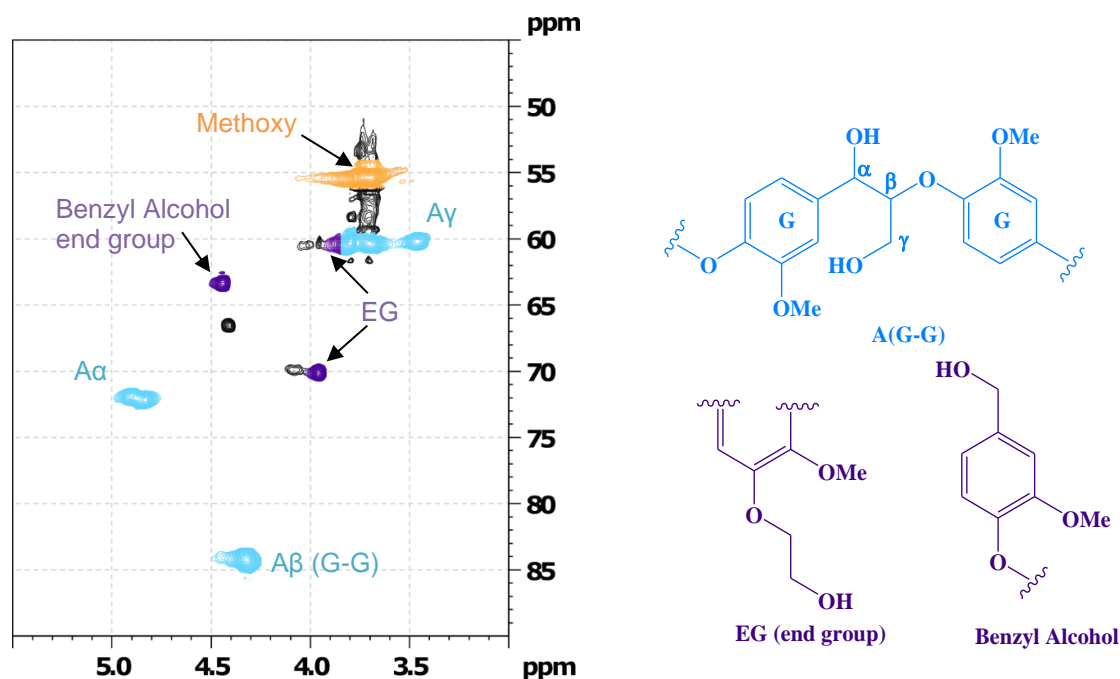


Figure 5-12 Partial HSQC spectrum of the starting material acquired in a 500 MHz Bruker NMR spectrometer

Figure 5-13 illustrates the partial 2D-HSQC of the product mixture after 24 h of RICO reaction. It shows how the benzyl alcohol groups in the polymer have been oxidised partially to aldehydes (G2 and G6 in brown colour). Another interesting point in this 2D-HSQC is that there is evidence of secondary alcohol oxidation to the benzylic ketone. Though to a minor extent, can also be seen in both the aromatic (G2 and G6 in magenta colour) and the aliphatic regions ($A'\beta$). However, it shows a small signal-to-noise in the spectra, hence it is only tentative evidence and further observation are needed to confirm/discard this. There is also a significant amount of etherification of secondary alcohol. Moreover, there is still the presence of remaining β -O-4' linkage (see blue spots in the aliphatic region of Figure 5-13).

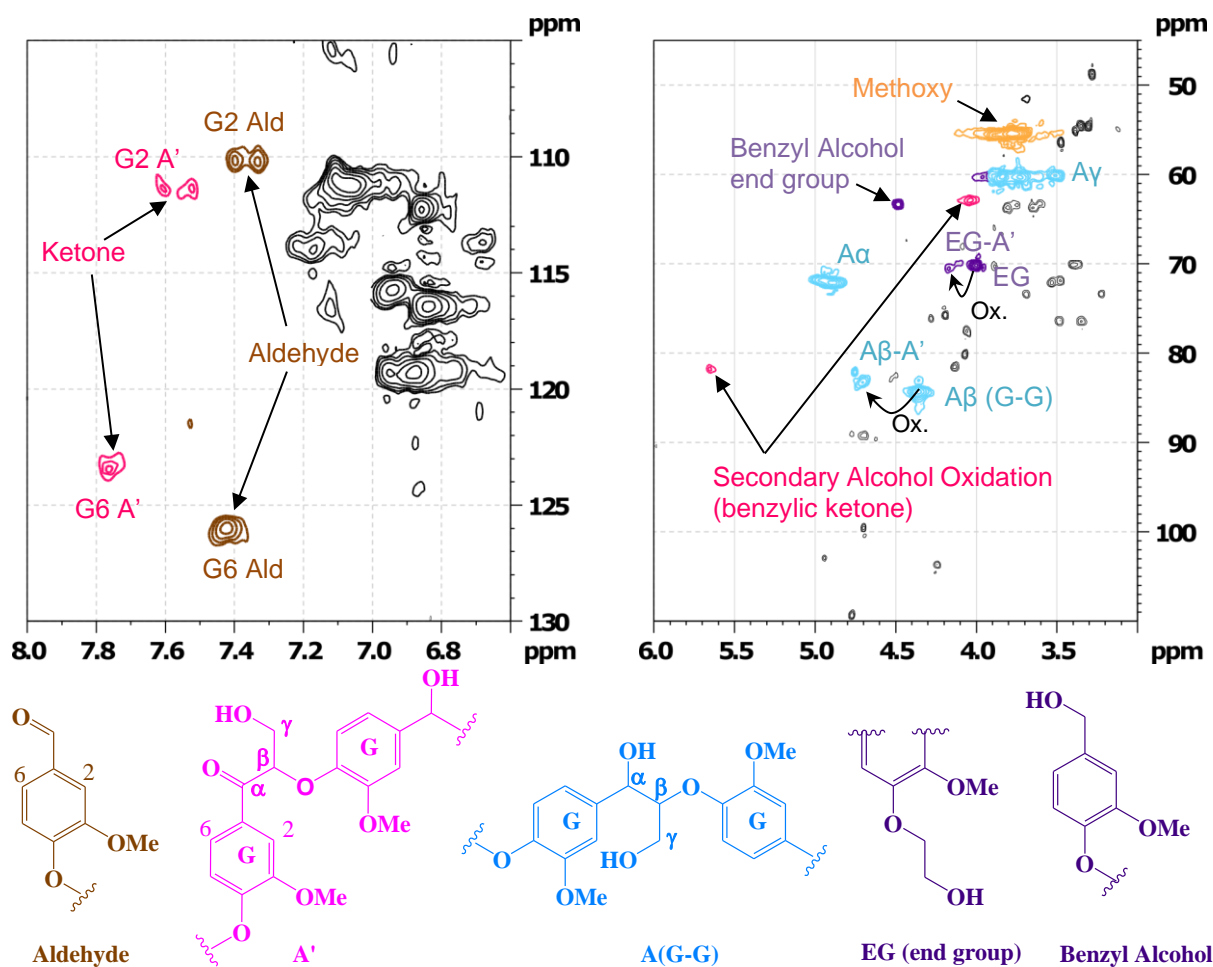
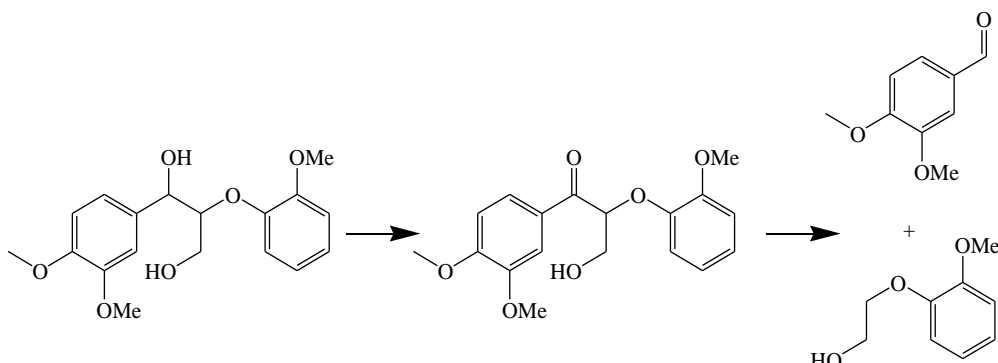


Figure 5-13: Partial HSQC spectrum after 24h of RICO reaction of the β -O-4' model polymer. Acquired in a 500 MHz Bruker NMR spectrometer. The left-hand panel shows the aromatic region. The right-hand panel shows the aliphatic region.

Due to solubility issues and difficulties in the separation of the products during the post-reaction protocol, exclusively qualitative analysis was carried out for this heptamer oxidation. Nevertheless, the formation of the aldehyde indicates C α -C β bond cleavage, leading to the proposed mechanism proposed in Scheme 5-5.



Scheme 5-5 Proposed mechanistic pathway for the C α -C β bond cleavage in β -O-4' G-type polymer

G-type β -O-4' linkage is present in softwood lignin. In general, this kind of lignin contains more resistant linkages than the SG type lignin (hardwood lignin) such as 5-5' and β -5'.³⁹ Hardwoods are more rapidly degraded than softwoods in alkaline delignification processes.⁴⁰ In this work, evidence of successful oxidation of both small dimers and the heptamer (G-polymer). This could be considered as the most restricted scenario. Dimeric model compounds and polymers with only one kind of inter-unit linkage have limitations as model compounds. The main goal of this section is to advance for a more complex highly functionalised model compounds, which contains different inter-unit linkages. This would allow extrapolating the results to real lignin better.

5.3.2 Oxidative cleavage of different inter-unit linkages in a hexamer model compound

A more complex lignin model compound, which is relatively closer to real lignin, was synthesised by our collaborator, Dr Gary N. Sheldrake and his research group from the School of Chemistry and Chemical Engineering at Queen's University in Belfast. The synthesis of the hexamer is described briefly in Chapter 2, Section 2.3.1. of this thesis.⁴¹ This model compound would represent better the chemically diverse structure of lignin, improving previous advance hexameric compounds.⁴² It consists mainly of three of the most common inter-unit linkages in lignin β -O-4', 5-5' and β -5', as shown in Figure 5-14. Here the stereochemistry of lignin substructures could influence on the lignin degradation.⁴⁰ For instance, the *erythro*/*threo* ratio of the side chain of β -O-4' could vary depending on the nature of the plant, being the *erythro* diastereoisomer form predominant on hardwood lignin.⁴³ Shimizu *et al.* also found that the delignification becomes easier when the content of syringyl S-units is higher than the G-units, and the *erythro* side chain is present in the structure. The *erythro*/*threo* ratio must be revealed in the model compounds to mimic the behaviour in lignin in a more efficient way. There are eight quiral centres in this hexameric model. Indeed, this model compound has about 64 stereoisomers, taking in consideration that the β -5' unit forms mainly *trans*-geometry, which are no independent.⁴¹ Sheldrake and co-workers established that this compound consists of a mixture of *erythro*/*threo* diastereoisomers, with an *erythro*/*threo* ratio of 5:1.

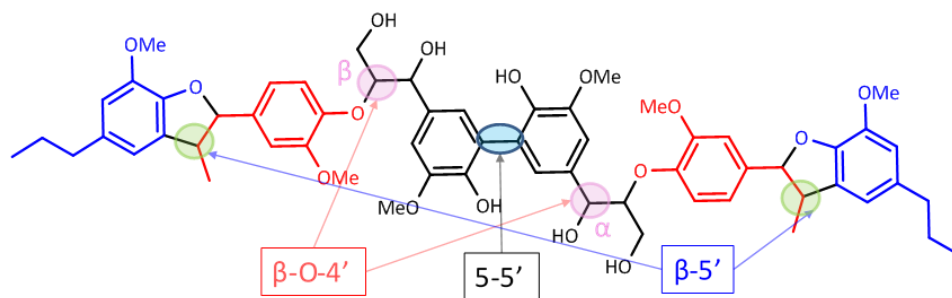


Figure 5-14 β -O-4', 5-5' and β -5' lignin linkages highlighted within the hexamer structure

The starting material was analysed to determine its actual molecular weight using a size exclusion technique, Advanced Polymer Chromatography (APC). Since it is a technique employed for polymers, the gel permeation chromatography of “small” molecules and oligomers results are given as molecular weight distribution. This distribution is defined by a series of average values such as the number average (M_n), weight average (M_w), Z average (M_z) molecular weights. The peak maxima give the molecular weight (M_p) of the polymer (See *Figure 5-15-B*). The polydispersity value would correspond to M_w/M_n .⁴⁴ After calibrating the instrument with Polystyrene standards as described in Chapter 2, *Section 2.2.3*, the starting material dissolved in THF showed the presence of two peaks (*Figure 5-15*). This double peak could be due to the separation of the stereoisomers. This idea could be related with two hypothesis: a) that the different three-dimensional arrangement of atoms within the hexamer for the different stereoisomers produces possible conformations that occupy different volumes and b) because one of them has a stronger interaction with the molecules of the eluent due to its greater dipole moment.⁴⁵ *Table 5-4* shows the average molecular weight values, M_p and polydispersity of the starting material.

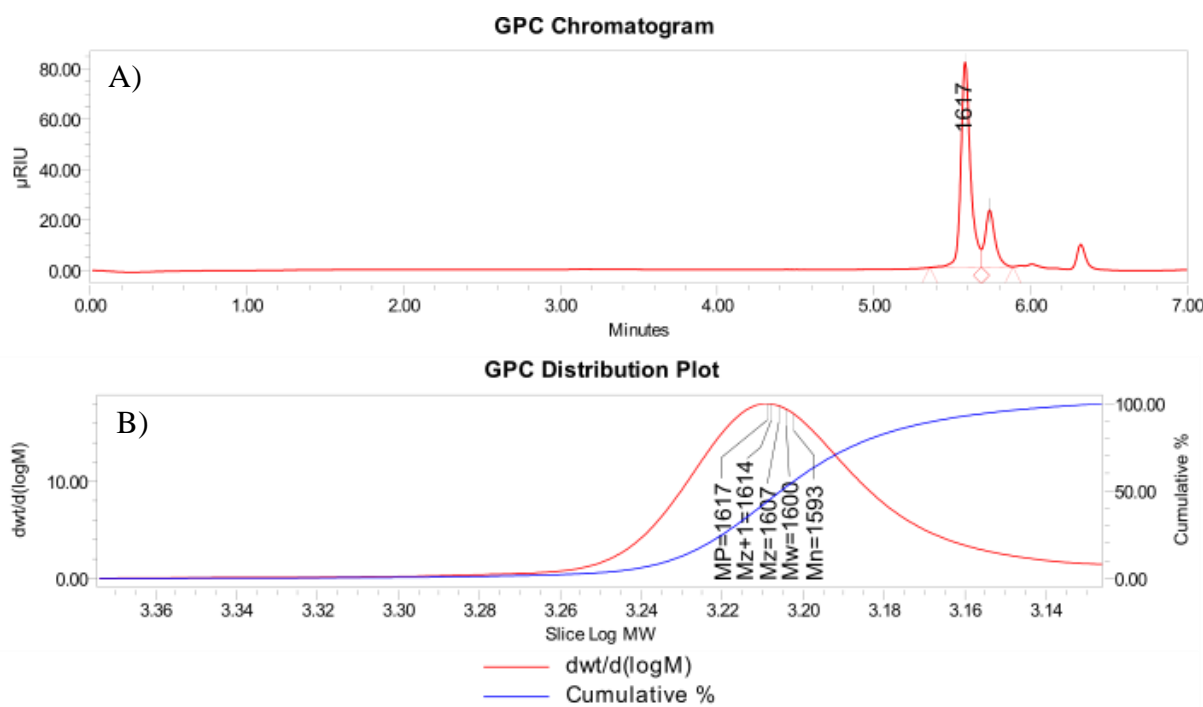


Figure 5-15 A) APC Chromatogram and B) Molecular weight distribution plot of the hexamer model compound obtained from APC analysis

Table 5-4 APC results obtained by dilution in THF

<i>Peak</i>	<i>Retention Time (min)</i>	<i>Mn</i>	<i>Mw</i>	<i>MP</i>	<i>Mz</i>	<i>Polydispersity</i>
<i>1</i>	5.581	1593	1600	1607	1607	1.004188
<i>2</i>	5.737	1288	1288		1289	1.000353

- ***Kinetic studies and potential inter-unit cleavage quantification***

The reaction was performed with the same molar equivalences of substrate, oxidant and metal [1:8:0.1] from 15 min up to 16 hours. After the reaction, the organic phase obtained from the extractions with ethyl acetate was dried in the vacuum. The dry solid products obtained were dissolved in THF (HPLC grade) to calculate the molecular weight. The calibration curve had a range of molecular weight between 66000 and 1250 Da, as explained in the experimental Chapter 2, *Section 2.3.3*. Consequently, any molecule with lower molecular weight than 1250 Da, could not be integrated to estimate its molecular weight accurately, but still visible on the chromatogram. The molecular weight of the hexamer model compound is theoretically 1047.19 g mol⁻¹. It can be analysed qualitatively, the same with any oxidation products detected. The results in *Figure 5-16* shows that the model compound is entirely degraded after 2 h of reaction. After the first minutes of reaction, there are still have some amount of hexamer remaining (same molecular weight as the starting material was found but less peak intensity). Moreover, an increase in the intensity of lower molecular weight molecules at higher retention time can be detected. In *Figure 5-15-B* the blue line corresponds to the sample after 2 h of RICO reaction. It presents a new peak sitting in between the two-hexamer peaks, suggesting the formation of a product with a smaller molecular weight (retention time of approximately 5.69 minutes). Also, after 16 hours, the *Figure* shows again a new peak (retention time of around 5.65 minutes) can be observed with a strong intensity, and no distinct hexamer peaks are detected. Peaks after the retention time 5.85 minutes are potential impurities, oligomers, within the sample, with the presence of these peaks appearing in all the samples.

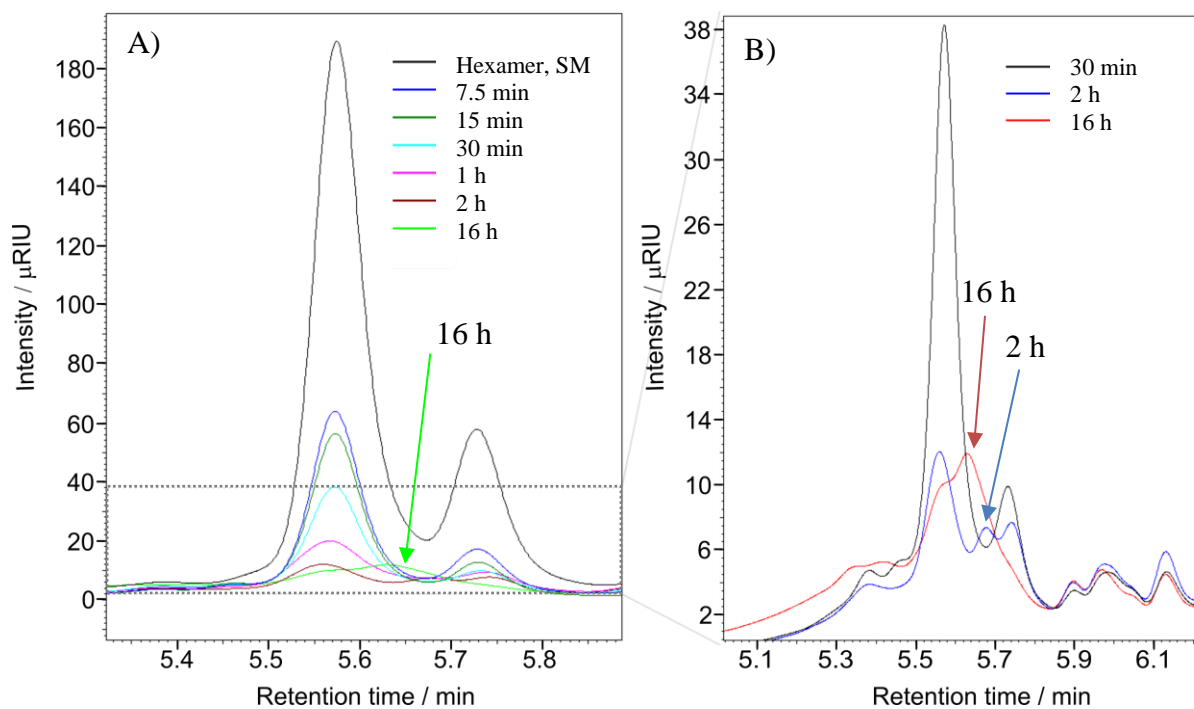


Figure 5-16 Overlap APC chromatogram of the reaction products of Hexamer in THF at different reaction times after RICO reaction. A) Reaction from 7.5 min to 16 hours of reaction, including the starting material (Black line) B) Zoom of the chromatogram for reaction products obtained after 30 min, 2 h and 16 hours. 171.7 mg, 0.196 mmol of Hexamer, 280 mg NaIO_4 and 0.23 mL of $\text{RuCl}_3 \cdot x\text{H}_2\text{O}$ stock solution. 30 mL of reaction solvent mixture of 2:1 Acetonitrile-deionise water, at 22 °C, 1 atm.

Thus, the GPC results show an evident degradation of the hexamer. Before any quantitative measurement, it is necessary to confirm that during the post-reaction protocol, the products are entirely recovered within the organic phase. Thus, the solid obtained during RICO reaction, separated before the extractions with ethyl acetate (see post-reaction protocol in Chapter 2, section 2.3.2.) and was analysed by FT-IR. This solid appears to precipitate at longer reaction times (> 2 h). The characteristic IR absorption frequencies of lignin materials and model compounds are reported in the literature.^{46–49} Between 3400–3500 cm^{-1} shows the band corresponding to the hydroxyl group (OH) in phenolic and aliphatic structures.⁴⁶ The following absorption band is the characteristic band at 2930 cm^{-1} for the elongation of the link carbon-hydrogen for methyl and methylene groups. Therefore it is assigned to the stretching vibration of C–H of CH_3 and CH_2 .⁴⁷ The absorption band at 2845 cm^{-1} is assigned to the stretching vibration of C–H of OCH_3 .⁴⁸ Moreover, two bands at 1509 and 1602 cm^{-1} are characteristic peaks of benzene rings due to the vibrations of C–C of aromatic skeleton.⁴⁹ Figure 5-17 shows how the filtrated contains a broad peak around 3400 cm^{-1} for hydroxyl groups in phenolic and

aliphatic structures. However, there is no peak around 2930 cm^{-1} indicating the absence of C-H of methoxy groups. The prominent peaks at 1602 and 1509 cm^{-1} representing the C-C of aromatic in the hexamer are also inexistent in the filtrated sample. In addition, a new peak at 1630 cm^{-1} is found, which is assigned in the literature to the δOH (water).⁵⁰ Therefore it is safe to assume that there are no remaining organic products left in the filtrate obtained during the work-up. This is because no peaks resembled of any organic bond present in the other two samples and, in particular, nothing in the C-C aromatic region ($1400\text{-}1610\text{ cm}^{-1}$).⁵¹

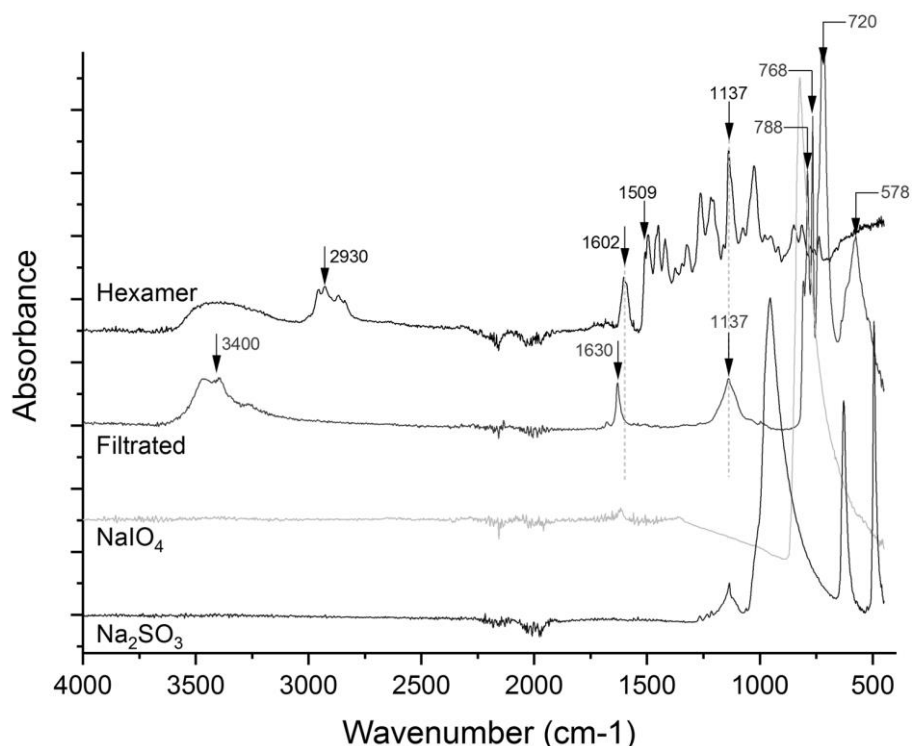
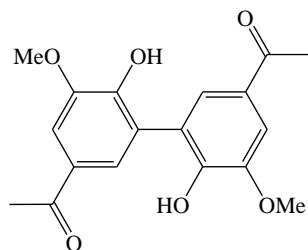


Figure 5-17 FT-IR spectrum of the hexamer, filtrated obtained after RICO reaction, oxidant (NaIO_4) and reductant (Na_2SO_3).

After confirming this, the products obtained after different reaction times were analysed by FT-IR. In general, Figure 5-18-A shows a decrease in intensity with longer reaction times, see the peak at 2930 cm^{-1} and in the C-C aromatic region ($1400\text{-}1610\text{ cm}^{-1}$). Also, a peak is found to be increasing at 3740 cm^{-1} together with a shift of the broad OH peak. The broad plateau peak has a smooth shoulder approximately 3200 cm^{-1} . To identify this features, a biphenyl intermediate (dimer) used in the synthesis of the hexamer (Scheme 5-6), was analysed by FT-IR.⁴¹ Figure 5-18-B shows the comparison of the FT-IR for this dimer against the hexamer and dry products after 2 h of RICO reaction for the hexamer. We can see the same peak at *ca.* 3700 cm^{-1} is present in both the dimer and the products.



Scheme 5-6 Intermediate biphenyl compound 1,1'-(6,6'-dihydroxy-5,5'-dimethoxy-[1,1'-biphenyl]-3,3'-diyl)bis(ethan-1-one), dimerised from acetovanillone.⁴¹

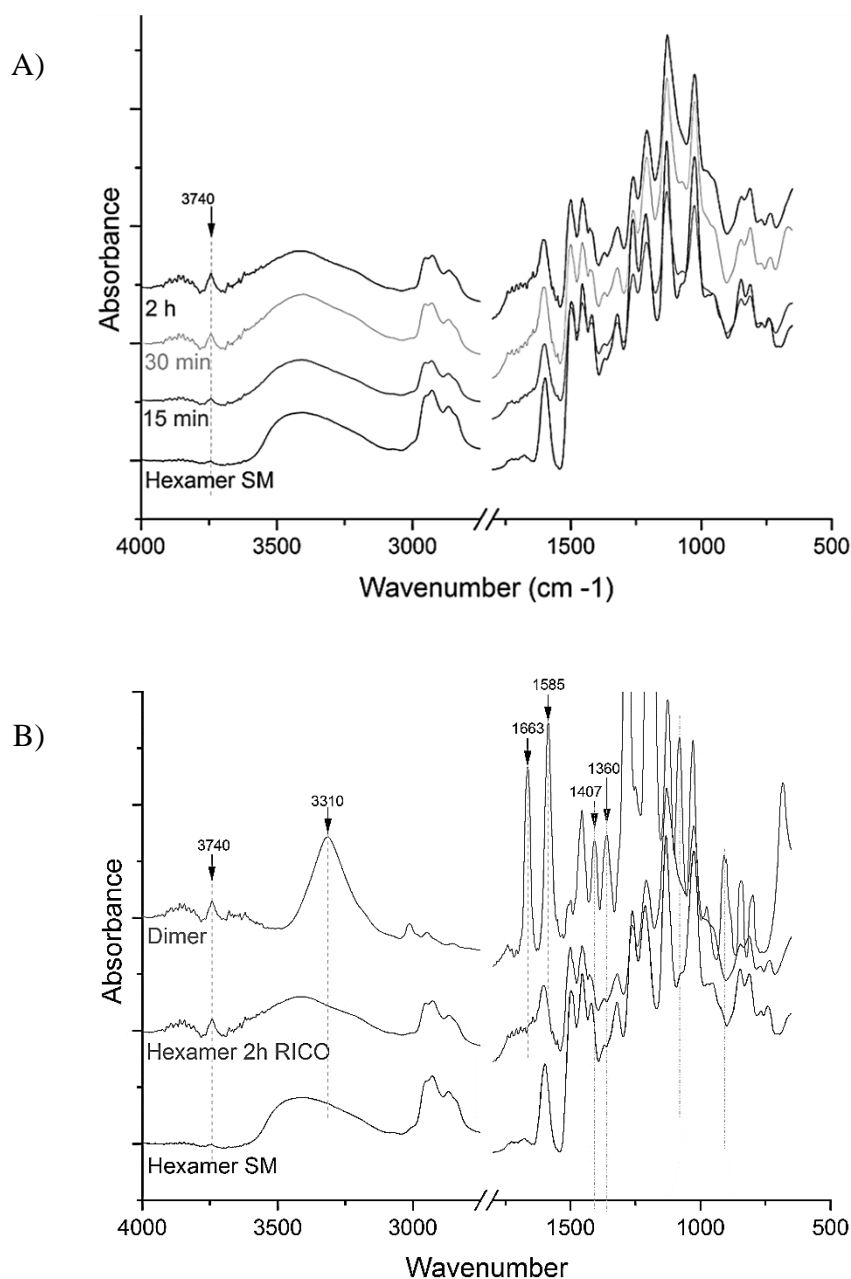


Figure 5-18 A) FT-IR for the time online dry sample after different times of RICO reaction vs starting material of hexamer. B) FT-IR comparison of the Dimer, the dry products after 2h of RICO reaction and the starting material of hexamer.

The quantitative ^1H NMR analysis of the products from the oxidation of hexamer confirms that the polymer is well degraded after 1 hour of RICO reaction. At this stage, it is not possible to make a conclusive comment about the changes in the functionalities from the NMR spectra. However, it is clearly shown that the peaks at δ 4.2 ppm and δ 4.9 ppm corresponding to α and β of the β -O-4' linkage have completely disappeared (*Figure 5-19*). After this, the potential percentage cleavage of the β -O-4', as well as the β -5' inter-unit linkages (δ 5.1 ppm), were quantified by integrating the peaks that correspond to their proton environments in the ^1H NMR. A sealed insert containing external standard with a known constant concentration of tetramethylsilane (TMS) in CDCl_3 was employed to calibrate the NMR spectra (see Chapter 2, *section 2.3.3*). The response factor for each environment was employed to get a time-online plot indicating the kinetics of this bond cleavage. We can see that the potential percentage cleavage the β -O-4' linkage is above 95 % for both α and the β carbons in just 2 hours of reaction. In addition, for the β -5' linkage, the potential percentage cleavage shows around 80 % of conversion after 2 hours (*Figure 5-20*).

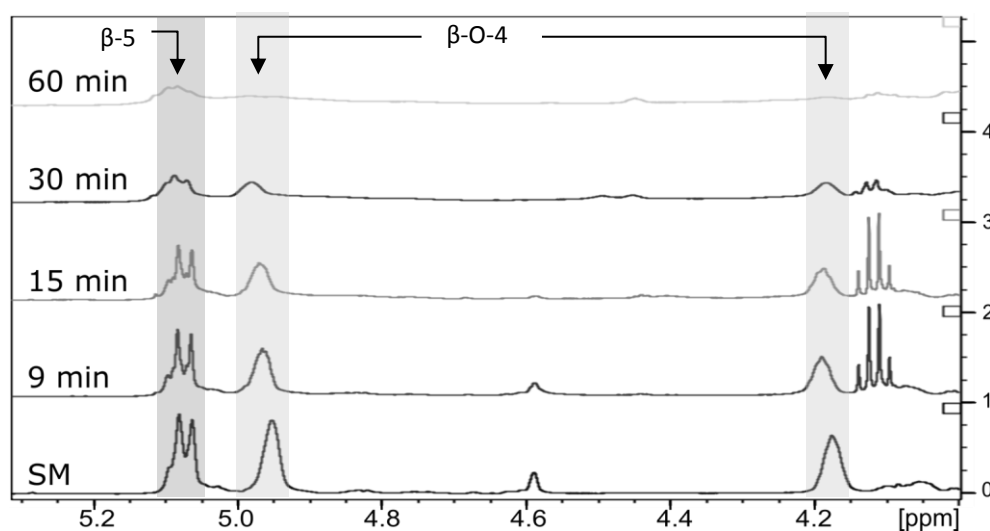


Figure 5-19. ^1H NMR comparison from bottom to top: Starting Material (SM), products obtained after 9 min, 15 min, 30 min and 1 h of RICO reaction.

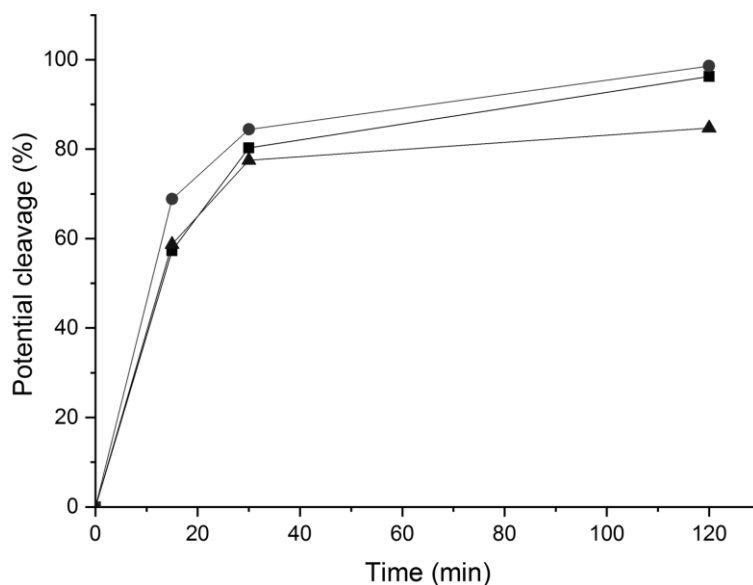


Figure 5-20. Potential percentage of inter-unit bond cleavage corresponding to the bonds β -O-4'(β) (-■-), β -O-4'(α)(-●-) and β -5'(-▲-), obtained by $^1\text{H-NMR}$ with the integration of the areas at δH of 4.19 ppm, 4.98 ppm and 5.08 ppm, respectively.

Figure 5-21 shows the ^{13}C NMR spectra of the products obtained at different reaction times. The environment associated with the 5-5' inter-unit linkage, in the middle of the hexamer structure, appears at δ 124 ppm. The results show how this area decreases as the reaction occurs. Indeed, it was not detected at all after 1 hour of RICO reaction, suggesting complete cleavage of the 5-5' bond. In order to quantify this bond cleavage, a calibration for each environment was done with the 2-D NMR, $^1\text{H-}^{13}\text{C}$ Heteronuclear Multiple Bond Correlation (HMBC) experiments.⁵² The potential bond cleavage of the targeted linkages was estimated from this analysis is shown in Figure 5-22. The results for the percentage cleavage suggest that the 5-5' linkage disappears after 30 min of the reaction, while there are still a 10 % remaining of the β -5' linkage. Nevertheless, the fact that the 5-5' degrade in a higher percentage than the β -5' linkage could be due to an overestimation of the measurement carried out using the ^{13}C . As mentioned in Chapter 2 (section 2.3.3.), ^{13}C has a lower sensitivity than the ^1H isotope. Hence, the difference obtained for the same bonds using ^1H or HSQC vs HMBC is due to the significant experimental error of the HMBC experiment (Figure 5-22).

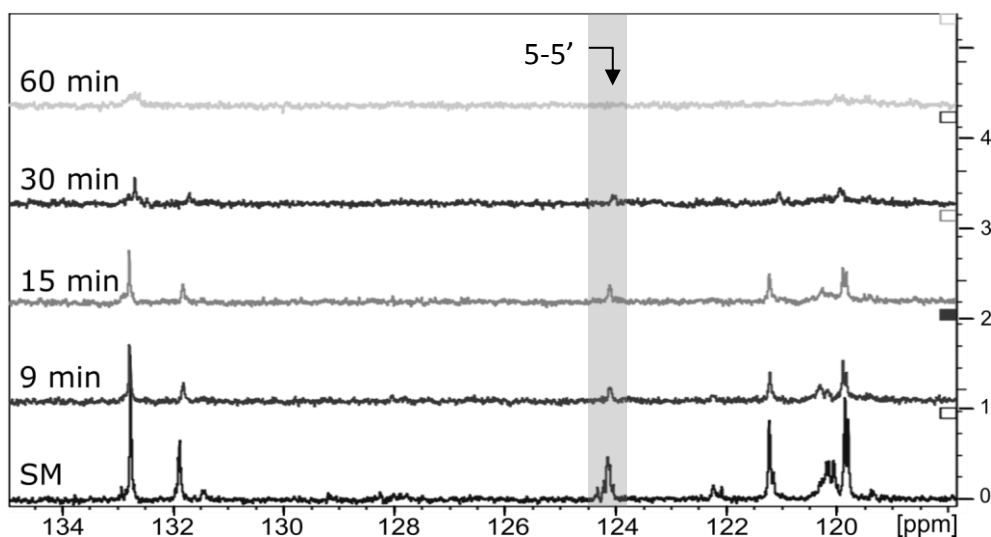


Figure 5-21. ^{13}C NMR comparison from the bottom to the top: Starting Material (SM), products obtained after 9 min, 15 min, 30 min and 1 h of RICO reaction.

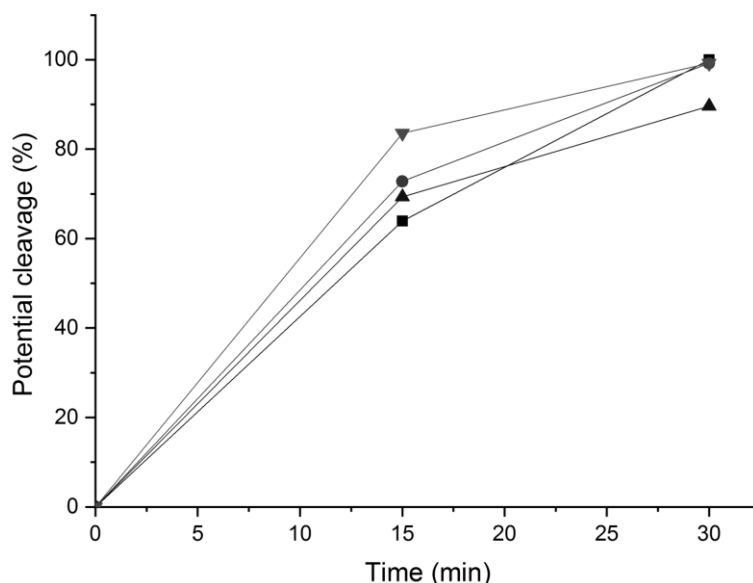


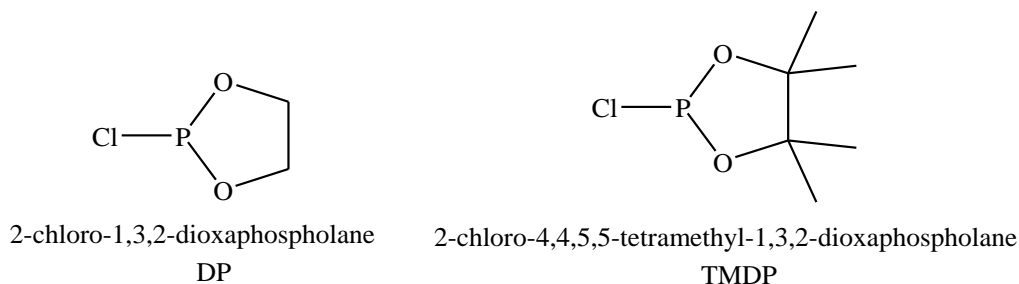
Figure 5-22. Potential percentage cleavages of the $\beta\text{-O-4' } (\beta)$ (-■-), $\beta\text{-O-4' } (\alpha)$ (-●-) and $\beta\text{-5' } (-\blacktriangle)$ and $5\text{-5' } (-\blacktriangledown)$ environments according to the HMBC.

Phosphitylation of the free hydroxyl groups using chlorophosphite reagents is commonly used for the characterisation of lignin materials and biofuels precursors.⁵³ It is also found as a useful quantification tool of functional groups such as carboxylic acids, phenols and aliphatic hydroxyl groups. Therefore ^{31}P -NMR could be an excellent alternative to quantify the 5-5' bond cleavage than the HMBC.

The ideal solvent mixture for ^{31}P NMR methodology is pyridine and CDCl_3 (1.6:1, v/v). Pyridine is the base to capture the hydrogen chloride liberated during the phosphorylation

reaction, therefore it needs to be in excess. The CDCl_3 dissolves the derivatised lignin and prevents the precipitation of pyridine-HCl salt. In all cases, a relaxation reagent as chromium (III) acetylacetonate ($\text{Cr}(\text{acac})_3$) is needed. The presence of the paramagnetic metal centre of $\text{Cr}(\text{acac})_3$, lowers the spin-lattice relaxation time of phosphorus nuclei, shortening the duration of the measurements significantly.⁵³

The phosphite reagent employed (*Scheme 5-7*) depends on the type of hydroxyl group to identify and quantify. For instance, 2-chloro-1,3,2-dioxaphospholane (DP) can distinguish better between the primary (γ -OH) and secondary (α -OH) alcohols of the propyl chains phenols and within the α -OH groups between *erythro*- and *threo*-conformations of β -O-4' structures. On the other hand, 2-chloro-4,4,5,5-tetramethyl-1,3,2-dioxaphospholane (TMDP) is better for quantifying the guaiacyl (G-units) and syringyl (S-units) phenols. The ^{31}P shifts of several lignin model and materials have been reported using both reagents DP⁵⁴ and TMDP.⁵⁴⁻⁵⁷ The different ^{31}P chemical shift typical in lignin using TMDP and DP can be found in *Table 5-5*.



Scheme 5-7 Phosphite reagents structure of the compounds employed in the phosphitylation reaction of hexamer for ^{31}P -NMR.

Table 5-5 ^{31}P -NMR chemical shifts of typical hydroxyl groups within Kraft lignin

Reactive groups	DP^a	TMDP^b
Carboxyl OH	126-127.8	133-137
<i>p</i> -Hydroxy-phenolic OH	127.8-129	137-138.6
Guaiacyl OH	129-130.5	138.-140.2
5-substituted OH	130.5-132	140-144.5
Total condensed phenolic OH	-*	140.2-145.2
5-5' condensed OH	-*	140.2-141.4
Primary Aliphatic OH	132-133.5	145.2-151.4 [#]
Secondary Aliphatic OH	133.5-136.5	

a,⁵⁴, *b*,^{57,56} * 5-substituted phenolic OH (*S*-units and 5-condensed *G*-units) overlap to the aliphatic primary OH. # Aliphatic OH groups cannot distinguish well using TMDP in most of the lignin.

For quantitative analysis, an internal standard (IS) is needed. N-hydroxy compound (N-hydroxynaphthalimide (δ 150.7 ppm))⁵⁸ was selected as IS for this experiments. Other IS alternatives such as cyclohexanol (δ 145.1 ppm)^{53,58-60} or cholesterol (δ 144.9 ppm)⁶¹ were widely used in the literature. Nevertheless, they are not baseline resolved from lignin derivate resonances, resulting in underestimated values for OH groups.⁵⁴

Table 5-6 ³¹P-NMR shifts for TMDP and DP treated internal standards

<i>Entry</i>	<i>Internal Standard</i>	<i>TMDP</i> δ ³¹ P (ppm)	<i>DP</i> δ ³¹ P (ppm)
1	cyclohexanol	145.1 ^a	
2	cholesterol	144.9 ^b	
3	N-hydroxyphthalimide	150.7 ^c -149.9 [*]	135.5 [*]
4	1-hydroxy-7-azabenzotriazole	150.6 ^c	
5	N-hydroxy-5-norborene-2,3-dicarboximide	151.9 ^c	
6	N-hydroxy-1,8-naphthalimide	153.6 ^c	
7	tris(2,4-di-tert-butylphenyl)phosphite	130.7 ^c	
8	Piperidine	138.7 ^c	

Ref.: a ^{62,56}, b⁶³, c⁵⁸ and *Experimental values

The hexamer derivatisation reaction was performed using both phosphite reagents DP and TMDP, and the selected IS. Figure 5-23 shows the ³¹P NMR spectra for the phosphatised products of the hexamer. The peak to integrate for the Aromatic-OH (Ar-OH) quantification has better resolution for when using the DP reagent (Figure 5-23-A). Nevertheless, it is essential to clarify that DP can be used as phosphorylation reagent in this case since this model compound does not contain S-units.⁵⁷

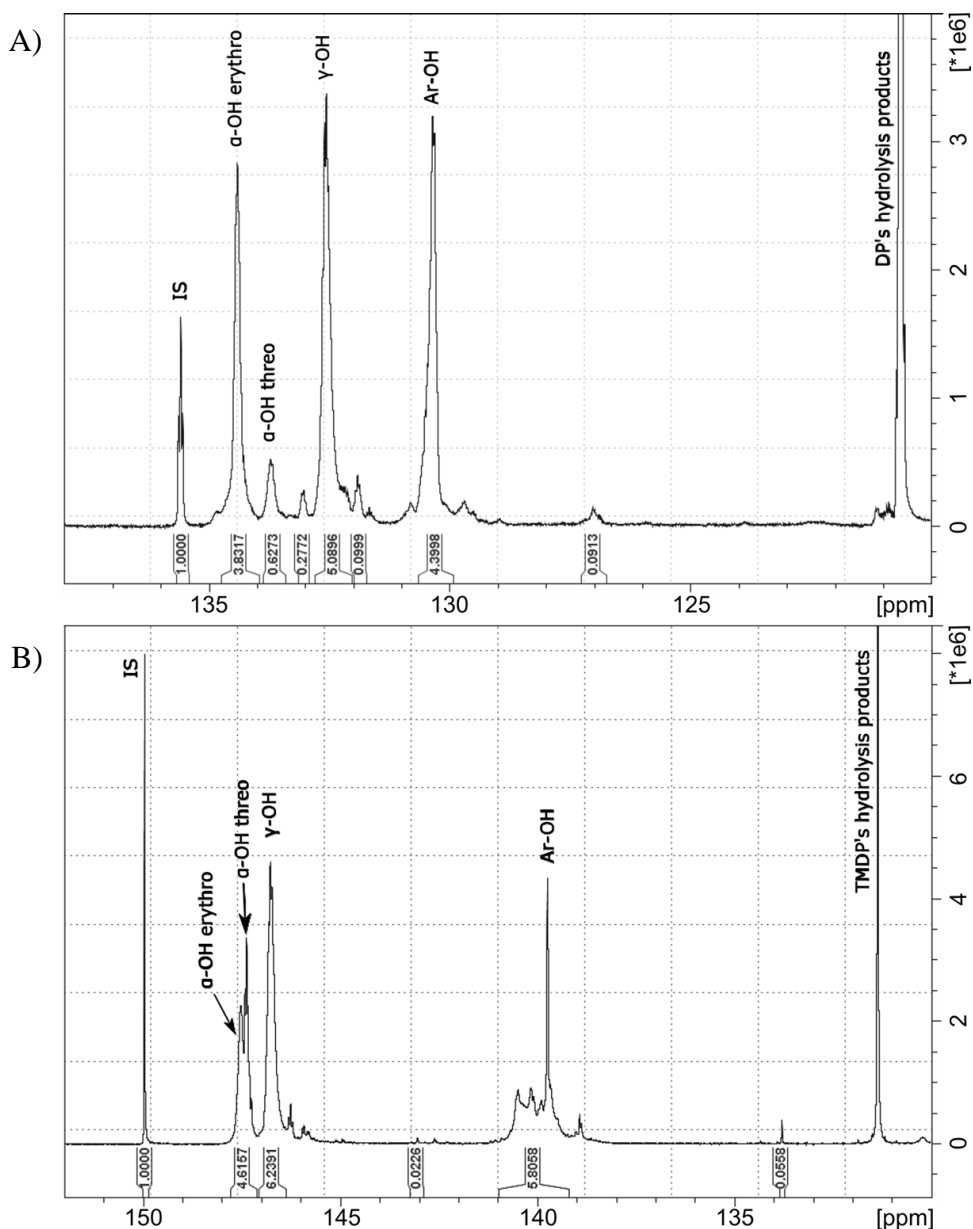


Figure 5-23 ^{31}P NMR of the Hexamer phosphatized with A) DP and B) TMDP

As previously mentioned, this polymer shows a diastereomeric isomer of β -O-4' structures possessing C_α hydroxyl groups in the molecule. ^{31}P NMR spectroscopy also allows quantification of the ratio of diastereomeric isomers present in a sample. These results confirm that the starting material has a high percentage of *erythro* and a small percentage of *threo* diastereoisomer. It has been proved that both diastereomeric forms decrease in parallel to the molecular weight. The degradation of *erythro* structures is more significant than that of the *threo* counterparts. Lower molecular weight seems to have significantly enriched in β -O-4' structures composed almost entirely of the stable *threo* diastereomer.⁶⁴

Derivatisation reaction would substitute the free OH of the molecules by the phosphite reagent employed (Figure 5-24). Using this technique, the main goal is to quantify the 5-5' inter-unit linkage percentage cleavage of the hexamer model compound associate to the Ar-OH (colour green).

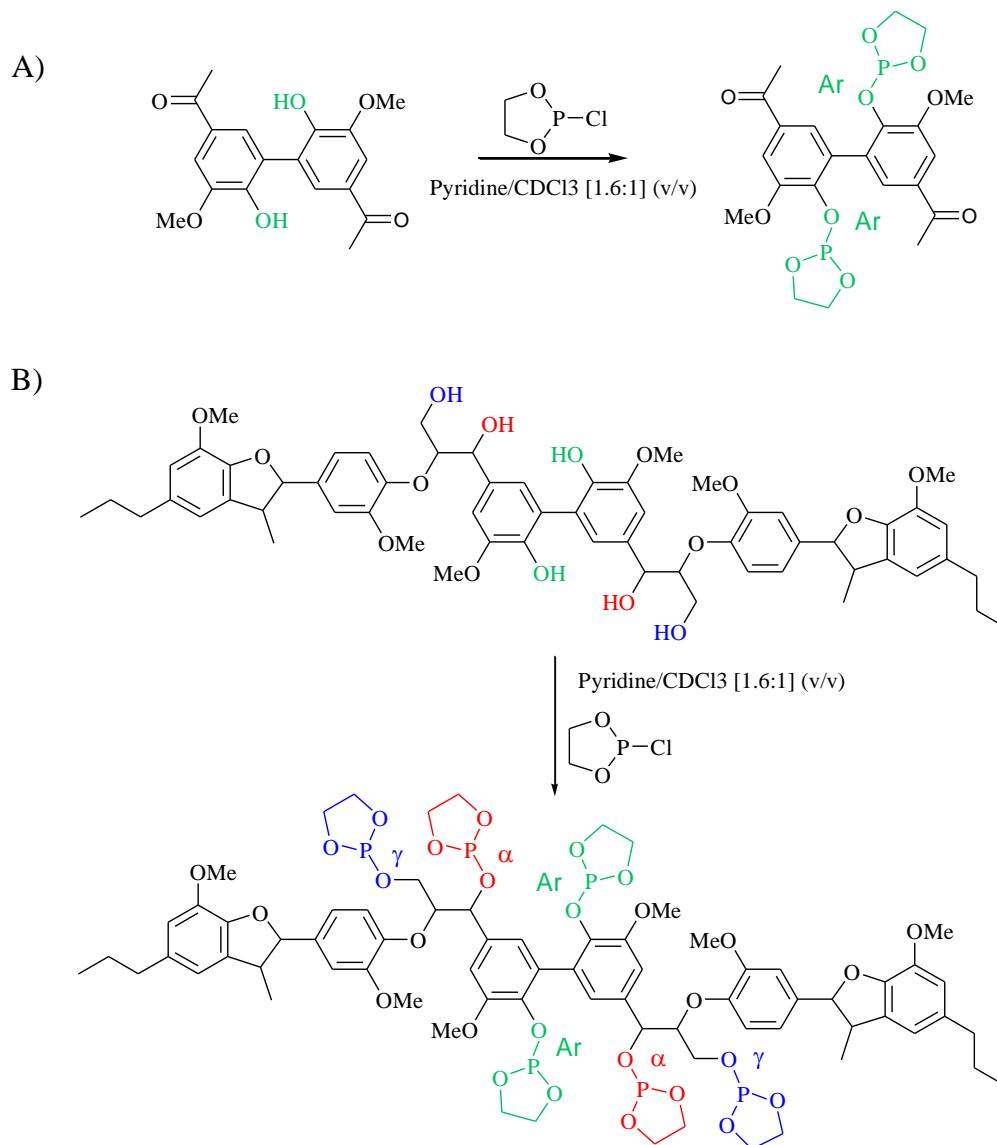


Figure 5-24 Phosphitylation of the dimer (A) and hexamer (B) after DP derivatization.

Firstly, qualitative analysis of the phosphatised internal standard selected (N-hydroxyphthalimide) and the dimer containing the 5-5' linkage was carried out to identify the Aromatic-OH chemical shifts present in the hexamer correctly. The ^{31}P shift of this internal standard in this case corresponds to 135.5 ppm. The Ar-OH is found in the range 130-130.7 ppm, as shown in Figure 5-25. These results are in agreement with the literature values for kraft lignin for the 5-substituted OH (Table 5-5)⁵⁴. Derivatisation of a) dimer, b) starting material of

hexamer and c) oxidations products after RICO reaction, were phosphorylated with DP as a reagent.

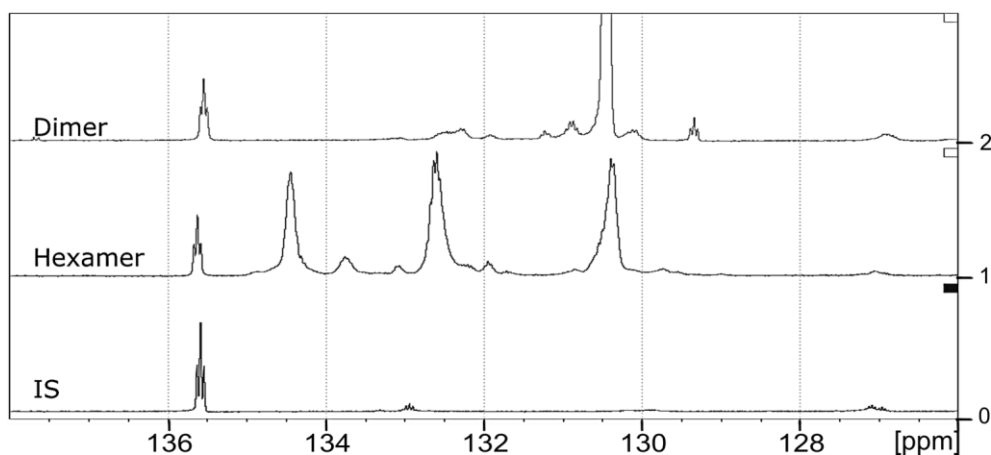


Figure 5-25 ^{31}P NMR spectrum from top to bottom of the Dimer, Hexamer and *N*-hydroxyphthalimide (IS) phosphatised with DP.

After the phosphorylation reaction of the dry reaction products obtained via RICO (Figure 5-26) we can see how the peak of the Ar-OH disappears in only 30 min of reaction. The α -erythro aliphatic-OH remains still visible in a small peak, confusing with the noisy baseline. Also, after 15 min the spectra show a new peak in the primary aliphatic region (γ -OH at 132 ppm).

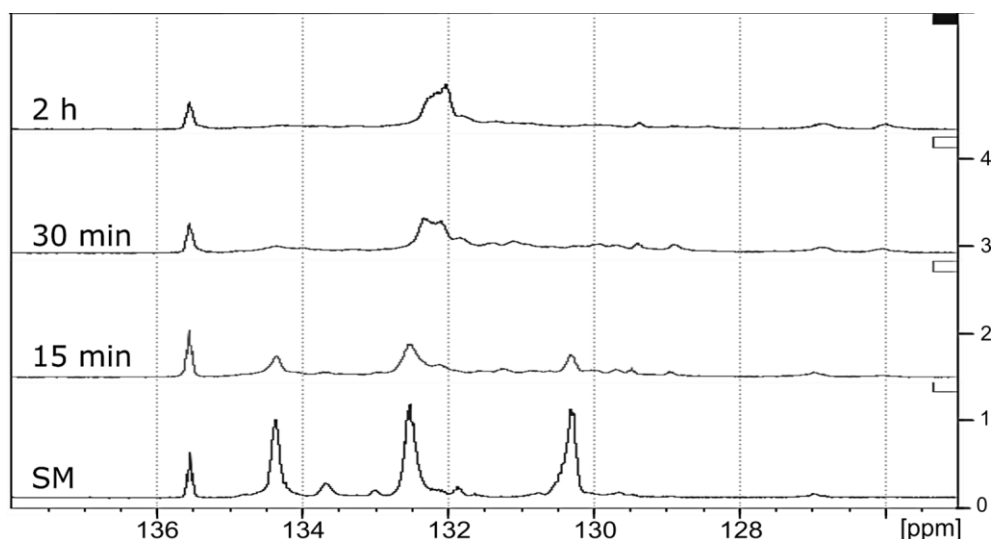


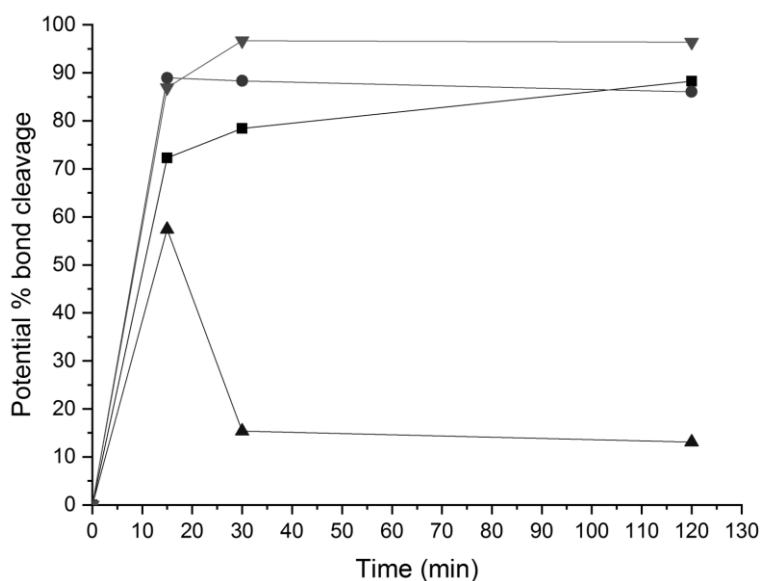
Figure 5-26 ^{31}P NMR spectra from the bottom to the top of the starting material of the hexamer (SM) followed by the dry oxidation products after 15 min, 30 min and 2 h of RICO reaction.

The potential percentage of cleavage has been quantitatively estimated by the integration of different regions.⁵² The calibration was performed using a TMS internal standard (IS) as

reference equal to 1 (as described in Chapter 2, *section 2.3.3*). The results show the same grade of degradation for the 5-5' linkage as for the α -OH *threo* achieving around 88 % of cleavage after 15 minutes of RICO reaction (*Table 5-7*). Time online study prove the formation of primary OHs, as a percentage of cleavage is descending. Interestingly, ^{31}P -NMR gives a very similar trend to the previous HMBC quantification for both β -O-4 (α) and 5-5', suggesting that the 5-5' inter-unit linkage is cleaved at a higher rate (*Figure 5-27*). On the other hand, a decrease in the potential cleavage percentage indicates the formation of the OH group. This is the case of the γ -OH corresponding to the formation of primary aliphatic OH in the oxidation product obtained (^{31}P -NMR at 132 ppm).

Table 5-7 Estimation of potential % cleavage by ^{31}P -NMR of the oxidation products after 15 min of RICO reaction of hexamer

Functional OH group	Object	Integration range [ppm]	$\nu(\text{F1})$ [ppm]	SM Integral [rel]	Integral [rel]	Potential % cleavage
Ar-OH	Integral 5	131-129.9	130.5	5.6439	0.7393	87
γ-OH	Integral 4	132.85-132	132.4	5.9552	2.5371	57
α-OH <i>threo</i>	Integral 3	133.9-133.4	133.7	0.7127	0.0789	89
α-OH <i>erythro</i>	Integral 2	135-133.9	134.5	4.4476	1.2345	72
IS	Integral 1	135.7-135.45	135.6	1	1	-



*Figure 5-27 Time online studies of the potential percentage cleavage of the α -OH erythron (-■-), α -OH *threo* (-●-), γ -OH (-▲-) and the Ar-OH (-▼-) obtained by ^{31}P -NMR.*

- ***Oxidation products identification.***

The reaction mixtures after RICO reactions of the hexamer were analysed. The time online study shows changes in concentration of a new environment found at 9.88 ppm in the ^1H NMR (Figure 5-28). It appears to be increasing in the similar rate that this linkage is cleavage possibly corresponding to an aldehyde. However, no more information could be conclusive from the reaction mixture.

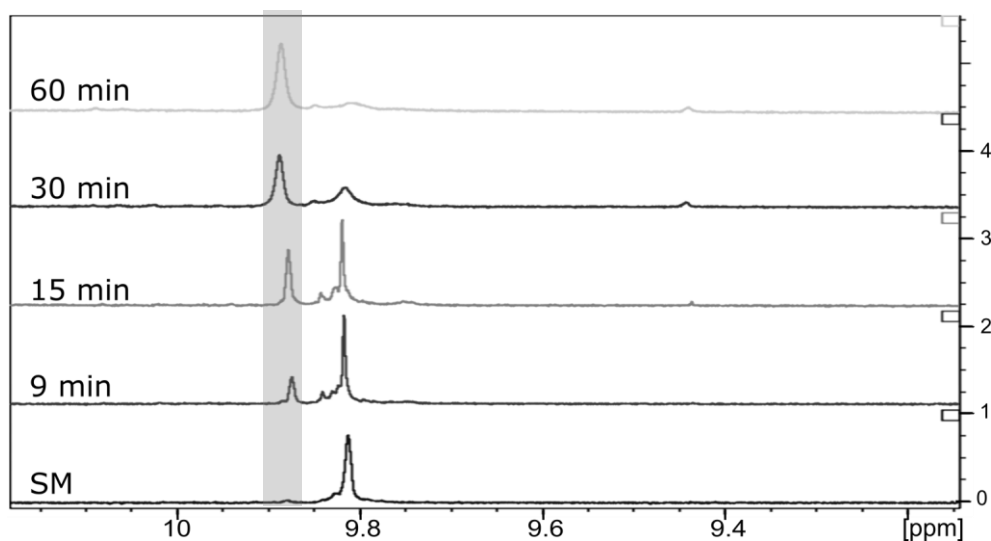
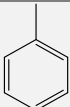
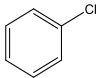
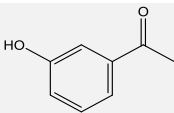
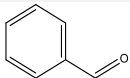
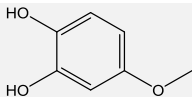
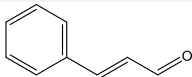
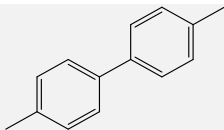
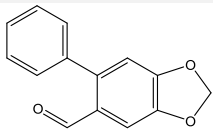
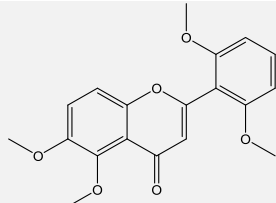
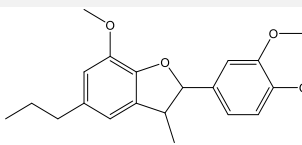


Figure 5-28. ^1H NMR comparison bottom to top: Starting Material, 7.5 min, 15 min, 30 min, 1 h of RICO reaction. 2D-HSQC NMR

Column chromatography was carried out to separate the products obtained after the RICO reaction of the hexamer model compound. The different fractions were dried in vacuum and re-dissolved in ethyl acetate for GC-MS analysis. Table 5-8 present all the compounds found in GC-MS from the separate fractions obtained.

Table 5-8 Possible oxidation products of hexamer found in the different fractions by GC-MS

Compound Number	Fraction	RT (min)	Compound	Formula	Structure
18	All	3.79	Toluene	C ₇ H ₈	
19	F1, F2	6.5	Chlorobenzene	C ₆ H ₅ Cl	
20	F3, F4	9.7	Ethanone,1-(3-hydroxyphenyl)	C ₈ H ₈ O ₂	
21	F1, F2	11.05	Benzaldehyde	C ₇ H ₆ O	
22	F2, F3, F4	12.18	4-Methoxybenzene-1,2-diol	C ₇ H ₈ O ₃	
23	F1	17.95	Cinnamaldehyde	C ₉ H ₈ O	
24	F2	21.27	4,4'-Dimethylbiphenyl	C ₁₄ H ₁₄	
25	F2	22.25	2-phenyl-4,5-methylenedioxybenzaldehyde	C ₁₄ H ₁₀ O ₃	
26	F2	24.86	2-(2,6-dimethoxyphenyl)-5,6-dimethoxy-4H-chromen-4-one [Tricin]*	C ₁₉ H ₁₈ O ₆	
27	F1, F2, F3	34.93	2-methoxy-4-(7-methoxy-3-methyl-5-propyl-2,3-dihydrobenzofuran-2-yl)phenol	C ₂₀ H ₂₄ O ₄	

Then, the HSQC obtained from each of the fractions collected were contrasted to the GC-MS results previously presented. As mentioned in earlier, HSQC experiments are a useful tool used for lignin characterisation. Table 5-9 summarise the chemical shift for the different C-H bonds identified in the hexamer as starting material. The results from HSQC have been assigned according to the scheme showed in Figure 5-29.

Table 5-9 Chemical shift of the areas $\delta C/\delta H$ (ppm) for the inter-unit linkages present in the hexamer model compound

Linkage/unit	Chemical shift of the peak $\delta C/\delta H$ (ppm)
Methoxy groups	56/3.8
β -O-4' (A γ)	61/3.6
β -O-4' (A α)	73/4.98
β -O-4' (A β)	87/4.19
β -5'	94/5.08
5-5'	No detected
Guaiacyl (G2)	111/7.0
Guaiacyl (G6)	121/7.07

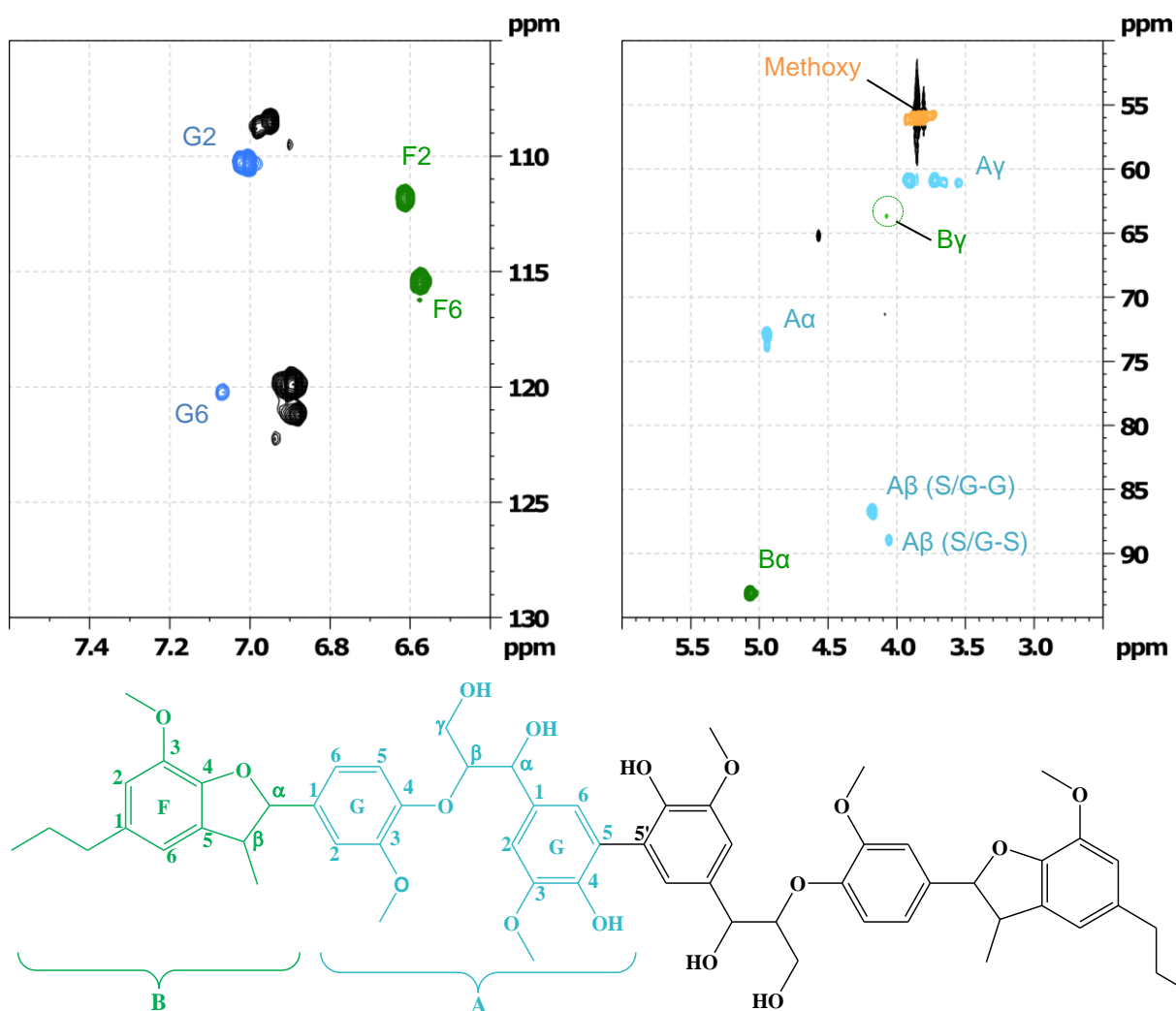


Figure 5-29 Partial HSQC spectrum of the starting material and its corresponding assignment corresponding to labelled on the hexamer structure

The HSQC of the first fraction collected shows not only that all the β -O-4' substructures (A) are not present in this sample, but that aldehydes have been formed (*Figure 5-30*). The β -5' inter-unit linkage in the phenylcoumaran substructure (B) is still present, and probably one of the G aromatic ring of the structure A. This bond is also challenging to cleave, for instance, Lange *et al.* reported that this inter-unit linkage was intact as benzofuran, after their oxidation reactions with [Co(salen)] catalysts.⁶⁵ The GC-MS of this specific fraction is also given an aldehyde as a main product, cinnamaldehyde (See *Appendix 7.5*). Therefore it could be the formation of the products 27 and 28 in the small percentage that the O-C β and the 5-5' bond were cleaved (*Scheme 5-8*). If we consider the option of benzaldehyde, it could form the products 29 and 30 in the case that both the C α -C β and the 5-5' bond were cleaved (*Scheme 5-9*).

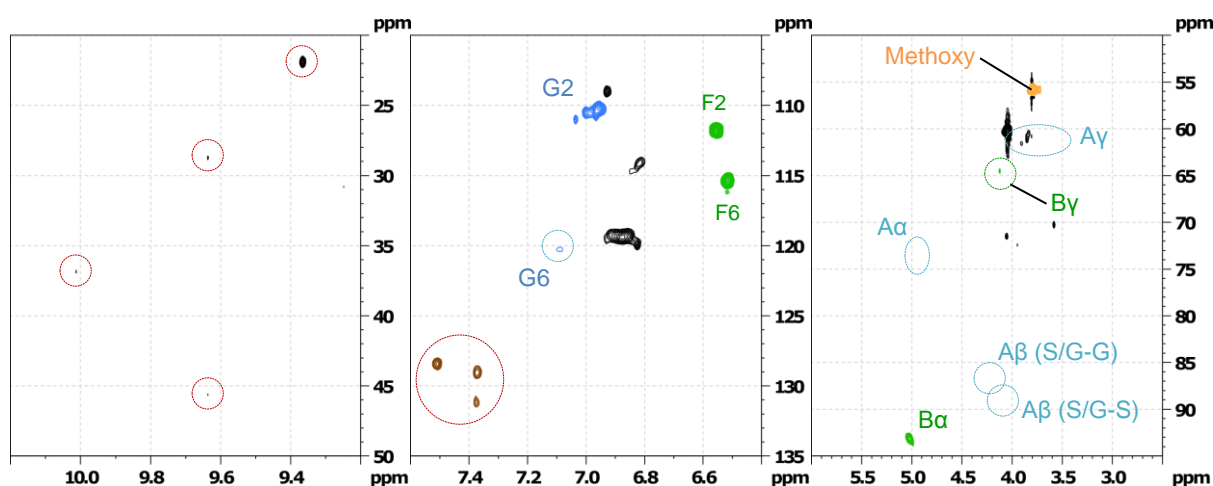
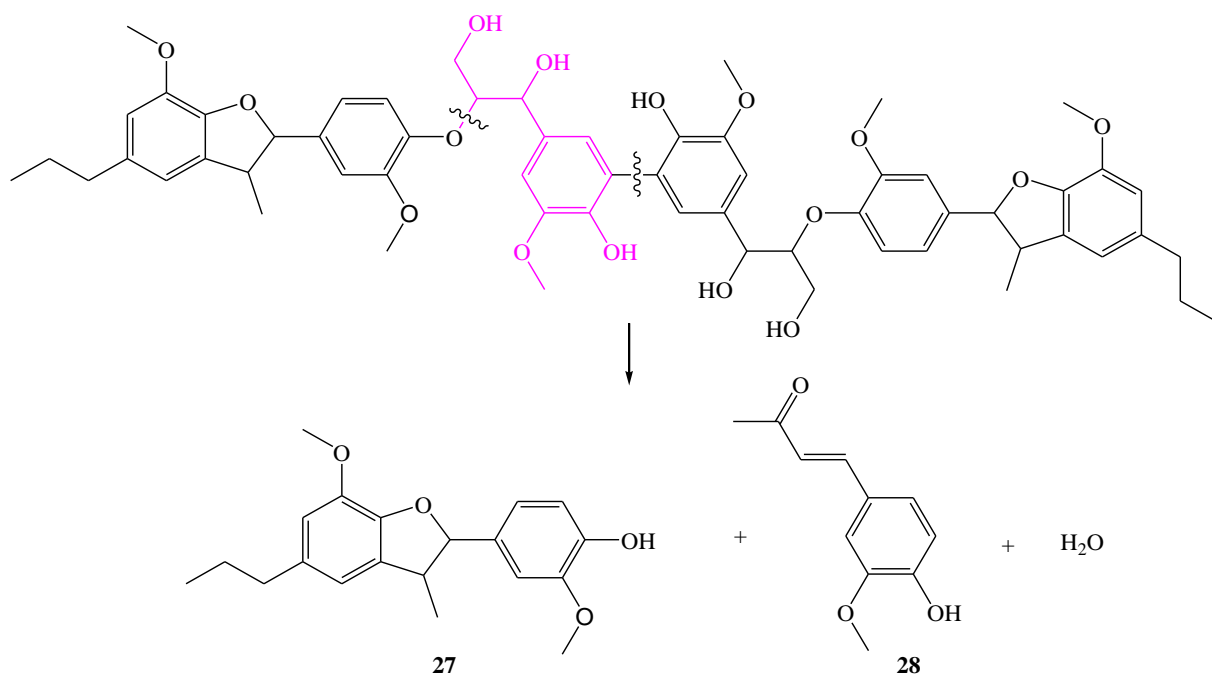
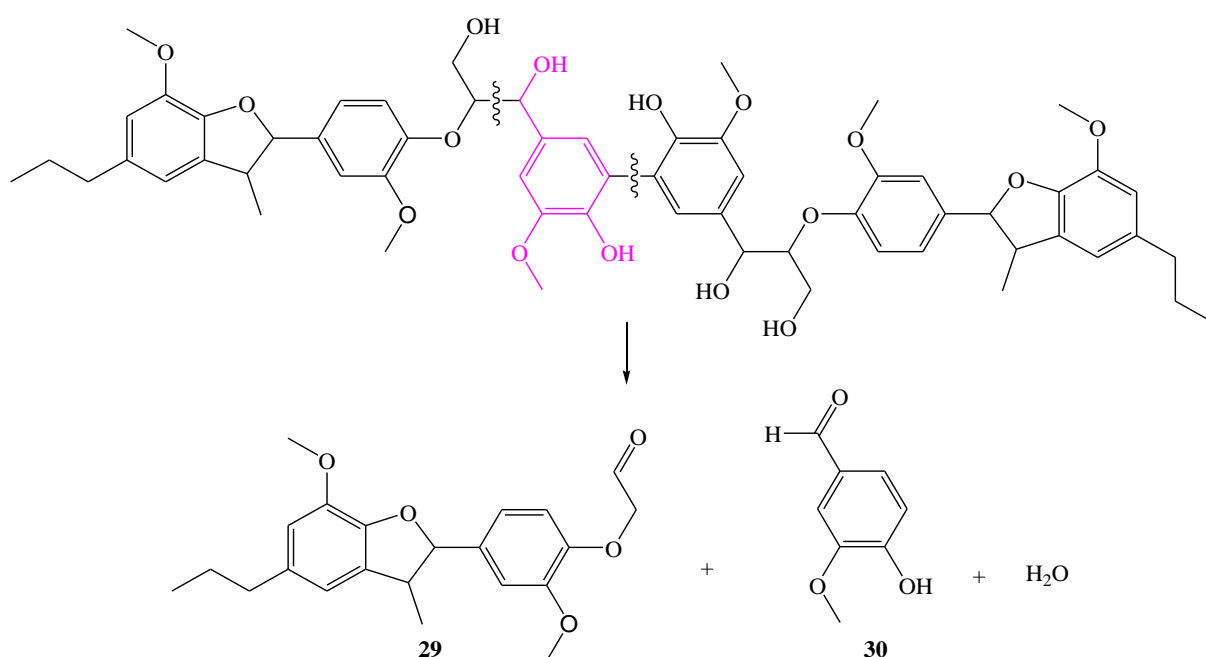


Figure 5-30 Partial HSQC spectrum of the fraction 1 separated by column chromatography of the oxidation of hexamer after 1h of RICO reaction.

The NMR of the second fraction collected separated by column chromatography shows still some β -O-4' linkage in this sample, but that also another possible aldehyde (see *Appendix*). The β -5' inter-unit linkage in the structure B is still present, and probably one of the G aromatic ring of the structure A. The GC-MS of this specific fraction is also given a hint of aldehyde (benzaldehyde). However, the NMR does not show the proton for the aldehydes around 9.6 - 9.4 ppm, even if there are new aromatic environments highlighted in brown on the spectrum. Moreover, it was found for the fraction (F2) in the GC-MS with the dimer of the biphenyl 5-5' but only for a concise time of reaction (15 min and 30 min). The other possible products contain the 5-5' linkage, compounds 24, 25, 26 in *Table 5-8*.



Scheme 5-8 Products: 27) 4-(7-methoxy-3-methyl-5-propyl-2,3-dihydrobenzofuran-2-yl)-2-methylphenol and 28) (E)-3-(4-hydroxy-3-methoxyphenyl)acrylaldehyde



Scheme 5-9 Products: 29) 2-(4-(7-methoxy-3-methyl-5-propyl-2,3-dihydrobenzofuran-2-yl)-2-methylphenoxy)acetaldehyde; and 30) 4-hydroxy-3-methoxybenzaldehyde

Among all the reaction products suggested by GC-MS (*Table 5-8*), the main reaction product identified by NMR was compound number **27**. Using HSQC experiments for that fractions (F1-F3), all the different environments for this molecule were assigned (see *Appendix*). It is actually

used as a starting material for the synthesis of the hexamer (See Chapter 2, *Scheme 2-4*, the compound dehydro-isoeugenol).⁴¹

5.4 Conclusions

RICO reaction is an effective catalytic system for the cleavage of inter-unit linkages present in lignin. In this work, the RICO monophasic solvent system enabled the conversion of model compounds with an insignificant formation of CO₂. For all the model compounds tested, the reaction led to the production of ketones and the opening of one of the aromatic rings to form aldehydes than can easily be oxidised to carboxylic acids. Formation of aldehydes during RICO reaction is also probable since alcohol formation is possible and the addition of quenching reagent, Na₂SO₃ may lead to further, mild oxidation of the alcohol to the aldehyde, as probed in previous studies.⁶⁶

In the case of biphenyl as a model compound for the 5-5' bond, one of the most difficult inter-unit linkages to cleave due to its high bond dissociation energy, it was observed that RICO reaction is able to open the ring to produce benzoic acid as the main product with a molar ratio of substrate:oxidant:metal of [1:2.67:0.1]. However, when the amount of oxidant NaIO₄ is increased (molar ratio [1:8:0.1]) an increase in the conversion from ca. 30 % to ca. 65 % was obtained, but also an essential decrease in the carbon mass balance, due to the production of new products, identified by GC-MS and TLC as cinnamaldehyde and some trans-cinnamic acid. Therefore, the ratio between the substrate, the oxidant and catalyst can effectively tune the selectivity.

In the oxidation of bibenzyl with a molar ratio of substrate:oxidant:metal [3:8:0.1], RuO₄ also attacks one of the aromatic rings producing hydrocinnamic acid. In the same way that the benzoic acid was formed from biphenyl. The production of a ketone such as 2-phenyl acetophenone, was also proved. This ketone could lead to the production of benzoic acid, also identified as a reaction product. Reaction starting with this ketone confirmed this pathway and produced some benzoic acid. On the contrary, for this substrate, no aldehyde was found as products.

The degradation of the hexamer model has been achieved *via* RICO reaction. By analysing the results obtained from APC, FT-IR and different NMR techniques it can clearly be established that the original structure of the hexamer has been degraded and broken into smaller components at short reaction times.

From the APC results, it can be proved that the starting substrates have been converted after 2 hours of RICO reaction. Furthermore, from the NMR analysis, it can be said that all the types of linkages present in the hexamer structure (β -O-4', β -5' and more importantly the 5-5') have been broken in good yields. ^1H NMR also shows the disappearance of chemical environments from the starting material and the appearance of a new chemical shift in the aldehyde region. This provides further evidence for the degradation of the hexamer and the formation of smaller products. Quantification using ^1H NMR was successfully carried out using a TMS sealed insert as an external standard. This allowed for the quantification of proton environments involved in the β -O-4' and β -5' inter-unit linkages. High percentage cleavages of these environments were obtained after a relatively short RICO reaction time of just two hours.

On the other hand, the ^1H NMR quantification technique was not applicable for the 5-5' linkage, since no proton is attached to the carbon environments involved in the linkage. Hence, quantification using HMBC 2D-NMR technique was tried parallel to the ^{31}P -NMR. It is necessary to have in consideration that this NMR technique is a lot less sensitive than that of the ^1H NMR. Therefore, the areas calculated have a far higher margin for error. Results obtained from both techniques were very similar, showing a faster cleavage for the 5-5' (*ca.* 85 %) in only 15 min of RICO reaction than for the C_α - C_β bond in the β -O-4' inter-unit linkage (*ac.* 60 %) followed by the β -5' as the harder to break. From these results what is particularly exciting is the 5-5' cleavage, proved by ^{31}P -NMR since the cleavage of this type of inter-unit linkage has yet to be reported with regards to complex lignin model compounds. To our knowledge, there is only one report of the cleavage of the 5-5' linkage in a simple phenolic lignin model compound, proved by the formation of methylguaiacol (7 %) and guaiacol (12 %).¹⁹

Moreover, the identification of one product after RICO reaction was established. This was identified using the GC-MS instrument and later confirmed and characterised through analysis of ^1H NMR, HSQC and HMBC. This product is thought to be a result of the breakage of the β -O-4' linkage and within the product structure the β -5' linkage remains intact. In addition, looking at the GC-MS results of products after a short RICO reaction time and lower molar ratio, a potential intermediate was identified. The product identified by the intermediate was biphenyl. This could potentially resemble the two central aromatic rings held together by the 5-5' inter-unit linkage.

5.5 References

1. Guadix-Montero, S.; Sankar, M., *Top. Catal.* **2018**, *61* (3–4), 183–198.
2. Wang, H.; Tucker, M.; Ji, Y., *J. Appl. Chem.* **2013**, *2013*, 1–9.
3. Ragauskas, A. J.; Beckham, G. T.; Biddy, M. J.; Chandra, R.; Chen, F.; Davis, M. F.; Davison, B. H.; Dixon, R. A.; Gilna, P.; Keller, M.; et al., *Science* **2014**, *344* (6185), 1246843.
4. Vishtal, A.; Kraslawski, A., *BioResources* **2011**, *6* (3), 3547–3568.
5. Parthasarathi, R.; Romero, R. A.; Redondo, A.; Gnanakaran, S., *J. Phys. Chem. Lett.* **2011**, *2* (20), 2660–2666.
6. Rinaldi, R.; Jastrzebski, R.; Clough, M. T.; Ralph, J.; Kennema, M.; Bruijninx, P. C. A.; Weckhuysen, B. M., *Angew. Chemie - Int. Ed.* **2016**, *55* (29), 8164–8215.
7. Patil, N. D. A Study of Lignin Depolymerization By Selective Cleavage of the C α -C β Linkages in Lignin Model Compounds Via Baeyer-Villiger Oxidation & an Investigation of the Channeling Reaction in Nitrogen-Doped Multiwalled Carbon Nanotubes (N-Mwcnts), University of Kentucky, 2014.
8. Umezawa, T.; Higuchi, T. A Novel C α -C β Cleavage of a β -O-4 Lignin Model Dimer with Rearrangement of the β -Aryl Group by Phanerochaete Chrysosporium. *Components* **1985**, *192* (1), 147–150.
9. Nowicka, E.; Sankar, M.; Jenkins, R. L.; Knight, D. W.; Willock, D. J.; Hutchings, G. J.; Francisco, M.; Taylor, S. H., *Chem. - A Eur. J.* **2015**, *21* (11), 4285–4293.
10. Zakzeski, J.; Bruijninx, P. C. a; Jongerius, A. L.; Weckhuysen, B. M., *Chem. Rev.* **2010**, *110* (6), 3552–3599.
11. Kaplan, D. L. *Biopolymers from Renewable Resources*; Springer Berlin Heidelberg: Berlin, Heidelberg, 1998.
12. Kameshwar, A. K. S.; Qin, W. *Production of Biofuels and Chemicals from Lignin*; Fang, Z., Smith, R. L., Eds.; Biofuels and Biorefineries; Springer Singapore: Singapore, 2016.
13. Bugg, T. D. H.; Ahmad, M.; Hardiman, E. M.; Rahmanpour, R., *Nat. Prod. Rep.* **2011**, *28* (12), 1883.
14. Pieper, D. H., *Appl. Microbiol. Biotechnol.* **2005**, *67* (2), 170–191.
15. Kärenlampi, Sirpa O. Hynninen, P. H., *Chemosphere* **1981**, *10* (4), 391–396.
16. Kamaya, Y.; Higuchi, T., *Wood Res.* **1984**, *70*, 25–28.
17. Jongerius, A. L.; Jastrzebski, R.; Bruijninx, P. C. A.; Weckhuysen, B. M., *J. Catal.* **2012**, *285* (1), 315–323.
18. Petrocelli, F. P.; Klein, M. T., *Ind. Eng. Chem. Prod. Res. Dev.* **1985**, *24* (4), 635–641.
19. Zakzeski, J.; Weckhuysen, B. M., *ChemSusChem* **2011**, *4* (3), 369–378.
20. Frunzke, J.; Loschen, C.; Frenking, G., *J. Am. Chem. Soc.* **2004**, *126* (2), 3642–3652.
21. Yao, Z. S.; Wei, X. Y.; Lv, J.; Liu, F. J.; Huang, Y. G.; Xu, J. J.; Chen, F. J.; Huang, Y.; Li, Y.; Lu, Y.; et al., *Energy and Fuels* **2010**, *24* (3), 1801–1808.
22. Carlsen, P. H. J.; Katsuki, T.; Martin, V. S.; Sharpless, K. B., *J. Org. Chem.* **1981**, *46* (19), 3936–3938.
23. Mander, L. N.; Williams, C. M., *Tetrahedron* **2003**, *59* (8), 1105–1136.
24. Yang, D.; Zhang, C., *J. Org. Chem.* **2001**, *66* (14), 4814–4818.
25. Orita, H.; Hayakawa, T.; Takehira, K., *Bull. Chem. Soc. Jpn.* **1986**, *59* (8), 2637–2638.
26. Becke, A. D., *J. Chem. Phys.* **1993**, *98* (7), 5648–5652.
27. Nowicka, E.; Hickey, N. W.; Sankar, M.; Jenkins, R. L.; Knight, D. W.; Willock, D. J.; Hutchings, G. J.; Francisco, M.; Taylor, S. H., *Chem. - A Eur. J.* **2018**, *24* (47), 12359–

- 12369.
28. Ma, L.; Lu, D.; Liang, H.; Zhu, S.; Ding, Y.; Shan, L.; Chen, Y., *J. Fuel Chem. Technol.* **2013**, *41* (5), 513–522.
 29. Pardini, V. L.; Vargas, R. R.; Viertler, H.; Utlely, J. H. P., *Tetrahedron* **1992**, *48* (35), 7221–7228.
 30. Sedai, B.; Díaz-Urrutia, C.; Baker, R. T.; Wu, R.; Silks, L. A.; Hanson, S. K., *ACS Catal.* **2013**, *3* (12), 3111–3122.
 31. Beckham, G. T. *Lignin Valorization: Emerging Approaches*; Energy and Environment Series; Royal Society of Chemistry, 2018.
 32. Elder, T.; Berstis, L.; Beckham, G. T.; Crowley, M. F., *ACS Sustain. Chem. Eng.* **2017**, *5* (8), 7188–7194.
 33. Hanson, S. K.; Baker, R. T.; Gordon, J. C.; Scott, B. L.; Thorn, D. L., *Inorg. Chem.* **2010**, *49* (13), 5611–5618.
 34. Chinnappan, B.; Shikha Baskar, D.; Ranjit S. Dhillon, P. *Biomass Conversion: The Interface of Biotechnology, Chemistry and Materials Science*; 2012.
 35. Bajpai, P. Lignin. In *Carbon Fibre from Lignin*; 2017; pp 11–15.
 36. Lancefield, C. S.; Ojo, O. S.; Tran, F.; Westwood, N. J., *Angew. Chem. Int. Ed. Engl.* **2015**, *54* (1), 258–262.
 37. Lancefield, C. S.; Westwood, N. J., *Green Chem.* **2015**, *17*, 1–27.
 38. Montgomery, J. R. D.; Lancefield, C. S.; Miles-Barrett, D. M.; Ackermann, K.; Bode, B. E.; Westwood, N. J.; Lebl, T., *ACS Omega* **2017**, *2* (11), 8466–8474.
 39. Li, C.; Zhao, X.; Wang, A.; Huber, G. W.; Zhang, T., *Chem. Rev.* **2015**, *115* (21), 11559–11624.
 40. Shimizu, S.; Yokoyama, T.; Akiyama, T.; Matsumoto, Y., *J. Agric. Food Chem.* **2012**, *60* (26), 6471–6476.
 41. Forsythe, W. G.; Garrett, M. D.; Hardacre, C.; Nieuwenhuyzen, M.; Sheldrake, G. N., *Green Chem.* **2013**, *15* (11), 3031.
 42. Kilpeläinen, I.; Tervilä-Wilo, A.; Peräkylä, H.; Matikainen, J.; Brunow, G., *Holzforschung* **1994**, *48* (5), 381–386.
 43. Santos, R. B.; Capanema, E. A.; Balakshin, M. Y.; Chang, H. M.; Jameel, H., *J. Agric. Food Chem.* **2012**, *60* (19), 4923–4930.
 44. Conventional GPC Polymers and Molecular Weight; Agilent Technologies: Barcelona, 2012.
 45. Glöckner, G. *Polymer Characterization by Liquid Chromatography*; Journal of Chromatography Library; Elsevier Science, 1987.
 46. Lisperguer, J.; Perez, P.; Urizar, S., *J. Chil. Chem. Soc.* **2009**, *54* (4), 460–463.
 47. Pérez, N.; Delgado, L., *Lat. Am. Appl. Res.* **2012**, *42*, 223–228.
 48. Xu, A.; Li, W.; Zhang, Y.; Xu, H., *RSC Adv.* **2016**, *6* (10), 8377–8379.
 49. Luong, N. D.; Binh, N. T. T.; Duong, L. D.; Kim, D. O.; Kim, D. S.; Lee, S. H.; Kim, B. J.; Lee, Y. S.; Nam, J. Do., *Polym. Bull.* **2012**, *68* (3), 879–890.
 50. Elhelece, W. A.; Abousekkina, M. M., *Eur. Chem. Bull.* **2013**, *2* (6), 328–334.
 51. Ibrahim, M. N. M.; Nor, M. Y. N.; Azian, H., *J. Appl. Sci.* **2006**, *6* (2), 292–296.
 52. Armstrong, R. D.; Hirayama, J.; Knight, D. W.; Hutchings, G. J., *ACS Catal.* **2019**, *9* (1), 325–335.
 53. Pu, Y.; Cao, S.; Ragauskas, A. J., *Energy Environ. Sci.* **2011**, *4* (9), 3154.
 54. Balakshin, M.; Capanema, E., *J. Wood Chem. Technol.* **2015**, *35* (3), 220–237.

55. Granata, A.; Argyropoulos, D. S., *J. Agric. Food Chem.* **1995**, *43* (6), 1538–1544.
56. Jiang, Z. -H H. and A. D. S. and G. A.; Argyropoulos, D. S.; Granata, A., *Magn. Reson. Chem.* **1995**, *33* (5), 375–382.
57. Constant, S.; Wienk, H. L. J. J.; Frissen, A. E.; Peinder, P. De; Boelens, R.; Van Es, D. S.; Grisel, R. J. H. H.; Weckhuysen, B. M.; Huijgen, W. J. J. J.; Gosselink, R. J. A. A.; et al., *Green Chem.* **2016**, *18* (9), 2651–2665.
58. Zawadzki, M.; Ragauskas, A., *Holzforschung* **2001**, *55* (3), 283–285.
59. Christophoridou, S.; Dais, P., *J. Agric. Food Chem.* **2006**, *54* (3), 656–664.
60. Nagy, M.; Kosa, M.; Theliander, H.; Ragauskas, A. J., *Green Chem.* **2010**, *12* (1), 31–34.
61. Tohmura, S.; Argyropoulos, D. S., *J. Agric. Food Chem.* **2001**, *49* (2), 536–542.
62. You, T.; Xu, F. Applications of Molecular Spectroscopic Methods to the Elucidation of Lignin Structure. In *Applications of Molecular Spectroscopy to Current Research in the Chemical and Biological Sciences*; InTech, 2016.
63. Aguayo, M. G.; Ruiz, J.; Norambuena, M.; Teixeira Mendonça, R., *Maderas. Cienc. y Tecnol.* **2015**, *17* (3), 625–636.
64. Koda, K.; Gaspar, A. R.; Yu, L.; Argyropoulos, D. S., *Holzforschung* **2005**, *59* (6), 612–619.
65. Lange, H.; Decina, S.; Crestini, C., *Eur. Polym. J.* **2013**, *49* (6), 1151–1173.
66. Nowicka, E.; Clarke, T. J.; Sankar, M.; Jenkins, R. L.; Knight, D. W.; Golunski, S.; Hutchings, G. J.; Willock, D. J.; Francisco, M.; Taylor, S. H., *Chem. - A Eur. J.* **2018**, *24* (3), 655–662.

CATALYTIC CONVERSION OF BIOMASS

CHAPTER 6. CONCLUSIONS AND FUTURE WORK.

S. Guadix-Montero
CARDIFF UNIVERSITY | CARDIFF CATALYSIS INSTITUTE

6 General conclusions and prospects

6.1 Conclusions

The aims and objectives of this project were to develop catalytic systems for the conversion of molecules derived from sustainable feedstock such as triglycerides and lignocellulosic biomass. The work presented here reports two different approaches to control the C-C bond cleavage over the C-O bond cleavage, and vice versa, for different biomass-derived molecules. The first approach was to develop heterogeneous catalysts for the selective scission of the C-O bond without affecting the C-C bond during glycerol hydrogenolysis. The second approach was aimed at developing a homogeneous catalytic strategy for lignin depolymerisation, where the most recalcitrant C-C inter-unit bond in lignin was broken without affecting the C-O inter-unit bond.

In the first approach, it has been proved that the combination of two metals can effectively tune the selectivity for specific bond cleavage. Chapter 3 reports, for the first time, the design of a noble Ru-based bimetallic catalyst containing Pd for glycerol hydrogenolysis. The catalytic performance of this catalyst was compared to other bimetallic such as PtRu and the monometallic Ru, Pd and Pt catalysts. This work investigates not only the effect of incorporating a second noble metal but also the study of the heat treatment along with the oxidation species present on the catalysts. Also, it explores the role of the support in aqueous phase reaction.

The results show that both bimetallic PtRu and PdRu catalysts are more active than their respective monometallic catalyst, Pt and Pd. The presence of a nanoalloys is required to achieve better C3 products yields, without compromising the activity, which agrees with the energy profiles obtained from computational studies. The use of the admixture Pd+Ru or Pt+Ru catalysts also confirmed this hypothesis, since their catalytic behaviour resembled the Ru monometallic catalysts. Mechanistically it is thought that in the bimetallic catalyst, Pd or Pt block the active sites of the Ru metal. Indeed, the presence of Ru metal was found the most active metal site on the catalyst, which allows the further dehydration and C-C bond cleavage of liquid products. Characterisation of the catalyst by SEM, TEM and EDX indicated that the catalyst maintained high dispersity with similar particle size distribution (*c.a.* 2 nm). XPS analysis proved that the catalyst calcined after reduction (R+C) shows a higher percentage of metal oxide species, which make them less active than the just reduced catalyst (R). However, high conversion usually leads to an increase of production of gas-phase products, such as CH₄

via the undesired C-C cleavage. On the contrary, the oxidation state of Pd varies with the nature of the support.

Between both bimetallic, PdRu/TiO₂ catalyst presents an exciting prospect for industrial use, where the long-term stability of a catalyst is highly desired. Indeed, this catalyst also showed excellent performance in the fix-bed reactors in comparison to the batch reactor configuration. The importance of choosing an appropriate support for the aqueous phase hydrogenolysis of glycerol was also demonstrated. The co-impregnation of the Pd and Ru metal precursors on different supports exhibited a change in the surface properties, which was more significant for the mesoporous metal oxides.

Among the different catalysts tested, PdRu over ZSM5 (80:1) zeolite showed the highest activity. The activity of PdRu/ZSM5 was similar to that of Ru/TiO₂ just reduced catalyst, obtaining a high percentage of gas phase products. The zeolite framework and acidity are found to play a crucial role in the activity of the catalyst for this reaction, following the order: ZSM5 >> MOR > HY. According to the XRD and UV-Raman results, ZSM5 and MOR maintain their structure during the catalyst synthesis and the reaction conditions. However, a decrease of the catalyst crystallinity was observed for the zeolite-based catalysts and big nanoparticles were present in the fresh catalyst. These were found to be Pd-rich, evidenced by a reflection in XRD along with SEM and TEM. Characterisation of the spent catalyst suggested that the metal was re-dispersed on the support, but no leaching was detected in the reaction mixture analysed by ICP after the reaction.

Overall, it can be concluded that bifunctional catalysts that contain both metal and acidic functionalities are crucial for the efficient hydrogenolysis of glycerol. The activity of the catalyst is influenced strongly by the acid properties of the support. Indeed, whether the acidity is through Lewis or Brønsted acid sites can change the selectivity. It was confirmed that a catalyst with more Lewis acid sites such as PdRu/ZSM5 favours not only the dehydration of glycerol but also the further hydrogenolysis to C1 products. From this study, it can be established that a moderate density of strong acid sites is required to have the desired catalyst performance. In term of 1,2-PDO yield, PdRu/TiO₂ was the best catalyst tested with *ca.* 60 % of glycerol conversion in 16 h (achieving a 1,2-PDO yield of 30 %). This is followed by PdRu/ZSM5 (80:1) with a 23 % yield to 1,2-PDO. These results should lead to further catalyst design studies to develop significantly more active and selective catalysts.

Regarding the second approach, the oxidation of lignin was studied using different model compounds. The data obtained from the application of Ruthenium Ion Catalysed Oxidation (RICO) reactions proved that it is a promising tool to achieve the breaking of the most recalcitrant C-C bonds in lignin model compounds. The work exhibits that the RICO reaction protocol differs depending on the substrate, along with the analytical methodologies needed in each case. Indeed, the development of a ternary solvent system of water-acetonitrile-ethyl acetate for the metal ions removal from the reaction mixture is crucial for qualitative and quantitative analysis.

The oxidation of different model compounds was accomplished and the cleavage of both C-O (β -O-4') and specially C-C (5-5', β -1' and β -5') inter-unit linkages was successfully achieved in lignin model compounds and polymers. For small lignin model compounds such as biphenyl (5-5') and bibenzyl (β -1), the cleavage of the C-C bond was feasible, achieving significant conversion with the formation of carboxylic acids with one phenyl ring. For more complex model compounds, depolymerisation of lignin model hexamer was followed by APC and NMR studies at short reaction times using catalytic amounts of ruthenium. 2-dimensional HSQC experiment proved that both α and β environments were easily disrupted in the β -O-4 inter-unit linkage. More importantly, ^{31}P -NMR confirmed that the cleavage of the more recalcitrant 5-5' linkage was also achieved, which was also suggested by ^{13}C and HMBC NMR experiment. This is one of the major accomplishments of this project. Because of the high bond dissociation energy of this C-C inter-unit linkage, many researchers have previously failed to achieve this target. Using RICO, the inter-unit linkage that seems more challenging to break fully was the β -5' phenylcoumaran structure of the hexamer. These β -5 bonds were substantially cleaved. However, part of them remained in the form of 2-methoxy-4-(7-methoxy-3-methyl-5-propyl-2,3-dihydrobenzofuran-2-yl)phenol, compound isolated using column chromatography and identified by NMR.

In addition, this thesis also reports an NMR methodology, to quantify the potential cleavage of inter-unit linkages present in lignin. This approach presents a tool to break the more challenging C-C inter-unit linkages effectively. Indeed, the full depolymerisation of complex lignin model compounds into smaller aromatic compounds achieved exhibit the potential of this method to be used for technical lignin.

In summary, the thesis findings extend our knowledge beyond the state-of-the-art reported earlier in the areas of catalytic biomass conversion. The results and achievements are moving us a step closer to accomplish a green and sustainable society.

6.2 Future work

The study presented in this thesis will be a useful guide to further develop catalysts for glycerol hydrogenolysis to propanediols with high selectivity. It is recommended that the control of the catalyst properties such as acid strength, the amount of appropriate strong acid sites, to obtain the desired product selectively. ^1H and ^{27}Al double-quantum magic-angle spinning (DQ-MAS) Solid-State NMR Spectroscopy could be used to investigate the Brønsted/Lewis acid synergy and spatial proximities of acid sites in PdRu/ZSM-5 and PdRu/MOR zeolites.¹ The catalytic properties of the most promising catalysts such as PdRu over TiO_2 and ZSM5 (80:1) could be improved by tuning their acidities. The results obtained by introducing tungsten into titania (PdRu/ $\text{Ti}_{0.9}\text{W}_{0.1}\text{O}_2$) suggest that this route can also achieve improvements in selectivity toward propanediols. However, the conversion was very low for this catalyst. More investigation into the role of this W doped catalyst and characterisation needs to be done. As future work, it is proposed the exploration of the potential of the photocatalytic properties of this catalyst for this glycerol hydrogenolysis.²

It was found that when the aqueous phase hydrogenolysis of glycerol was performed in a fix-bed reactor, the reaction rate was better compared to when it was carried out in an autoclave batch reactor. One impressive result that would be worthy of investigating is the effect of the *in-situ* reduction of PtRu/ TiO_2 catalyst in this kind of reactors. The *in-situ* reduced PtRu/ TiO_2 catalyst was less active compared to the *ex-situ* reduced PtRu/ TiO_2 catalyst. However, the *in-situ* reduced PtRu/ TiO_2 catalyst was more selective for C3 products, enhancing the formation of 1,3-PDO. Hence, it would be really recommended to study the effect of the *in-situ* reduction on the bimetallic catalyst and their oxidation states, and how important is the passivation of the catalyst for this reaction. Nevertheless, for PtRu/ TiO_2 , it has been discussed that the catalyst suffers from deactivation during the reaction; therefore, the reaction time is limited.

In the last years, there has been considerable interest in the idea of using for hydrogenolysis *in-situ* hydrogen production. Working without the addition of external H_2 would make this process more sustainable. Therefore, it is endorsed to perform a catalytic transfer hydrogenation (CTH) reaction using the bimetallic PdRu catalysts. A convenient H_2 donor source would be recommended, for instance, ethanol, formic acid (FA), or 2-propanol.³⁻⁹

The thesis findings for the application of RICO chemistry to complex model compounds should encourage researchers to use this optimised strategy in the oxidation of different technical lignin. It should be noted that the structure of this hexamer model compound contains many of the desired functional groups in lignin. However, it has still some limitations as a lignin model compound because of the lack of functional groups on the propyl side chain.¹⁰ The methodologies proposed in this work for the estimation of the potential cleavage of the β -O-4', β -5' and 5-5' inter-unit linkages can be used in the depolymerisation of technical lignin. However, more investigation of the reaction mechanism is recommended as the future work of this project. The theoretical pathways for forming phenylglyoxal through the [3+2] addition of ruthenium tetroxide and biphenyl was found the most efficient one. Performing DFT calculations of other model compounds would elucidate a better understanding of how the RuO₄ attack the aromatic ring of different inter-unit linkages. Also, it can be evaluated the differences in performance between phenolic and non-phenolic substituted model compounds of phenolic and nonphenolic model compounds using this RICO chemistry.

On the other hand, there were two severe issues in this method that would need to take into account: 1) the difficulty in the recovery and quantitative analysis of the organic product, water-soluble and highly volatile compounds, such as carboxylic acids; 2) the poor mass balance if the substrate: oxidant: catalyst is not optimised. This is something frequent observed in RICO chemistry. To find out all the products obtained using RICO chemistry two-dimensional gas chromatography (GC \times GC-MS/FID), 3D NMR and long-range correlation (HMBC) spectra could be used, including extensive IR spectroscopy.¹¹ After qualitative identification and quantification, it is then a case of optimising reaction conditions to ensure maximum efficiency of the catalytic process.

It is challenging to use technical lignin due to its complexity. For instance, Luo *et al.* used supercritical water and heterogeneous catalyst for the conversion of the highly substituted model compound.¹² The authors reported the breakage of the C-C bond to afford the formation of valuable aldehydes and benzoic acid. However, they fail in their attempt to reproduce their result using real lignin because of solubility issues. As mentioned in Chapter 1, the change of the solvent in RICO chemistry could modify the selectivity of products obtained. Therefore, it is recommended to perform RICO using a biphasic system and contrast the results with that in the monophasic solvent system. This could be an interesting approach to study, especially in the cases where the substrate is not soluble in acetonitrile.

As can be seen, the development of this thesis has also led to several future research projects related to the different lines of research presented throughout this work.

6.3 References

1. Yu, Z.; Li, S.; Wang, Q.; Zheng, A.; Jun, X.; Chen, L.; Deng, F., *J. Phys. Chem. C* **2011**, *115* (45), 22320–22327.
2. Folli, A.; Bloh, J. Z.; Armstrong, K.; Richards, E.; Murphy, D. M.; Lu, L.; Kiely, C. J.; Morgan, D. J.; Smith, R. I.; Mclaughlin, A. C.; et al., *ACS Catal.* **2018**, *8* (8), 6927–6938.
3. Yuan, J.; Li, S.; Yu, L.; Liu, Y.; Cao, Y., *Chinese J. Catal.* **2013**, *34* (11), 2066–2074.
4. Tedsree, K.; Li, T.; Jones, S.; Chan, C. W. A.; Yu, K. M. K.; Bagot, P. a J.; Marquis, E. a; Smith, G. D. W.; Tsang, S. C. E., *Nat. Nanotechnol.* **2011**, *6* (5), 302–307.
5. Seretis, A.; Tsiakaras, P., *Fuel Process. Technol.* **2016**, *142*, 135–146.
6. Vasiliadou, E.; Lemonidou, A., *Catalysts* **2014**, *4* (4), 397–413.
7. Martin, A.; Armbruster, U.; Gandarias, I.; Arias, P. L., *Eur. J. Lipid Sci. Technol.* **2013**, *115* (1), 9–27.
8. Musolino, M. G.; Scarpino, L. A.; Mauriello, F.; Pietropaolo, R., *Green Chem.* **2009**, *11* (10), 1511.
9. Freitas, I. C.; Manfro, R. L.; Souza, M. M. V. M., *Appl. Catal. B Environ.* **2018**, *220*, 31–41.
10. Forsythe, W. G.; Garrett, M. D.; Hardacre, C.; Nieuwenhuyzen, M.; Sheldrake, G. N., *Green Chem.* **2013**, *15* (11), 3031.
11. Rinaldi, R.; Jastrzebski, R.; Clough, M. T.; Ralph, J.; Kennema, M.; Bruijnincx, P. C. A.; Weckhuysen, B. M., *Angew. Chemie - Int. Ed.* **2016**, *55* (29), 8164–8215.
12. Luo, F.; Zhou, T.; Li, X.; Luo, Y.; Shi, Z., *Org. Chem. Front.* **2015**, *2*, 1066–1070.

7 Appendix

7.1 EDX

Table 7-1 EDX - Elemental mapping for the 2 wt. % PdRu/TiO₂ catalyst nanoparticle

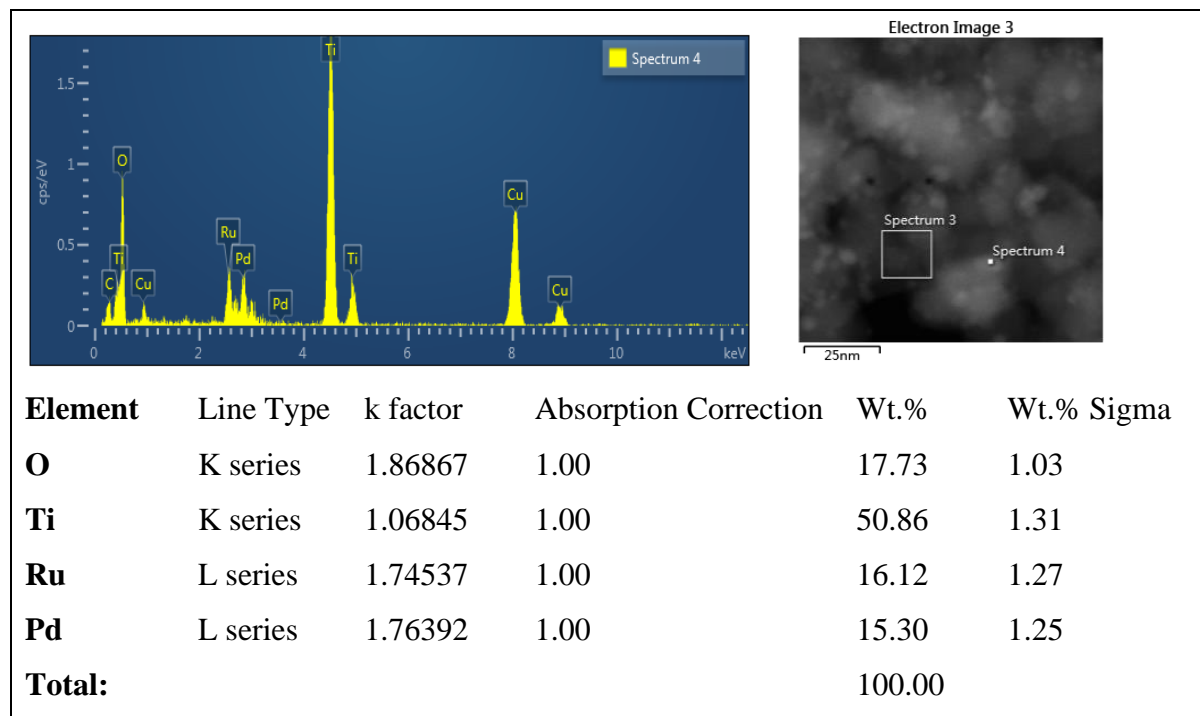
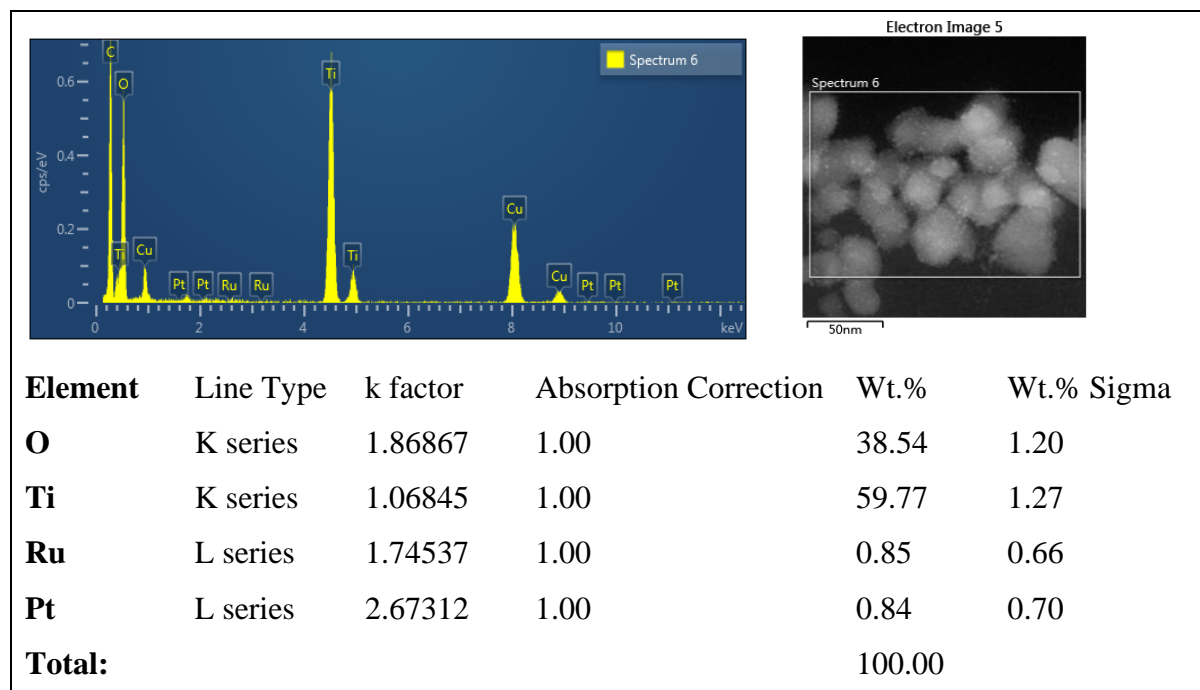


Table 7-2 EDX - Elemental mapping for the 2 wt. % PtRu/TiO₂ catalyst



7.2 SEM-EDX

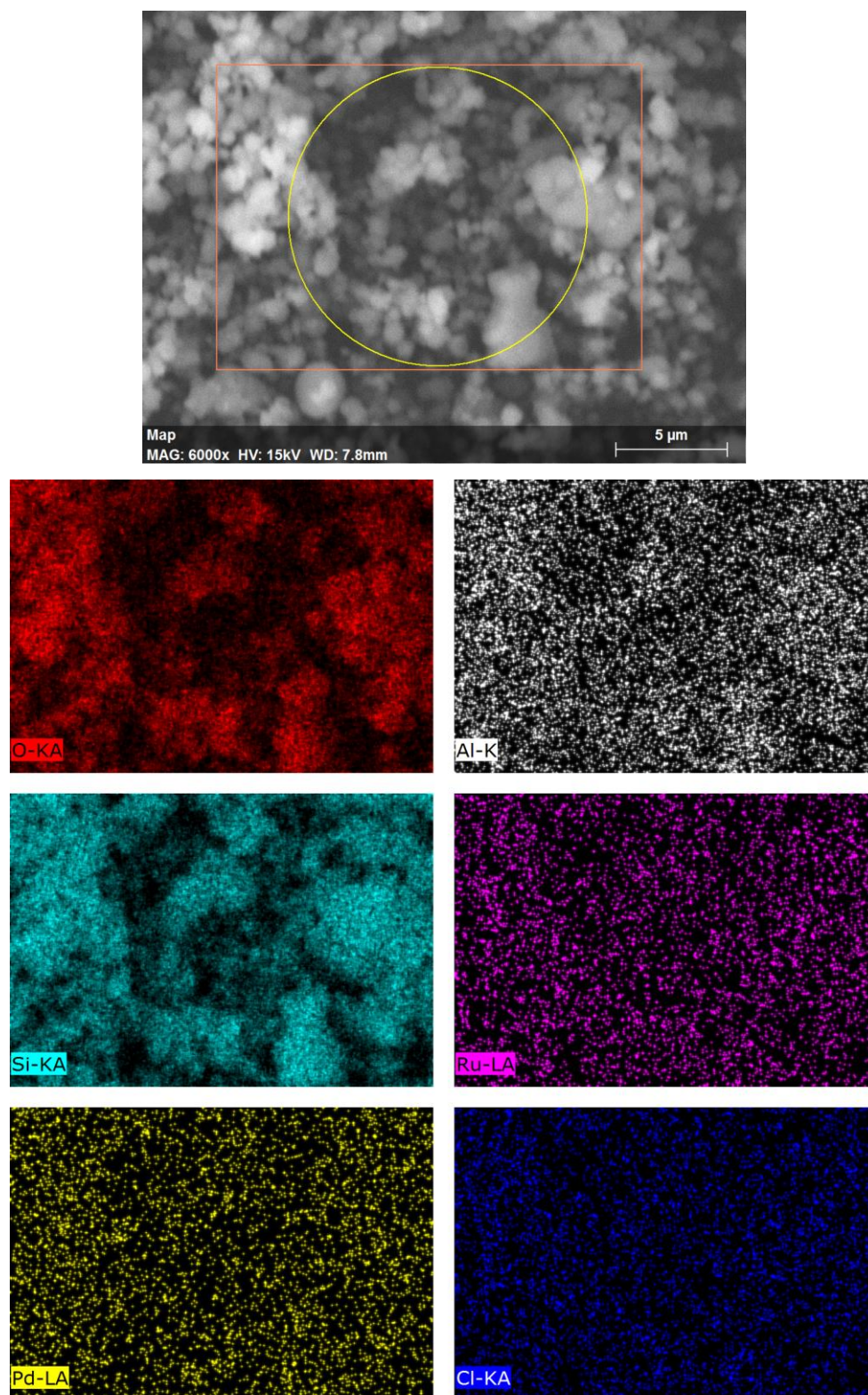


Figure 7-1 Elemental mapping for the 2 wt. % PdRu/ZSM-5 (80:1) catalyst. Scale bar of 5 μm

7.3 XRD

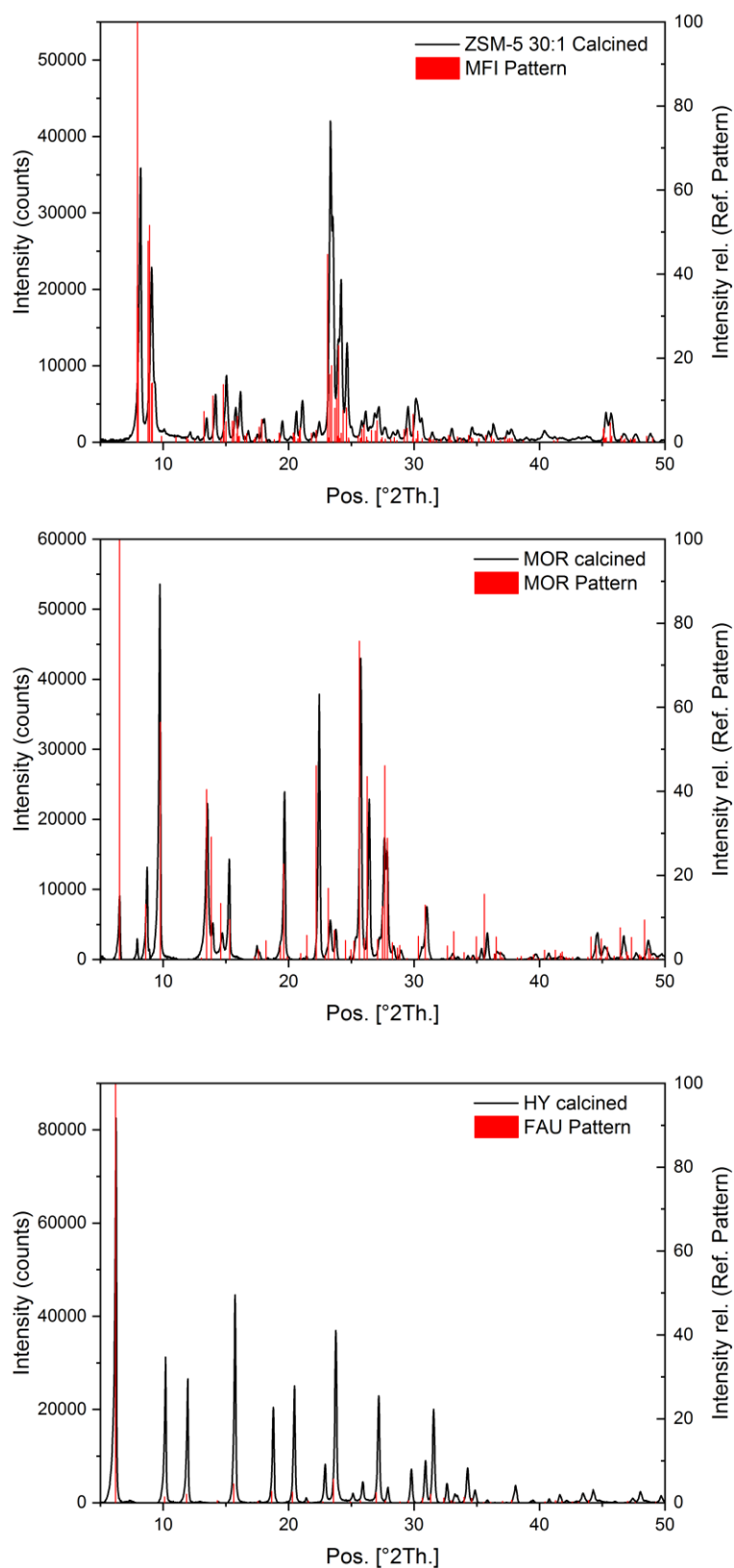


Figure 7-2 XRD spectra of the calcined ZSM5 [30:1], MOR and HY calcined. XRD Diffraction patterns for the MFI, MOR and FAU frameworks (red bands) overly.⁵⁰

7.4 NH₃-TPD

Peak Analysis

Data Set:RuPd/ZSM5[30:1]

BaseLine:Constant

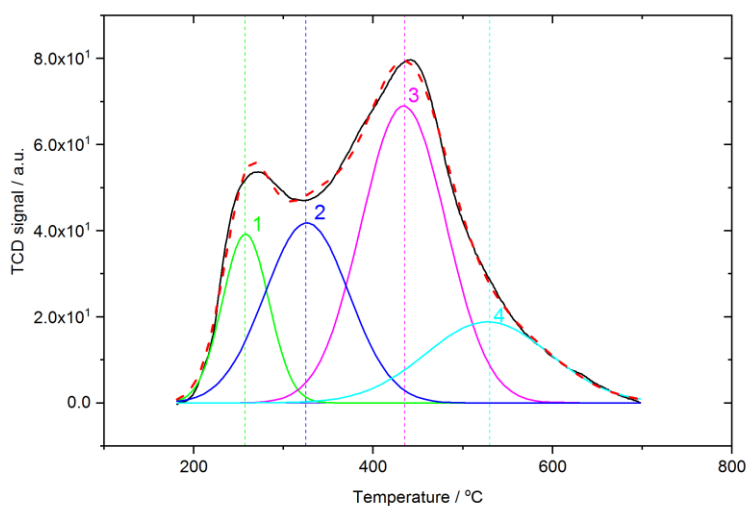
Chi²=1.57255E+000

Adj. R-Square=9.97570E-001

of Data Points=424.

SS=6.47892E+002

Degree of Freedom=412.



Fitting Results

Peak Index	Peak Type	Area Intg	FWHM	Max Height	Center Grvty	Area IntgP
1.	Gaussian	2533,80173	60,84859	39,17881	257,75539	13,44026
2.	Gaussian	8142,82908	110,96551	68,93744	433,97694	43,1927
3.	Gaussian	4930,01635	110,92325	41,79708	326,14804	26,1507
4.	Gaussian	3245,68071	163,20696	18,81339	527,6147	17,21634

Peak Analysis

Data Set:RuPd/ZSM5-50:1

BaseLine:Constant

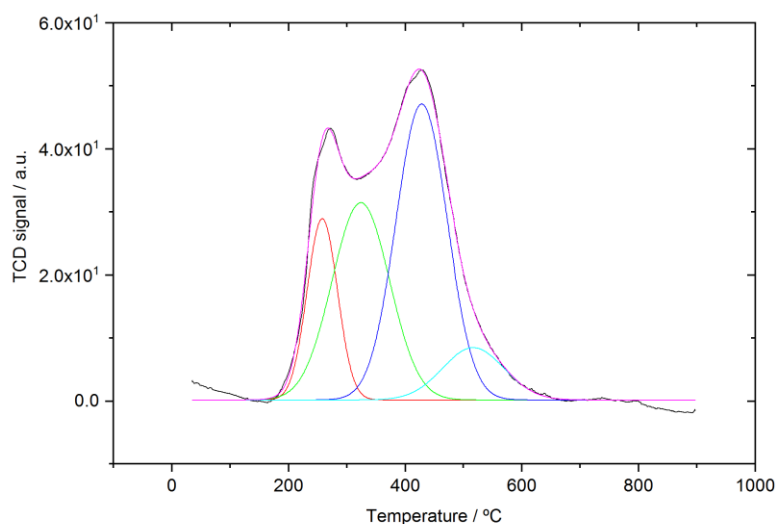
Chi²=9.1765E-001

Adj. R-Square=9.99718E-001

of Data Points=721

SS=6.496952E+002

Degree of Freedom=708



Fitting Results

Peak Index	Peak Type	Area Intg	FWHM	Max Height	Center Grvty	Area IntgP
1.	Gaussian	1874,66425	61,21426	28,76884	257,64368	11,92757208
2.	Gaussian	3859,01971	115,80917	31,30404	323,73165	32,55451016
3.	Gaussian	5186,44288	103,7617	46,95581	427,952	46,04536682
4.	Gaussian	1105,50843	125,08989	8,30233	516,58984	9,472550946

Peak Analysis

Data Set: RuPd/ZSM5-80:1

BaseLine: Constant

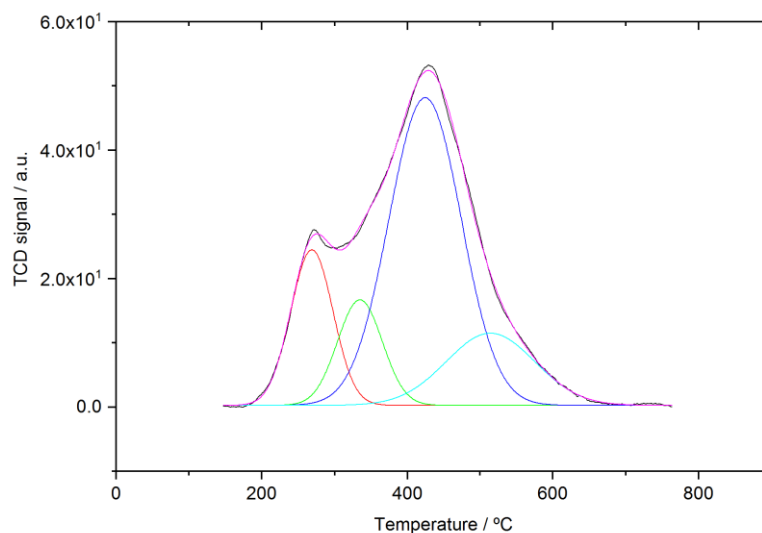
Chi²=1.5291E-001

Adj. R-Square=9.99948E-001

of Data Points=499

SS=7.431254E+001

Degree of Freedom=486



Fitting Results

Peak Index	Peak Type	Area Intg	FWHM	Max Height	Center Grvty	Area IntgP
1.	Gaussian	1765.38247	68.45308	24.48041	268.64651	16.44298223
2.	Gaussian	1268.61535	72.45548	16.70443	334.62245	11.81789703
3.	Gaussian	5975.23419	117.13366	48.1758	424.18024	55.65404171
4.	Gaussian	1726.95659	144.42869	11.48684	514.06167	16.08507902

Peak Analysis

Data Set: RuPd/ZSM5-[200-400:1]

BaseLine: Constant

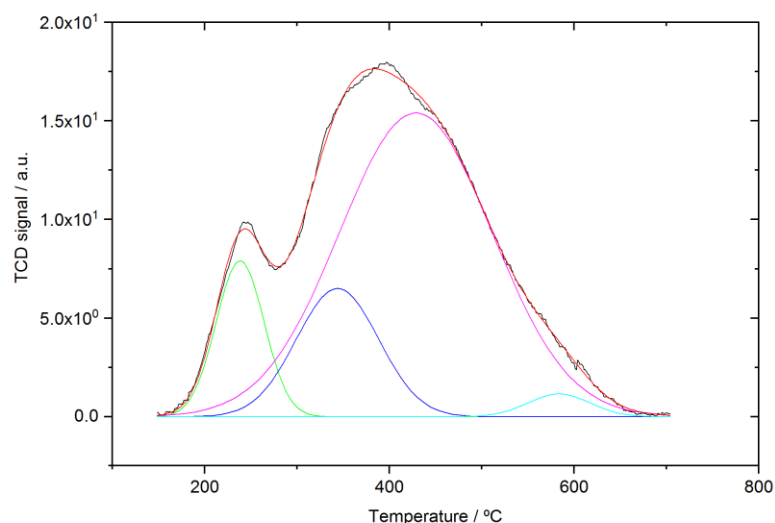
Chi²=3.41061E-002

Adj. R-Square=9.99044E-001

of Data Points=453.

SS=1.50408E+001

Degree of Freedom=441.



Fitting Results

Peak Index	Peak Type	Area Intg	FWHM	Max Height	Center Grvty	Area IntgP
1.	Gaussian	515.28757	61.33346	7.89479	238.30531	11.36148
2.	Gaussian	724.29559	104.70268	6.49873	343.70578	15.96986
3.	Gaussian	3198.35123	195.27567	15.39909	428.57531	70.51985
4.	Gaussian	97.45679	79.49512	1.1519	583.79932	2.14881

Peak Analysis

Data Set: RuPd/Mordenite

BaseLine: Constant

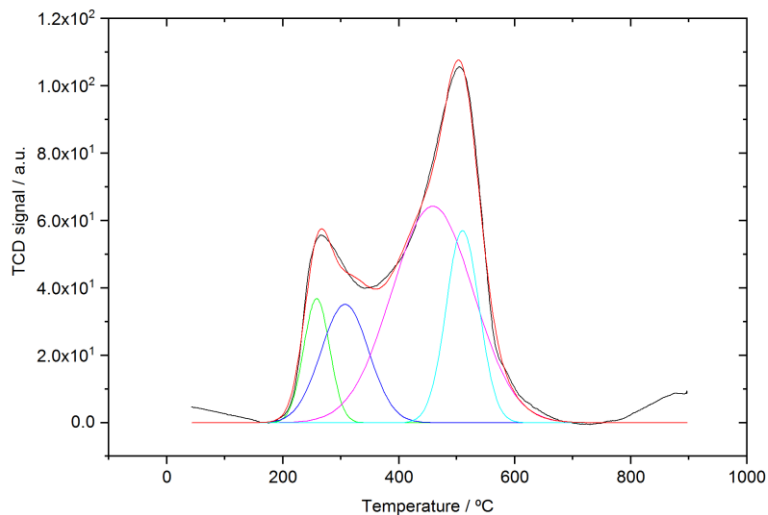
Chi²=1.00245E+001

Adj. R-Square=9.89218E-001

of Data Points=715.

SS=7.04722E+003

Degree of Freedom=703.



Fitting Results

Peak Index	Peak Type	Area Intg	FWHM	Max Height	Center Grvty	Area IntgP
1.	Gaussian	2062,79565	52,63938	36,81402	258,32253	9,76319
2.	Gaussian	3616,60681	96,75964	35,11356	307,02591	17,11737
3.	Gaussian	11349,12833	165,98817	64,23225	458,07594	53,71533
4.	Gaussian	4099,75559	67,5757	56,99479	510,12292	19,40411

Peak Analysis

Data Set: RuPd/HY Zeolite

BaseLine: Constant

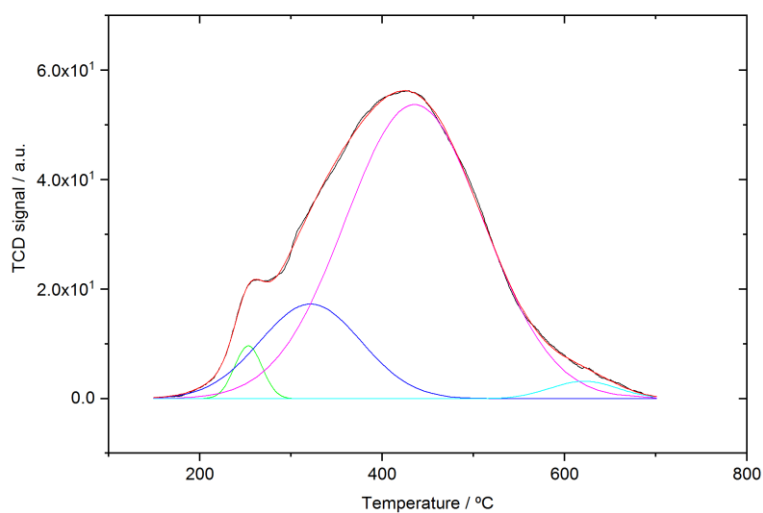
Chi²=1.56649E-001

Adj. R-Square=9.99586E-001

of Data Points=459.

SS=7.00222E+001

Degree of Freedom=447.



Fitting Results

Peak Index	Peak Type	Area Intg	FWHM	Max Height	Center Grvty	Area IntgP
1.	Gaussian	365,34388	35,61069	9,63805	253,10758	2,75504
2.	Gaussian	2404,72204	130,90534	17,27445	321,23981	18,13388
3.	Gaussian	10200,52493	178,42888	53,72295	435,23404	76,92163
4.	Gaussian	290,34166	87,23638	3,17807	621,3806	2,18945

Peak Analysis

Data Set:RuPd/Ti0,9W0,1O2

Date:03/02/2019

BaseLine:Constant

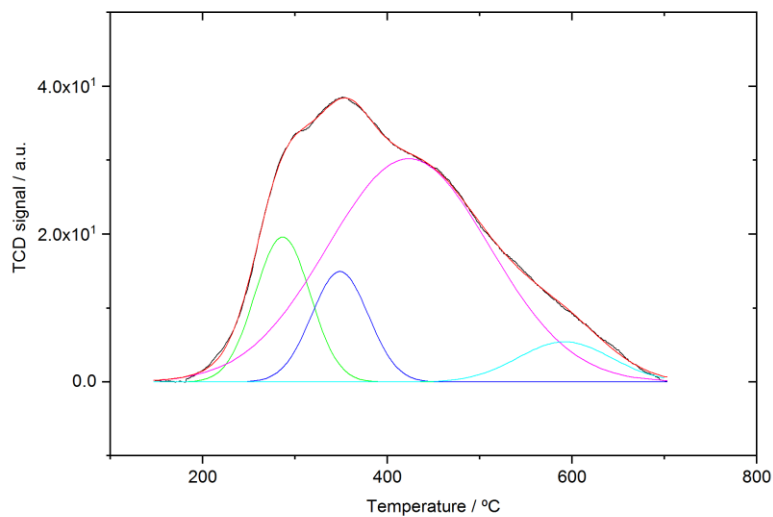
Chi²=6.25439E-002

Adj. R-Square=9.99634E-001

of Data Points=449.

SS=2.73317E+001

Degree of Freedom=437.



Fitting Results

Peak Index	Peak Type	Area Intg	FWHM	Max Height	Center Grvty	Area IntgP
1.	Gaussian	1470,01689	70,43522	19,60654	286,42499	14,77326
2.	Gaussian	1149,25203	72,24987	14,94328	348,47385	11,54966
3.	Gaussian	6652,393	207,30059	30,19504	423,02241	66,85467
4.	Gaussian	678,86613	118,88828	5,44055	592,05126	6,82241

Peak Analysis

Data Set:RuPd/TiO2

BaseLine:Constant

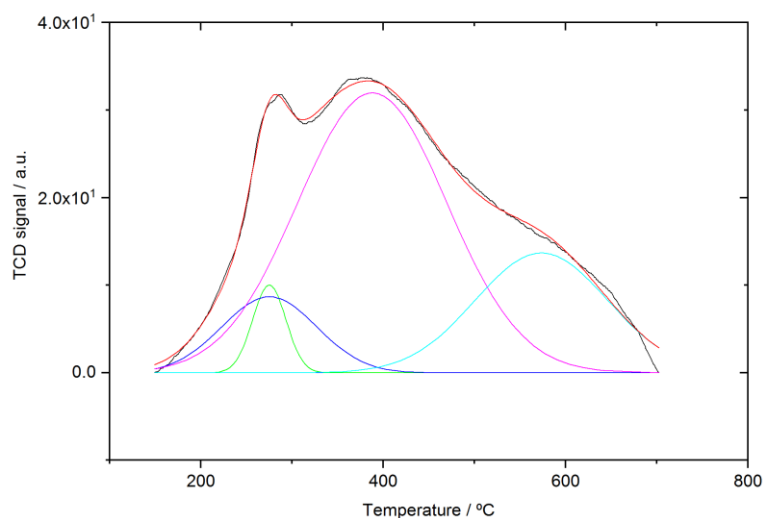
Chi²=3.27120E-001

Adj. R-Square=9.97038E-001

of Data Points=450.

SS=1.43279E+002

Degree of Freedom=438.



Fitting Results

Peak Index	Peak Type	Area Intg	FWHM	Max Height	Center Grvty	Area IntgP
1.	Gaussian	458,90766	43,09157	10,00462	274,9975	4,35467
2.	Gaussian	1123,56759	122,48564	8,6846	274,99819	10,66176
3.	Gaussian	6559,84015	193,26986	31,94535	387,93548	62,24764
4.	Gaussian	2395,98074	171,01888	13,67796	573,60072	22,73594

Peak Analysis

Data Set: RuPd/SiO2

BaseLine: Constant

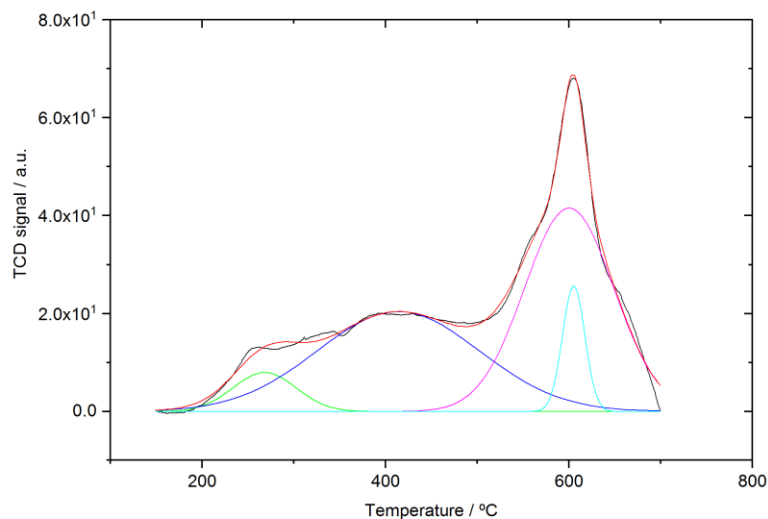
Chi²=1.06576E+000

Adj. R-Square=9.95368E-001

of Data Points=446.

SS=4.62540E+002

Degree of Freedom=434.



Fitting Results

Peak Index	Peak Type	Area Intg	FWHM	Max Height	Center Grvty	Area IntgP
1.	Gaussian	690,91246	81,45899	7,97046	267,97598	6,2933
2.	Gaussian	4528,17127	208,95035	20,40094	413,87426	41,24569
3.	Gaussian	4972,05087	114,89028	41,52307	600,24935	45,28885
4.	Gaussian	787,39682	28,89042	25,60399	605,2655	7,17215

Peak Analysis

Data Set: RuPd/Al2O3

BaseLine: Constant

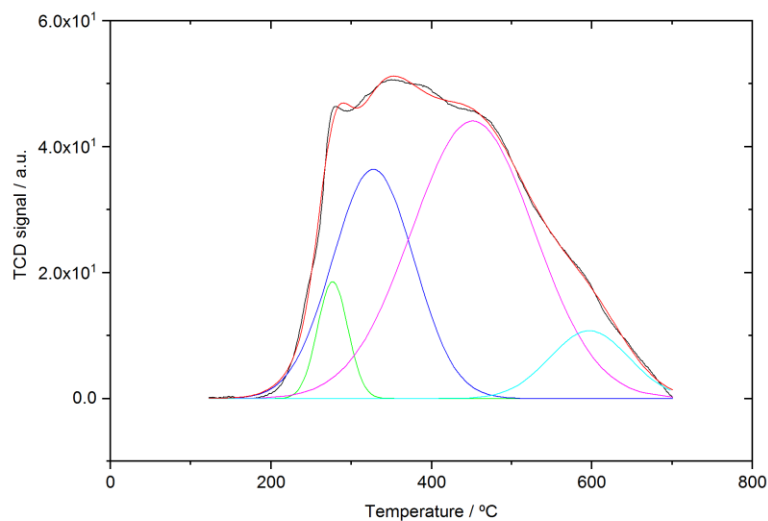
Chi²=4.83192E-001

Adj. R-Square=9.98671E-001

of Data Points=471.

SS=2.21785E+002

Degree of Freedom=459.



Fitting Results

Peak Index	Peak Type	Area Intg	FWHM	Max Height	Center Grvty	Area IntgP
1.	Gaussian	878,15034	44,50546	18,53631	276,77845	5,75384
2.	Gaussian	4620,768	119,28882	36,39706	327,3673	30,27633
3.	Gaussian	8456,24927	180,37098	44,06888	451,71834	55,40728
4.	Gaussian	1306,81525	116,15882	10,758	596,85643	8,56255

7.5 RICO

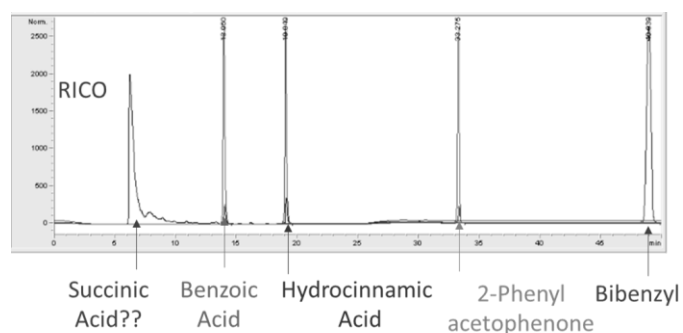


Figure 7-3 HPLC chromatogram Bibenzyl after RICO reaction corresponding to the organic phase in Acetonitrile after extractions overlapped with the commercial standards of the product identified

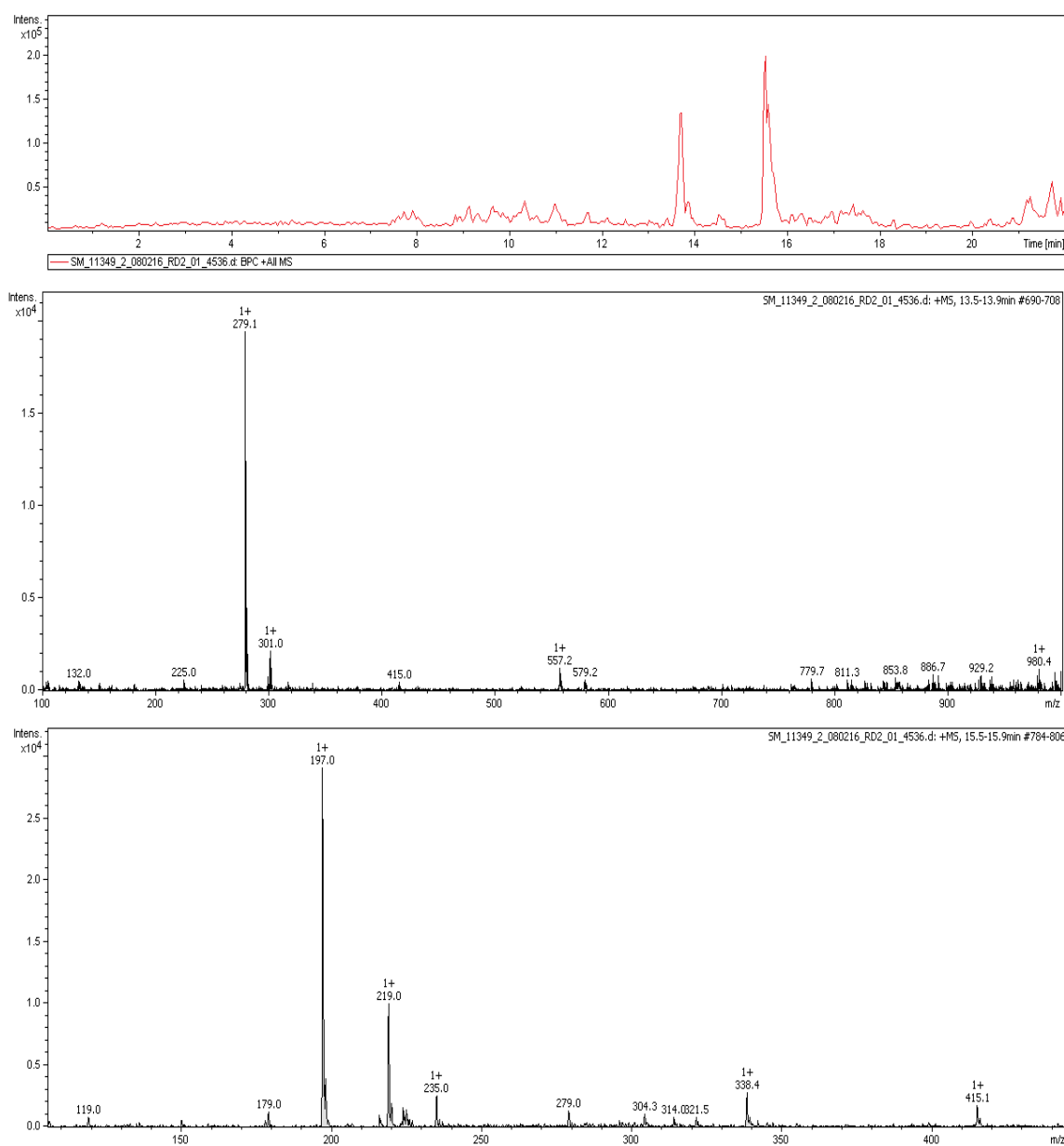


Figure 7-4 LC-MS results for the 2h RICO reaction sample of bibenzyl, 2-phenylacetophenone

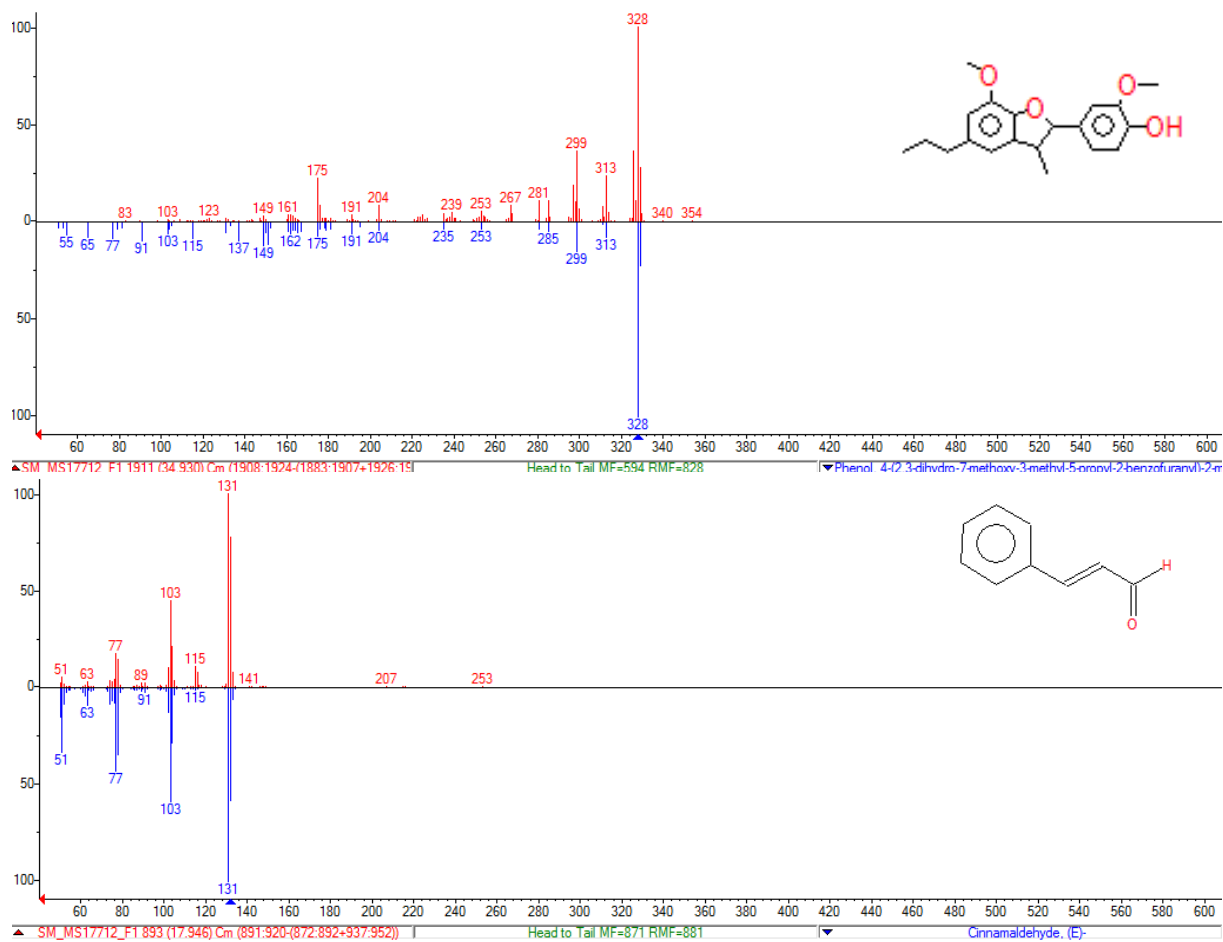


Figure 7-5 Head-to-tail comparison of mass spectra of some of the products obtained from the oxidation of the hexamer using RICO.

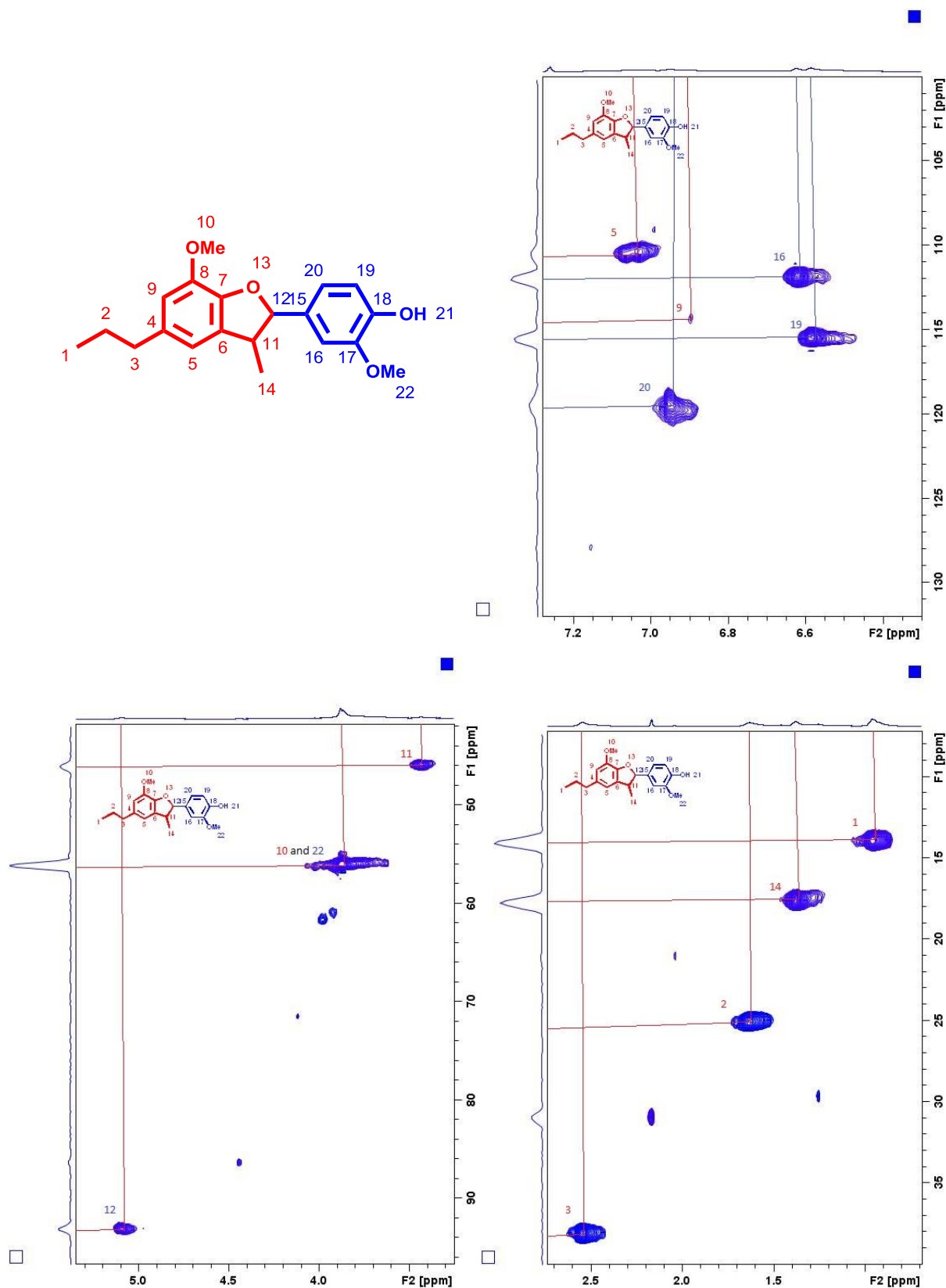


Figure 7-6 Partial 2D-HSQC NMR spectra of the product obtained from the oxidation of hexamer using RICO.

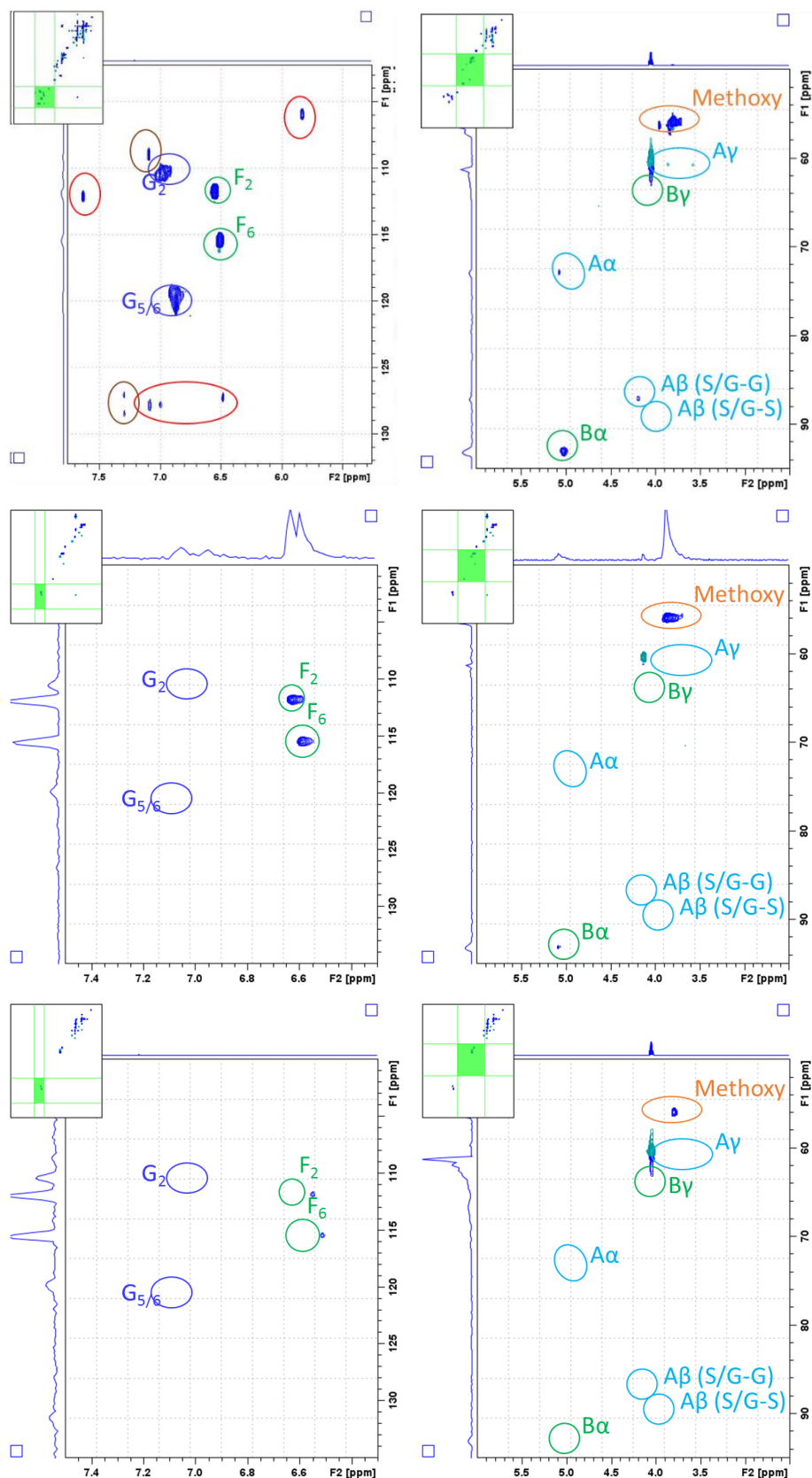


Figure 7-7 Partial 2D-HSQC NMR spectra of the fractions (2,3 and 4) obtained from column chromatography to the organic phase extracted from the reaction mixture after 1 h of RICO reaction of the hexamer.